First-Principles Investigations of Structural Vibrations and Point Defects in 2D Materials: Insights from Electronic Structure Methods and Raman Spectroscopy

Dissertation
zur Erlangung des Doktorgrades
an der Fakultät für Mathematik, Informatik und Naturwissenschaften
Fachbereich Physik
der Universität Hamburg

vorgelegt von
Alaa Hussein Akkouch

Hamburg
2023

Gutachter/innen der Dissertation:	Dr. Mariana Rossi
	Prof. Dr. Michael Potthoff
Zusammensetzung der Prüfungskommission:	Prof. Dr. Daniela Pfannkuche
	Prof. Dr. Michael Potthoff
	Dr. Mariana Rossi
	Dr. Christian Carbogno
	Dr. Katharina J. Franke
Vorsitzender der Prüfungskommission:	Prof. Dr. Daniela Pfannkuche
Datum der Disputation:	27.11.2023
Vorsitzender Fach-Promotionsausschusses PHYSIK:	Prof. Dr. Wolfgang J. Parak
Leiter des Fachbereichs PHYSIK:	Prof. Dr. Günter H. W. Sigl
Dekan der Fakultät MIN:	Prof. Dr. Heinrich Graener

Eidesstattliche Versicherung

Hiermit versichere ich an Eides statt, die vorliegende Dissertationsschrift selbst verfasst und keine anderen als die angegebenen Hilfsmittel und Quellen benutzt zu haben.
Die eingereichte schriftliche Fassung entspricht der auf dem elektronischen Speichermedium.
Die Dissertation wurde in der vorgelegten oder einer ähnlichen Form nicht schon einmal in einem früheren Promotionsverfahren angenommen oder als ungenügend beurteilt.

Hamburg, den 15.12.2023

Preface

The research for this comprehensive dissertation was carried out between April 2019 and August 2023 at the Fritz Haber Institute of the Max Planck Society and the Max Planck Institute for the Structure and Dynamics of Matter. Throughout this period, Dr. Mariana Rossi provided guidance and supervision. The contents of this thesis draw upon the publications outlined in the List of publications section.

Acknowledgments

I would like to express my sincere gratitude to my supervisor, Mariana Rossi, for her guidance, support, and insightful supervision throughout my Ph.D.

I am grateful to all my colleagues at the Fritz Haber Institute and Max Planck Institute for the Structure and Dynamics of Matter. I would like to thanks each and every one of them. Special appreciation goes to the members of my research group, particularly Alan, Dimitri, Yair, and Nathaniel.

I would like to thank my best friend, Hebatallah, for being an unwavering source of support and a good listener throughout my Ph.D. journey and always.

I wish also to acknowledge the German Research Foundation (Deutsche Forschungsgemeinschaft) and Matthias Scheffler for their financial support, which has made this research possible.

أود أن أعبر عن امتناني العميق لعائلتي - أمي وأبي وحمودي وأسعد وميمو - على دعمهم الثابت طوال رحلتي. لقد كنتم مصدر تحفيزي الأول، مما يدفعني لتحقيق أي شيء أضعه في ذهني. حضوركم في حياتي جعل كل شيء أسهل وأخف عبئًا. معرفة أنكم بجانبي يمنحني القوة والثقة للتغلب على أي تحدي ومتابعة أحلامي. سلامتكم وسعادتكم هما الأهم بالنسبة لي، وأنا ممتنة إلى الأبد لمحبتكم ودعمكم. شكرًا لكم على الايمان الدائم بي والوقوف بجانبي في هذه الرحلة.

Contents

Abstract

The characterization of the properties of two-dimensional transition metal dichalcogenides (TMDC) at the atomic scale is currently an important topic of research with potential implications in diverse areas such as medicine and optoelectronics. In this context, Raman spectroscopy emerges as a powerful analytical technique for material characterization. There has been extensive interest in the application of Raman spectroscopy to two-dimensional (2D) materials like graphene and TMDCs. In particular, TMDC monolayers that exhibit intriguing electronic properties that can be tuned at the nanoscale. While Raman spectroscopy has been widely used in TMDCs to identify the number of layers and detect high concentration of defects, it presents certain limitations in terms of resolution and sensitivity. To overcome some of these limitations, a new technique called Tip-Enhanced Raman Spectroscopy (TERS) has emerged to improve the optical resolution and surpass the diffraction limit.

This thesis presents contributions to the development and application of TERS using a novel theoretical approach based on first principles calculations within the FHI-aims code package. The method combines Time-Dependent Density Functional Theory (TD-DFT) and Density Functional Perturbation Theory (DFPT), extending it to include the local field generated by the tip. Advantages of this approach are discussed, such as the effects of chemical interactions on TERS images, and the significance of considering chemical effects for accurate theory-experiment comparisons.

As Raman spectroscopy and TERS offer an interesting application in examining defects in TMDCs monolayers, a comprehensive study to investigate the structural, electronic, and vibrational properties of point defects in TMDC monolayers with M = Mo/W and X = S/Se is presented. This research was conducted with Density Functional Theory (DFT) calculations employing the HSE06 hybrid exchange correlation functional, along with many-body van der Waals (VDW) corrections. The study considers both neutral and charged point defects, compensating for charged defects using the virtual crystal approximation (VCA). The impact of finite temperature and pressure on defect stability is also taken into account. The vibrational contributions to the free energy is proved to be significant and cannot be disregarded. For instance, vibrational effects alter the stability transition between adatoms and monovacancies by approximately 300–400 K.

The computational technique for calculating TERS was applied to investigate defects in pristine and defective MoS_2 clusters. The results show potential future spectroscopic applications in defects investigation for 2D materials, as TERS enables the exploration of nanoscale spectroscopic fingerprints in the vicinity of the defect that was previously inaccessible with conventional Raman techniques.

Zusammenfassung

Die Charakterisierung der Eigenschaften von zweidimensionalen Übergangsmetall-Dichalcogeniden (TMDC) auf atomarer Ebene ist derzeit ein wichtiges Forschungsthema mit potenziellen Auswirkungen auf verschiedene Bereiche wie Medizin und Optoelektronik. In diesem Zusammenhang erweist sich die Raman-Spektroskopie als eine leistungsstarke Analysetechnik zur Materialcharakterisierung. Das Interesse an der Anwendung der Raman-Spektroskopie auf zweidimensionale (2D) Materialien wie Graphen und TMDCs ist groß. Insbesondere TMDC-Monoschichten weisen faszinierende elektronische Eigenschaften auf, die auf der Nanoskala eingestellt werden können. Während die Raman-Spektroskopie bei TMDCs weit verbreitet ist, um die Anzahl der Schichten zu bestimmen und eine hohe Konzentration von Defekten zu erkennen, weist sie gewisse Einschränkungen in Bezug auf Auflösung und Empfindlichkeit auf. Um einige dieser Einschränkungen zu überwinden, wurde eine neue Technik namens Tip-Enhanced Raman Spectroscopy (TERS) entwickelt, um die optische Auflösung zu verbessern und die Beugungsgrenze zu überwinden.

In dieser Arbeit wird ein Beitrag zur Entwicklung und Anwendung von TERS unter Verwendung eines neuartigen theoretischen Ansatzes auf der Grundlage von First-Principles-Berechnungen innerhalb des FHI-Aims-Codepakets vorgestellt. Die Methode kombiniert die zeitabhängige Dichtefunktionaltheorie (TD-DFT) und die Störungstheorie der Dichtefunktionaltheorie (DFPT) und erweitert sie um das von der Spitze erzeugte lokale Feld. Die Vorteile dieses Ansatzes werden erörtert, z. B. die Auswirkungen chemischer Wechselwirkungen auf TERS-Bilder und die Bedeutung der Berücksichtigung chemischer Effekte für genaue Vergleiche zwischen Theorie und Experiment.

Da die Raman-Spektroskopie und TERS eine interessante Anwendung bei der Untersuchung von Defekten in TMDC-Monolayern bieten, ist eine umfassende Studie zur Untersuchung der strukturellen, elektronischen und schwingungstechnischen Eigenschaften von Punktdefekten in TMDC-Monoschichten mit M=Mo/W und X=S/Se wird vorgestellt. Diese Untersuchung wurde mit Berechnungen der Dichtefunktionaltheorie (DFT) unter Verwendung des hybriden Austauschkorrelationsfunktionals HSE06 und Vielkörper-Van-der-Waals-Korrekturen (VDW) durchgeführt. Die Studie berücksichtigt sowohl neutrale als auch geladene Punktdefekte und kompensiert geladene Defekte mit Hilfe der virtuellen Kristallnäherung (VCA). Der Einfluss von Temperatur und Druck auf die Defektstabilität wird ebenfalls berücksichtigt. Die Beiträge von Schwingungen zur freien Energie erweisen sich als signifikant und können nicht vernachlässigt werden. Zum Beispiel verändern Schwingungseffekte den Stabilitätsübergang zwischen Adatomen und Monovakanzen um etwa 300-400 K.

Das Rechenverfahren zur Berechnung von TERS wurde zur Untersuchung von Defekten in reinen und defekten MoS_2-Clustern eingesetzt. Die Ergebnisse zeigen potenzielle künftige spektroskopische Anwendungen bei der Untersuchung von Defekten in 2D-Materialien auf, da TERS die Erforschung nanoskaliger spektroskopischer Fingerabdrücke in der Nähe des Defekts ermöglicht, die mit konventionellen Raman-Techniken bisher unzugänglich waren.

List of Publications

I Borja Cirera, Yair Litman, Chenfang Lin, Alaa Akkoush, Adnan Hammud, Martin Wolf, Mariana Rossi, and Takashi Kumagai. Charge transfer-mediated dramatic enhancement of raman scattering upon molecular point contact formation. Nano Letters, 22(6):2170–2176, 2022 [1].

II Yair Litman, Franco P Bonafé, Alaa Akkoush, Heiko Appel, and Mariana Rossi. First-principles simulations of tip enhanced raman scattering reveal active role of substrate on high-resolution images. The Journal of Physical Chemistry Letters, 14:6850–6859, 2023 [2].

III Alaa Akkoush, Yair Litman, and Mariana Rossi. A hybrid-dft study of intrinsic point defects in mx2 (m= mo, w; x= s, se) monolayers. physica status solidi (a), 2023 [3].

Declaration of contribution

I A. Akkoush programmed scripts to calculate normal modes and Raman intensities that were used in this paper. Additionally, she programmed the density response visualization as cube files within the FHI-aims package, and provided assistance in manuscript writing.

II A. Akkoush conducted an earlier implementation of TERS in the FHI-aims package, which exhibited origin dependence. This realization motivated the development of the current new implementation. Also, A. Akkoush programmed a Python script capable of executing DFPT local field calculations and generating TERS images of molecules. Her contributions extended to manuscript preparation. The script can be accessed at: `https://github.com/sabia-group/TERS_Tutorial`.

III A. Akkoush collaborated with her supervisor, Mariana Rossi, throughout the whole research process.

1 | Introduction

Raman spectroscopy was first discovered by Sir Chandrasekhara Raman in 1928 [4], and since then it has been a highly effective method to examine the fundamental vibrations of atoms in solids and molecules. Raman spectrospy is a non-destructive inelastic light scattering technique and it offers valuable insights into various properties of materials, including structural, vibrational and (opto)electronic properties [5–8]. Its extensive use is particularly notable in two-dimensional (2D) materials like graphene and transition metal dichalcogenides (TMDCs) [9–11]. As such, Raman spectroscopy can reveal valuable insights into various physical and structural properties of TMDCs, like identifying the number of layers, the effects of charge doping, and the influence of disorder [12–14]. The chemical composition of TMDCs can be described as MX_2, where M represents a transition metal atom from groups IV to X, and X denotes a chalcogenide element (S, Se, Te). TMDCs exhibit a layered structure with the formula X-M-X, where the metal atoms are between two planes of chalcogen atoms. Covalent bonds hold the atoms within the same layer together, while weak van der Waals interactions govern the coupling between adjacent layers. These layers can arrange themselves in different stacking orders, with the two most prevalent structures being the trigonal prismatic phase (referred to as 1H for monolayers and 2H for bulk crystals) and the octahedral prismatic phase (referred to as 1T) as shown in Figure 1.1 [15]. These materials exhibit exceptional characteristics, such as high optical absorption, strong bound excitons, and enhanced photoluminescence, which make them highly promising for various applications [16, 17].

Basal Plane View

Cross-Section View

1H-MoS$_2$ **1T-MoS$_2$**
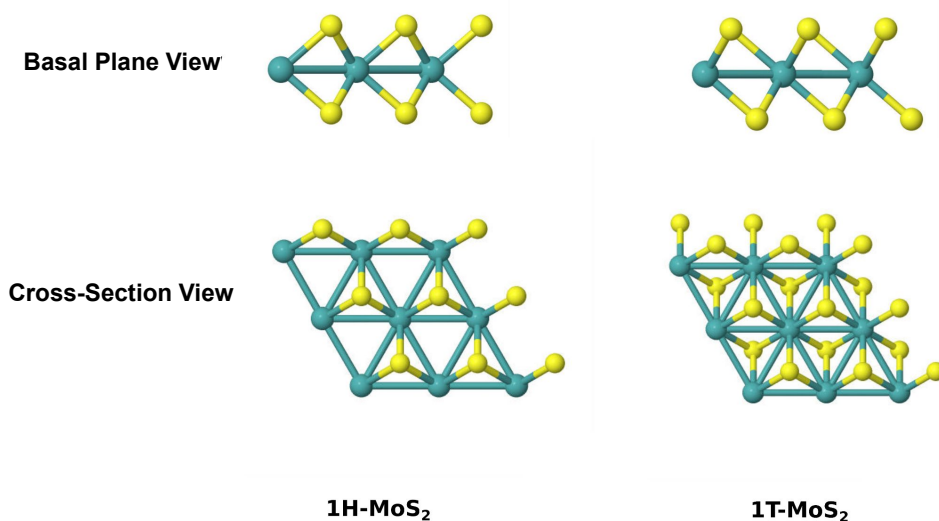
Figure 1.1: MoS$_2$ monolayer in the 1H phase (left) and in the 1T phase (right), featuring both basal plane view and cross-section view.

One fascinating application is the characterization of defects in these 2D materials using Raman spectroscopy. For instance, in a monolayer of MoS_2, it has been observed that the Raman modes E' and A'_1 (that are shown in Figure 3.2) undergo frequency shifts. The E' mode experiences a red shift, while the A'_1 mode undergoes a blue shift, with increasing concentration of sulfur vacancies [18]. However, Raman spectroscopy has inherent limitations, like a weak signal compared to other spectroscopies and limited spatial resolution [19]. To overcome these limitations, techniques have been developed to fulfill the requirements of investigating nanoscale and sub-micrometer composites, some of these techniques are tip-enhanced Raman spectroscopy (TERS) and surface-enhanced Raman spectroscopy (SERS) [20]. These techniques offer exciting opportunities to explore and visualize defects through high-resolution imaging. Specifically, in TERS where the signal is greatly enhanced by utilizing a metal tip to confine the electromagnetic field. This combination of Raman spectroscopy with the near-field enhancement results in a significant amplification of the signal [21–23]. Using TERS, nanoscale defects and wrinkles on MoS_2 have been examined with a spatial resolution of approximately 18 nm. This enabled the identification of localized inhomogeneities [24]. In ref. [25], TERS and TEPL (tip-enhanced photoluminescence) nanospectroscopy and nanoimaging were combined and the researchers analyzed the nanoscale heterogeneities including edges, grain boundaries, and nucleation sites of WSe_2 monolayers.

The arrangement of layers significantly influences the characteristics and behavior of TMDC materials. For example, the 1H phase of MoS_2 exhibits semiconductor properties with a direct band gap, whereas the 1T phase of MoS_2 is metallic [26]. Moreover, among most of the chemically distinct bulk TMDCs formed by (Mo or W) and (S, Se, or Te), the 1H phase is the thermodynamically stable configuration, while the 1T phase can be achieved as a metastable phase [15, 27]. The electronic properties of TMDCs not only depend on their stacking order but also on the number of layers. For instance, most TMDCs undergo a transition from an indirect band gap to a direct band gap semiconductor when they reach the monolayer limit [28, 29]. The direct bandgap at K point in the Brillouin zone of semiconductor monolayer of MoS_2 is demonstrated in the band structure in Figure 1.2. Building upon this understanding, the present work focuses on comprehensively investigating the properties of 1H monolayer MX_2.
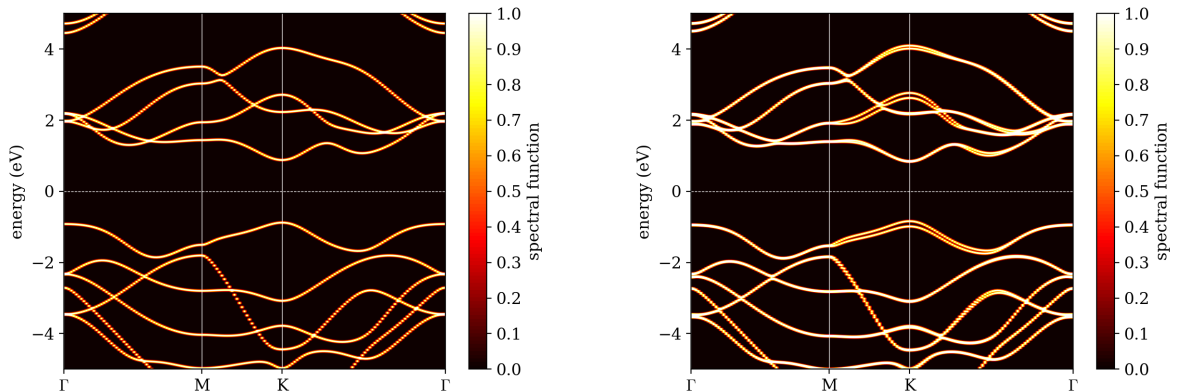
Figure 1.2: The electronic band structure of pristine MoS_2 without spin orbit coupling (left) and with spin orbit coupling (right), as computed from a density-functional theory calculation using the PBE exchange-correlation functional.

Experimentally, TMDCs just like graphene can be created through a mechanical exfoliation technique which is commonly known as the "sticky tape" method. This technique is efficient but it has limitations in terms of scalability, in which the size and thickness of the flakes are hard to control so that it restricts its applicability. To address the scalability issue, an alternative method called liquid-phase exfoliation has been developed. This technique involves the use of lithium and allows for the production of larger quantities of TMDC flakes [30]. However, it is important to note that this method may result in a phase transition from the 2H to the 1T structure, that might not be desirable when investigating the materials' properties [31]. Another method is known as molecular beam epitaxy (MBE) that involves the growth of TMDCs on passivated surfaces [32]. A commonly used and practical method is chemical vapor deposition (CVD). CVD enables the synthesis of high-quality TMDC films over large areas [33]. The advantage of CVD is its affordability and the fact that it does not require ultrahigh vacuum chambers [34].

The discussed synthesis processes result in inevitable formation of defects such as vacancies, intercalation, and substitutional atoms. The type and concentration of defects depend on the chosen synthesis method. For example, it was shown that for CVD synthesis of monolayer WSe_2 a higher defect concentration of mono Se vacancy of approximately 1.48% was measured, followed by molecular epitaxy (ME) with around 0.85% and then MBE with around 0.49% [35]. Therefore, it is crucial to investigate and understand the nature of defects in TMDCs not only to understand their impact on the chemical, optical, and electronic properties but also to provide better identification of experimental observations. For example, point defects influence the charge trapping and electron$-$hole recombination in WSe_2 monolayers which is relevant for building high performance photoactive devices [36]. Also, the introduction of Mo vacancies in $MoSe_2$ monolayer decreases the band gap, considerably shifting the material from the semiconducting character towards the metallic. Moreover, it has been shown by both theory and experiments that Mo/W defects can induce p$-$type doping for MoS_2/WS_2 monolayers, while sulphur defects induce n$-$type doping [37, 38], since the sulfur vacancies shift the Fermi level to the bottom of the conduction band. As an illustration, the unfolded band structure of MoS_2 with sulfur divacancies, shown in Figure 1.3, demonstrates the formation of three distinct states, including two shallow states near the valence band maximum (VBM) and the conduction band minimum (CBM), as well as a deep state.

This work comprehensively addresses the quantitative description of thermodynamic stability for point defects in 1H monolayer TMDCs using a first-principles theoretical framework. The primary objective is to gain insights into how the stability of defects is influenced by temperature, pressure, and the contact with an electron reservoir, through the use of density functional theory (DFT) in combination with ab initio atomistic thermodynamics [39]. Additionally, this thesis focuses on characterizing the local vibrational signatures of these defects through the simulation of TERS using a newly developed algorithm based on Density-Functional Perturbation Theory (DFPT) and Time-Dependent Density Functional Theory (TD-DFT).

The thesis is structured as follows:

Chapter 2 provides a detailed overview on the theoretical foundations underlying the electronic-structure calculations utilized in this study. The chapter primarily emphasizes the significance of DFT and DFPT methods in understanding the properties of the materials under investigation. Moreover, the chapter highlights the importance of hybrid functionals in the context of TMDCs and Hybrid Inorganic Organic Systems, emphasizing their role in accurately capturing
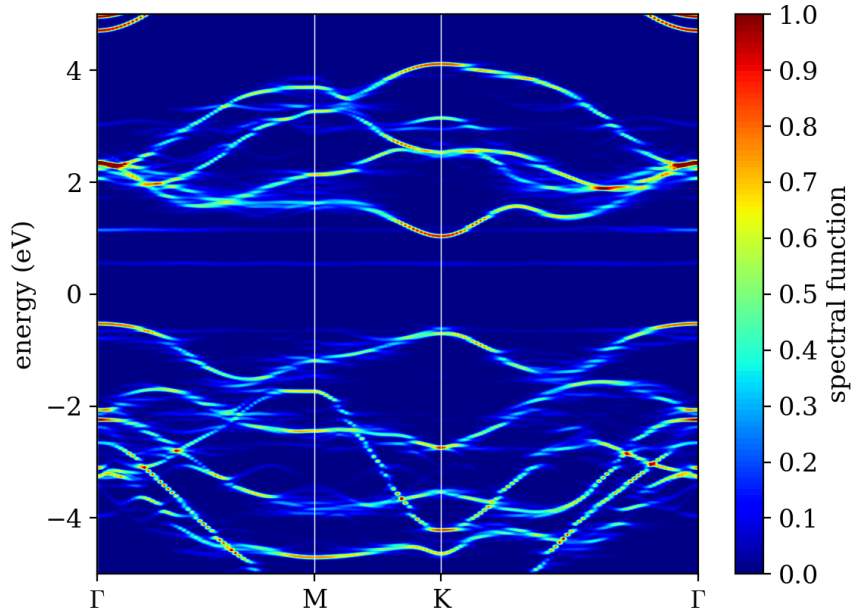
Figure 1.3: Electronic band structure of a MoS_2 monolayer with sulfur divacancies, calculated without spin orbit coupling and using the PBE exchange-correlation functional.

the electronic and structural properties of these materials.

Chapter 3 describes the theory of Raman spectroscopy and the exploration of near-field methods like TERS. The enhancement of both homogeneous field and near-field are examined, with a particular emphasis on the work showcasing enhanced Raman spectroscopy through molecular point contact. The implementation of TERS using DFPT and its integration with TD-DFT are also addressed.

Chapter 4 delves into the modeling of defects using the supercell approach in first principles methods. Various aspects of defect characterization are covered, including the calculation of formation energy, Gibbs formation energy, and the investigation of charged defects. The chapter also explores charge compensation schemes and presents a hybrid-DFT study on point defects in TMDCs, showing their influence on the local vibrational fingerprints through the calculation of TERS.

2 | Electronic Structure Methods

This chapter explores the solution of the electronic many body non-relativistic Schrödinger equation. The numerical cost to solve Schrödinger equation scales exponentially with the number of electrons. As a result, several approximate methods, collectively known as ab-initio methods, have been developed to provide an approximate solution, primarily focusing on ground-state properties. Some techniques like Hartree-Fock (HF) theory and methods that are based on HF (Configuration Interaction (CI), Coupled-Cluster (CC) and Møller-Plesset perturbation theory) approximate the wavefunction with varying levels of electronic correlation. While these methods provide accurate results, they still require significant computational resources. On the other hand, methods like DFT is based on the electronic density, instead of wavefunction. These methods are more efficient for systems comprising thousands of atoms, including bulk and surface systems.

In this chapter, the theoretical frameworks of these mentioned methods will be briefly discussed, and an overview of their principles and capabilities is provided.

2.1 The Many-Body Hamiltonian

The many-body non-relativistic Hamiltonian operator $\hat{H}$ is[1]:

$$\hat{H} = \hat{T}_n + \hat{T}_e + \hat{V}_{n-e} + \hat{V}_{e-e} + \hat{V}_{n-n} \tag{2.1}$$

Let $\vec{r}_i$ represent the position vector of an electron indexed by i, and let $\vec{R}_I$ denote the position vector of a nuclei indexed by I and ∇_I^2 represents the Laplacian operator acting on the coordinate of particle. The variables Z_I and M_I correspond to the nuclear charge and nuclear mass, respectively. Then the different terms are:

- The kinetic energy of the nuclei,

$$\hat{T}_n = -\frac{1}{2} \sum_{I=1}^{N} \frac{\nabla_I^2}{M_I}$$

- The kinetic energy of the electrons,

$$\hat{T}_e = -\frac{1}{2} \sum_{i=1}^{n} \nabla_i^2$$

---

[1] The electron mass, electron charge and $\hbar$ are set to unity

- The Coulombic interaction between the nuclei and electrons,

$$\hat{V}_{n-e} = -\frac{1}{2} \sum_i^n \sum_I^N \frac{Z_I}{|\vec{r}_i - \vec{R}_I|}$$

- The Coulombic interaction between the electrons,

$$\hat{V}_{e-e} = \frac{1}{2} \sum_{i=1}^n \sum_{j>i}^n \frac{1}{|\vec{r}_i - \vec{r}_j|}$$

- The Coulombic interaction between the nuclei,

$$\hat{V}_{n-n} = \frac{1}{2} \sum_{i=1}^N \sum_{j>i}^N \frac{Z_I Z_J}{|\vec{R}_I - \vec{R}_J|}$$

The ground-state energy of an atomic system with n electrons can be determined by solving an eigenvalue problem, defined by Schrödinger equation,

$$\hat{H}\Psi(\vec{r}_i, \vec{R}_I) = E\Psi(\vec{r}_i, \vec{R}_I), \tag{2.2}$$

using the many-electron Hamiltonian, denoted as $\hat{H}$, as defined in equation 2.1. The wave function $\Psi(\vec{r}_i, \vec{R}_I)$ represents the full many-particle system. The eigenvalue problem of the Schrödinger equation can be exactly solved numerically for small systems with very few degrees of freedom. However, it becomes exceedingly challenging and computationally infeasible to account for all the possible interactions between all the electrons and nuclei in systems with many electrons. As a result, various approximations are developed to overcome these computational hurdles, allowing for tractable calculations. The first approximation is the Born-Oppenheimer approximation, where the motion of the electrons is decoupled from that of the nuclei. The electron mass is assumed to be very small and this allows to exclude the kinetic energy term of the nuclei, treating them as stationary and described by fixed coordinates $\{\vec{R}_I\}$. An approximate method to solve the electronic structure will be discussed below.

2.2 Density-functional theory (DFT)

2.2.1 Hohenberg-Kohn theorem

The Hohenberg-Kohn theorem provides a fundamental basis for DFT in understanding electronic systems [40]. The total energy can be written as a functional of the density $E[\rho]$ and the ground state energy $E_0[\rho]$ is minimized when the electron density is equal to the exact (Born-Oppenheimer) ground-state density ρ_0. In other words, $E_0[\rho_0]$ is the minimum possible energy for the system, and any other electron density ρ will have a higher energy than ρ_0.

The Kohn-Sham approach [41] was proposed by Kohn and Sham to provide a practical formulation to find $E[\rho_0]$.
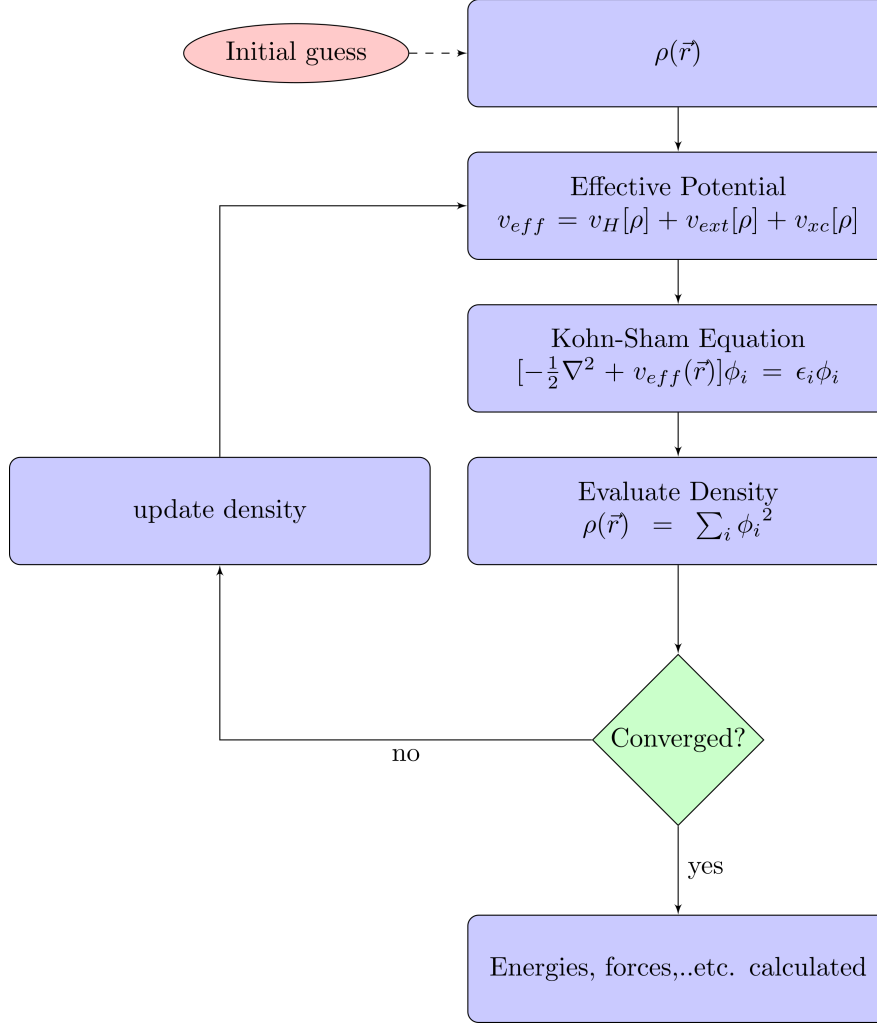
Figure 2.1: The Kohn-Sham self-consistent calculation workflow of DFT; an iterative procedure that involves several steps to obtain an accurate description of the electronic structure of a system.

2.2.2   The Kohn-Sham equations

A universal functional $F[\rho]$ is defined as:

$$F[\rho] = T_e[\rho] + E_{e-e}[\rho] = T_s[\rho] + E_H[\rho] + E_{xc}[\rho], \tag{2.3}$$

where, $E_H[\rho]$ the Hartree energy term that is the classical Coulombic interaction between the electrons in the system, T_s is the non-interacting kinetic energy and E_{xc} represents the exchange-correlation energy that captures the effects of electron-electron quantum interactions beyond the Hartree term and the non-interacting kinetic energy term.

Following the work of Kohn and Sham [41], by mapping the interacting system into a non-interacting system, it is then possible to define,

$$T_s[\rho] = -\frac{1}{2}\sum_{i=1}^{N}\langle\phi_i|\nabla^2|\phi_i\rangle \quad and \quad \rho_s(\vec{r}) = \sum_{i=1}^{N}|\phi_i|^2, \tag{2.4}$$

where ϕ_i are the single particle orbitals. In the Kohn-Sham scheme, the total energy functional is given by equation 2.5, where the various contributions are combined as,

$$E_{KS}[\rho] = T_s[\rho] + E_H[\rho] + E_{ext}[\rho] + E_{xc}[\rho]. \tag{2.5}$$

Here, $E_{ext}[\rho]$ represents the energy arising from the interaction of electrons with an external potential given by the nuclei. Then, minimization of $E_{KS}[\rho]$ under the constraint of conserving the number of electrons leads to a recipe to minimize the electron density, which involves solving a set of N individual Kohn-Sham particle equations,

$$[-\frac{1}{2}\nabla^2 + v_{eff}(\vec{r})]\phi_i(\vec{r}) = \epsilon_i\phi_i(\vec{r}), \tag{2.6}$$

where $v_{eff} = v_H + v_{xc} + v_{ext}$. The above equation can be written in a simplified form as,

$$\hat{h}^{KS}\phi_i(\vec{r}) = \epsilon_i\phi_i(\vec{r}). \tag{2.7}$$

Finally, the total energy can be calculated in terms of the eigenenergies ϵ_i as,

$$E_{KS}[\rho] = \sum_{i}^{N}\epsilon_i - \frac{1}{2}\int v_H(\vec{r})\rho(\vec{r})d\vec{r} - \int v_{xc}(\vec{r})\rho(\vec{r})d\vec{r} + E_{xc}[\rho], \tag{2.8}$$

the three terms on the right-hand side of the equation is aimed at addressing the concern of double-counting that emerges when summing the eigenvalues.

The Kohn Sham equations 2.6 are solved self-consistently because the Kohn-Sham potential is dependent on the electron density. The calculation starts by assuming an initial trial density, often chosen to be the density of a collection of free atoms. With this trial density, the Kohn-Sham potential can be computed. Using the calculated potential, the Kohn-Sham equations are solved to obtain a new density. This process is iterated in a self-consistency loop until the calculation reaches convergence, meaning that the density no longer changes significantly between iterations. The iterative cycle of updating the density and potential continues until the desired convergence is achieved, as depicted in details in sketch 2.1.

Looking at equation 2.8, the exchange-correlation functional E_{xc} is yet to be determined. The accuracy of DFT in the KS formulation relies on finding an appropriate formulation for E_{xc}. Therefore, finding a reliable and accurate expression for E_{xc} is a major challenge in the development of DFT. It is important to note that if the exact functional was known, DFT could provide an exact description of the ground-state electronic properties of the system. However, due to the complexity of the exchange-correlation interaction, approximations are necessary.

2.2.3 Exchange-correlation approximations
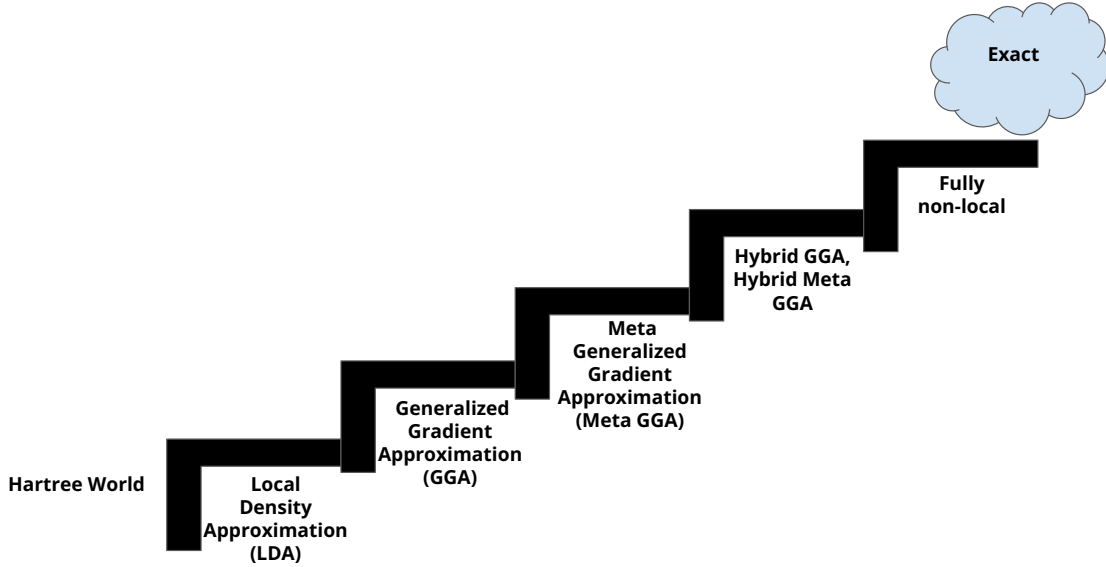
Figure 2.2: Jacob's Ladder for five generations of DFT Functionals.

Exchange-correlation functionals are described in a hierarchical structure often referred to as the Jacob's Ladder, that represents different levels of approximation ranging from the zero exchange-correlation (Hartree) limit to the exact form of the functional (exact), as described by J. Perdew in [42] and shown in scheme 2.2. Our focus is on exploring the hybrid inorganic-organic interfaces and TMDCs, which exhibit a combination of delocalized and localized electronic states. These systems display a range of interactions, from physisorptive systems primarily influenced by van der Waals forces, to chemisorptive systems where charge transfer can occur and bonds can be formed and broken.

Local Density Approximations (LDA):

The local density approximation (LDA) serves as the foundation for more sophisticated functionals due to its simple form. In LDA, the density is approximated as a homogeneous electron gas, as discussed in the original paper by Kohn and Sham [41], and it is assumed to be locally dependent on the position $\vec{r}$. The energy functional can be expressed as,

$$E_{xc}^{LDA} = \int \rho(\vec{r})\epsilon_{xc}(\rho(\vec{r}))d\vec{r}, \tag{2.9}$$

where ϵ_{xc} is the exchange-correlation energy of the homogeneous electron gas of the defined density $\rho(\vec{r})$ at point $\vec{r}$. Therefore, LDA works well for metals since the electrons are nearly free, but it is less accurate for systems with fast varying electron density like in single atoms or small to medium molecules and semiconductors. Initially employed for interfaces due to its artificial energy minimum between subsystems, LDA was later found to underestimate the adsorption distances compared to experimental observations. Additionally, LDA exhibits a significant overbinding effect for intra-molecular bonds in molecules due to the strong variation

of electron density in space, leading to shorter inter-atomic distances [43–45]. And for periodic systems, the estimation of band gaps is significantly underestimated. LDA introduces a self-interaction error for electrons, that causing destabilization of highly localized Kohn-Sham orbitals and delocalization error, in which both concepts will be discussed later.

To enhance the description of the inhomogeneous electron system, the inclusion of the gradient of the electron density in the expression of the exchange-correlation energy has been done. It is referred to as the Generalized Gradient Approximation (GGA), it is constructed to take into account the second-order gradient expansion when the density changes slowly. The inclusion of the density gradient makes GGA a semi-local functional.

Generalized Gradient Approximations (GGA):

Several Generalized Gradient Approximation (GGA) functionals with different parameterizations have been developed to improve the accuracy of the exchange-correlation term in DFT calculations. The GGA functional E_{xc}^{GGA} has a generalized form, as shown in equation 2.10, where $\rho(\vec{r})$ represents the electron density, and $\epsilon_{xc}(\rho(\vec{r}), \nabla\rho(\vec{r}))$ is the exchange-correlation energy density functional that depends on the electron density and also its gradient, as follows,

$$E_{xc}^{GGA} = \int \rho(\vec{r})\epsilon_{xc}(\rho(\vec{r}), \nabla\rho(\vec{r}))d\vec{r}. \tag{2.10}$$

The various approximations at the GGA level to estimate exchange and correlation energies will be discussed below.

Performance of GGA Functionals:

GGA functionals showed better performance in the prediction of cohesive energies and lattice constants in inorganic bulk materials compared to the LDA [46, 47]. PBE is the most popular and used form of GGA functional in physics applications [47]. It has shown improvement in the atomization energies compared to LDA, although in some cases it can overestimate or underestimate by approximately 1 eV [48]. When PBE is utilized with solids, it significantly improves the cohesive energies compared to LDA, although it has a tendency to underestimate the binding strength, which is the opposite trend of LDA [49, 50]. There were also many tweaked versions of PBE proposed in literature, such as rPBE [51], PBEsol [52], and revPBE [53]. Each has been developed to fulfill specific theoretical constraints or to enhance the description of particular property of the system. rPBE and revPBE have shown improvements in accurately describing chemisorption [53], while PBEsol tends to slightly overestimate the adsorption energies of chemisorbed species [54].

There exists some challenges with Kohn-Sham DFT such as the self-interaction error (SIE), that originates from the classical coloumb interaction, in which the electron interacts with itself [55]. The incorporation of the HF exchange in HF theory cancels out the self-interaction part of the Coulomb potential for single particles, but on the other hand HF lacks correlation energy. In KS-DFT, this cancellation cannot be achieved straightforward because of the use of the exchange-correlation functionals like LDA and GGA that mimic the exchange potential and approximate the correlation energy, but does not completely eliminate the self-interaction error. This deficiency becomes particularly problematic for systems that exhibit strong localization effects, such as defects or surfaces. In such cases, SIE can result in significant systematic errors.

Another fundamental source of error in KS-DFT is the delocalization error (DE), that is explained in Appendix A. The concept of DE is closely related to SIE. DE and SIE are equivalent for systems with one electron. Functionals that eliminate DE also eliminate SIE, while functionals free of SIE can still be affected by significant DE [55, 56]. DE in DFT calculations causes several problems, for example, overestimation of binding energies, lower reaction barriers and incorrect representations of reaction rates [57], overestimation of the electric polarizabilities of systems, impacting the accuracy of calculations involving electric field interactions [58], inaccurate predictions of band gaps [59], affecting the alignment of chemical potentials, which is essential for studying semiconductor systems electron transport in molecular junctions and electron transfer at material interfaces [60]. Mitigating this issue is, therefore, essential for applications shown in this thesis.

LDA and GGA tend to cause delocalization, whereas HF method often leads to localization of electrons [61]. In order to tackle the problem of electron localization/delocalization, hybrid functionals have been developed. These functionals combine HF exchange with a local or semi-local exchange-correlation functional in order to closely achieve accurate behaviour [62].

Hybrid Functionals:

The combination of Hartree-Fock theory, which corrects the self-interaction error, with semi-local functionals, which incorporate both exchange and correlation effects that are ignored in HF, is known as (global) hybrid exchange-correlation functionals. A fixed fraction α of the exact exchange, that can be determined empirically or by employing the adiabatic connection theorem, is mixed with the standard DFT functionals and result in,

$$E_{\text{xc}}^{\text{hybrid}} = E_{\text{xc}}^{\text{DFT}} + \alpha(E_{\text{x}}^{\text{HF}} - E_{\text{x}}^{\text{DFT}}). \tag{2.11}$$

There exist a number of hybrid functionals, each that has a purpose that depends on the studied system and the investigated properties. For instance, PBE0 is an extention of the PBE functional that accounts for 25% of HF exchange [63] and can be expressed as,

$$E_{\text{xc}}^{\text{PBE0}} = E_{\text{xc}}^{\text{PBE}} + \frac{1}{4}(E_{\text{x}}^{\text{HF}} - E_{\text{x}}^{\text{PBE}}). \tag{2.12}$$

Another example is B3LYP, a heavily parameterized functional that relies on molecular data and accounts for 20% of HF exchange. However, B3LYP is not commonly used for hybrid inorganic-organic interfaces due to its focus on molecular properties, that causes inconsistencies for metals

Table 2.1: Lattice constants (Å) for different TMDC materials (MoSe$_2$, MoS$_2$, WS$_2$, and WSe$_2$) from experimental measurements, and first principles calculations using different parameter values of ω and α.

Material	MoSe2	MoS2	WS2	WSe2
Lattice Constant (Å)				
Experimental	3.30 [70]	3.16 [70]	3.15 [71]	3.28 [71]
$\omega = 0.5$, $\alpha = 0.5$	3.251	3.137	3.137	3.262
$\omega = 0.472$, $\alpha = 0.5$	3.249	3.135	3.152	3.260
$\omega = 0.11$, $\alpha = 0.25$	3.262	3.144	3.157	3.271

and interfaces [64].

It is important to note that HF exchange energy present in equation 2.11 is not calculated based on the optimal HF Slater determinant as in HF theory. Instead, it is evaluated using the orbitals of the non-interacting KS system. Therefore, the non-local evaluation of E_x^{HF} results in the exchange-correlation approximation no longer being a local approximation. However, the long-range (LR) part of this exchange interaction poses computational challenges, particularly for metals and narrow-bandgap semiconductors that require dense k-points sampling [65]. Therefore, Heyd et al. proposed the Heyd-Scuseria-Ernzerhof (HSE) hybrid functional [66], where only the short-range (SR) exchange is treated by mixing a fraction of the HF exchange. This is achieved through the partitioning of the electron-electron interaction using a smooth range-separation function (partitioning the Coulomb operator), as:

$$\frac{1}{r} = \frac{\text{erfc}(\omega r)}{r} + \frac{\text{erf}(\omega r)}{r}. \tag{2.13}$$

Where the function erf represents the standard error function (LR), while erfc represents its complement (SR). The parameter ω is used to control the range of separation. When ω tends towards zero, the long-range interaction diminishes, while when ω approaches infinity, the short-range interaction vanishes.

The HSE exchange-correlation approximation then reads,

$$E_{xc}^{HSE} = \alpha E_x^{HF,SR}(\omega) + (1-\alpha)E_x^{PBE,SR}(\omega) + E_x^{PBE,LR}(\omega) + E_c^{PBE}(\omega). \tag{2.14}$$

The HSE functional offers significant advantages for molecular electronics and related fields by enabling the modeling of molecules attached to conducting surfaces, and it has shown that it gives good results for structural and electronic property calculations in both molecules and solids, thus, it is convenient for studying complex systems like surface chemisorption and impurities in semiconductors [67, 68]. Moreover, HSE06 functional has shown to provide accurate characterization of the electronic structure in perfect crystals and a wide range of defects in group-IV semiconductors [69]. In this thesis, we utilize HSE06, where $\alpha = 0.25$ with $\omega = 0.11$ Bohr^{-1}. This choice of ω has shown to provide lattice constants closer to experimental values for monolayer TMDCs, as shown in table 2.1.

Despite the advantages of HSE06 in accurately describing various properties, there are still some limitations. For example, cohesive energies are generally underestimated in HSE06 [72]. It has been shown that the combination of DFT (PBE/HSE06) with the van der Waals (vdW) interactions results in significant improvement in the cohesive properties of ionic solids and semiconductor [73].

2.2.4 Van Der Waals Interactions (vdW)

vdW forces are also known as dispersion forces that arise from instantaneous fluctuations of the electronic clouds surrounding atoms and molecules. They were originally proposed by F. London in the early 1930s, and they play a significant role in intermolecular interactions [74]. This interaction is expressed as a multipole expansion series of the Coulomb potential, where each term is inversely proportional to the distance between the interacting particles ($\frac{1}{R}$) and given by the equation:

$$E_{VDW} = -\sum_{n=6}^{\infty} \frac{C_n}{R^n}. \tag{2.15}$$

The dominant contribution in the above equation comes from the first term ($\propto \frac{1}{R^6}$) that corresponds to the induced dipole-dipole interactions and it is attributed to the attractive forces between particles at large distances. Therefore, to account for long range interactions as vdW interactions, they can be integrated into DFT in two popular ways:

1. Functionals with non-local correlation: Non-local correlation terms are introduced to these functionals in order to capture the long range interactions. The electron density and its gradients at different points in space are considered in the exchange-correlation potential [75, 76].

2. Empirical or semi-empirical corrections: These corrections are added to the DFT energies. The most common approach is the pairwise-additive dispersion correction, which is applied to the DFT-optimized Kohn-Sham energy and has the form,

$$E_{VDW} = -\frac{1}{2} \sum_{A \neq B} f_{damp}(R_{AB}) \frac{C_{6,AB}}{R_{AB}^6}, \tag{2.16}$$

where A and B represent all combinations of atoms in the system, R_{AB} is the interatomic distance between atoms A and B, $C_{6,AB}$ is the effective interaction parameter between atoms A and B, and f_{damp} is a damping function that is empirically determined based on the method employed.

Various schemes have been developed to determine the C_6 coefficients for vdW interactions [77–80]. The following have been employed in this thesis:

1. TS-vdW: This method focuses on two-body vdW interactions. It proposes a mixing scheme to determine C_6 coefficients for heteronuclear interactions when having the knowledge of

the corresponding homonuclear coefficients. As such,

$$C_{6,AB} = \frac{2C_{6,AA}C_{6,BB}}{\frac{\alpha_B^0}{\alpha_A^0}C_{6,AA} + \frac{\alpha_A^0}{\alpha_B^0}C_{6,BB}}, \tag{2.17}$$

where $C_{6,AA}$ and $C_{6,BB}$ are the homonuclear $C_{6,AB}$ coefficients, and α_A^0 and α_B^0 are the corresponding reference polarizabilities [81].

2. vdW^{surf}: To account for collective effects in surface systems, such as screening, the pairwise vdW interaction described earlier needs to be modified using Lifshitz-Zaremba-Kohn model (LZK) [82, 83]. Then the expression for the vdW energy in the LZK model is given by,

$$E_{vdW}^{surf} \approx - \int dV \, n_s \frac{C_{6,As}}{R^6}, \tag{2.18}$$

where index A denotes a distant molecule, s represents an individual atom of the surface, and n_s is the number of atoms per unit volume of the surface [84].

3. Many Body vdW Schemes: When the density of a system increases, then the impact of collective interactions becomes more pronounced. Therefore, the many-body dispersion (MBD) model [85] offers a more precise and realistic description of interactions in a wide range of systems compared to two-body interactions described above. MBD considers the system as a collection of harmonic oscillators. The interaction between oscillators is truncated at the dipole terms, resulting in a Hamiltonian,

$$\hat{H}_{\text{dipHO}} = \sum_i \frac{\hat{\mathbf{P}}_i^2}{2} + \sum_i \frac{m_i \nu_i^2}{2}|\hat{\mathbf{r}}_{\mathbf{i}} - \mathbf{R}_{\mathbf{i}}|^2 + \sum_{j<i} q_i q_j (\hat{\mathbf{r}}_i - \mathbf{R}_i) \cdot \hat{\mathbf{T}}(\mathbf{R}_j - \mathbf{R}_i) \cdot (\hat{\mathbf{r}}_j - \mathbf{R}_j),$$

where $\hat{\mathbf{r}}$ and $\hat{\mathbf{p}}$ are the positions and momenta of the oscillators, respectively, q_i are the charges that determine the strength of the interaction between the oscillators, m_i is the mass of the oscillator, ν_i is the frequency, R_i are the centers of the oscillators, and $\hat{\mathbf{T}}(\mathbf{R}_j - \mathbf{R}_i)$ is a dipole-dipole interaction tensor.

To use the MBD model, the dipole-dipole interaction tensor needs to be defined. Then the polarizability is converted from an atomic property to a continuous function. A recent development, is the non-local MBD correction, that expands its applicability to ionic systems [86]. MBD-NL introduces a more generalized approach to obtain the polarizability of a *density* through the Vydrov-Van Voorhis (VV) functional, instead of atomic polarizabilities as in the previous methods. The screened polarizability is then calculated, taking into account screening effects. This process is repeated until convergence is achieved then the final $\hat{\mathbf{T}}$ is used and the Hamiltonian is diagonalized inorder to get the vdW energy.

vdW forces have a significant influence on the thermodynamic stability and electronic properties of TMDCs, where the layers are held together by vdW forces. Specifically, MBD-NL method has significant impact on hybrid organic-inorganic interfaces and systems

as shown for benzene adsorbed on Ag(111). For instance, HSE was used with MBD and showed good agreement with experimentally measured adsorption distance and adsorption energy [87].

2.2.5 Spin-Orbit coupling (SOC)

Spin-orbit coupling (SOC) refers to the relativistic interaction between the spin of an electron and its orbital motion. The spin of the electron is quantum mechanically described as the intrinsic angular momentum, while the orbital motion describes the movement of the electron within an external potential, such as an electric field or crystal potential. SOC has a profound impact on the electronic and optical properties of materials. For example, SOC can cause energy level splitting and lifting of degeneracy in electronic states, that can in turn, lead to the emergence of novel states and phases, such as excitons [88]. It is particularly strong in transition metals due to their large nuclear charge and this leads to significant changes in the electronic and magnetic properties of TMDCs [89].

The SOC correction used in this work is integrated as a correction to the scalar-relativistic eigenvectors in a post-processing manner. Details of the SOC implementation in FHI-aims and the derivation of the SOC Hamiltonian from the Dirac equation are explained in reference [90].

2.3 Density Functional Perturbation Theory (DFPT)

In this thesis, DFPT was employed to calculate the response of the electronic structure with respect to an external electric field perturbation. DFPT is implemented in FHI-aims package (the details of the implementation are shown in reference [91]). FHI-aims is an ab initio package that offers an all-electron approach combined with a real-space grid representation of the density. FHI-aims expresses the Kohn-Sham orbitals $\phi_i(\vec{r})$ as a linear combination of basis functions. The basis functions used are localized numeric atom-centered orbital (NAO) basis functions. FHI-aims provides pre-constructed basis sets for all elements of the periodic table. These basis sets are organized in tiers, with increasing accuracy achieved by adding radial functions and hydrogen-like functions [92].

2.3.1 The general procedure of Coupled Perturbed Self-Consistent Field (CPSCF)

In the context of time-independent perturbation theory, the Kohn-Sham energy functional in equation 2.5 is augmented with an additional small electronic perturbation denoted as $E_E[\rho]$. This perturbation accounts for the effects of external influences or interactions beyond the basic Kohn-Sham framework. The corresponding operator for this perturbation that has the form $\hat{h}_E = -\boldsymbol{r} \cdot \boldsymbol{E}$. By including this perturbation, the modified Kohn-Sham energy functional captures additional contributions to the total energy of the system.

We can expand the Kohn-Sham Hamiltonian, single particle wavefunction, and energy around a small electric field with a strength of e_γ along the direction γ. The expansions can be written

as follows:

$$\hat{h}_{KS}(e\gamma) = \hat{h}_{KS}^0 + \hat{h}_{KS}^1 e_\gamma + \dots \tag{2.19}$$

$$\psi_p(e_\gamma) = \psi_p^0 + \psi_p^1 e_\gamma + \dots \tag{2.20}$$

$$\epsilon_p(e_\gamma) = \epsilon_p^0 + \epsilon_p^1 e_\gamma + \dots \tag{2.21}$$

Here, $\hat{h}_{KS}^0$, ψ_p^0, and ϵ_p^0 represent the zeroth-order terms, while $\hat{h}_{KS}^1$, ψ_p^1, such that the perturbed Hamiltonian $\hat{h}_{KS}^1$ is,

$$\hat{h}_{KS}^1 = \frac{\partial \hat{h}_{KS}}{\partial e_\gamma} = \hat{t}_s^1 + \hat{v}_{ext}^1 + \hat{v}_H^1 + \hat{v}_{xc}^1 + \hat{\nu}_E \tag{2.22}$$

Where $\hat{\nu}_E = -\boldsymbol{r}$, making use of equations (2.20)–(2.21) in the Schrödinger equation, we obtain:

$$(\hat{h}_{KS}^0 + \hat{h}_{KS}^1 e_\gamma)(|\psi_p^0\rangle + |\psi_p^1\rangle e_\gamma) = (\epsilon_p^0 + \epsilon_p^1 e_\gamma)(|\psi_p^0\rangle + |\psi_p^1\rangle e_\gamma) \tag{2.23}$$

By considering the first order of e_γ, we arrive at the well-known Sternheimer equation:

$$(\hat{h}_{KS}^0 - \epsilon_p^0)|\psi_p^1\rangle = -(\hat{h}_{KS}^1 - \epsilon_p^1)|\psi_p^0\rangle \tag{2.24}$$

By multiplying the equation with $\langle\psi_q^0|$ and numerically solving equation 2.24 after expanding the response of the wave functions, we obtain the following expression for the density response $\rho^1(\mathbf{r})$:

$$\rho^1(\mathbf{r}) = \sum_p f(\epsilon_p)(\psi_p^0(\mathbf{r})\psi_p^1(\mathbf{r}) + \psi_p^1(\mathbf{r})\psi_p^0(\mathbf{r})). \tag{2.25}$$

The term $f(\epsilon_p)$ corresponds to the occupation numbers of states with eigenvalues ϵ_p. The expression sums over all the states p and involves the contributions from both the first-order wavefunctions ψ_p^1 and the unperturbed wavefunction ψ_p^0.

We can approximate the total energy E_{tot}, knowing that the electric field $\boldsymbol{E} = (e_x, e_y, e_z)$ that in turn can be expressed as a superposition of homogeneous electrical fields with strengths e_γ aligned along the different Cartesian axes γ, by using a Taylor expansion in the zero-field limit:

$$E_{tot}(\mathbf{E}) \approx E_{tot}^0 + \sum_\gamma \mu_\gamma e_\gamma + \frac{1}{2}\sum_{\gamma,\delta} \alpha_{\gamma\delta} e_\gamma e_\delta + \dots \tag{2.26}$$

Where E_{tot}^0 is the energy of the system in the absence of an electric field, μ_γ is the dipole moment of the system along the γ direction, $\alpha_{\gamma\delta}$ is the polarizability of the system, and higher-order terms have been neglected. Here, γ and δ are cartesian directions. The polarizability $\alpha_{\gamma\delta}$ is defined as the second derivative of the electronic energy $E_E[\rho]$ with respect to the electric field components e_γ and e_δ at $\boldsymbol{E} = 0$:

$$\alpha_{\gamma\delta} = \frac{\partial^2 E_E[\rho]}{\partial e_\gamma \partial e_\delta}\bigg|_{\boldsymbol{E}=0} \tag{2.27}$$

The corresponding energy to the above mentioned $\hat{h}_E$ operator has the form,

$$E_E[\rho] = -\sum_\gamma \int r_\gamma e_\gamma \rho(\mathbf{r}) d\mathbf{r}, \tag{2.28}$$

then substituting equation 2.28 in equation 2.27, the polarizability of the system in its ground state is,

$$\alpha_{\gamma\delta} = -\int r_\gamma \frac{\partial \rho_0(\mathbf{r})}{\partial e_\delta}\bigg|_{\boldsymbol{E}=0} d\mathbf{r}. \tag{2.29}$$

Where ρ_0 is the ground-state density. For periodic systems, the polarization P and polarizability are defined per the unit cell volume V. This leads to,

$$\alpha_{\gamma\delta} = V \frac{\partial P_\gamma}{\partial e_\delta}\bigg|_{\boldsymbol{E}=0} = -\int_{u.c} r_\gamma \frac{\partial \rho_0(\mathbf{r})}{\partial e_\delta}\bigg|_{\boldsymbol{E}=0} d\mathbf{r}, \tag{2.30}$$

evaluating this expression directly by a definite integral is not possible due to the ill-defined nature of $\hat{r}_\gamma$ in periodic boundary conditions. Instead, the position operator is replaced by exploiting the commutation relation

$$[\hat{h}_{\mathrm{KS}}^0, \mathbf{r}] = -\nabla. \tag{2.31}$$

Details can be found in ref [91]. The next chapter will delve further into the electromagnetic theory, presenting both the classical treatment of the electromagnetic field and the quantum treatment of the system's polarization, connecting to DFPT.

3 | Probing Structural Vibrations with Raman Spectroscopy

3.1 Introduction

In this chapter, the principles and theoretical foundations of Raman spectroscopy, including classical and quantum descriptions are briefly described. In addition to the calculation of Raman intensities, and a practical applications on MoS_2 monolayers is presented. TERS and its applications is then discussed as a higher resolution method that enhances the Raman signal and overcomes diffraction limit of Raman. The development of local near-field effects from first principles and the role of substrates in chemical enhancement are then presented.

3.2 Principles of Raman Spectroscopy

The fundamental principle of Raman spectroscopy is the interaction between light and matter [93]. In this technique, a sample is exposed to light from a source, which excites the sample and results in scattered photons being emitted in various directions. These scattered photons can undergo two types of scattering: elastic scattering and inelastic scattering. The dominant interaction is elastic scattering, known as Rayleigh scattering, where there is no change in frequency, as depicted in scheme 3.1. However, a small fraction of the photons undergo inelastic scattering, leading to a frequency shift known as Raman scattering.

In Raman scattering, there are two possible indirect transitions, via virtual state: (1) the transition of the system from its ground state to a higher vibrational excited state, causing a red shift in frequencies. This shift in the frequency is recognized as the Stokes shift, and attributed to the Stokes Raman scattering. (2) Anti-Stokes Raman scattering, which involves scattered photons possessing greater energy than the incident photons. This corresponds to the system transitioning from a higher vibrational state to the ground state, inducing a blue shift in frequencies.

In a Raman spectrum, the Stokes scattering peaks have a stronger intensity compared to the anti-Stokes scattering peaks. This is because the ground state, is more populated than the higher energy state in thermodynamic equilibrium. Consequently, the rate of transitions from the more populated lower state to the higher state (Stokes transitions) is higher than the rate in the opposite direction (anti-Stokes transitions).
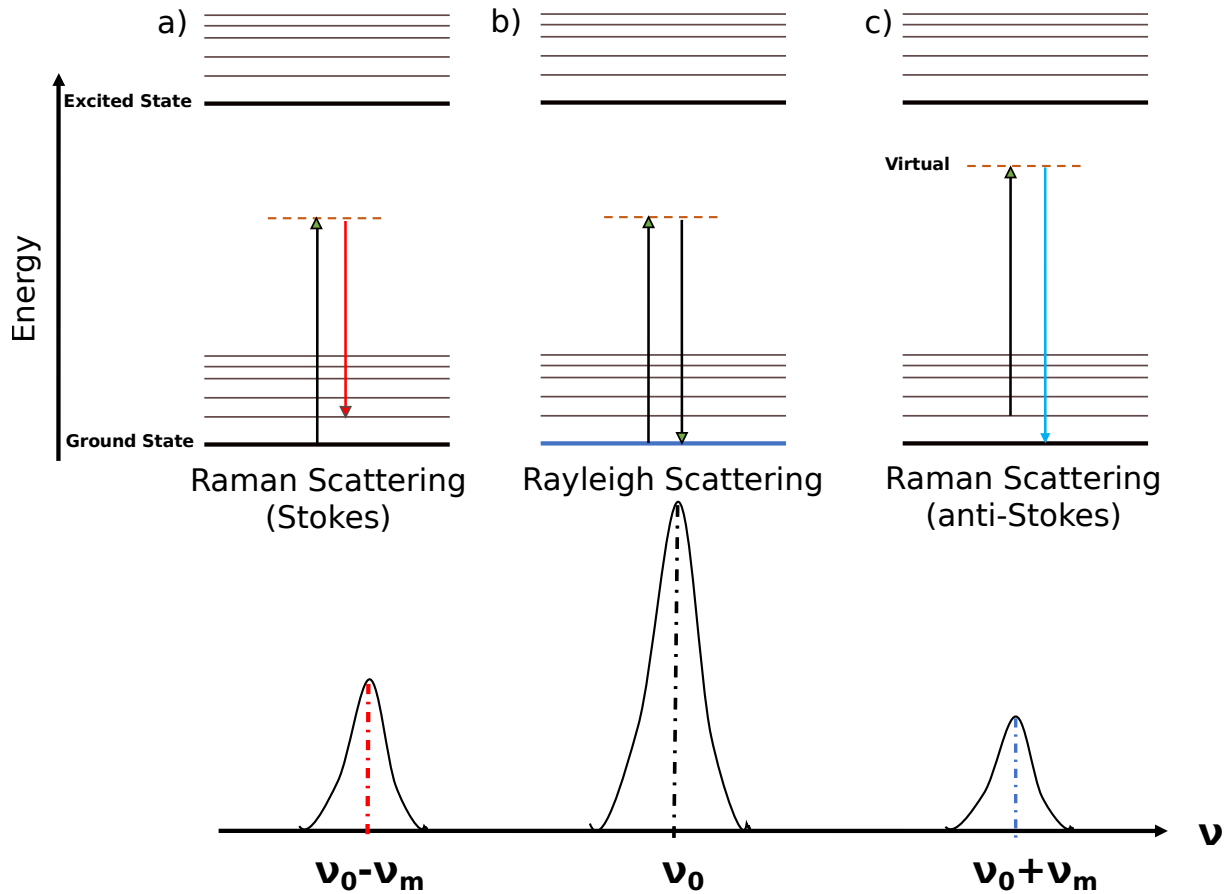
Figure 3.1: Schematic representation of a) Stokes, b) Rayleigh and c) anti-Stokes Raman scattering, the thick lines represent the electronic states while the thin lines correspond to the vibrational states.

3.2.1 Understanding Raman Scattering: Classical Description and Theory

The classical theory of the Raman effect is based on the concept of molecular polarizability. As such, distortion in the electron density is caused due to the application of external electric field on the molecule. This distortion in turn creates an induced electric dipole moment, $\boldsymbol{\mu}$, in the molecule that is proportional to the product of the polarizability, $\boldsymbol{\alpha}$, and the strength of the applied electric field, $\boldsymbol{E}$, as,

$$\mu_i = \alpha_{ij} E_j. \tag{3.1}$$

Looking at equation 3.1, the polarizability is a tensor of rank 2. One can consider an electric field in the j direction with the form,

$$E_j = E_j^0 \cos(2\pi\nu_0 t). \tag{3.2}$$

The sinusoidal representation of the electric field is based on the assumptions of classical electromagnetic theory. The assumption of monochromaticity assumes that the wave consists of a single frequency, allowing us to describe the electric field with a specific frequency. Therefore,

$$\mu_i = \alpha_{ij} E_j^0 \cos(2\pi\nu_0 t), \tag{3.3}$$

where E_j^0 is the amplitude of the electric field and ν_0 is the frequency of the incident field.

Moreover, the polarizability tensor can be expanded in terms of the normal coordinate, $\boldsymbol{u}$, using a Taylor series around equilibrium position as follows,

$$\alpha_{ij} = \alpha_{ij}^0 + \sum_k \left(\frac{\partial \alpha_{ij}}{\partial u_k}\right)\Big|_0 u_k + \sum_{k,l} \left(\frac{\partial^2 \alpha_{ij}}{\partial u_k \partial u_l}\right)\Big|_0 u_k u_l + \cdots \tag{3.4}$$

The subscript "0" in the derivative corresponds to the value at the equilibrium position. The first term α_{ij}^0 corresponds to the value of the polarizability tensor at the equilibrium point, u_k and u_l correspond to the k-th and l-th normal vibrations of the molecule, respectively.

Considering only the first approximation term for one normal mode n, then: $\alpha_{ij} = \alpha_{ij}^0 + \alpha_n' u_n$, where $\alpha_n' = \left(\frac{\partial \alpha_{ij}}{\partial u_n}\right)\Big|_0$.

We consider that the normal coordinate behaves like a harmonic oscillator, so that it has the following form $u_n = A_n \cos(2\pi\nu_n t + \phi_n)$, where ν_n is the vibrational frequency, with the amplitude of the normal vibration A_n, and ϕ_n is the initial phase of the vibration. Then, we obtain

$$\mu_i = \alpha_{ij}^0 E_j^0 \cos(2\pi\nu_0 t) + \frac{1}{2}\alpha_N' E_j^0 A_n \cos\left[2\pi(\nu_0 \pm \nu_n)t \pm \phi_n\right]. \tag{3.5}$$

This oscillating dipole moment changes its direction periodically. This oscillation causes the emission of electromagnetic radiation as scattered light with shifted frequency that is directly related to the frequency of the dipole's oscillation.

According to the classical description, Raman scattering involves the interaction of a sinusoidal electric field with a vibrating molecule, resulting in an equation of a dipole moment that consists of three terms: the induced dipole moment with the same frequency as the incident light of frequency ν_0, Rayleigh scattering term, an anti-Stokes term at frequency $\nu_0 + \nu_n$ and a Stokes term at frequency $\nu_0 - \nu_n$.

At this level of approximations, we obtain a condition (selection rules) for the existence of Raman scattering,

$$\alpha_n' \neq 0. \tag{3.6}$$

In other words, Raman scattering is active only for vibrational modes that produce a change in polarizability. This selection rule depends on the symmetry properties of the molecule or the crystal and are determined by group theory [94]. In our investigation, we focus on the dynamic behavior of solids. In crystal, the normal mode displacement has the form,

$$u_n = A_n(\boldsymbol{q}, \omega_n) \cos(\boldsymbol{q} \cdot \boldsymbol{r} - \omega_n t), \tag{3.7}$$

where $\boldsymbol{q}$ and ω_n represent the wavevector and frequency of the normal mode, respectively.

As it was explained earlier that the polarizability tensor α_{ij} describes the response of individual molecules or atoms to an electric field, a similar quantity called the susceptibility tensor χ_{ij}. χ_{ij} describes the collective response of a bulk material to an electric field. Therefore, within the linear regime, the induced polarization in solids is given as $p_i = \chi_{ij} E_j$.

Using the fact that the incident electromagnetic wave is defined as $E_j = E_j^0 \cos(\boldsymbol{k_j} \cdot \boldsymbol{r} - \omega_j t)$, we arrive at a similar expression for the electric polarization as for the molecules (equation. 3.5),

$$
\begin{aligned}
p_i = &\chi_{ij}^0 E_j^0 \cos(\omega_0 t) \\
&+ \frac{1}{2} \frac{\partial \chi_{ij}}{\partial u_n} A_n(\boldsymbol{q}, \omega_n) E_j^0 \left[\cos\left((\boldsymbol{k_j} - \boldsymbol{q}) \cdot \boldsymbol{r} - (\omega_j - \omega_n) t \right) \right. \\
&\left. + \cos\left((\boldsymbol{k_j} + \boldsymbol{q}) \cdot \boldsymbol{r} - (\omega_j + \omega_n) t \right) \right].
\end{aligned}
\tag{3.8}
$$

The momentum conservation principle, expressed as $\boldsymbol{k_s} \pm \boldsymbol{q} = \boldsymbol{k_j}$, where $\boldsymbol{k_s}$ represents the momentum of scattered light and the $\pm$ sign relates to Stokes and anti-Stokes processes. The magnitude of the momentum transfer, $\boldsymbol{q} = |\boldsymbol{k_j} - \boldsymbol{k_s}|$, is notably smaller than the typical Brillouin Zone (BZ) size in crystalline systems. As a result, this interaction is confined to vibrations occurring at the BZ center (Γ point).

The expression $\frac{\partial \chi_{ij}}{\partial u_n} A_n(\mathbf{q}, \omega_n)$ within the given context establishes the definition of the Raman tensor $R_{ij,n}$. This tensor quantifies how susceptible χ_{ij} is to the displacement of the vibrational mode u_n. The importance of the Raman tensor becomes apparent when investigating the Raman active modes, which exhibit non-zero intensity. This intensity, denoted as I, and defined as follows [95, 96]:

$$
I \propto \left| e_i^I \cdot R_{ij,n} \cdot e_j^S \right|^2.
\tag{3.9}
$$

Here, $\mathbf{e}^I$ and $\mathbf{e}^S$ denote the polarization vectors characterizing the incident and scattered light, respectively. The intensity of a Raman mode originates from the interaction among the components of the Raman tensor with the polarization of both the incident and scattered light. To end up wit a non-zero intensity signal, the Raman tensor has to have a non-zero matrix elements. The values of these matrix elements are defined by the particular irreducible representation of the phonon modes. For further reading, the reader is to referred to the comprehensive work by Peter Y. Yu and Manuel Cardona [97].

3.2.2 Quantum Treatment

As the electromagnetic radiation is treated using classical methods, the system interaction to the radiation is treated using quantum mechanics. The induced electric dipole moment arises from a transition between an initial state i and a final state f. The complete transition electric dipole is represented as follows,

$$
p_{fi} = \langle \psi_f | \hat{p} | \psi_i \rangle.
\tag{3.10}
$$

In this equation, $|\psi_f\rangle$ and $|\psi_i\rangle$ correspond to the perturbed wave functions of the initial and final states of the system, respectively, and the operator $\hat{p}$ is electric dipole moment operator for the system, written as,

$$\hat{p} = \sum_j r_j. \tag{3.11}$$

In analogy to the wavefunction expansion discussed earlier (as described in section 2.3), dipole transition moments can also be formulated as a series expansion:

$$p_{fi} = p_{fi}^{(0)} + p_{fi}^{(1)} + p_{fi}^{(2)} + \ldots. \tag{3.12}$$

Where,

$$p_{fi}^{(0)} = \langle \psi_f^{(0)} | \hat{p} | \psi_i^{(0)} \rangle \tag{3.13}$$

$$p_{fi}^{(1)} = \langle \psi_f^{(1)} | \hat{p} | \psi_i^{(0)} \rangle + \langle \psi_f^{(0)} | \hat{p} | \psi_i^{(1)} \rangle \tag{3.14}$$

$$p_{fi}^{(2)} = \langle \psi_f^{(1)} | \hat{p} | \psi_i^{(1)} \rangle + \langle \psi_f^{(2)} | \hat{p} | \psi_i^{(0)} \rangle + \langle \psi_f^{(0)} | \hat{p} | \psi_i^{(2)} \rangle \tag{3.15}$$

The transition moment $p_{fi}^{(0)}$ corresponds to a direct transition between the unperturbed states f and i. The first-order is associated with conventional Rayleigh and Raman scattering phenomena. While, the second-order term components are related to hyper Rayleigh and Raman scattering effects. In this work, we focus on the first order transition moment and using equation 3.11, it becomes,

$$p_{fi}^{(1)} = \int \left[\psi_f^{(1)*}(\mathbf{r}) \psi_i^{(0)}(\mathbf{r}) + \psi_f^{(0)*}(\mathbf{r}) \psi_i^{(1)}(\mathbf{r}) \right] \mathbf{r} \, d\mathbf{r}. \tag{3.16}$$

Now, $\psi_f^{(1)*}(\mathbf{r}) \psi_i^{(0)}(\mathbf{r}) + \psi_f^{(0)*}(\mathbf{r}) \psi_i^{(1)}(\mathbf{r})$ resembles the first-order electronic density, $\rho_{fi}^{(1)}$, associated with the transition between the initial state and the final state, then,

$$p_{fi}^{(1)} = \int \boldsymbol{r} \rho_{fi}^{(1)}(\boldsymbol{r}) d\mathbf{r}. \tag{3.17}$$

This is analogous to the polarizability term introduced (equation 2.29) in the DFPT (section 2.3), that is the method of focus in this work.

3.2.3   Example: MoS$_2$ monolayer

As an illustration, in figure 3.2, the Raman spectra of MoS$_2$ monolayer and bulk are shown. The two prominent peaks are the ones that correspond to the E_{2g}/E_{2g}' mode and to A_{1g}/A_{1g}' modes. The primes refer to the monolayer modes. E_{2g}/E_{2g}' is the in-plane vibration of the S and Mo
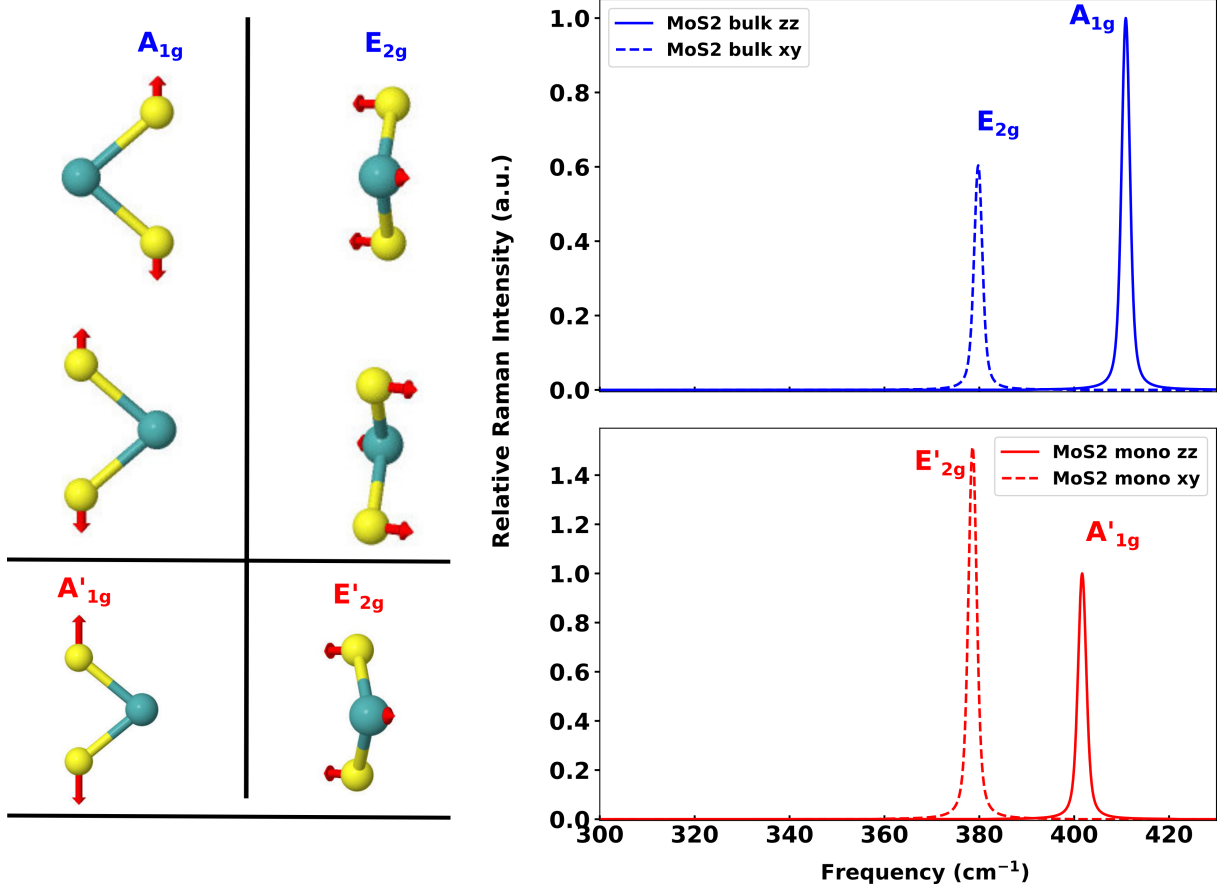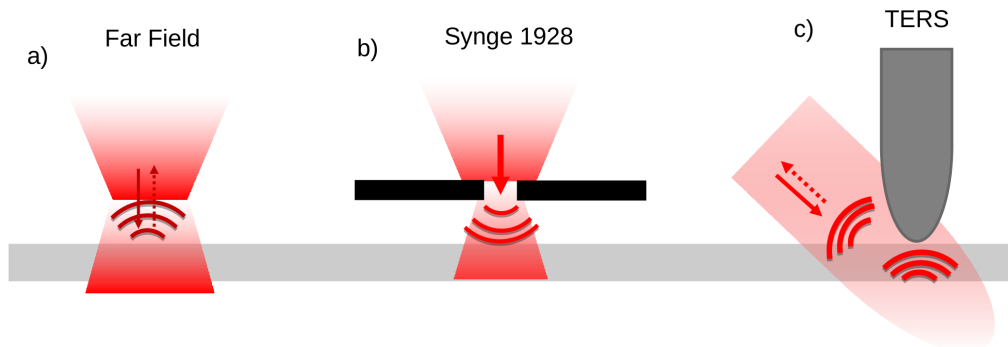
Figure 3.2: Left: Schematic representation of phonon active modes and their symmetry labels in bulk and monolayer. Right: The relative Raman spectra are presented, normalized with respect to the intensity of the Raman mode associated with the polarizability tensor element zz of MoS_2, for both bulk and monolayer structures. The Raman intensity accounts for the zz and xy polarizability tensor components, showcasing the corresponding results. The calculations are performed using PBE+MBD.

atoms, while in A_{1g}/A'_{1g} Mo atoms move in opposite directions in the out of plane direction, where this mode acts red shifted in the monolayer. It is shifted from 410.8 cm^{-1} in the bulk to 402 cm^{-1} in the monolayer, indicating a change in the vibrational properties of the lattice due to the reduction in dimensionality.

The calculation of the polarizability tensor was performed using DFPT with the PBE exchange-correlation functional. As it was demonstrated above, that the arrangement of polarizations has a notable impact on the interactions between the electric field vectors and the Raman tensors associated with particular vibrational modes. For the A_{1g} mode, the basis functions of this mode is z^2 in the D3h symmetry group. While, for the E_{2g} mode, the choice of polarization along the xy direction results in a non-zero dot product in equation 3.9. More details about the the Raman tensor for D3h symmetry which TMDCs belong to is found in reference [98]

The calculation of Raman intensity was done through a python script, that I have wrote during my PhD that is distributed with the FHI-aims program package under the name "*get_vibrations.py*". This script was based on previous existing infrastructure.

3.3 Principles of Tip-enhanced Raman spectroscopy (TERS)


Figure 3.3: Schematic representation of various optical imaging techniques. (a) Far-field microscopy: Traditional microscopy technique where the resolution is limited by the diffraction limit of light. (b) Synge's idea of metal surface with aperture (c) Tip-enhanced Raman spectroscopy (TERS).

The diffraction limit is defined as the minimum resolvable distance between two point-like objects based on the interference pattern formed by diffracted light. To overcome this limit, extensive efforts has been made to enhance the resolution of Raman spectroscopy. These efforts date back to the 1920s, first with Synge who proposed an enhancement of resolution by using a metal plate with a small illuminated opening [99]. Pohl et al. in 1983 managed to successfully implemented Synge's idea by using a metal-coated quartz crystal tip with a small aperture [100]. They have achieved a sub-diffraction-limited imaging with a spatial resolution of 25 nm. However, the development of scanning probe microscopy techniques such as atomic force microscopy (AFM) [101] and scanning tunneling microscopy (STM) [102], enabled the invention of a new technique called Near-field scanning optical microscopy (NSOM) [103, 104]. This technique combines scanning probe microscopy with optical microscopy and thus allows for a sub-diffraction-limit resolution. It uses a metal-coated optical fiber tip as a near-field probe [105, 106]. Another practical method was developed to overcomes limitations of NSOM called Scattering scanning near-field optical microscopy (s-SNOM) [107]. It utilizes a nanoparticle at the focal point of light as a complementary element to the aperture. It avoids the issues associated with the aperture tip [108] and it allows for spatial resolution determined by the size of the tip apex radius [109, 110]. Further trials have been investigated to enhance the s-SNOM technique such as TERS [21–23], which combines Raman spectroscopy with near-field enhancement for highly sensitive imaging.

TERS utilizes what is called the localized surface plasmons (LSPs) [111], which are activated by scattering at irregularities on the tip apex, that in turn offers enhanced Raman spectroscopy. To explain the concept of LSP, the valence electrons of the metal at the tip apex start to oscillate collectively when an electric field matches the LSPs' frequency at resonance. These oscillations, can be mathematically described as a quasi-particle called plasmon. For metal nanopartiles since the valence electrons are those who undergo the collective oscillation is then called localized surface plasmon (LSP). The amplification of the TERS signal is influenced by factors like electron density, effective mass, apex radius of the tip, and the choice of metal. Normally the metal is either silver or gold [112, 113]. These factors predominantly contribute to the electromagnetic enhancement in TERS.

In addition to the electromagnetic enhancement provided by LSPs, there is another contribution known as the chemical enhancement in TERS. The chemical enhancement in TERS can be attributed to several factors: (1) charge transfer between the molecule and the metal tip, (2) orbital hybridization between the molecule and the tip in the electronic ground state, and (3) resonance between the external field and a molecular electronic transition. It is important to note that the separation between chemical and electromagnetic enhancement is not a clear cut [114–116]. These enhancements will be further explored and quantified in sections 3.4 and 3.5.
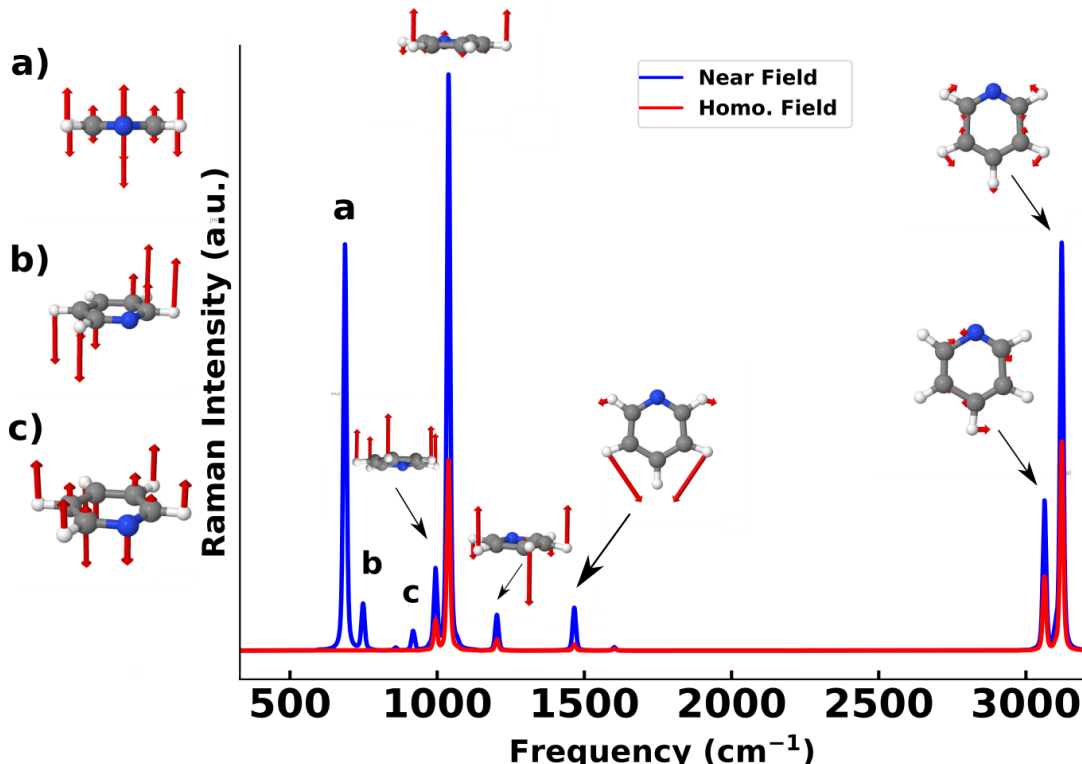
Figure 3.4: Raman spectra of Pyridine, in red using homogeneous field and in blue using near field with tip at 4 AA above the center of mass using PBE+TS-VDW and tight settings, in the FHI-aims code.

3.3.1 Accounting for Local Near-Field Effects in Ab Initio DFPT

To simulate TERS, a combination of DFPT and time-dependent density functional theory (TDDFT) is employed. DFPT, as discussed in chapter 2, allows for the computation of the electronic density's response to an electric field, which determines the non-resonant vibrational Raman cross sections. On the other hand, TDDFT enables the calculation of the near-field distribution for various atomistic tip geometries. By combining DFPT and TDDFT, it becomes possible to account for the near-field effects, considering the different tip geometries. Details will be discussed in subsection 3.4 and an example is given in the next subsection.

3.3.2   Example: Pyridine

Figure 3.4 shows the Raman spectra of Pyridine obtained using both homogeneous and near field method that will be presented in the next section. This method is an approximation to TERS spectroscopy, where the PBE+TS-VDW exchange correlation functional is used, and only the α_{zz} component of polarizability is taken into account. We use the method developed and described in section 3.4 to compute TERS. This just serves as pedagogical example. For the TERS simulation, the Pyridine center of mass molecule was placed 4 Å below the tip. The homogeneous field Raman spectrum of Pyridine has six Raman-active modes in this direction, which are demonstrated in figure 3.4.

New modes become Raman active with TERS, which are in-plane modes and labeled as a, b, and c in the figure. This suggests that TERS is useful in enhancing Raman scattering and making previously inactive modes active, which could provide more insights into the molecular properties and structure of molecules and materials. More details are given in the next section.

3.4   Paper I: First-Principles Simulations of Tip-Enhanced Raman Scattering Reveal Active Role of Substrate Influence High-Resolution Images

As mentioned previously, TERS is a high resolution imaging technique operating at sub-atomic scales. It enables the enhancement of Raman scattering signals through a highly localized electromagnetic field. Theoretically, most implementations depend on simplistic approximations of the local electric field that in turn lead to inaccuracies in the interpretation of experimental data. To overcome this hurdle, a novel method is proposed in this work that is based on TD-DFT and DFPT. TD-DFT provides the distribution of the local field generated by the metalic tip. On the other hand, DFPT enables the computation of density response taking into account the realistic local electric fields experienced by the molecules due to the tip instead of just a homogeneous field.

Letter

First-Principles Simulations of Tip Enhanced Raman Scattering Reveal Active Role of Substrate on High-Resolution Images

Yair Litman,*,[¶] Franco P. Bonafé,[¶] Alaa Akkoush, Heiko Appel, and Mariana Rossi*
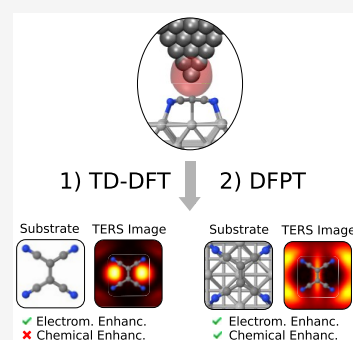
Read Online

ACCESS | Metrics & More | Article Recommendations | SI Supporting Information

ABSTRACT: Tip-enhanced Raman scattering (TERS) has emerged as a powerful tool to obtain subnanometer spatial resolution fingerprints of atomic motion. Theoretical calculations that can simulate the Raman scattering process and provide an unambiguous interpretation of TERS images often rely on crude approximations of the local electric field. In this work, we present a novel and first-principles-based method to compute TERS images by combining Time Dependent Density Functional Theory (TD-DFT) and Density Functional Perturbation Theory (DFPT) to calculate Raman cross sections with realistic local fields. We present TERS results on free-standing benzene and C_{60} molecules, and on the TCNE molecule adsorbed on Ag(100). We demonstrate that chemical effects on chemisorbed molecules, often ignored in TERS simulations of larger systems, dramatically change the TERS images. This observation calls for the inclusion of chemical effects for predictive theory-experiment comparisons and an understanding of molecular motion at the nanoscale.

1) TD-DFT   2) DFPT

Substrate | TERS Image   Substrate | TERS Image
✓ Electrom. Enhanc.   ✓ Electrom. Enhanc.
✗ Chemical Enhanc.   ✓ Chemical Enhanc.

The atomic motion in materials and molecules drives structural changes and chemical reactions, thus, being of fundamental importance in areas as diverse as nanotechnology and biochemistry. Usually, vibrational modes are characterized indirectly through vibrational spectroscopy techniques that are incapable of resolving the motion of individual nuclei. Visualizing such motions with high spatial and temporal resolution is a long-sought goal that would allow an unambiguous understanding of certain physical and chemical processes.[1] For individual molecules adsorbed on certain substrates, this visualization has been recently addressed by tip-enhanced Raman scattering (TERS).[2]

TERS spectroscopy is a powerful technique developed in the last two decades that seamlessly integrates the chemical specificity provided by Raman spectroscopy with the spatial sensitivity of scanning probe microscopy (SPM).[3−6] Similar to other surface-enhanced techniques, the working principle of TERS relies on using the strongly localized plasmonic field produced at the tip apex by an external electromagnetic field, which enhances the Raman signal by several orders of magnitude.[7,8] Unlike conventional spectroscopic techniques, where the spatial resolution is limited by the Rayleigh diffraction limit, near-field-enhanced techniques do not present this optical restriction. Indeed, depending on the shape of the tip apex and other experimental parameters, TERS setups can lead to subnanometer spatial resolution.[9] TERS has been used to monitor catalytic processes at the nanoscale,[10] study plasmon-driven chemical reactions,[11,12] characterize 2D materials,[13−15] and probe redox reactions at the solid/liquid interface.[16,17] Arguably, the most impressive achievement obtained with TERS is the real space visualization of the

vibrational modes of a single molecule, reported a few years ago.[2]

Regarding the physical processes underlying single-molecule TERS and the associated simulation protocols, there are still many points that need clarification. Besides the enhancement due to the strong localization of plasmonic electromagnetic fields (EM), there are three other possible enhancement mechanisms normally discussed in the literature and referred to as "chemical mechanisms":[18] (i) the enhancement due to the chemical interaction (e.g., orbital hybridization) between molecule and substrate or molecule and tip in the electronic ground state (chem-GS); (ii) the enhancement due to a resonance of the external field with a molecular electronic transition (chem-R); and (iii) the enhancement due to a charge transfer caused by the excitation-induced charge reorganization between the molecule and substrate or tip (chem-CT). While the EM mechanism is believed to be dominant in most cases, its relative importance is still under debate.[19−21] For example, when the distance between a tip and a molecule is small enough to form a molecular point contact, a dramatic enhancement likely caused by chem-CT has been reported.[22−25]

Several methods to simulate TERS spectroscopy have recently been developed, with the aim of helping to interpret
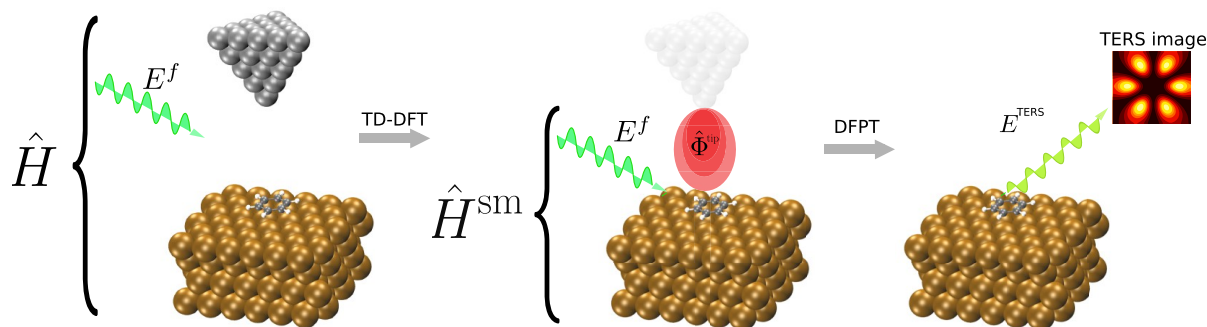
Figure 1. Schematic depiction of the proposed method. The full system and its corresponding full Hamiltonian, $\hat{H}$ (left), are approximated by that of the substrate−molecule subsystem, $\hat{H}^{sm}$ (center), which includes the perturbative terms associated with the external far field, E^f, and the local field generated by the tip plasmonic oscillations, $\hat{\Phi}^{tip}$, obtained from TD-DFT calculations. The calculation of TERS spectra proceeds through density-functional perturbation theory for the calculation of polarizability tensors.

the increasing amount of experimental observations. There are methods based on phenomenological assumptions, which describe the localization of the near field by a bell-shaped function with a predefined width[2,26,27] or which describe the local field by an oscillating dipole.[28,29] These methods are relatively easy to implement and computationally inexpensive, but they are not *ab initio* and, thus, have limited predictive power. Other methods incorporate a realistic (classical) description of the near field,[30−32] but the computational cost becomes prohibitively expensive for medium-sized systems, and a quantum description is restricted to a small region. All of these methods have provided valuable insights in specific situations. However, it is known that the exact atomistic structure of the tip influences the near field in nanoplasmonic junctions[33−35] and that considering the electronic quantum effects in the description of nanoplasmonic fields is mandatory in certain conditions.[33,35]

In this work, we present a methodology that bridges the gap between some of the existing approaches. Our methodology incorporates a realistic description of the near field and retains a modest computational cost, making it applicable to adsorbed and large molecules. To achieve this, we employ density functional perturbation theory (DFPT) to compute the electric-field response of the electronic density that defines the nonresonant vibrational Raman cross sections but incorporate a realistic near-field distribution which we obtain from time-dependent density functional theory (TD-DFT) calculations of different atomistic tip geometries. In this way, we can capture the chem-GS and EM Raman enhancement mechanisms in our calculations at a cost comparable to phenomenological methods for medium and large systems but within a first-principles framework.

We consider a system composed of a molecule placed between a substrate and a metallic tip that lies at some position above the molecule (see Figure 1). If the distance between the tip and the substrate is larger than a few angstroms, there is no overlap of the corresponding charge densities, and therefore the interaction between the two components is dictated essentially by classical electrostatics.[36] We study the effect induced on this system by a time-dependent transverse electromagnetic field, hereafter termed the external far field. Within the dipole approximation, this field is homogeneous. By formally separating the tip Hamiltonian from that of the rest of the system, we can write

$$\hat{H}(t) = \hat{H}_0^{\,sm} - \hat{\overline{\mu}}^{\,sm} \cdot \overline{E}^f(t) + \hat{H}_0^{\,tip} - \hat{\overline{\mu}}^{\,tip} \cdot \overline{E}^f(t) + \hat{V}^{int}(t) \tag{1}$$

where the labels "sm", "tip", and "int" refer to the substrate plus molecule subsystem, the tip subsystem, and the interaction between subsystems, respectively. H_0 refers to the unperturbed Hamiltonians, $\hat{\overline{\mu}}$ are the corresponding dipole operators, and $\overline{E}^f(t) = (\lambda_x \hat{n}_x + \lambda_y \hat{n}_y + \lambda_z \hat{n}_z) \cos(\omega_0 t)$, where $\lambda_{x,y,z}$ are the electromagnetic field strengths, ω_0 is the electromagnetic field frequency, and $\hat{n}_{x,y,z}$ are unit vectors along each Cartesian direction. In the expression above, it is implicit that we work in a Coulomb gauge.

To move forward, we make further assumptions. The first assumption is that the tip is not influenced by the presence of the molecule and substrate (justified by the previously assumed long distance between these components and a neutral molecule−substrate subsystem). This allows the calculation of the time-dependent electronic density ρ_{tip} by the real-time propagation of the Kohn−Sham states of the isolated tip under the influence of an external field in TD-DFT, assuming a dipolar light−matter coupling. Then, the (electrostatic) interaction between the tip and the rest of the system can be computed as

$$\hat{V}_{int}(\boldsymbol{r}_{sm}, t; \boldsymbol{R}_{tip}) = \int d\boldsymbol{r} \frac{\rho_{tip}(\boldsymbol{r}, t; \boldsymbol{R}_{tip})}{|\boldsymbol{r} - \hat{\boldsymbol{r}}_{sm}|} = \hat{\Phi}_{tip}(\boldsymbol{r}_{sm}, t; \boldsymbol{R}_{tip}) \tag{2}$$

where $\boldsymbol{r}_{sm}$ refers to the positions of the electrons belonging to the substrate−molecule subsystem and $\boldsymbol{R}_{tip}$ refers to the position of nuclei of the tip subsystem. In eq 2, we defined the time-dependent electrostatic potential of the tip, $\hat{\Phi}_{tip}$ (often called Hartree potential), which is a central quantity for the current method. Indeed, under the current assumptions, the effect exerted on the substrate by the tip can be described by its Hartree potential. The ';' symbol in eq 2 has been used to emphasize the parametric dependence of $\hat{\Phi}_{tip}$ on the position and spatial arrangement of the nuclei in the tip, $\boldsymbol{R}_{tip}$.

The second assumption is that the strength of the external far field is small, such that the response of the tip lies in the linear regime; i.e., one can perform a Taylor expansion of $\hat{\Phi}_{tip}$ around zero-field strength ($\lambda = 0$) and truncate it at first order. The linear response regime was confirmed for the calculations presented throughout the paper (see Figure S4) and can be also verified in experimental setups. Then, considering that the
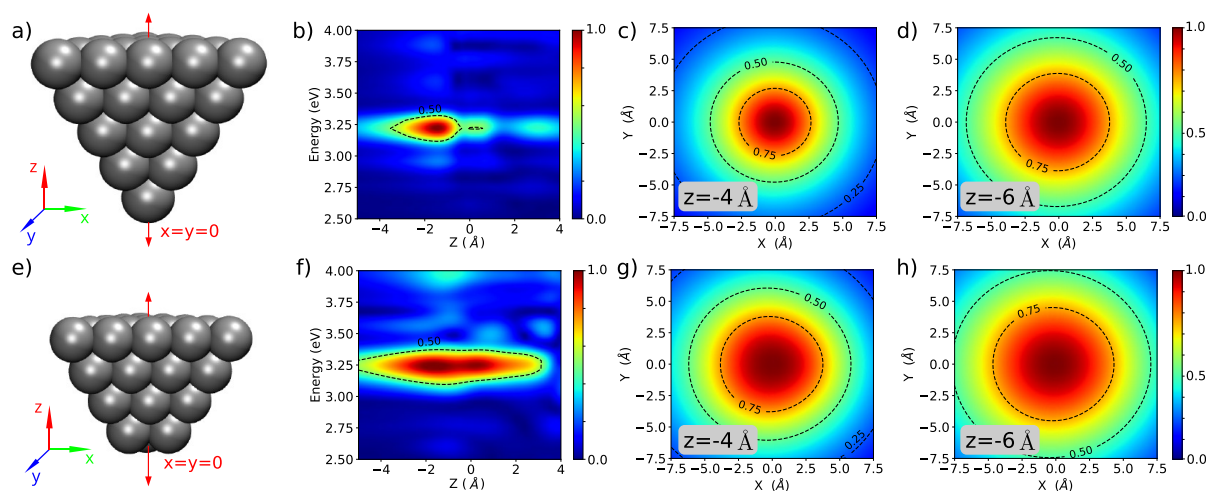
Figure 2. Energy and spatial dependence of the tip Hartree potential from TD-DFT simulations. Panel (a) shows the structure of the tip-A model. Panel (b) shows the normalized $\tilde{\Phi}^{\text{tip}}$ along the $(x = 0, y = 0, z)$ line. Panels (c) and (d) show normalized two-dimensional cuts at 3.22 eV and z equal to 4 and 6 Å below the tip apex. Panels (e)−(h) are analogous to panels (a)−(d) for the tip-B model. In all plots the origin is defined at the center of the tip apex position.

system is at the ground state before an excitation by the laser field, $\hat{\Phi}^{\text{tip}}(t = 0) = \hat{\Phi}^{\text{tip}}_{\text{GS}}$, and that responses are local in the frequency domain in the linear regime,[37] we can write the substrate−molecule Hamiltonian in a particular Cartesian direction α as,

$$\hat{H}^{\text{sm}} = \hat{H}^{\text{sm}}_0 + \hat{\Phi}^{\text{tip}}_{\text{GS}} + \lambda_\alpha \left[-\hat{\mu}^{\text{sm}}_\alpha + \left. \frac{\partial \tilde{\Phi}_{\text{tip}}(\omega_0; \boldsymbol{R}_{\text{tip}})}{\partial \lambda_\alpha} \right|_{\lambda_\alpha=0} \right]$$

(3)

where $\tilde{\Phi}_{\text{tip}}(\omega_0; \boldsymbol{R}_{\text{tip}})$ denotes a time Fourier transform of $\hat{\Phi}_{\text{tip}}(t; \boldsymbol{R}_{\text{tip}})$ evaluated at ω_0. In the last line, a perturbation of the substrate−molecule subsystem is neatly defined. The first term inside the square brackets describes the dipole interaction between the substrate with the homogeneous far field, while the second term describes the interaction with the local field generated by the tip. The latter term gives rise to the EM enhancement mechanism and the modified selection rules present in TERS spectroscopy. See a more detailed derivation of eq 3 in Section I of the Supporting Information (SI). Equation 3 is suitable to be treated within the *time-independent* DFPT in order to find the static polarizability of the molecule and substrate, α, which enables the calculation of the nonresonant Raman signal.[38] In this work we calculate harmonic nonresonant Raman intensities, I^{Raman} as

$$I^{\text{Raman}}(\omega_i) \propto \left| \frac{\partial \alpha_{zz}}{\partial Q_i} \right|^2$$

(4)

where α_{zz} is the zz component of the polarizability tensor and Q_i and ω_i represent the eigenmode and eigenfrequency of the i-th vibrational normal mode, respectively. In this work, we consider exclusively the α_{zz} component since it is the direction normally regarded as the most relevant in TERS experiments[2,25] and allows us to compare with previously reported spectra.[26,29] However, the method can be used to describe any polarization dependence of the incoming and detected light by including other components of the polarizability tensor in the

calculation of the Raman signal.[25,39,40] Furthermore, it is possible to combine this approach with more sophisticated approximations of the Raman signal that can capture the anharmonicity of the vibrational modes, which could be relevant for more flexible molecules.[41,42]

In Figure 1, we show a schematic depiction of the proposed method. The electronic oscillations created by the external field generate an oscillating Hartree potential, $\hat{\Phi}^{\text{tip}}$, whose gradient is the so-called local (longitudinal) electric field, and its maximum intensity is situated a few angstroms below the tip apex.[43] The advantage of centering the approach on $\hat{\Phi}^{\text{tip}}$ rather than the local field and its gradient is, besides its mathematical simplicity, the fact that all the terms in the multipolar expansion are automatically incorporated and no origin-dependence problems arise. All magnetic contributions are ignored as usually done for nonmagnetic materials.[44] We note that the enhancement of the incident field is included, while the enhancement of the scattered field is ignored. To obtain the correct dependence of the enhanced Raman intensity with respect to the local field, the incorporation of dipole reradiation effects are required.[31,45] Approximate corrections, based on the dressed tensor formalism, can be incorporated by choosing a coordinate origin and performing a Taylor expansion with respect to the incident fields.[44,46] Within the formalism presented in this paper, a modified version of the latter approach would lead to an unphysical origin dependence. Thus, and similarly to most of the existing methods to simulate TERS images,[2,20,29,47] the predicted signal intensity reported in this work follows a $|E|^2$ dependence instead of the expected $|E|^4$ for large tip-molecule distances.[18,31,48]

We start by analyzing the local Hartree potential generated by different Ag tip geometries. We considered tetrahedral tips with a one-atom apex (tip-A) and a three-atom apex (tip-B) as shown in Figure 2a,e, respectively.[22] The fields $\tilde{\Phi}^{\text{tip}}$ were calculated using the Octopus code[49,50] with the LDA exchange-correlation functional (see simulations details in Section II in the SI). The use of an arguably small model tip structure to study plasmonic near-field distributions from an atomistic first-principles perspective is justified by the fact that
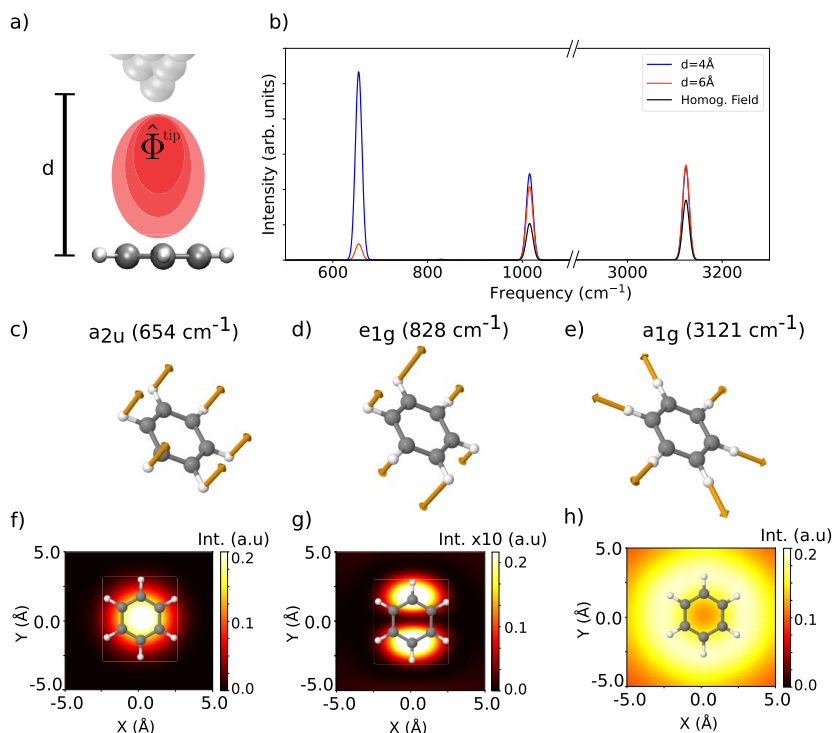
Figure 3. TERS simulation of gas-phase benzene from local-field DFPT calculations. (a) Sketch of the simulation setup. (b) Simulated harmonic TERS spectrum of the benzene molecule for different tip−molecule distances, d, compared to the homogeneous-field case. Only the signal coming from the α_{zz} component is shown for all cases. The observed enhancement is nonlinear with the molecule−tip distance since higher-order derivatives of the local potential start to contribute to the signal at the shortest distances.[44] (c−e) Normal mode eigenvectors of selected vibrational modes with their respective symmetries and frequencies. (f−h) TERS images of the selected vibrational modes for a molecule−tip apex distance of 4 Å. See Figure S12 in the SI for the TERS image of the 1015 cm^{-1} peak.

the plasmon peak of Ag clusters is well separated from the interband transitions even for small clusters.[51−53] Figure 2b,f shows the magnitude of $\tilde{\Phi}^{tip}$ as a function of the laser energy and distance from the tip apex. In both cases, the maximum $\tilde{\Phi}^{tip}$ is found at 1.4 Å below the tip apex and at 3.22 eV. The intensity of the potential decays to its half-value at 4 and at 5 Å below the tip apex for tip-A and tip-B, respectively. We analyzed larger tip sizes and verified that the overall shape of $\tilde{\Phi}^{tip}$ is not significantly altered and the plasmonic peak approaches the visible range in agreement with previous studies[51] (Figure S3 in the SI). The two-dimensional cuts of $\tilde{\Phi}^{tip}$ for tip-A and tip-B, presented in the remaining panels of Figure 2, show that the field maximum is found exactly below the apex of tip-A and below the three atoms that constitute the tip apex for tip-B. Interestingly, at 6 Å below the tip apex, the shape of $\tilde{\Phi}^{tip}$ of the two models becomes indistinguishable, which suggests that, for substrate−tip distance greater than 6 Å, the fine details of the apex should be negligible in TERS imaging experiments. In passing, we note that at 4 Å below the tip apex the distribution of the local field resembles that of a 2D Gaussian function to some extent. However, a Gaussian profile can neither adequately describe the rapid change of intensity at the center of the distribution nor capture any radial asymmetry (see Section III in the SI).

We proceeded by computing TERS spectra for the free-standing benzene molecule. Benzene has been investigated several times as a proof-of-concept molecule[26,29] and it allows us to compare the current method with others proposed in the literature. We calculated Raman intensities with the FHI-

aims[54] code and the LDA functional, where the DFPT implementation[55] has been extended to include the local field as prescribed by eq 3 and to account for plasmonic terms in the electronic-density response of metallic clusters.[56] We consider a benzene molecule in a flat orientation, as depicted in Figure 3a, and compute the TERS spectra for different tip−molecule distances, d, as shown in Figure 3b. In these calculations, tip-A was used, and its apex was aligned to the center of the benzene molecule. We remark that only the signal coming from the α_{zz} component of the polarizability tensor is shown. By analyzing the projected density of states of the benzene−tip system (see Section III in the SI) we concluded that, for distances larger than 3 Å, the assumption that there is no chemical interaction between the two subsystems is valid. Moreover, by analyzing the molecularly induced dipole at different tip−molecule relative positions, we verified that we are within the applicability realm of first-order perturbation theory at these molecule−tip distances (see Section II in the SI).

The inhomogeneity of the local field induces changes in the TERS spectra in two distinctive ways compared to the standard (homogeneous field) Raman spectrum. On one hand, the intensity of the peaks at 1015 and 3121 cm^{-1} (a_{1g}) is enhanced with respect to the homogeneous field case. On the other hand, the a_{2u} mode at 654 cm^{-1} which is Raman inactive becomes active in the TERS spectrum, which denotes a new selection rule arising from the spatial variation of the local field. In Figure 3 panels (c)−(e), we show the normal mode eigenvectors of selected vibrational modes, and in panels (f)−
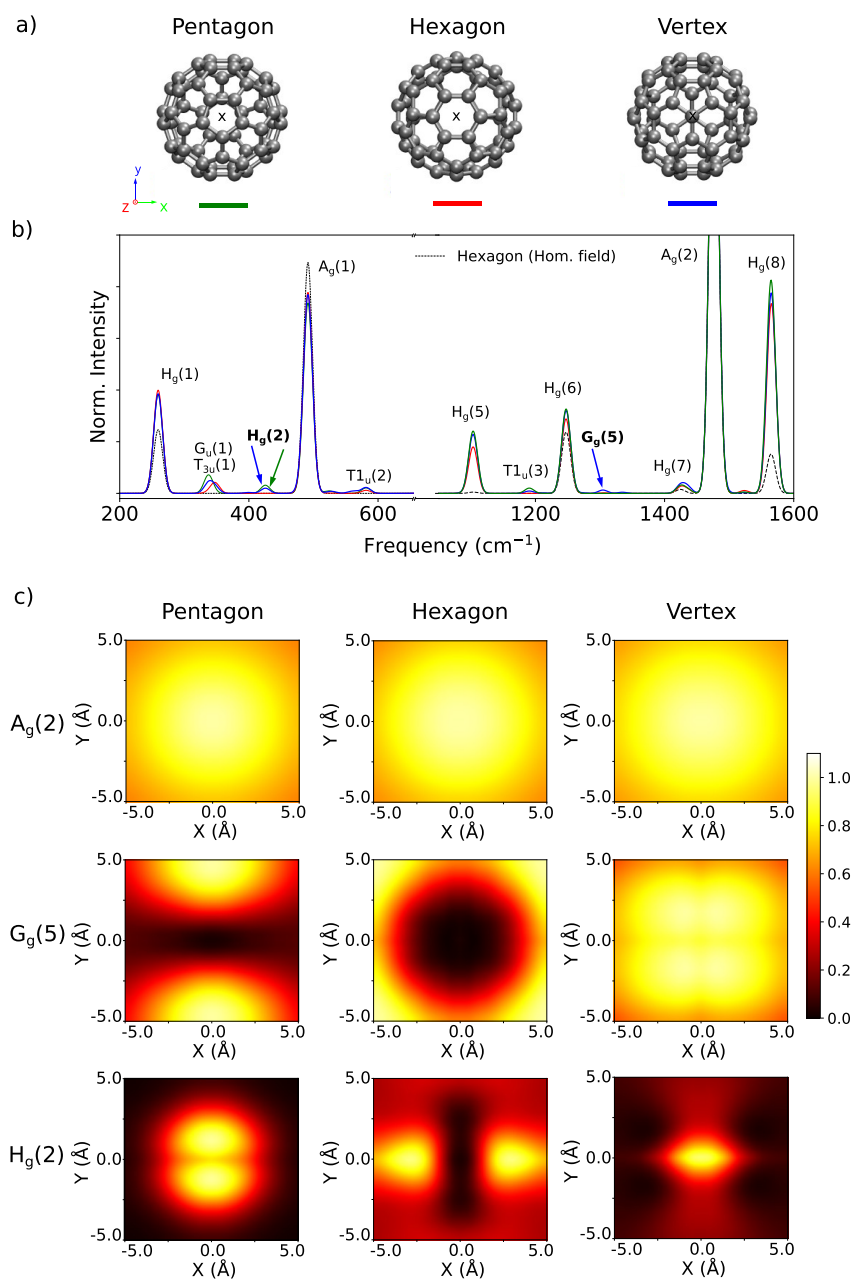
Figure 4. (a) Depiction of C_{60} molecular orientations. Pentagon (green), hexagon (red), and vertex (blue) refer to the molecular geometries with the corresponding face closest to the tip. (b) TERS spectra of the C_{60} molecule with the tip apex placed at 4 Å above the "X" mark in (a). The intensities of the spectra are normalized with respect to the intensity of the Ag(2) peak. (c) TERS images for the $A_g(2)$, $G_g(5)$, and $H_g(2)$ vibrational modes. In all cases, the intensities are normalized to the corresponding spectrum maximum.

(h), their corresponding TERS images. The images were obtained by computing the TERS spectra at different lateral positions of the tip with respect to the molecule at a constant height of 4 Å. The intensities of the corresponding vibrational mode were then plotted in a 2D heat map. While the images of the modes located at 828 and 3121 cm^{-1} show distinctive patterns that are comparable to the ones obtained by other methods, the results for the mode located at 654 cm^{-1} obtained by our approach differs significantly.[26,29] Although all of the methods would agree if the local field would be modeled by a given set of parameters, this example demonstrates the advantage of employing a parameter-free method, with easy-to-verify assumptions.

An interesting application of TERS spectroscopy is the determination of relative molecular orientations.[9,44,57] Here, we evaluated the possibility of identifying the orientation of the C_{60} molecule using the current framework. In Figure 4, we report the TERS spectra of C_{60} in three different orientations. While we observe that the local field causes a nonuniform enhancement of peak intensities, the peaks that are active in the calculations with a homogeneous field, i.e., the H_g and A_g modes, are not sensitive to the specific molecular orientation.
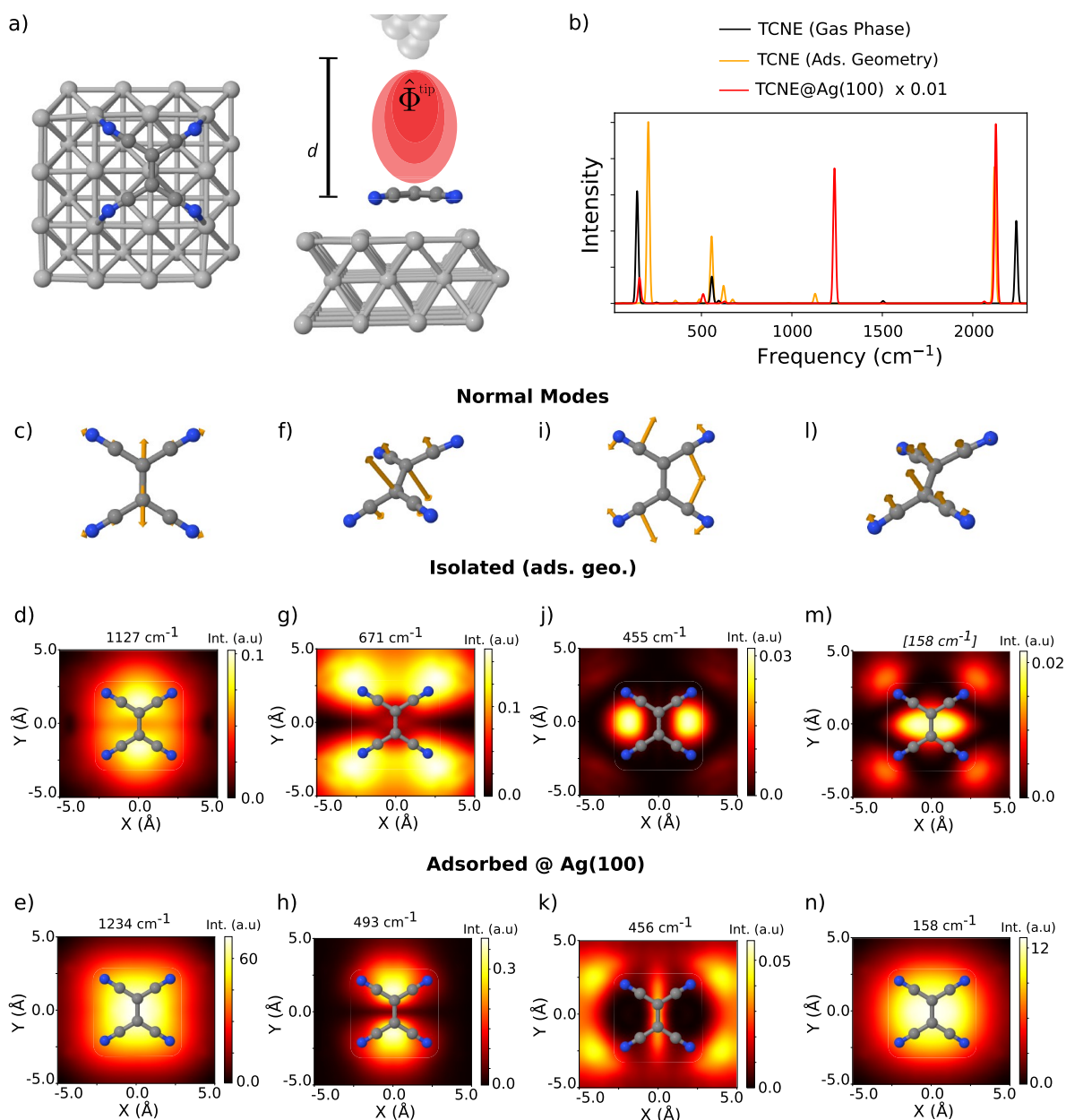
Figure 5. (a) Sketch of simulation setup of TCNE adsorbed on a Ag(100) cluster. (b) Simulated TERS image of TCNE in isolation (TCNEgas, black), of TCNE in isolation but at the adsorbed geometry (TCNEads, orange), and of TCNE at the Ag(100) cluster discussed in the text (TCNE@Ag(100), red). Tip apex was placed on the molecular center of mass at a distance of 4 Å. (c, f, i, and l) Normal mode displacement vectors of selected vibrational modes of TCNE@Ag(100). The surface has been deleted for clarity. (d, g, j, and m) TERS images of the depicted normal modes for TCNEads. (e, h, k, and n) TERS images of the depicted normal modes for TCNE@Ag(100). In all cases a molecule−apex distance of 4 Å was employed. Frequency within square brackets in panel (m) denotes the lack of an equivalent normal mode eigenvector in the TCNEads calculation.

Conversely, some of the new peaks that emerge due to the local field, such as $G_g(5)$ and $H_g(2)$, present a more pronounced orientation dependence. Indeed, the corresponding TERS images, depicted in Figure 4, display characteristic patterns that could be used to identify the molecular orientation in sufficiently sensitive TERS experiments.

Finally, we consider the tetracyanoethylene (TCNE) molecule as a representative of strong interaction with metallic substrates.[58] TCNE is a strong electron acceptor due to the

four cyano-group low-energy orbitals conjugated to the central C−C bond[59] and has been investigated as a room temperature molecular magnet.[60] To study the impact of chem-GS enhancements on TERS spectra, we consider three scenarios: (i) The TCNE molecule with its optimized geometry in the gas phase (TCNEgas), (ii) the molecule adsorbed on Ag(100) (TCNE@Ag(100)), and (iii) the molecule in the gas-phase but fixed at the adsorbed geometry (TCNEads). The Ag(100) surface was modeled by a 3-layer 4 × 4 cluster, and we

employed the PBE functional in our DFPT calculations (see more details and convergence tests in Section II of the SI). The size limitation of the cluster models employed here is dictated only by technical issues regarding the implementation of DFPT for systems with fractional occupations, which can be easily overcome in the near future. In fact, we have recently computed TERS images of semiconducting systems containing nearly 200 atoms.[61] Still, a few algorithmic hurdles need to be overcome to further increase the applicability of the method, as implemented in the FHI-aims code. For instance, the formulation of the DFPT response in real space and with the presence of a local field under periodic boundary conditions needs to be addressed.

TCNE is a planar molecule in the gas-phase. Upon adsorption with a flat orientation, the TCNE molecule arcs with the CN groups pointing toward the Ag atoms, and the nitrogen atoms coordinate Ag atoms that form a 3×3 square, as depicted in Figure 5a. The TCNE molecule becomes negatively charged upon adsorption, exhibiting an elongated central C−C bond.[59] We estimated the molecular charge to be 0.6 e using a procedure described elsewhere.[62] The TCNEgas, TCNEads, and TCNE@Ag(100) TERS spectra, calculated according to eq 4, are presented in Figure 5b with black, orange, and red curves, respectively. The TCNEgas spectrum presents three main peaks. The ones at 144 and 557 cm^{-1} correspond to out-of-plane modes, while the vibrations at 2239 cm^{-1} correspond to the in-plane CN stretching mode. The TCNEads spectrum also presents three major peaks at 207, 555, and 2119 cm^{-1}, which correspond to analogous vibrational modes. However, due to the deformation of the molecular geometry, some of the vibrational frequencies are considerably red or blue-shifted. In addition, this spectrum presents several satellite peaks of relatively low intensity. The TCNE@Ag(100) spectrum is around 2 orders of magnitude more intense than the other spectra due to chem-GS enhancement. While the peak at 2127 cm^{-1} preserves the CN stretch character and is considerably enhanced, the modes at around 200 and 550 cm^{-1} mix with other normal modes and show a relatively smaller intensity enhancement. A new high-intensity peak appears at 1235 cm^{-1} and corresponds to the central C−C stretching mode.

In the remaining panels in Figure 5, we present TERS images for selected vibrational modes. To make a legit comparison and to isolate the effect caused by chem-GS enhancement, we only compare TCNEads with TCNE@Ag(100) (same molecular geometry), and in the evaluation of eq 4, we use the normal modes associated with the TCNE@Ag(100) structure. The TERS images of the central C−C stretching mode are shown in panels (d) and (e) and present comparable shapes with most of the Raman signal localized in the vicinity of the molecular center. However, the TCNEads image shows two clearly separated spots with the highest intensity at each side of the molecule along the central C−C bond axis. The intensity at the center of the molecule is relatively small, as shown in the 1D spectra. In panels (g), (h), (j), (k), (m), and (n) we present other vibrational modes that show TERS activity, including out-of-plane and in-plane molecular motions. The TERS images when including the Ag atoms are remarkably different even though we are considering the same geometry and nuclear displacements in the calculations. This observation proves that the symmetry of the normal modes does not exclusively determine TERS images and chem-GS effects can play a decisive role in

determining the shape and intensity of the image. Moreover, neither a normal-mode analysis, a simple symmetry argument, nor a frequency comparison between TCNEads and TCNE@Ag(100) calculations seems to be able to predict, *a priori*, the impact of the chem-GS enhancement on the shape of the TERS images. We also verified that adding a negative charge to the TCNEads calculations does not reproduce the TCNE@Ag(100) results (see Figure S14 in the SI). This highlights once again the necessity of a first-principles calculation including the substrate.

In summary, we have presented a new first-principles method to compute TERS spectra and images that retains computational efficiency. The method does not rely on simplistic models for the tip geometry and its generated field and is able to capture EM and chem-GS types of Raman signal enhancement. It enables the calculation of TERS spectra and images at a substantially reduced computational cost. In fact, as shown in SI, Section V, we estimate a 4 orders of magnitude reduction in computational cost with respect to full real-time TD-DFT simulations.[63,64] We presented results for three molecules: Two that physisorb on metallic substrates (benzene and C_{60}) and one that chemisorbs (TCNE). For the former cases, we showed that the predicted TERS images differ from simplified approaches unless specific parameters are calibrated and confirmed that TERS spectroscopy can be used determine molecular orientations, even for highly symmetric molecules. For the latter, we showed that the chemical interaction between the molecule and the substrate leads to drastic changes in the TERS images, which reveal that the chemical enhancement shows atomic-scale variation.

The method proposed in this paper can be seamlessly coupled to *ab initio* (path integral) molecular dynamics simulations, to capture anharmonic and finite temperature (quantum) anharmonic effects.[41,65,66] A calculation of the Raman intensities from a TD-DFT evaluation of the frequency-dependent polarizability tensors is also possible and would give access to resonant Raman scattering, thus capturing the chem-R enhancement mechanism.[63,67] Moreover, by using methods with lower computational cost, such as density functional tight-binding,[68] one could in principle converge the calculations with respect to the tip size.

The accuracy of the method we propose remains to be fully benchmarked, since a reference theoretical TERS calculation including all effects of light−matter coupling in the semi-classical limit[69,70] has not yet been reported in the literature. Nevertheless, this method bridges an important gap in terms of accuracy and computational cost among existing approaches to TERS simulations, facilitating the interpretation of TERS experiments for realistic complex systems. We hope that the reported results motivate new single-molecule TERS experiments on inorganic−organic interfaces composed of chemisorbed molecules relevant to electronic and light-harvesting applications.[71−73]

■ ASSOCIATED CONTENT

Data Availability Statement

A tutorial to generate TERS images for the benzene molecule with the FHI-aims code with all the necessary input files is available at https://github.com/sabia-group/TERS_Tutorial.

ⓢ Supporting Information

The Supporting Information is available free of charge at https://pubs.acs.org/doi/10.1021/acs.jpclett.3c01216.

Detailed derivation of eq 3, further computational details, and validation tests (PDF)

■ AUTHOR INFORMATION

Corresponding Authors

Yair Litman − *Yusuf Hamied Department of Chemistry, University of Cambridge, Cambridge CB2 1EW, United Kingdom; MPI for the Structure and Dynamics of Matter, 22761 Hamburg, Germany;* orcid.org/0000-0002-6890-4052; Email: yl899@cam.ac.uk

Mariana Rossi − *MPI for the Structure and Dynamics of Matter, 22761 Hamburg, Germany; Fritz Haber Institute of the Max Planck Society, 14195 Berlin, Germany;* orcid.org/0000-0002-3552-0677; Email: mariana.rossi@mpsd.mpg.de

Authors

Franco P. Bonafé − *MPI for the Structure and Dynamics of Matter, 22761 Hamburg, Germany;* orcid.org/0000-0002-2069-6776

Alaa Akkoush − *MPI for the Structure and Dynamics of Matter, 22761 Hamburg, Germany; Fritz Haber Institute of the Max Planck Society, 14195 Berlin, Germany*

Heiko Appel − *MPI for the Structure and Dynamics of Matter, 22761 Hamburg, Germany*

Complete contact information is available at:
https://pubs.acs.org/10.1021/acs.jpclett.3c01216

Author Contributions

¶(Y.L. and F.P.B.) These authors contributed equally.

Notes

The authors declare no competing financial interest.

■ REFERENCES

(1) Gross, L. Recent advances in submolecular resolution with scanning probe microscopy. *Nat. Chem.* **2011**, *3*, 273−278.

(2) Lee, J.; Crampton, K. T.; Tallarida, N.; Apkarian, V. A. Visualizing vibrational normal modes of a single molecule with atomically confined light. *Nature* **2019**, *568*, 78−82.

(3) Hayazawa, N.; Inouye, Y.; Sekkat, Z.; Kawata, S. Metallized tip amplification of near-field Raman scattering. *Opt. Commun.* **2000**, *183*, 333−336.

(4) Anderson, M. S. Locally enhanced Raman spectroscopy with an atomic force microscope. *Appl. Phys. Lett.* **2000**, *76*, 3130−3132.

(5) Stöckle, R. M.; Suh, Y. D.; Deckert, V.; Zenobi, R. Nanoscale chemical analysis by tip-enhanced Raman spectroscopy. *Chem. Phys. Lett.* **2000**, *318*, 131−136.

(6) Steidtner, J.; Pettinger, B. Tip-enhanced raman spectroscopy and microscopy on single dye molecules with 15 nm resolution. *Phys. Rev. Lett.* **2008**, *100*, 236101.

(7) Zrimsek, A. B.; Chiang, N.; Mattei, M.; Zaleski, S.; McAnally, M. O.; Chapman, C. T.; Henry, A.-I.; Schatz, G. C.; Van Duyne, R. P. Single-molecule chemistry with surface- and tip-enhanced Raman spectroscopy. *Chem. Rev.* **2017**, *117*, 7583−7613.

(8) Chulhai, D. V.; Hu, Z.; Moore, J. E.; Chen, X.; Jensen, L. Theory of linear and nonlinear surface-enhanced vibrational spectroscopies. *Annu. Rev. Phys. Chem.* **2016**, *67*, 541−564.

(9) Zhang, R.; Zhang, Y.; Dong, Z. C.; Jiang, S.; Zhang, C.; Chen, L. G.; Zhang, L.; Liao, Y.; Aizpurua, J.; Luo, Y.; et al. Chemical mapping of a single molecule by plasmon-enhanced Raman scattering. *Nature* **2013**, *498*, 82−86.

(10) van Schrojenstein Lantman, E. M.; Deckert-Gaudig, T.; Mank, A. J. G.; Deckert, V.; Weckhuysen, B. M. Catalytic processes monitored at the nanoscale with tip-enhanced Raman spectroscopy. *Nat. Nanotechnol.* **2012**, *7*, 583−586.

(11) Sun, M.; Zhang, Z.; Zheng, H.; Xu, H. In-situ plasmon-driven chemical reactions revealed by high vacuum tip-enhanced Raman spectroscopy. *Sci. Rep.* **2012**, *2*, 647.

(12) O'Callahan, B. T.; El-Khoury, P. Z. A closer look at tip-enhanced Raman chemical reaction nanoimages. *J. Phys. Chem. Lett.* **2022**, *13*, 3886−3889.

(13) Farhat, P.; Avilés, M. O.; Legge, S.; Wang, Z.; Sham, T.-K.; Lagugné-Labarthet, F. Tip-enhanced Raman spectroscopy and Tip-enhanced photoluminescence of MoS2 flakes decorated with gold nanoparticles. *J. Phys. Chem. C* **2022**, *126*, 7086−7095.

(14) Birmingham, B.; Liege, Z.; Larson, N.; Lu, W.; Park, K. T.; Lee, H. W. H.; Voronine, D. V.; Scully, M. O.; Zhang, Z. Probing interaction between individual submonolayer nanoislands and bulk MoS2 using ambient TERS. *J. Phys. Chem. C* **2018**, *122*, 2753−2760.

(15) Rahaman, M.; Rodriguez, R. D.; Plechinger, G.; Moras, S.; Schüller, C.; Korn, T.; Zahn, D. R. T. Highly localized strain in a MoS2/Au heterostructure revealed by tip-enhanced Raman spectroscopy. *Nano Lett.* **2017**, *17*, 6027−6033.

(16) Martín Sabanés, N.; Ohto, T.; Andrienko, D.; Nagata, Y.; Domke, K. F. Electrochemical TERS elucidates potential-induced molecular reorientation of adenine/Au(111). *Angew. Chem., Int. Ed.* **2017**, *56*, 9796−9801.

(17) Zeng, Z.-C.; Huang, S.-C.; Wu, D.-Y.; Meng, L.-Y.; Li, M.-H.; Huang, T.-X.; Zhong, J.-H.; Wang, X.; Yang, Z.-L.; Ren, B. Electrochemical tip-enhanced Raman spectroscopy. *J. Am. Chem. Soc.* **2015**, *137*, 11928−11931.

(18) Jensen, L.; Aikens, C. M.; Schatz, G. C. Electronic structure methods for studying surface-enhanced Raman scattering. *Chem. Soc. Rev.* **2008**, *37*, 1061−1073.

(19) Zhang, C.; Chen, B.-Q.; Li, Z.-Y. Optical origin of subnanometer resolution in tip-enhanced Raman mapping. *J. Phys. Chem. C* **2015**, *119*, 11858−11871.

(20) Fiederling, K.; Kupfer, S.; Gräfe, S. Are charged tips driving TERS-resolution? A full quantum chemical approach. *J. Chem. Phys.* **2021**, *154*, 034106.

(21) Latorre, F.; Kupfer, S.; Bocklitz, T.; Kinzel, D.; Trautmann, S.; Gräfe, S.; Deckert, V. Spatial resolution of tip-enhanced Raman spectroscopy − DFT assessment of the chemical effect. *Nanoscale* **2016**, *8*, 10229−10239.

(22) Cirera, B.; Litman, Y.; Lin, C.; Akkoush, A.; Hammud, A.; Wolf, M.; Rossi, M.; Kumagai, T. Charge transfer-mediated dramatic enhancement of Raman scattering upon molecular point contact formation. *Nano Lett.* **2022**, *22*, 2170−2176.

(23) Aiga, N.; Takeuchi, S. Single-molecule raman spectroscopy of a pentacene derivative adsorbed on the nonflat surface of a metallic tip. *J. Phys. Chem. C* **2022**, *126*, 16227−16235.

(24) Gieseking, R. L. M.; Lee, J.; Tallarida, N.; Apkarian, V. A.; Schatz, G. C. Bias-dependent chemical enhancement and nonclassical stark effect in tip-enhanced raman spectromicroscopy of CO-terminated Ag tips. *J. Phys. Chem. Lett.* **2018**, *9*, 3074−3080.

(25) Yang, B.; Chen, G.; Ghafoor, A.; Zhang, Y.-F.; Zhang, X.-B.; Li, H.; Dong, X.-R.; Wang, R.-P.; Zhang, Y.; Zhang, Y. Chemical enhancement and quenching in single-molecule tip-enhanced Raman spectroscopy. *Angew. Chem., Int. Ed.* **2023**, *62*, e202218799.

(26) Chen, X.; Liu, P.; Hu, Z.; Jensen, L. High-resolution tip-enhanced Raman scattering probes sub-molecular density changes. *Nature Comm.* **2019**, *10*, 2567.

(27) Duan, S.; Tian, G.; Luo, Y. Visualization of vibrational modes in real space by tip-enhanced non-resonant Raman spectroscopy. *Angew. Chem., Int. Ed.* **2016**, *55*, 1041−1045.

(28) Iwasa, T.; Nobusada, K. Nonuniform light-matter interaction theory for near-field-induced electron dynamics. *Phys. Rev. A* **2009**, *80*, 043409.

(29) Takenaka, M.; Taketsugu, T.; Iwasa, T. Theoretical method for near-field Raman spectroscopy with multipolar Hamiltonian and real-time-TDDFT: Application to on- and off-resonance tip-enhanced Raman spectroscopy. *J. Chem. Phys.* **2021**, *154*, 024104.

(30) Chen, H.; McMahon, J. M.; Ratner, M. A.; Schatz, G. C. Classical electrodynamics coupled to quantum mechanics for calculation of molecular optical properties: a RT-TDDFT/FDTD approach. *J. Phys. Chem. C* **2010**, *114*, 14384−14392.

(31) Payton, J. L.; Morton, S. M.; Moore, J. E.; Jensen, L. A hybrid atomistic electrodynamics-quantum mechanical approach for simulating surface-enhanced Raman scattering. *Acc. Chem. Res.* **2014**, *47*, 88−99.

(32) Liu, P.; Chulhai, D. V.; Jensen, L. Single-molecule imaging using atomistic near-Field tip-enhanced Raman spectroscopy. *ACS Nano* **2017**, *11*, 5094−5102.

(33) Zhang, P.; Feist, J.; Rubio, A.; García-González, P.; García-Vidal, F. J. Ab initio nanoplasmonics: The impact of atomic structure. *Phys. Rev. B* **2014**, *90*, 161407.

(34) Barbry, M.; Koval, P.; Marchesin, F.; Esteban, R.; Borisov, A. G.; Aizpurua, J.; Sánchez-Portal, D. Atomistic near-field nanoplasmonics: Reaching atomic-scale resolution in nanooptics. *Nano Lett.* **2015**, *15*, 3410−3419.

(35) Urbieta, M.; Barbry, M.; Zhang, Y.; Koval, P.; Sánchez-Portal, D.; Zabala, N.; Aizpurua, J. Atomic-scale lightning rod effect in plasmonic picocavities: A classical view to a quantum effect. *ACS Nano* **2018**, *12*, 585−595.

(36) Zhu, W.; Esteban, R.; Borisov, A. G.; Baumberg, J. J.; Nordlander, P.; Lezec, H. J.; Aizpurua, J.; Crozier, K. B. Quantum mechanical effects in plasmonic structures with subnanometre gaps. *Nat. Commun.* **2016**, *7*, 11495.

(37) Marques, M. A.; Ullrich, C. A.; Nogueira, F.; Rubio, A.; Burke, K.; Gross, E. K. *Time-dependent density functional theory*; Springer: Berlin, 2006; Vol. *706*.

(38) Long, D. A. *The Raman Effect*; John Wiley and Sons: New York, 2002.

(39) Ru, E. C. L.; Etchegoin, P. G. *Principles of Surface-Enhanced Raman Spectroscopy: And Related Plasmonic Effects*; Elsevier: Amsterdam, 2008.

(40) McQuarrie, D. A. *Statistical mechanics*; University Science Books: Mill Valley, CA, 2000.

(41) Berne, B. J.; Pecora, R. *Dynamic light scattering*; John Wiley & Sons: New York, 1976.

(42) Raimbault, N.; Athavale, V.; Rossi, M. Anharmonic effects in the low-frequency vibrational modes of aspirin and paracetamol crystals. *Phys. Rev. Mater.* **2019**, *3*, 053605.

(43) Peller, D.; Roelcke, C.; Kastner, L. Z.; Buchner, T.; Neef, A.; Hayes, J.; Bonafé, F.; Sidler, D.; Ruggenthaler, M.; Rubio, A.; et al. Quantitative sampling of atomic-scale electromagnetic waveforms. *Nat. Photonics* **2021**, *15*, 143−147.

(44) Chulhai, D. V.; Jensen, L. Determining molecular prientation with surface-enhanced Raman scattering using inhomogenous electric fields. *J. Phys. Chem. C* **2013**, *117*, 19622−19631.

(45) Ausman, L. K.; Schatz, G. C. On the importance of incorporating dipole reradiation in the modeling of surface enhanced Raman scattering from spheres. *J. Chem. Phys.* **2009**, *131*, 084708.

(46) Janesko, B. G.; Scuseria, G. E. Surface enhanced Raman optical activity of molecules on orientationally averaged substrates: Theory of electromagnetic effects. *J. Chem. Phys.* **2006**, *125*, 124704.

(47) Duan, S.; Tian, G.; Ji, Y.; Shao, J.; Dong, Z.; Luo, Y. Theoretical modeling of plasmon-enhanced Raman images of a single molecule with subnanometer resolution. *J. Am. Chem. Soc.* **2015**, *137*, 9515−9518.

(48) Gersten, J.; Nitzan, A. Electromagnetic theory of enhanced Raman scattering by molecules adsorbed on rough surfaces. *J. Chem. Phys.* **1980**, *73*, 3023−3037.

(49) Andrade, X.; Strubbe, D.; De Giovannini, U.; Larsen, A. H.; Oliveira, M. J. T.; Alberdi-Rodriguez, J.; Varas, A.; Theophilou, I.; Helbig, N.; Verstraete, M. J.; et al. Real-space grids and the Octopus code as tools for the development of new simulation approaches for electronic systems. *Phys. Chem. Chem. Phys.* **2015**, *17*, 31371−31396.

(50) Tancogne-Dejean, N.; Oliveira, M. J. T.; Andrade, X.; Appel, H.; Borca, C. H.; Le Breton, G.; Buchholz, F.; Castro, A.; Corni, S.; Correa, A. A.; et al. Octopus, a computational framework for exploring light-driven phenomena and quantum dynamics in extended and finite systems. *J. Chem. Phys.* **2020**, *152*, 124119.

(51) Douglas-Gallardo, O. A.; Berdakin, M.; Frauenheim, T.; Sánchez, C. G. Plasmon-induced hot-carrier generation differences in gold and silver nanoclusters. *Nanoscale* **2019**, *11*, 8604−8615.

(52) Negre, C. F. A.; Perassi, E. M.; Coronado, E. a.; Sánchez, C. G. Quantum dynamical simulations of local field enhancement in metal nanoparticles. *J. Phys.: Condens. Matter* **2013**, *25*, 125304.

(53) Bonafé, F. P.; Aradi, B.; Guan, M.; Douglas-Gallardo, O. A.; Lian, C.; Meng, S.; Frauenheim, T.; Sánchez, C. G. Plasmon-driven sub-picosecond breathing of metal nanoparticles. *Nanoscale* **2017**, *9*, 12391−12397.

(54) Blum, V.; Gehrke, R.; Hanke, F.; Havu, P.; Havu, V.; Ren, X.; Reuter, K.; Scheffler, M. Ab initio molecular simulations with numeric atom-centered orbitals. *Comput. Phys. Commun.* **2009**, *180*, 2175−2196.

(55) Shang, H.; Raimbault, N.; Rinke, P.; Scheffler, M.; Rossi, M.; Carbogno, C. All-electron, real-space perturbation theory for homogeneous electric fields: theory, implementation, and application within DFT. *New J. Phys.* **2018**, *20*, 073040.

(56) Baroni, S.; de Gironcoli, S.; Dal Corso, A.; Giannozzi, P. Phonons and related crystal properties from density-functional perturbation theory. *Rev. Mod. Phys.* **2001**, *73*, 515−562.

(57) El-Khoury, P. Z.; Aprà, E. Spatially resolved mapping of three-dimensional molecular orientations with 2 nm spatial resolution through tip-rnhanced Raman scattering. *J. Phys. Chem. C* **2020**, *124*, 17211−17217.

(58) Wegner, D.; Yamachika, R.; Zhang, X.; Wang, Y.; Crommie, M. F.; Lorente, N. Adsorption site determination of a molecular monolayer via inelastic tunneling. *Nano Lett.* **2013**, *13*, 2346−2350.

(59) Miller, J. S. Tetracyanoethylene (TCNE): the characteristic geometries and vibrational absorptions of its numerous structures. *Angew. Chem., Int. Ed.* **2006**, *45*, 2508−2525.

(60) Manriquez, J. M.; Yee, G. T.; McLean, R. S.; Epstein, A. J.; Miller, J. S. A room-temperature molecular/organic-based magnet. *Science* **1991**, *252*, 1415−1417.

(61) Akkoush, A.; Litman, Y.; Rossi, M. A hybrid-DFT study of intrinsic point defects in MX2 (M = Mo, W; X = S, Se) Monolayers. *Phys. Status Solidi A* **2023**, 2300180.

(62) Kumagai, T.; Ladenthin, J. N.; Litman, Y.; Rossi, M.; Grill, L.; Gawinkowski, S.; Waluk, J.; Persson, M. Quantum tunneling in real space: Tautomerization of single porphycene molecules on the (111) surface of Cu, Ag, and Au. *J. Chem. Phys.* **2018**, *148*, 102330.

(63) Zhao; Jensen, L.; Schatz, G. C. Pyridine Ag20 cluster: A Model system for studying surface-enhanced raman scattering. *J. Am. Chem. Soc.* **2006**, *128*, 2911−2919.

(64) Tsuneda, T.; Iwasa, T.; Taketsugu, T. Roles of silver nanoclusters in surface-enhanced Raman spectroscopy. *J. Chem. Phys.* **2019**, *151*, 094102.

(65) Rossi, M. Progress and challenges in ab initio simulations of quantum nuclei in weakly bonded systems. *J. Chem. Phys.* **2021**, *154*, 170902.

(66) Litman, Y.; Behler, J.; Rossi, M. Temperature dependence of the vibrational spectrum of porphycene: a qualitative failure of classical-nuclei molecular dynamics. *Faraday Discuss.* **2020**, *221*, 526−546.

(67) Brehm, M.; Thomas, M. Computing bulk phase resonance Raman spectra from ab initio molecular dynamics and real-time TDDFT. *J. Chem. Theory Comput.* **2019**, *15*, 3901−3905.

(68) Hourahine, B.; Aradi, B.; Blum, V.; Bonafé, F.; Buccheri, A.; Camacho, C.; Cevallos, C.; Deshaye, M. Y.; Dumitrică, T.; Dominguez, A.; et al. DFTB+, a software package for efficient approximate density functional theory based atomistic simulations. *J. Chem. Phys.* **2020**, *152*, 124101.

(69) Jestädt, R.; Ruggenthaler, M.; Oliveira, M. J. T.; Rubio, A.; Appel, H. Light-matter interactions within the Ehrenfest−Maxwell−Pauli−Kohn−Sham framework: fundamentals, implementation, and nano-optical applications. *Adv. Phys.* **2019**, *68*, 225−333.

(70) Flick, J.; Rivera, N.; Narang, P. Strong light-matter coupling in quantum chemistry and quantum photonics. *Nanophotonics* **2018**, *7*, 1479−1501.

(71) Wang, H.; Levchenko, S. V.; Schultz, T.; Koch, N.; Scheffler, M.; Rossi, M. Modulation of the Work Function by the Atomic Structure of Strong Organic Electron Acceptors on H-Si(111). *Adv. Electron. Mater.* **2019**, *5*, 1800891.

(72) Riede, M.; Mueller, T.; Tress, W.; Schueppel, R.; Leo, K. Small-molecule solar cells—status and perspectives. *Nanotechnology* **2008**, *19*, 424001.

(73) Zhang, F.; Kahn, A. Investigation of the high electron affinity molecular dopant F6-TCNNQ for hole-transport materials. *Adv. Funct. Mater.* **2018**, *28*, 1703780.

Supplemental Information: First-Principles Simulations of Tip Enhanced Raman Scattering Reveal Active Role of Substrate on High-Resolution Images

Yair Litman,[1, 2, 3, a)] Franco P. Bonafe,[2, 3] Alaa Akkoush,[2, 4] Heiko Appel,[2] and Mariana Rossi[2, 4, b)]

[1)] *Yusuf Hamied Department of Chemistry, University of Cambridge, Lensfield Road, Cambridge, CB2 1EW,UK*

[2)] *MPI for the Structure and Dynamics of Matter, Luruper Chaussee 149, 22761 Hamburg, Germany*

[3)] *These authors contributed equally*

[4)] *Fritz Haber Institute of the Max Planck Society, Faradayweg 4–6, 14195 Berlin, Germany*

(Dated: 13 July 2023)

[a)]Electronic mail: yl899@cam.ac.uk

[b)]Electronic mail: mariana.rossi@mpsd.mpg.de

I. THEORY

A. Systems in the Presence of a Near Field

Consider a system perturbed by a transverse electromagnetic field. Under the long-wavelength approximation, the system is described by a Hamiltonian of the form

$$\hat{\boldsymbol{H}} = \hat{\boldsymbol{H}}_0 - \hat{\boldsymbol{\mu}} \cdot \boldsymbol{E}_\perp^n(t), \tag{1}$$

where $\hat{\boldsymbol{H}}_0$ refers to the unperturbed Hamiltonian, $\hat{\boldsymbol{\mu}}$ the system dipole operator, and $\boldsymbol{E}_\perp^n(t) = (\lambda_x \hat{\boldsymbol{n}}_x + \lambda_y \hat{\boldsymbol{n}}_y + \lambda_z \hat{\boldsymbol{n}}_z) \cos(\omega_0 t)$, where $\lambda_{x,y,z}$ are the electromagnetic field strengths and $\hat{\boldsymbol{n}}_{x,y,z}$ are unit vectors in each Cartesian direction. For clarity, in the following we consider the perturbation along a particular Cartesian direction α, since they are separable, but the derivation is easily generalized. Moreover, we consider, for the current derivation, that nuclei are clamped in space.

We shall consider that our system can be divided in two clearly distinguishable parts that we name 'sm' (i.e. substrate plus molecule) and tip which allows us to write the Hamiltonian of the full system as

$$\hat{H}_\alpha = \hat{H}_0^{\text{sm}} - \lambda_\alpha \hat{\mu}_\alpha^{\text{sm}} \cos(\omega_0 t) + \hat{H}_0^{\text{tip}} - \lambda_\alpha \hat{\mu}_\alpha^{\text{tip}} \cos(\omega_0 t) + \hat{H}^{\text{int}}, \tag{2}$$

where the label 'int' refers to 'sm-tip' interaction.

We will assume that the tip is not influenced by the presence of the molecule, which allow us to write a tip Hamiltonian,

$$\hat{H}_\alpha^{\text{tip}} = \hat{H}_0^{\text{tip}} - \lambda_\alpha \hat{\mu}_\alpha^{\text{tip}} \cos(\omega_0 t), \tag{3}$$

and obtain the time-dependent wave function $\left| \Psi_\alpha^{\text{tip}}(\boldsymbol{r}^{\text{tip}}, t) \right\rangle$ without reference to the molecule subsystem. Moreover, the lack of influence of the molecule on the tip implies that the interaction is purely electrostatic (charge transfer or dispersion are not possible). This approximation is reasonable for neutral molecules and for all but very small tip-molecule distances. Under the previous assumptions the interaction Hamiltonian gets transformed in an effective interaction Hamiltonian, $\hat{H}^{\text{int,eff}}$ defined as the following expectation value

$$\langle \Psi_\alpha^{\mathrm{tip}}(\boldsymbol{r}^{\mathrm{tip}}, t; \boldsymbol{R}^{\mathrm{tip}}) | \, \hat{H}^{\mathrm{int}}(\boldsymbol{r}^{\mathrm{tip}}, \boldsymbol{r}^{\mathrm{sm}}, t) \, | \Psi_\alpha^{\mathrm{tip}}(\boldsymbol{r}^{\mathrm{tip}}, t; \boldsymbol{R}^{\mathrm{tip}}) \rangle = \hat{H}_\alpha^{\mathrm{int}}(\boldsymbol{r}^{\mathrm{sm}}, t; \boldsymbol{R}^{\mathrm{tip}})$$

$$= e \int d\boldsymbol{r} \frac{\rho_\alpha^{\mathrm{tip}}(\boldsymbol{r}, t; \boldsymbol{R}^{\mathrm{tip}})}{|\hat{\boldsymbol{r}}^{\mathrm{sm}} - \boldsymbol{r}|} \qquad (4)$$

$$= e \hat{\Phi}_\alpha^{\mathrm{tip}}(\boldsymbol{r}^{\mathrm{sm}}, t; \boldsymbol{R}^{\mathrm{tip}})$$

where $\boldsymbol{r}_{\mathrm{sm}}$ ($\boldsymbol{r}_{\mathrm{tip}}$) refers to the position of electrons that belong to the substrate-molecule (tip) subsystem, $\boldsymbol{R}_{\mathrm{tip}}$ refers to position of nuclei that belong to the tip subsystem, and the ';' symbol has been used to emphasis the parametric dependence. $\hat{\Phi}_\alpha^{\mathrm{tip}}(\boldsymbol{r}, t; \boldsymbol{R}^{\mathrm{tip}})$ is the time-dependent Hartree potential generated by the tip upon interaction with the α component of the far field, and it depends on the position operator and parametrically on the coordinates of the tip. It represents the key quantity of the new approach. For reasons that will become clear later, we shall expand the time-dependent Hartree potential around zero field strength,

$$\hat{\Phi}_\alpha^{\mathrm{tip}}(\boldsymbol{r}, t; \boldsymbol{R}^{\mathrm{tip}}) = \hat{\Phi}_\alpha^{\mathrm{tip}}(\boldsymbol{r}, t; \boldsymbol{R}^{\mathrm{tip}})|_{\lambda_\alpha=0} + \lambda_\alpha \left. \frac{\partial \hat{\Phi}_\alpha^{\mathrm{tip}}(\boldsymbol{r}, t; \boldsymbol{R}^{\mathrm{tip}})}{\partial \lambda_\alpha} \right|_{\lambda_\alpha=0} + O(\lambda^2)$$

$$\approx \hat{\Phi}_{\mathrm{GS}}^{\mathrm{tip}}(\boldsymbol{r}; \boldsymbol{R}^{\mathrm{tip}}) + \lambda_\alpha \left. \frac{\partial \hat{\Phi}_\alpha^{\mathrm{tip}}(\boldsymbol{r}, t; \boldsymbol{R}^{\mathrm{tip}})}{\partial \lambda_\alpha} \right|_{\lambda_\alpha=0} \qquad (5)$$

where we used the fact that in the absence of an external field, the tip is in the electronic ground state (GS). Since we consider a continuous laser and using the fact that linear responses are local in the frequency domain (i.e. the density oscillates predominantly at the frequency of the external field), we can conveniently write

$$\left. \frac{\partial \hat{\Phi}_\alpha^{\mathrm{tip}}(\hat{\boldsymbol{r}}, t; \boldsymbol{R}^{\mathrm{tip}})}{\partial \lambda_\alpha} \right|_{\lambda_\alpha=0} = \Re \left[\left. \frac{\partial \tilde{\Phi}_\alpha^{\mathrm{tip}}(\boldsymbol{r}, \omega_0; \boldsymbol{R}^{\mathrm{tip}})}{\partial \lambda_\alpha} \right|_{\lambda_\alpha=0} \right] \cos(\omega_0 t) \qquad (6)$$

where $\tilde{\Phi}^{\mathrm{tip}}$ denotes the Fourier transform the tip Hartree potential. We note that since we are interested in the simulation of time-independent TERS spectroscopy which represents a steady-state excitation, we have the freedom to arbitrarily define the initial time and therefore keep either the real or imaginary part in Eq. 6. However, for later consistency, we have chosen the former and will use this fact later on.

By introducing Eq. 4, 5 and 6 into Eq. 2 and collecting all the terms that depend on the molecular degrees of freedom and are linear on λ, we arrive at the following expression for

the molecular Hamiltonian

$$\hat{H}_\alpha^{\text{sm}} = \hat{H}_0^{\text{sm}} + \hat{H}_\alpha^{\text{int}}(\hat{\boldsymbol{r}}^{\text{sm}}, t; \boldsymbol{R}^{\text{tip}}) - \lambda_\alpha \mu_\alpha^{\text{sm}} \cos(\omega_0 t)$$

$$= \hat{H}_0^{\text{sm}} + \hat{\Phi}_{\text{GS}}^{\text{tip}}(\boldsymbol{r}; \boldsymbol{R}^{\text{tip}}) + \lambda_\alpha \left\{ -\mu_\alpha^{\text{sm}} + \Re \left[\frac{\partial \tilde{\Phi}_\alpha^{\text{tip}}(\boldsymbol{r}, \omega_0; \boldsymbol{R}^{\text{tip}})}{\partial \lambda_\alpha} \bigg|_{\lambda_\alpha = 0} \right] \right\} \cos(\omega_0 t) \tag{7}$$

We remark that the previous expression is origin independent and that Eq. 3 presented in the main text represents its *time-independent* version.

B. Time Independent Density Functional Perturbation Theory

In the framework of Kohn–Sham (KS) DFT, the total energy can be expressed as functional of the electron density, ρ, as

$$E^{(0)}[\rho] = T_s[\rho] + E_{\text{ext}}[\rho] + E_{\text{H}}[\rho] + E_{\text{xc}}[\rho] + E_{\text{nn}}[\rho] \tag{8}$$

where T_s, E_{ext}, E_{H}, E_{xc}, and E_{nn} are the kinetic energy of non-interacting electrons, the external energy due to the the electron-nuclei electrostatic attraction, the Hartree energy, the exchange-correlation energy, and the nuclei-nuclei electrostatic interaction energy , respectively.

The ground-state total energy is obtained variationally under the constraint that the number of electrons is constant which leads to the Kohn–Sham single-particle equations

$$\hat{h}_{\text{KS}} \psi_p = \epsilon_p \psi_p, \tag{9}$$

where ψ_p and ϵ_p are the KS single particle states and energies, and

$$\hat{h}_{\text{KS}} = \hat{t}_{\text{s}} + \hat{\nu}_{\text{ext}} + \hat{\nu}_{\text{H}} + \hat{\nu}_{\text{xc}} \tag{10}$$

is the KS single particle Hamiltonian. All the terms on the right hand-side of the previous equation are single-particle operators which represent the kinetic energy, $\hat{t}_{\text{s}}$, the external potential, $\hat{\nu}_{\text{ext}}$, the Hartree potential, $\hat{\nu}_{\text{H}}$ and the exchange-correlation functional, $\hat{\nu}_{\text{xc}}$. The ground-state electronic density is computed by $\rho_{\text{GS}}(\mathbf{r}) = \sum_p f(\epsilon_p)|\psi_p(\mathbf{r})|^2$ where f is the occupation function.

We now consider a perturbation due to an external electromagnetic field, in the framework of *time independent* perturbation theory. The energy functional gets an extra term, $E_E[\rho]$, and the perturbed KS single-particle Hamiltonian can be expressed as

$$\hat{h}_{KS}(\epsilon_\alpha) = \hat{h}_{KS}^{(0)} + \hat{h}_{KS}^{(1)}\lambda_\alpha + \dots \tag{11}$$

where λ_α is the strength of the external field along the direction α, $\hat{h}_{KS}^{(1)}$ is the first order response of the Hamiltonian operator given by

$$\hat{h}_{KS}^{(1)} = +\hat{\nu}_{ext}^{(1)} + \hat{\nu}_{H}^{(1)} + \hat{\nu}_{xc}^{(1)} + \hat{\nu}_E, \tag{12}$$

and $\hat{\nu}_E^{(1)}$ is the (still not specified) coupling operator between the system and the external electromagnetic field. By introducing analogous expansions for the single-particle states $(\psi_p = \psi_p^{(0)} + \psi_p^{(1)}\epsilon_\alpha + \dots)$ and their eigenenergies $(\epsilon_p = \epsilon_p^{(0)} + \epsilon_p^{(1)}\lambda_\alpha + \dots)$, one reaches the well-known Sternheimer equation which reads

$$(\hat{h}_{KS}^{(0)} - \epsilon_0)\psi_p^{(1)} = -(\hat{h}_{KS}^{(1)} - \epsilon_1)\psi_p^{(0)}. \tag{13}$$

The solution of the Sternheimer equation gives direct access to the density response defined as

$$\rho_\alpha^{(1)}(\boldsymbol{r}) = \frac{\partial\rho(\boldsymbol{r})}{\partial\lambda_\alpha} = \sum_p f(\epsilon_p)[\psi_p^{(1)}(\boldsymbol{r})\psi_p^{(0)}(\boldsymbol{r}) + \psi_p^{(0)}(\boldsymbol{r})\psi_p^{(1)}(\boldsymbol{r})], \tag{14}$$

and allows for the calculation of the induced dipole as

$$\mu_\alpha^{ind} = \sum_{\beta=1}^{3} \lambda_\beta \int d\boldsymbol{r}\,\rho_\beta^{(1)}(\boldsymbol{r})r_\alpha = \sum_\beta \lambda_\beta \alpha_{\alpha\beta}, \tag{15}$$

in which we identify the components of the polarizability tensor as

$$\alpha_{\alpha\beta} = \frac{\partial\mu_\alpha^{ind}}{\partial\lambda_\beta} = \int d\boldsymbol{r}\,\rho_\beta^{(1)}(\boldsymbol{r})r_\alpha. \tag{16}$$

It is central to the following developments that we arrived to Eq. 16 without determining the specific nature of the perturbation, $\hat{\nu}_E$, besides the assumption that it is weak enough to allow the omission of electrical non-linear effects. We now consider different suitable forms for $\hat{\nu}_E$.

1. Homogeneous Field Perturbation

In most of the Raman experiments the frequency of the (monochromatic) external electromagnetic field falls in the visible range. In these cases, the field remains approximately constant across the molecular dimensions and it is valid to apply the long-wavelength approximation. Thus, for this homogeneous and time-independent field, E_E is expressed as

$$E_E[\rho] = -\boldsymbol{\lambda} \cdot \int d\boldsymbol{r} \rho(\boldsymbol{r})\boldsymbol{r}, \tag{17}$$

and the corresponding single-particle operator becomes

$$\hat{\nu}_E = -\boldsymbol{r}. \tag{18}$$

2. Linear Field

The next step towards the inclusion of spatial-dependent fields is to consider a field with a non-vanishing gradient. The extra energy term becomes

$$E_E[\rho] = -\sum_{\alpha} \lambda_{\alpha} \left[\int d\boldsymbol{r} \rho(\boldsymbol{r})r_{\alpha} - \sum_{\beta} \frac{1}{2} \int d\boldsymbol{r} \frac{\partial \lambda_{\alpha}}{\partial r_{\beta}} \rho(\boldsymbol{r})r_{\alpha}r_{\beta} \right], \tag{19}$$

and the single-particle operator is given by

$$\hat{h}_{\mathrm{KS}}^{(1)} = \hat{\nu}_{\mathrm{ext}}^{(1)} + \hat{\nu}_{\mathrm{H}}^{(1)} + \hat{\nu}_{\mathrm{xc}}^{(1)} - r_{\alpha} - \sum_{\beta} \frac{1}{2} \frac{\partial \lambda_{\alpha}}{\partial r_{\beta}} r_{\alpha}r_{\beta}. \tag{20}$$

It is clear to see that this approach becomes impractical rather quickly if one wants to consider higher-order derivatives. Moreover, if the field is not strictly linear, the previous expression becomes origin dependent since the value of $\frac{\partial \lambda_{\alpha}}{\partial r_{\beta}}$ is position dependent.

3. Inclusion of Near Fields

We now consider that the Hamiltonian is given by Eq. 7, but in its *time independent* form. The perturbation up to the first order is given by

$$-\mu_{\alpha} + \Re \left[\frac{\partial \tilde{\Phi}_{\alpha}^{\mathrm{tip}}(\boldsymbol{r}, \omega_0; \boldsymbol{R}^{\mathrm{tip}})}{\partial \lambda_{\alpha}} \bigg|_{\lambda_{\alpha}=0} \right] \tag{21}$$

and the energy gain can be expressed as

$$E_E[\rho] = \sum_\alpha \lambda_\alpha \left[-\int d\boldsymbol{r} \rho(\boldsymbol{r}) r_\alpha + \int d\boldsymbol{r} \rho(\boldsymbol{r}) \Re \left[\frac{\partial \tilde{\Phi}_\alpha^{\mathrm{tip}}(\boldsymbol{r}, \omega_0; \boldsymbol{R}^{\mathrm{tip}})}{\partial \lambda_\alpha} \Bigg|_{\lambda_\alpha=0} \right] \right]. \qquad (22)$$

The first order response of the Hamiltonian operator is given by

$$\hat{h}_{\mathrm{KS}}^{(1)} = \hat{\nu}_{\mathrm{ext}}^{(1)} + \hat{\nu}_{\mathrm{H}}^{(1)} + \hat{\nu}_{\mathrm{xc}}^{(1)} - r_\alpha + \Re \left[\frac{\partial \tilde{\Phi}_\alpha^{\mathrm{tip}}(\boldsymbol{r}, \omega_0; \boldsymbol{R}^{\mathrm{tip}})}{\partial \lambda_\alpha} \Bigg|_{\lambda_\alpha=0} \right]. \qquad (23)$$

We note that in this case, the ground-state KS Hamiltonian $\hat{h}_{\mathrm{KS}}^0$ also gets modified by the addition of the $\Phi_{\mathrm{GS}}^{\mathrm{tip}}$ term.

Summary of approximations and assumptions in the derivation of Eq 7

What follows is a point-by-point summary of the approximation and assumptions employed in the previous section:

- Eq. 1: Dipole coupling between the system and the far-field.

- Eq. 2: The interaction between the tip and substrate is dictated by classical electrostatics.

- Eq. 3: the tip is not influenced by the presence of the substrate.

- Eq. 5: the external far field strength is small enough, such that the response of the tip lies in the linear regime.

- Eq. 11: the external far field strength is small enough, such that the response of the substrate is linear with respect of the local field strength.

II. METHODS

A. DFT and DFPT calculations

All the electronic DFT and DFPT calculations were carried out using FHI-aims code[1] with the 'light' default settings for numerical grids and basis sets. The calculations for the benzene molecule were carried out with LDA exchange correlation functional as parameterized by Perdew and Wang[2]. The calculations for the TCNE molecule in the gas phase

and adsorbed on Ag(100) were carried out with the PBEexchange-correlation functional instead, to have a better description of the charge transfer between the metal substrate and the molecule. A pair-wise van der Waals correction specifically tailored for hybrid organic-inorganic systems was used in all the calculation containing the Ag(100) surface[3]. The Ag(100) cluster was modeled by a 3-layer 4×4 cluster where only the first two top layers were allowed to relax and the atoms on the bottom one were kept fixed in their bulk positions. Selected calculations were repeated with a 3-layers 5×6 cluster model, see discussion in section IV. The cluster models were created using the atomic simulation environment (ASE)[4] using a 4.157 Å lattice constant for Ag. The geometries were relaxed within FHI-aims up to a maximum residual force component per atom of 0.005 eV/A. In Fig. S1, the minimum energy structures of the TCNE molecule adsorbed in the cluster models are depicted.

We compared the projected density of stated (PDOS) of the cluster calculations with the ones obtained from periodic calculations using a 3-layer Ag 3×4 slab and a k-grid of $4 \times 4 \times 1$. As shown in Fig. S2, the PDOS of TCNE on the cluster model is in reasonable agreement with the periodic calculations and markedly different from the gas phase PDOS.

The calculation of the Raman intensities were performed by the evaluation of Eq. 4 in the main text by a symmetric finite difference approach. All the atoms in the molecule were displaced by 0.002 Å along all Cartesian directions. All the presented TERS images were computed with 0.5 Å $\times$ 0.5 Å resolution after verifying with the benzene molecule that using a 0.25 Å$\times$ 0.25 Å resolution does not result in significant changes on the image.

B.   TD-DFT calculations

The real-time TDDFT calculations were carried out with the Octopus code[5,6] , employing the adiabatic local density approximation (ALDA) to describe exchange-correlation effects unless stated otherwise. The field perturbation was introduced by a Dirac delta perturbation in time, also known as 'kick', at the initial time with field strength k, $\boldsymbol{E} = -\hbar k/e\delta(t)$, which causes the initial wavefunction to instantaneously acquire a phase factor. We utilized a time step of 0.0065 atomic units of time to integrate the time-dependent Kohn-Sham equations of motion and run the simulations for 30000 steps, saving the Hartree potential every 10 steps in cube file format. We employed field strengths between 5×10^{-4} Å^{-1} and 1.5×10^{-3}
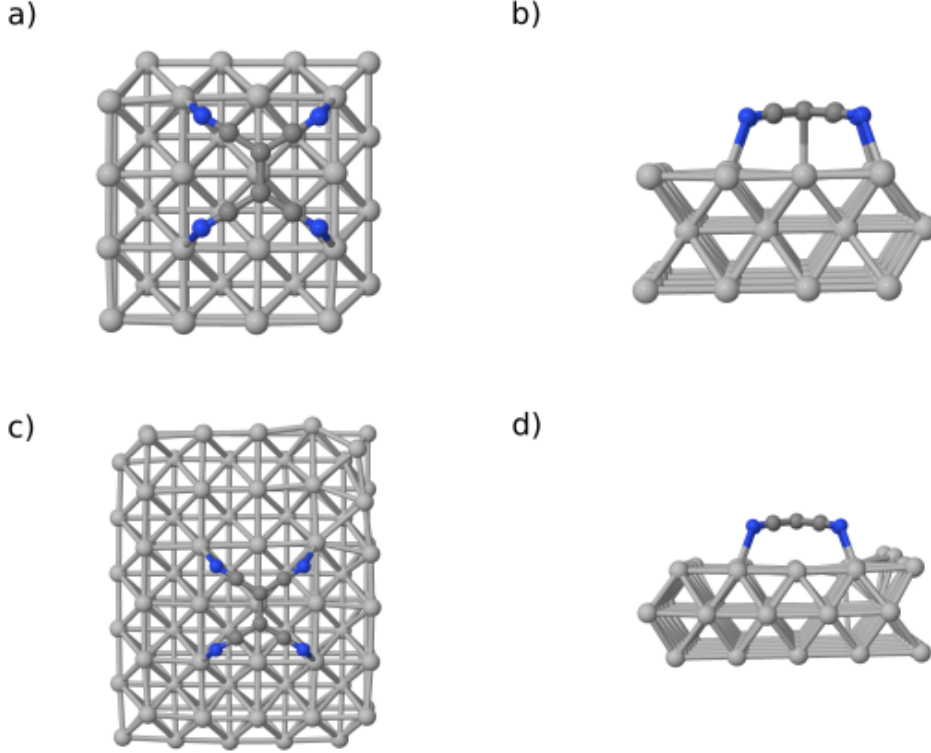
FIG. S1: Top and lateral view of 4 x 4 (top) and 5 x 6 (bottom) cluster models employed to study the adsorption of the TCNE molecule adsorbed at Ag(100).

Å^{-1}, and verified to be within the linear-response regime (see Fig. S4). The derivative of Φ^{tip} with respect to the field strength was obtained as

$$
\begin{aligned}
\frac{\partial \tilde{\Phi}^{\text{tip}}(\boldsymbol{r}, \omega)}{\partial \lambda_\gamma^{\text{far}}} &= \frac{\int dt e^{i\omega t} \phi^{\text{tip}}(\boldsymbol{r}, t)}{\int dt e^{i\omega t} \hbar k / e \delta(t)}, \\
&= \frac{\int dt e^{i\omega t} \phi^{\text{tip}}(\boldsymbol{r}, t)}{\hbar k / e}.
\end{aligned}
\tag{24}
$$

In all the TERS calculations the plasmonic frequency was chosen, i.e. $\omega = 3.22 eV$.

III.   VALIDATION TEST

In Fig. S3, we show $\tilde{\Phi}^{\text{tip}}$ obtained for different tip sizes. The overall shape of $\tilde{\Phi}^{\text{tip}}$ below the tip apex is not significantly modified. However, the plasmonic peak approaches the visible range in agreement with previous studies[7].
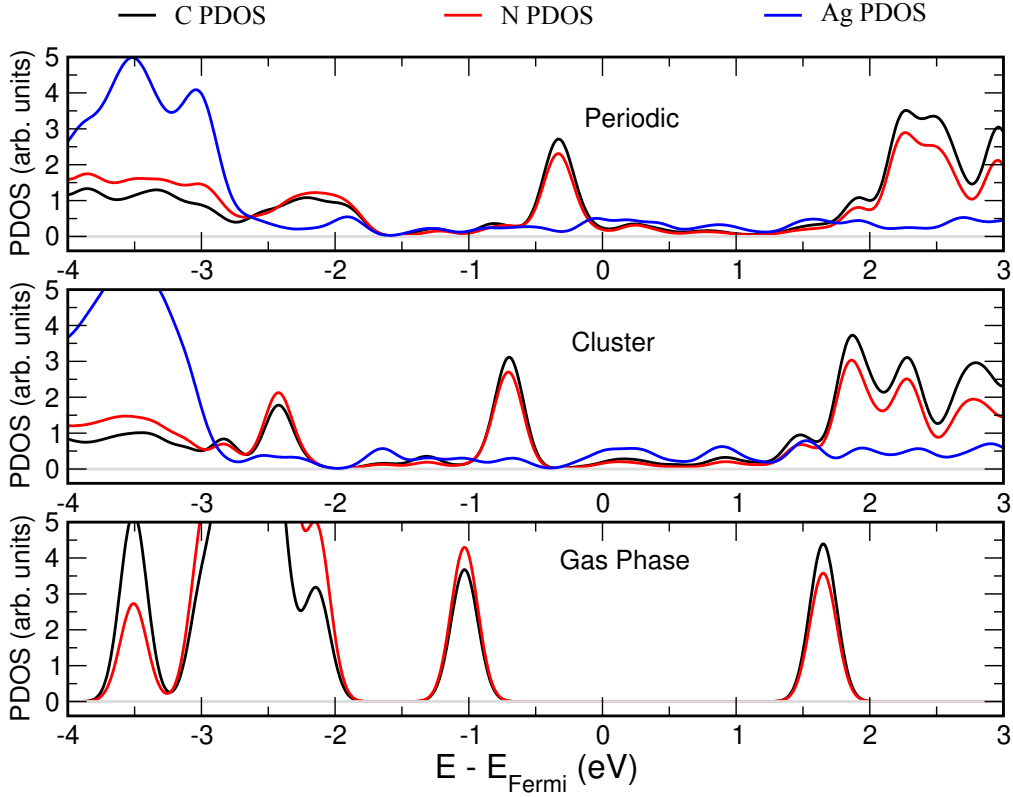
FIG. S2: Projected density of states of TCNE molecule adsorbed at Ag(100) periodic slab (top), TCNE molecule adsorbed at Ag(100) cluster (center), and TCNE molecule in the gas phase (bottom). Carbon, nitrogen and silver atomic PDOS are depicted by black, red and blue curves, respectively. A baseline depicted as a gray line has been added for clarity in all the panels.

In Fig. S4 we show the dependence of $\tilde{\Phi}^{tip}$ with respect to the kick strength. At all the considered positions below the the tip apex, a linear dependence is observed

We studied the dependence of the molecular induced dipole, μ^{ind}, with respect to the kick strength by performing TD-DFT simulations with a kick for a system composed of tipA and a benzene molecule at 4 Å below it. Fig. S5a shows the three different tip-molecule relative positions considered for this test. To isolate the molecular contribution from the much larger tip contribution, we computed μ^{ind} by integrating a region containing only the molecule (see Fig. S5b). We verified that in this region, the electronic density integrates to the number of electrons in the molecule. In Fig. S5, we show the dependence of μ^{ind} with respect to the kick
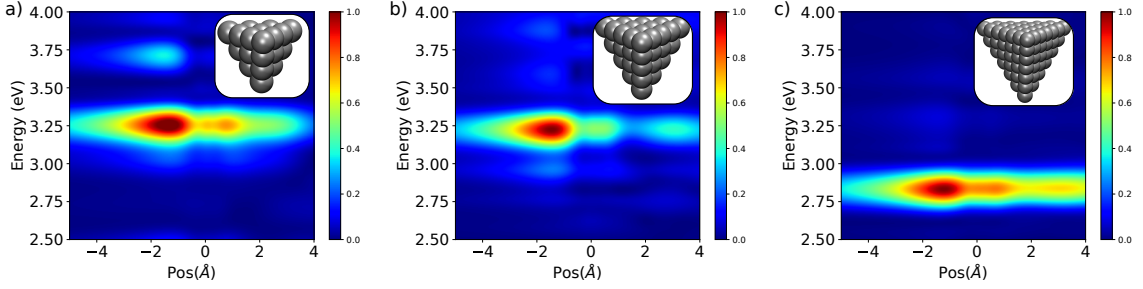
FIG. S3: Comparison $\tilde{\Phi}_{\text{tip}}$ for different tip sizes. a) Tip smaller than tip-A (20 Ag atoms) b) tip-A (35 Ag atoms) c) Tip bigger than tip-A (84 Ag atoms). The tip apex was set at the origin of coordinates as depicted in Figure 2a in the main text.
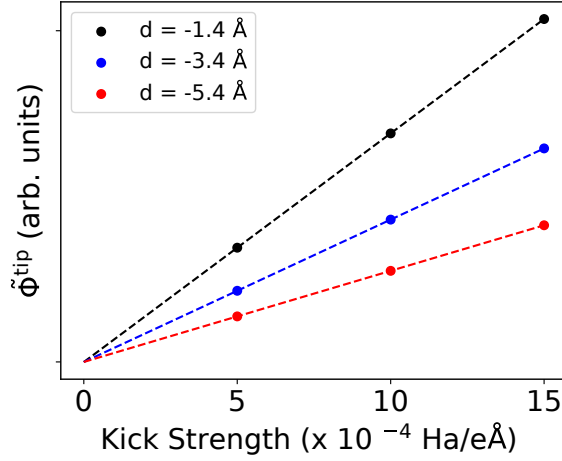
FIG. S4: Linearity of $\tilde{\Phi}^{\text{tip}}$ with respect to the kick strength. Dots corresponds to $\tilde{\Phi}^{\text{tip}}$ values at different distances, d, below the tip apex. Dashed lines are linear fits of the data points.

strength and find a linear dependence. This confirms that we are within the applicability realm of first-order perturbation theory. Moreover, the change of intensity of the induced dipole follows the same trend as the TERS image presented in the main text (see Fig3 g) with a maximum at d=2.5Å.

To analyze the shape of the local electromagnetic field, $\partial\tilde{\Phi}_{\text{tip}}/\partial z$, we fitted it by a Gaussian function defined as

$$f(x,y) = A_0 e^{-\left(\frac{1}{2\sigma_x^2}(x-x_0)^2 + \frac{1}{2\sigma_y^2}(y-y_0)^2\right)} + B_0, \tag{25}$$

S11
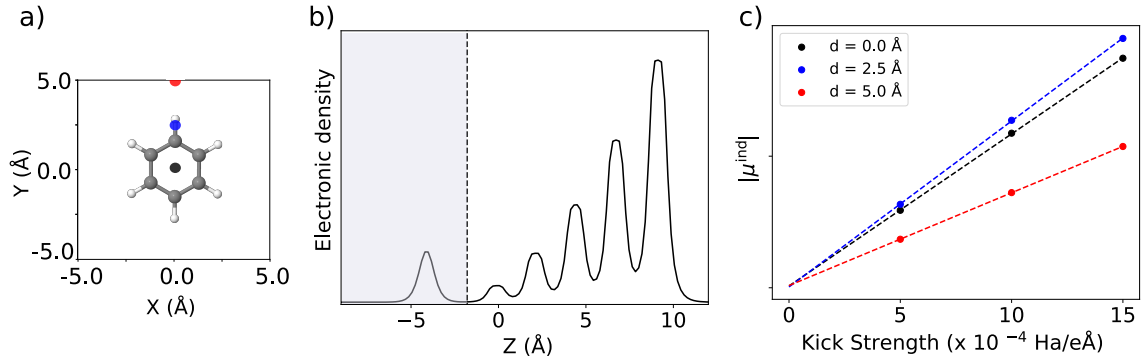
FIG. S5: a) Visual representation of the benzene molecule and the the 3 lateral positions of the tip apex considered for this test. b) Electronic density along the z-direction (main tip axis) integrated along the orthogonal xy plane. Molecular induced dipoles, μ^{ind}, were obtained by integrating the electronic density for $\infty < z < -1.8$ Å (gray area) c) Dependence of $|\mu^{\mathrm{ind}}|$ at 532 nm with respect to the kick strength at different tip-molecule relative positions.

where (x_0, y_0) are the coordinates of maximum, and A_0 and B_0 are a normalization constant and an offset, respectively.

Fig. S6 and S7 show two-dimensional Gaussian fits of $\partial \tilde{\Phi}_{\mathrm{tip}}/\partial z$ for tip-A model structure at 4 Å and 1.5 Å below the tip apex, respectively. On the former case, the Gaussian fit reproduces to some extent the reference TD-DFT data, but the fit presents a more moderate increase at its center and underestimates the maximum intensity by 20%. On the latter case, a Gaussian fit completely misses the rapid variation and sign change of local field observed in the reference data. In Fig. S8 and S9, we show analogous plots for the tip-B model structure. While a Gaussian fit for the data at 1.5 Å is clearly inadequate, at 4.0 Å the fit looks acceptable besides the fact that it cannot capture the radial asymmetry present in the reference data. We remark that in this work only tip-molecule distances greater than 4 Å have been considered.
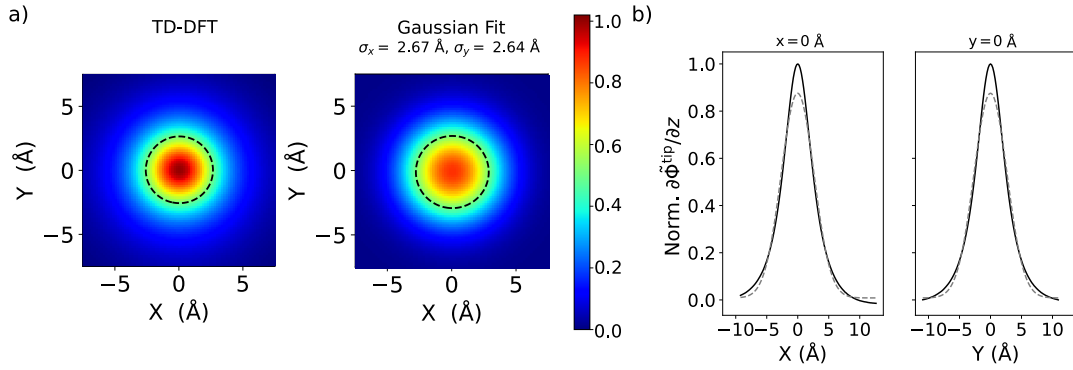
FIG. S6: Gaussian fit of a two-dimensional slice of $\partial\tilde{\Phi}_{\text{tip}}/\partial z$ for tip-A model structure at 4 Å below the tip apex. a) Normalized two-dimensional heat map. Dashed lines represent 0.5 isocontours. b) One dimensional cuts along x=0 Å and y=0 Å. Solid black line and gray dashed line represent the reference and Gaussian fit data, respectively. The tip apex was set at the origin of coordinates as depicted in Figure 2a in the main text.
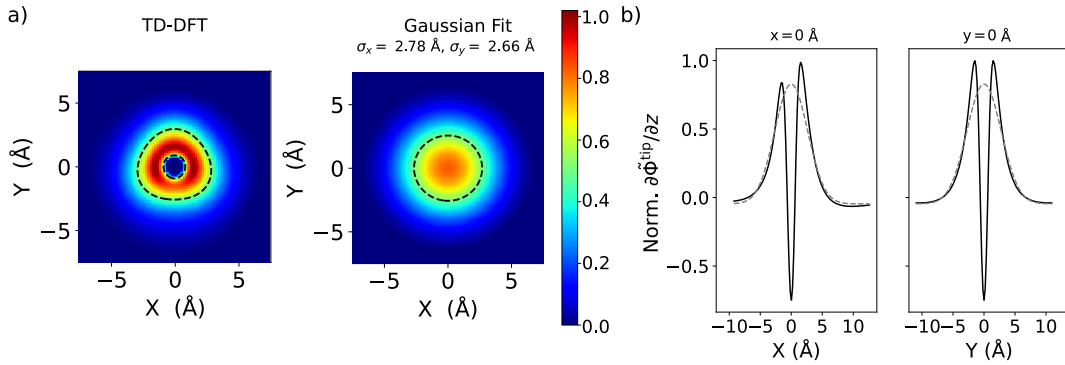

FIG. S7: Same as figure S6 for a slice taken at 1.5 Å below the tip apex.
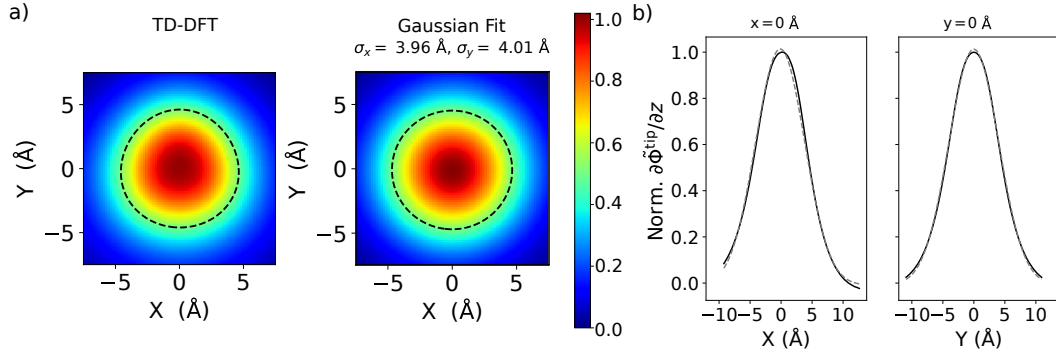
FIG. S8: Same as figure S6 for a tip-B model structure.
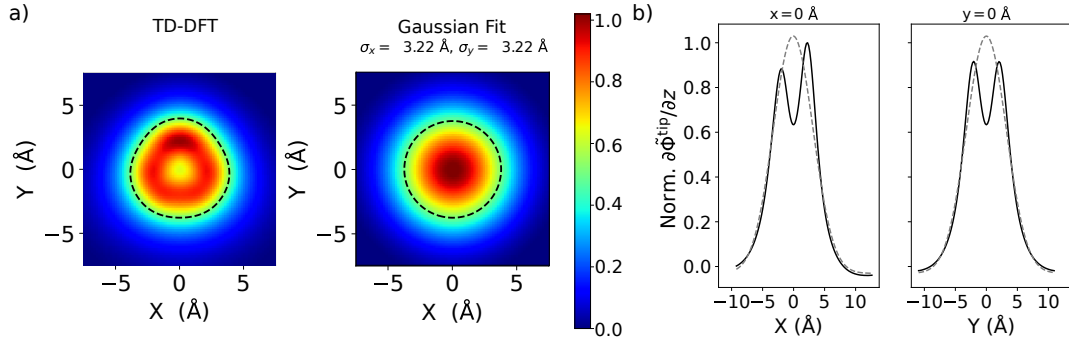
FIG. S9: Same as figure S7 for a tip-B model structure.
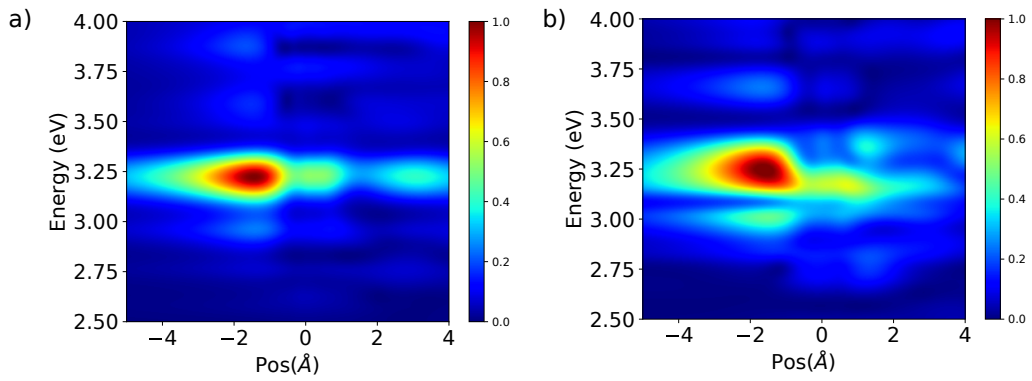
FIG. S10: Comparison of $\tilde{\Phi}_{\text{tip}}$ of Tip-A computed using a) LDA and b) PBE exchange correlation functionals.
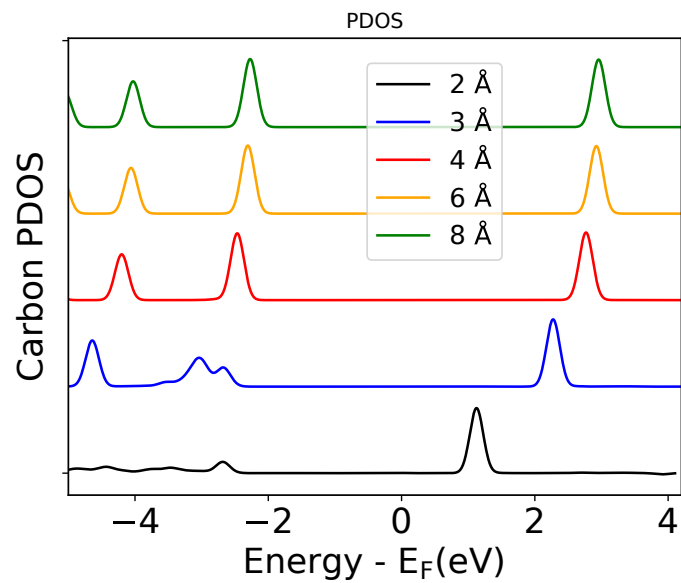
FIG. S11: Projected electronic density of states of benzene molecules as a function of molecule-tip distance.

IV. ADDITIONAL TERS IMAGES

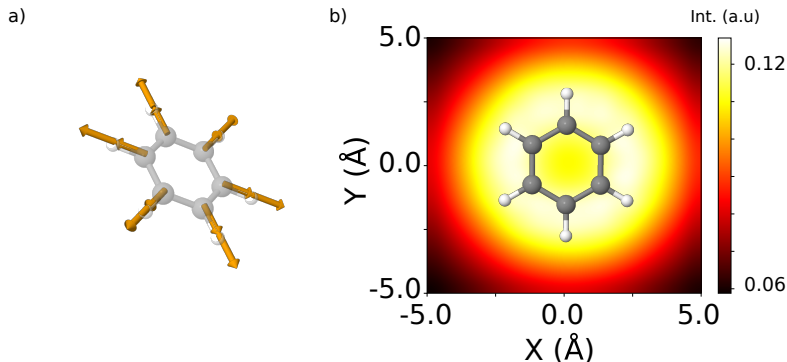In Fig. S12 and S14, we show further TERS images for the benzene and TCNE molecules, respectively.

FIG. S12: TERS simulation of gas-phase benzene from local-field DFPT calculations. Normal mode displacements (a) and TERS images (b) of the the 1015 cm^{-1} (a_{1g}) mode for a molecule-tip apex distance of 4 Å.

To further verify the convergence of the TERS calculations with respect to the cluster size, we performed TERS simulations at some representative tip-molecule relative positions. In Fig. S13, we show the position dependence of the TERS signal along the molecular axis for six vibrational normal modes. In all cases, the results obtain with the small cluster are in semi-quantitative agreement with the ones obtained with the larger cluster.

V. COMPUTATIONAL SAVING OF THE PROPOSED METHOD

The reduced computational cost of the DFPT calculation with respect to the full real-time TDDFT simulations can be easily verified by comparing the two methods. However, as two different implementations are used for both methods, a completely fair, code-independent comparison is not possible at the moment. Instead, we state the cost of a typical calculation of each type with both codes, operating at optimal conditions of parallelization in CPUs. The timing for the TDDFT run (using the Octopus code) with a Dirac-delta perturbation to calculate the polarisability of a system comprising a silver tip A plus a benzene molecule (47 atoms) is of 324 core-hours (Intel Xeon IceLake-SP processors), in the Raven supercomputer
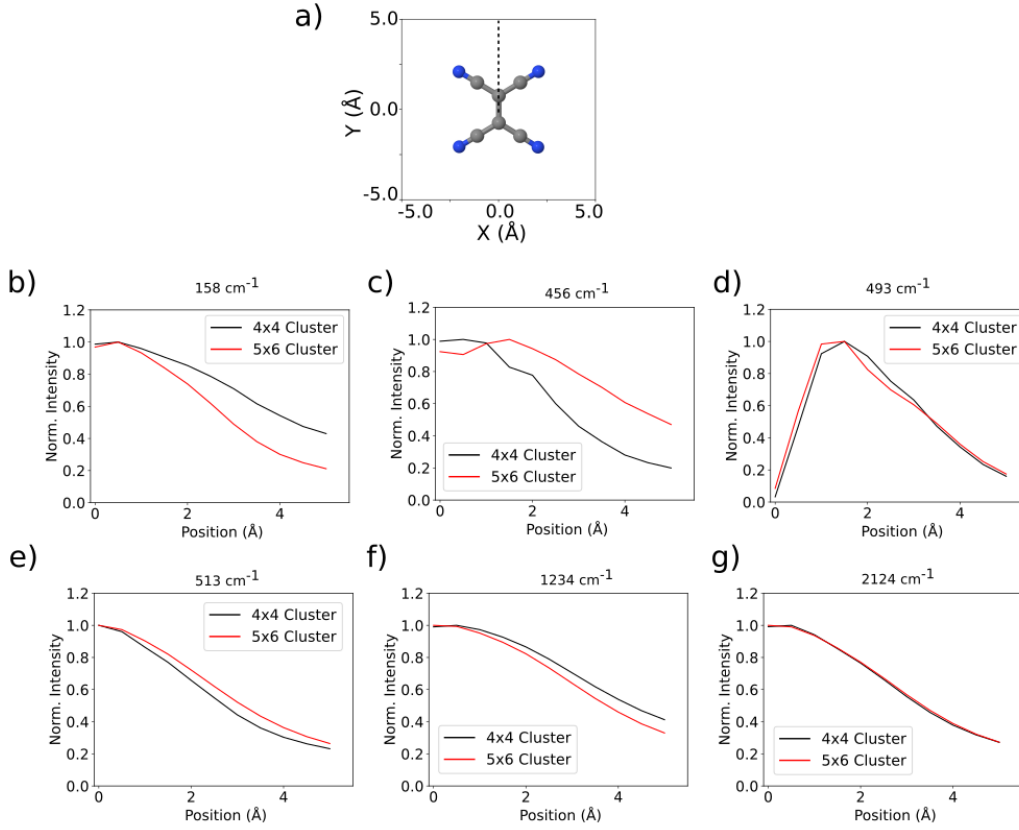
FIG. S13: a) Schematic depictions of the axis along which the TERS calculations were performed. b)-g) Normalized TERS intensity for selected vibrational modes.

installed at the Max-Planck Computing and Data Facility (https://docs.mpcdf.mpg.de). The computational cost of the DFPT calculations (using the FHI-aims code) on the equivalent system and machine is 0.02 core hours. While it is true that the DFPT calculation needs as input the Hartree potential obtained from the TDDFT run, the same potential can be used for any tip position, while each tip position demands a separate TDDFT calculation. The comparison of the cost demonstrates an approximately 15000-fold increase in computational efficiency, which will become larger for tip models containing more metal atoms. Furthermore, while the DFPT calculations have a $N \log(N)$ scaling with respect to the number of atoms (N) up to systems with an $\approx$ size of around 1000, the TDDFT implementation scales as N^3.
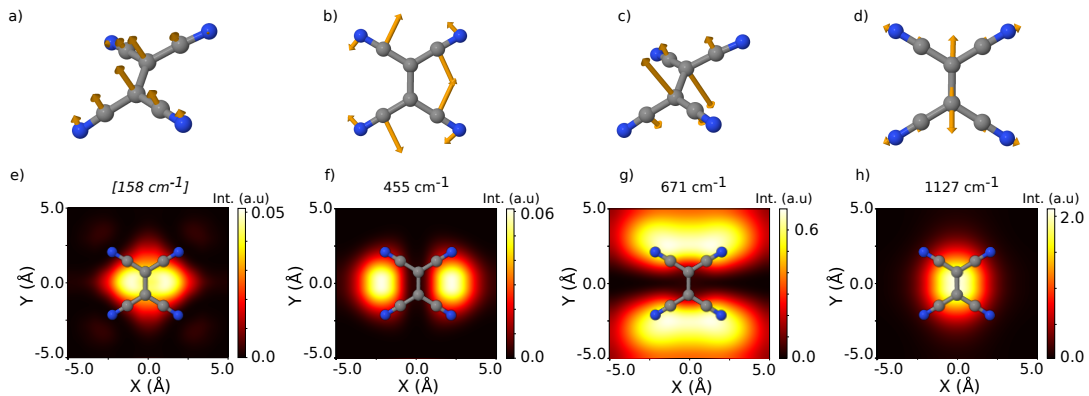
FIG. S14: Simulated TERS images of TCNE in isolation, but at the adsorbed geometry with the addition of 1 electron to the molecule without further geometry relaxation (TCNEads-1e). a), b), c) and d) Normal mode displacements of selected vibrational modes of TCNE@Ag(100). The surface has been deleted for clarity. e), f), g) and h) TERS images of the depicted normal modes for TCNEads. In all cases a molecule-apex distance of 4 Å was employed. Frequency within square brackets in panel e) denotes the lack of an equivalent normal mode eigenvector in the TCNEads1e calculation.

REFERENCES

[1]V. Blum, R. Gehrke, F. Hanke, P. Havu, V. Havu, X. Ren, K. Reuter, and M. Scheffler, Comp. Phys. Comm. **180**, 2175 (2009).

[2]J. P. Perdew and Y. Wang, Phys. Rev. B **45**, 13244 (1992).

[3]V. G. Ruiz, W. Liu, E. Zojer, M. Scheffler, and A. Tkatchenko, Phys. Rev. Lett. **108**, 146103 (2012).

[4]A. H. Larsen, J. J. Mortensen, J. Blomqvist, I. E. Castelli, R. Christensen, M. Dułak, J. Friis, M. N. Groves, B. Hammer, C. Hargus, E. D. Hermes, P. C. Jennings, P. B. Jensen, J. Kermode, J. R. Kitchin, E. L. Kolsbjerg, J. Kubal, K. Kaasbjerg, S. Lysgaard, J. B. Maronsson, T. Maxson, T. Olsen, L. Pastewka, A. Peterson, C. Rostgaard, J. Schiøtz, O. Schütt, M. Strange, K. S. Thygesen, T. Vegge, L. Vilhelmsen, M. Walter, Z. Zeng, and K. W. Jacobsen, J. Phys.: Condens. Matter **29**, 273002 (2017).

[5]X. Andrade, D. Strubbe, U. De Giovannini, A. H. Larsen, M. J. T. Oliveira, J. Alberdi-Rodriguez, A. Varas, I. Theophilou, N. Helbig, M. J. Verstraete, L. Stella, F. Nogueira, A. Aspuru-Guzik, A. Castro, M. A. L. Marques, and A. Rubio, Phys. Chem. Chem. Phys. **17**, 31371 (2015).

[6]N. Tancogne-Dejean, M. J. T. Oliveira, X. Andrade, H. Appel, C. H. Borca, G. Le Breton, F. Buchholz, A. Castro, S. Corni, A. A. Correa, U. De Giovannini, A. Delgado, F. G. Eich, J. Flick, G. Gil, A. Gomez, N. Helbig, H. Hübener, R. Jestädt, J. Jornet-Somoza, A. H. Larsen, I. V. Lebedeva, M. Lüders, M. A. L. Marques, S. T. Ohlmann, S. Pipolo, M. Rampp, C. A. Rozzi, D. A. Strubbe, S. A. Sato, C. Schäfer, I. Theophilou, A. Welden, and A. Rubio, J. Chem. Phys. **152**, 124119 (2020).

[7]O. A. Douglas-Gallardo, M. Berdakin, T. Frauenheim, and C. G. Sánchez, Nanoscale **11**, 8604 (2019).

3.5 Paper II: Charge Transfer-Mediated Dramatic Enhancement of Raman Scattering upon Molecular Point Contact Formation

The pursuit of significant enhancement in Raman scattering using plasmonic nanostructures has garnered considerable interest, particularly in the context of surface- and tip-enhanced Raman scattering/spectroscopy (SERS and TERS). Recently, a breakthrough in low-temperature TERS experiments have accomplished sub-molecular spatial resolution that facilitates the direct observation of individual vibrational modes in their real spatial context [21–23, 112]. In this work, a low-temperature TERS experimental was realized, which measures the evolution of Raman scattering of a single C60-molecule in a tip-substrate junction as the tip-substrate distance is varied. Two distinct transport regimes are observed: the tunneling regime and the molecular point contact (MPC) regime.

A drastic enhancement of the Raman intensity was observed in the case of MPC for different substrates (coinage and transition metal surfaces), and with the help of DFT calculations, this enhancement was attributed to charge-transfer excitation. The DFT calculations provided valuable insights into the Raman enhancement mechanisms observed in current-carrying molecular junctions. This work provides insights that highlight the complex nature of the Raman enhancement mechanisms and gives a deeper understanding of the interactions between the tip, molecule, and surface in TERS experiments.

Charge Transfer-Mediated Dramatic Enhancement of Raman Scattering upon Molecular Point Contact Formation

Borja Cirera, Yair Litman, Chenfang Lin, Alaa Akkoush, Adnan Hammud, Martin Wolf, Mariana Rossi, and Takashi Kumagai*

Read Online

ACCESS | Metrics & More | Article Recommendations | Supporting Information

ABSTRACT: Charge-transfer enhancement of Raman scattering plays a crucial role in current-carrying molecular junctions. However, the microscopic mechanism of light scattering in such nonequilibrium systems is still imperfectly understood. Here, using low-temperature tip-enhanced Raman spectroscopy (TERS), we investigate how Raman scattering evolves as a function of the gap distance in the single C_{60}-molecule junction consisting of an Ag tip and various metal surfaces. Precise gap-distance control allows the examination of two distinct transport regimes, namely tunneling regime and molecular point contact (MPC). Simultaneous measurement of TERS and the electric current in scanning tunneling microscopy shows that the MPC formation results in dramatic Raman enhancement that enables one to observe the vibrations undetectable in the tunneling regime. This enhancement is found to commonly occur not only for coinage but also transition metal substrates. We suggest that the characteristic enhancement upon the MPC formation is rationalized by charge-transfer excitation.

KEYWORDS: Tip-enhanced Raman spectroscopy, Single-molecule spectroscopy, Current-carrying molecular Junction, Plasmonic nanocavity
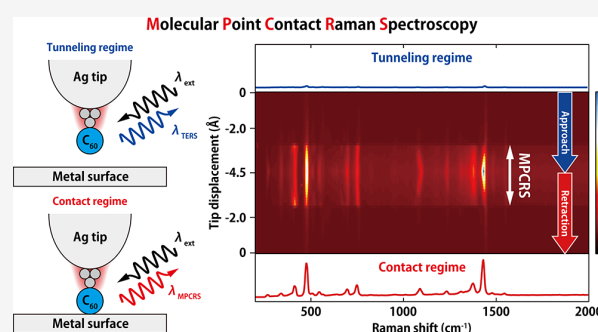
Giant enhancement of Raman scattering using plasmonic nanostructures has attracted increasing interest because of its potential for ultrasensitive chemical analysis, known as surface- and tip-enhanced Raman scattering/spectroscopy (SERS and TERS).[1] In particular, single-molecule SERS/TERS is a powerful tool to study molecular systems in nanoscale environments. Remarkably, advanced low-temperature TERS experiments recently demonstrated Raman imaging with the submolecular spatial resolution reaching ∼1.5 Å, enabling to visualize individual vibration modes in real space.[2,3] The exceptional sensitivity of TERS can be obtained when a plasmonic tip is brought in close proximity to the adsorbed molecule anchored on a flat metal surface (below a few Å gap distance). In such extreme junctions, atomic-scale structures (corrugation) on metal nanostructures play a crucial role to generate atomically confined electromagnetic fields through excitation of localized surface plasmon resonance (LSPR).[4−6] Also, quantum mechanical effects, for example, electron tunneling across the junction, have a significant impact on the gap plasmon,[7] which will be related to the enhancement mechanisms in TERS. In addition to the electromagnetic enhancement effect through the LSPR excitation, chemical interactions between molecule and metal cluster(s) can also largely contribute to the Raman scattering

enhancement.[8] This chemical enhancement effect was found to be particularly important when the molecule is fused between two metal nanoclusters[9] which may be manifested as a dramatic change of SERS/TERS spectra in plasmonic nanojunction fused with molecules.[10,11] In addition, a correlation between electric current (conductance) and Raman spectra of molecular junctions was also reported in SERS of mechanical break junction[12,13] and "fishing-mode" TERS[14] experiments, which is accounted for by molecular orientation in the junction. However, the exact mechanism is still imperfectly understood. More recently, we found that atomic-point contact formation in plasmonic scanning tunneling microscope (STM) junctions results in dramatic Raman enhancement, and the exceptional sensitivity is demonstrated for an ultrathin oxide film on the Ag(111) surface[15] and even for a Si(111)-7 × 7 surface.[16] Here, we show that the dramatic Raman enhancement is operative also
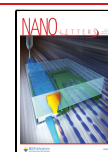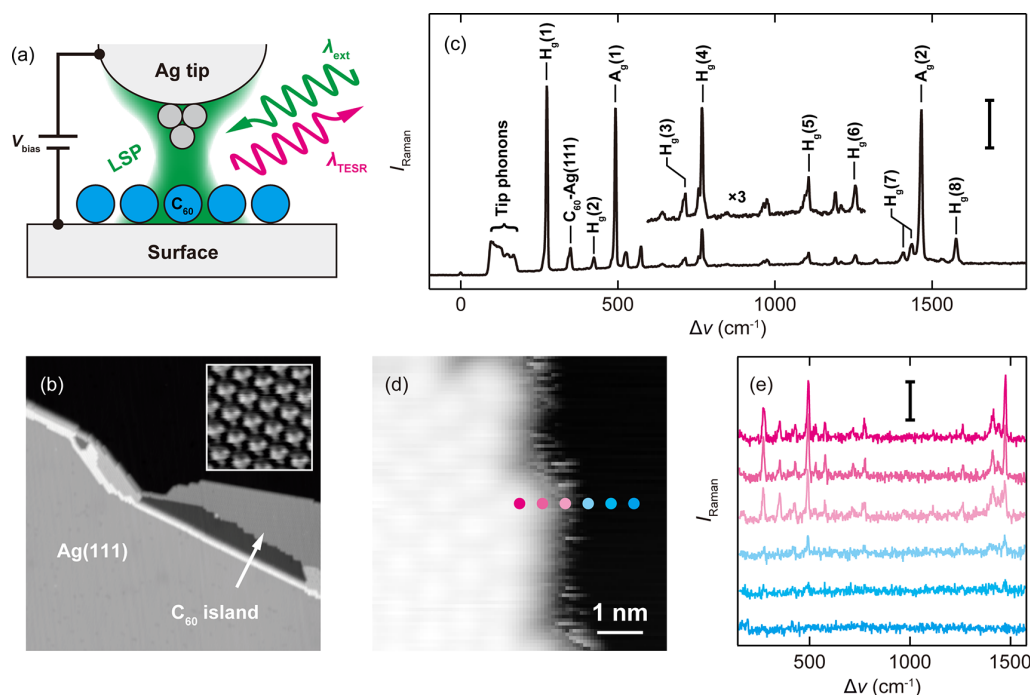
Figure 1. (a) Scheme of the TERS experiment. (b) STM image of C_{60} molecules on Ag(111) under illumination at λ_{ext} = 532 nm at 10 K (V_{bias} = 0.6 V, j_{STM} = 100 pA; inset: V_{bias} = 0.1 V, j_{STM} = 2.6 nA). (c) TERS spectra obtained over a C_{60} molecule in the island at λ_{ext} = 532 nm (Ag tip, λ_{ext} = 532 nm, P_{inc} = 0.33 mWμm^{-2}, 10 K, scale bar = 500 cps). (d) STM image of the edge of a C_{60} island where the Raman spectra of (e) are acquired (V_{bias} = 10 mV, j_{STM} = 10 pA). (e) TERS spectra acquired across the edge of the island. The location is indicated in (d) (V_{bias} = 10 mV, j_{STM} = 10 pA, λ_{ext} = 633 nm, P_{inc} = 0.5 × 10^5 W cm^{-2}, 10 K, scale bar = 500 cps). All acquisition parameters are listed in Table S1.

for molecular point contact (MPC) using single C_{60} junctions and propose that the underlying mechanism is rationalized by charge transfer enhancement.

We first show TERS of C_{60} molecules adsorbed on the Ag(111) surface. Figure 1a depicts schematically the TERS experiment in the STM junction consisting of an Ag tip, an ordered monolayer of C_{60} molecules, and the Ag(111) surface kept at ~10 K (see Supporting Information for details). The junction is illuminated by a narrowband continuous-wave laser at a wavelength (λ_{ext}) of 532 or 633 nm, which generates a tightly confined field at atomic-scale protrusions existing on the tip apex.[17] Figure 1b shows the STM image of C_{60} islands on the Ag(111) surface recorded under illumination (λ_{ext} = 532 nm) with an incident power density (P_{inc}) of 0.33 mW cm^{-2} at the junction. The STM appearance represents the lowest unoccupied molecular orbital (LUMO) when a hexagon of C_{60} is facing toward the surface,[18] which is in agreement with previous simulations.[19] The stationary tripod shape also indicates the absence of rotation of the C_{60} molecules. Although no far-field Raman signal is detected, the intense Raman peaks from the C_{60} molecules can be observed when the Ag tip is brought into the tunneling regime (Figure 1c). The Raman intensity (I_{Raman}) linearly depends on the P_{inc} (see Figure S1 in Supporting Information), indicating a spontaneous Raman process. The I_{Raman} is affected by the tip conditions, whereas the peak positions are not significantly shifted (see Figure S2 in Supporting Information). We estimated the spatial resolution to be <1 nm by recording TERS at the edge of a C_{60} island (Figure 1d,e).

The TERS peaks of C_{60} are assigned according to previous Raman studies of a solid-state sample at 20 K and the isolated

C_{60} molecule[20,21] as well as the DFT simulations conducted for the experimental configuration (see Figure S3 in Supporting Information). The calculated frequencies of the Raman active C_{60} vibrations on Ag(111) and in the gas phase are listed in Table S2 (Supporting Information). An isolated C_{60} molecule has in total 174 vibrational degrees of freedom and the icosahedral symmetry yields 10 distinct Raman-active modes ($2A_g + 8H_g$). The TERS spectrum involves all of the Raman active modes, and the relative intensities between the A_g and H_g modes are also similar to those observed in a solid state for λ_{ext} = 514 nm,[22] whereas most of the modes are red-shifted compared to those in a solid state. Red-shifts of C_{60} vibrations were also observed in SERS on a rough Ag substrate.[23] The observed red-shifts on the Ag(111) surface are confirmed by the DFT simulations (see Table S2 in Supporting Information), which can be attributed to softening of the C_{60} modes due to the electronic density rearrangement through orbital hybridization between C_{60} and Ag(111). As can be seen in Figures S4 and S5 (Supporting Information), the unoccupied molecular states strongly hybridize with the surface, and the LUMO is partially filled. This may be the origin of the vibrational red-shifts because electron transfer to an antibonding orbital delocalized over the entire molecule causes expansion of the molecule and hence softening of the intramolecular bonds.

The TERS peaks in Figure 1c have a shoulder (the $H_g(7)$ mode appears to be split). This could arise from lifting of vibrational degeneracies for the H_g modes due to contact with the surface (see Table S3 in Supporting Information). However, because the A_g modes are not degenerate, the shoulder might involve interference between the electronic and
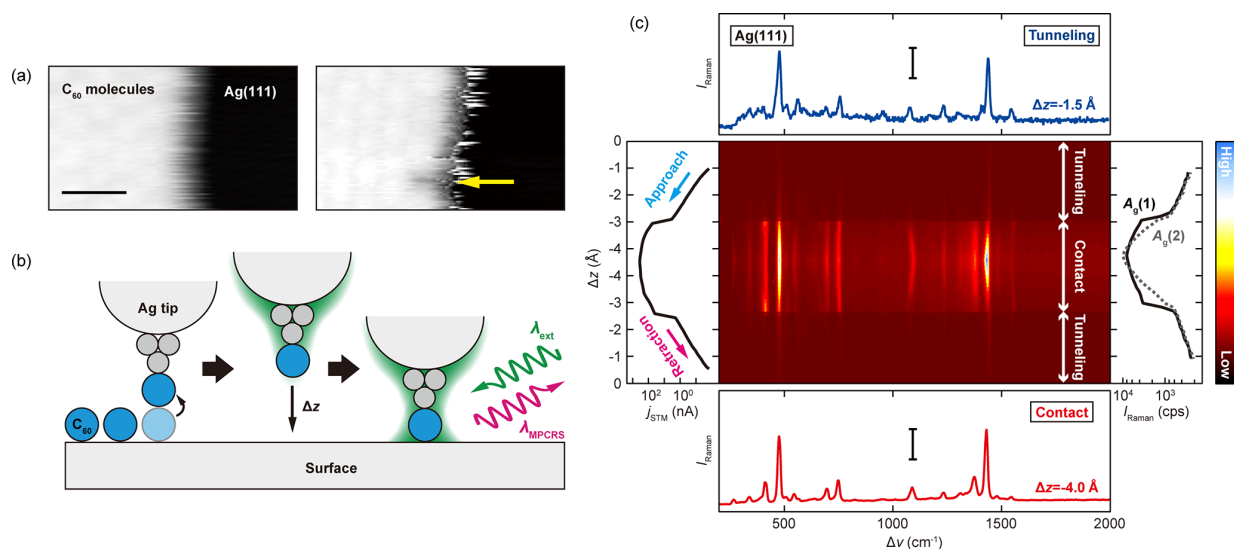
Figure 2. (a) STM images before and after picking a single C_{60} molecule from the island (V_{bias} = 0.5 V, j_{STM} = 50 pA, 10 K, scale bar = 2 nm). (b) Schematic of the Δz-dependent TERS measurement in a single C_{60} molecule junction. (c) Δz-dependent TERS spectra measured on the Ag(111) surface recording one cycle of C_{60}-tip approach and retraction (λ_{ext} = 532 nm, P_{inc} = 0.33 mWμm^{-2}, 10 K). The left panel shows the simultaneously obtained $j_{STM}-\Delta z$ curve. Although the V_{bias} is nominally set to zero, the j_{STM} occurs due to a photovoltage (estimated to be $\sim$1 mV). The right panel shows the intensity of the A_g modes as a function of the Δz. The color scale correspods to 600−12000 cps. The top and bottom panels show the TERS spectra in the tunneling and MPC regime, respectively. The scale bar corresponds to 200 (top) and 5000 cps (bottom).
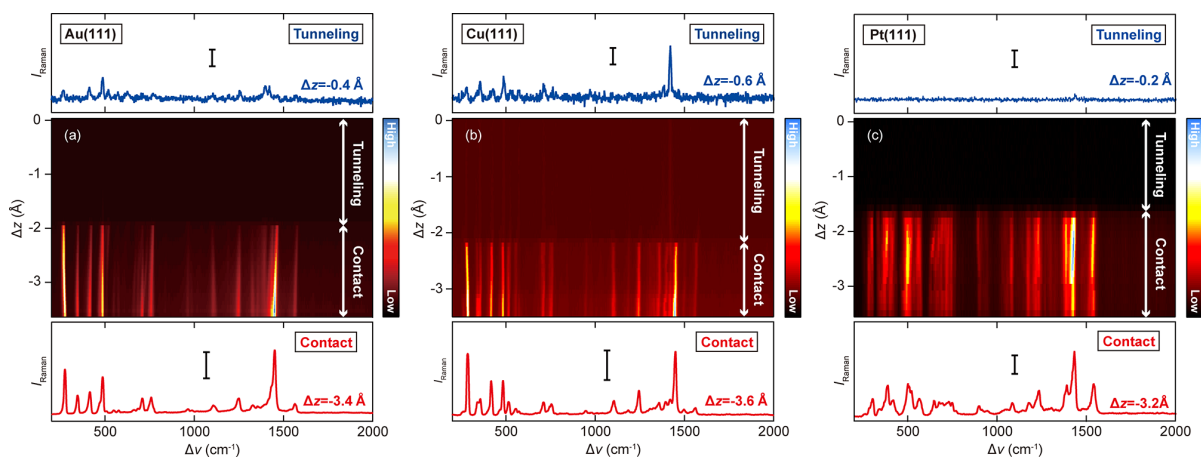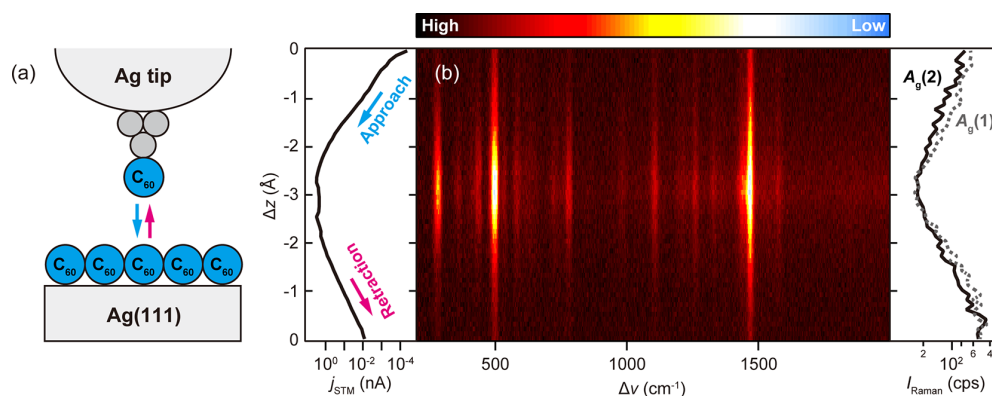

Figure 3. (a−c) Δz-dependent TERS spectra measured on the Au(111), Cu(111), and Pt(111) surfaces, respectively (Au(111): λ_{ext} = 532 nm, P_{inc} = 0.33 mWμm^{-2}, V_{bias} = 0 V, 10 K, Cu(111): λ_{ext} = 633 nm, P_{inc} = 0.45 mWμm^{-2}, V_{bias} = 0 V, 10 K, Pt(111): λ_{ext} = 633 nm, P_{inc} = 0.45 mWμm^{-2}, V_{bias} = 0 V, 10 K). The color scale corresponds to (a) 600−200 000 cps, (b) 0−16 000 cps, (c) 1500−5000 cps. The top and bottom panels show the TERS spectra in the tunneling and MPC regime, respectively. The scale bar corresponds to 100 (top) and (a) 10 000, (b) 5000, (c) 1000 cps (bottom).

vibrational Raman scattering pathways, yielding a Fano-like line shape.[24] Furthermore, the TERS spectrum shows more vibrational modes in addition to the 10 Raman-active modes of free C_{60}. The peak at 347 cm^{-1} was observed in the previous SERS experiment,[23] which can be assigned to the C_{60}-surface "bouncing" mode based on the DFT simulations. The other peaks that are Raman nonactive in the isolated C_{60} molecule appear due to symmetry-lowering caused by the adsorption onto the surface.

Next, we examine the gap-distance dependence of single-C_{60} TERS including reversible formation and breaking of MPC. As depicted in Figure 2, a single C_{60} molecule on Ag(111) is transferred to the Ag tip apex (hereafter denoted as C_{60}-tip),

and then it is moved toward the bare Ag(111) surface until the molecule contacts the surface and subsequently it is retracted. The middle panel of Figure 2c displays a waterfall plot of the TERS spectra recorded as a function of relative displacement of the tip−surface distance (Δz) when the C_{60}-tip approaches the surface. The vertical and horizontal axis corresponds to Δz and Raman shift ($\Delta \nu$), respectively, and the color scale represents I_{Raman}. A remarkable observation is the abrupt increase of the TERS intensity when the C_{60}-tip contacts the surface. The MPC formation is evident in the STM current (j_{STM}) simultaneously recorded with the TERS spectra. The j_{STM} shows a well-known jump-to-contact behavior that occurs when the junction is fused by a point contact.[25] The symmetric

Figure 4. (a) Schematic of the Δz-dependent TERS measurement in a C_{60}–C_{60} junction. (b) Δz-dependent TERS spectra obtained for one approach and retraction cycle of a monolayer C_{60} film on Ag(111) (λ_{ext} = 532 nm, P_{inc} = 0.33 mWμm^{-2}, V_{bias} = 0 V, 10 K), together with the simultaneously obtained j_{STM}–Δz curve (left) and the intensity of the A_g modes (right). The color scale corresponds to 750−1100 cps.

behavior of the TERS spectra and the j_{STM}–Δz curve with respect to the turning point indicates that the process is reversible. The TERS intensity is not dependent on the amount of the direct current flowing in the junction (see Figure S6 in Supporting Information).

In Figure 2c, some of the vibration modes exhibit a continuous peak shift as a function of Δz, which is more pronounced after MPC formation. The DFT calculations predict that a mechanical deformation of C_{60} results in blue-shifts for all vibrational modes (see Table S4 in Supporting Information), whereas the electronic charge rearrangement caused by the MPC formation results in red-shifts as discussed above. In experiment, we observe that some vibrational peaks are red-shifted as the Δz decreases (e.g. $H_g(7)$, $H_g(8)$, and $A_g(2)$, see Figure S7 in Supporting Information), while some peaks are blue-shifted (e.g., $H_g(5)$) when the MPC is further squeezed, implicating complex contributions from the mechanical deformation and the charge density rearrangement.

In order to demonstrate that the MPC-induced Raman enhancement is not a peculiar phenomenon of the Ag tip–C_{60}–Ag(111) junction, we performed the same experiment on the Au(111), Cu(111), and Pt(111) surfaces (Figure 3a−c, respectively). On Au(111), the TERS intensity in the tunneling regime becomes smaller than that on Ag(111) due to the reduced field enhancement compared to Ag. The Cu(111) surface interacts with C_{60} more strongly than Ag(111) and Au(111), while the plasmonic enhancement is expected to be similar to Au in the visible range. In addition, as an example of transition metals, we used the Pt(111) surface that is not generally used in TERS due to its weaker plasmonic resonance in the visible regime compared to coinage metals.[26] Indeed, the TERS intensity on Pt(111) is very weak in the tunneling regime (Figure 3c). However, for all these surfaces the intense Raman signals appear abruptly upon MPC formation. We evaluated the enhancement factor ρ_{MPC} for the $A_g(2)$ peak on each substrate, which is defined as the ratio between the intensity at 1 Å above and below the MPC: $\rho_{MPC,Ag(111)}$ = 15.4 ± 0.4, $\rho_{MPC,Au(111)}$ = 275 ± 15, $\rho_{MPC,Cu(111)}$ = 29.3 ± 2.6, $\rho_{MPC,Pt(111)}$ = 78.8 ± 6.4. The exact enhancement factors are affected by the LSPR properties of the junction, the excitation wavelength, and possibly the adsorption geometry of C_{60} on the tip. However, these results indicate that the exceptional sensitivity of MPC-TERS can be commonly obtained for different metal substrates.

In order to further examine the impact of the contact surface on the TERS enhancement at the MPC, we measured a double-C_{60} junction on Ag(111) (Figure 4a). As can be seen in Figure 4b, both j_{STM}–Δz curve and TERS intensity do not exhibit an abrupt change. The j_{STM}–Δz curve is in agreement with previous experiments on Cu(111).[27] The absence of a jump-to-contact behavior in the contact regime is explained by a gradual transition of the interaction between two C_{60} molecules from the attractive (van der Waals) to repulsive (Pauli) range.[28] This result shows that chemical interactions at the MPC play a critical role in the enhancement mechanism.

The enhancement in SERS/TERS can be generally classified into electromagnetic (EM) and chemical effects. The former is determined by the plasmonic properties of metallic nanostructures. Theoretically, the chemical effects can be further classified into (1) chemical interactions (orbital hybridization) in a molecule−metal system at the electronic ground state, which changes the static polarizability, (2) charge transfer resonance including excited states of a hybrid molecule−metal system (CT), or (3) resonant transition within molecular orbitals (resonance Raman, RR).[8] The continuous increase of the TERS intensity in the tunneling regime will be dominated by the EM enhancement.

The MPC-induced enhancement will be explained by chemical effects rather than EM enhancement because an abrupt increase of the gap plasmon is unlikely.[5,6,29] We first considered a change in the static polarizability whose square is proportional to the Raman intensity. To this end, we simulated the static polarizability tensor using a generalized-gradient density functional approximation (see Section 9 in Supporting Information). Although the computed value of the zz component of the polarizability tensor depends on the tip−C_{60} geometry (see Table S5 in Supporting Information) and the magnitude of the lateral lattice vectors of the simulation cell (see Table S6 and Figure S8 in Supporting Information), its change before and after MPC formation does not rationalize the observed enhancement factors. Therefore, we believe that the abrupt Raman enhancement at the MPC is explained by an additional charge-transfer contribution. This mechanism is associated with the local electronic structure of the system. Scanning tunneling spectroscopy (STS) shows that a significant change of the local electronic structure occurs upon the MPC formation. As can be seen in Figure 5a, the STS intensity exhibits a peak around zero-bias at the MPC, which is
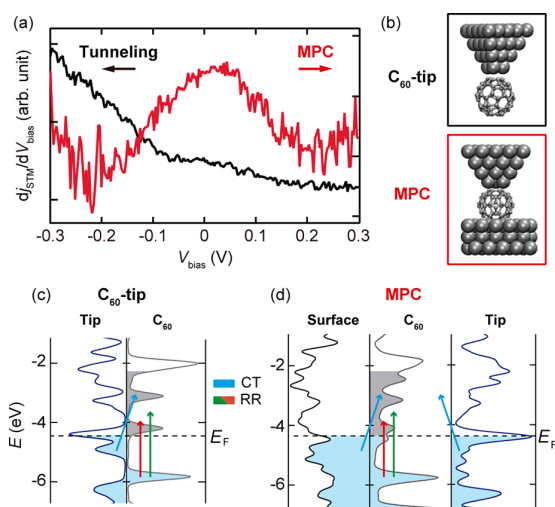
Figure 5. (a) Scanning tunneling spectra obtained for a C_{60}-tip in the tunneling and MPC (black: set-point of V_{bias} = −300 mV, j_{STM} = 5 nA, V_{mod} = 5 mV at 883 Hz, red: set-point of V_{bias} = −300 mV, j_{STM} = 27 μA, V_{mod} = 5 mV at 883 Hz). (b) Models of C_{60}-tip and MPC used in the DFT calculations. (c,d) Calculated projected density of states for C_{60}-tip and MPC. The arrows show possible resonance paths in the system (blue arrow: CT, red/green arrows: molecular resonance). The gray areas represent the molecular unoccupied states that can be reached with λ_{ext} = 532 nm.

absent in the tunneling regime and indicates the increase of the density of states (DOS) around the Fermi level. A significant change in the local DOS may be consistent with the DFT simulations (Figure 5b−d, see also Section 5 in Supporting Information). Figure 5c,d displays the calculated projected DOS for the C_{60}-tip and the MPC. The C_{60} states at the MPC are further broadened than those for the C_{60}-tip configuration. In the tunneling regime (Figure 5c), relatively narrow molecular states may lead to a strong wavelength dependence for the RR process. Similarly, resonant CT into the excited states may not be efficient because the transition is limited within the reach with the visible excitation. These processes will be largely affected upon the MPC formation (Figure 5d). The broadened molecular states may lead to additional RR and CT channels and the latter involves transition from the continuum states of both tip and surface to the molecular states (and *vice versa*).[30,31] The MPC-induced enhancement occurs for a different excitation wavelength (see Figure S9 in Supporting Information), which may be consistent with widely spread resonant channels. The charge-transfer mechanism is also consistent with the result of the double-C_{60} junction because the change of the DOS is less pronounced due to the weak interaction between two molecules, which results in a reduced orbital hybridization in the junction and thus hampers the additional charge-transfer enhancement. The charge-transfer enhancement at the MPC will be generally operative for other metallic substrates as orbital hybridization and a concomitant change of the DOS upon MPC formation is commonly expected.[32,33] Additionally, the chemical enhancement mechanism induced by charge transfer could be further modified if the applied V_{bias} results in the redistribution of the electron density within the molecule in the junction.[34,35]

The selection rule with an extremely confined field is another important subject in TERS. However, significant mixing of the normal modes, caused by adsorption of C_{60} on

the surface (and/or tip), hampers to clarify the symmetry of the vibration modes (see Table S3 in Supporting Information). Additionally, the detailed information on the field distribution in the junction is also not available. A strong local field-gradient might break the conventional selection rule that is based on the dipole approximation.[36] In the present case, however, the quadrupole or magnetic dipole active modes are not clearly observed. The contribution of the local field gradient may not be significant for relatively large molecules physically adsorbed on flat surfaces.[37] In order to discuss the accurate selection rule, it is desirable to perform extended atomistic first-principles calculations which can provide a consistent treatment of atomistic structures, orbital hybridization and charge density responses (polarizability) as well as propagation of the EM fields in a unified manner, like the Maxwell−time-dependent DFT scheme.[38]

In summary, we investigated TERS of current-carrying molecular junctions including a single C_{60}, and how Raman scattering evolves as a function of the gap distance. The transition from the tunneling to MPC regime was continuously monitored by moving C_{60}-tip toward various single-crystal metal surfaces. By recording simultaneously TERS and the electric current in STM, we showed that the abrupt Raman enhancement occurs when the MPC is formed. This enhancement is commonly observed for different substrates exhibiting distinct plasmonic properties and the interaction with C_{60}, namely Ag(111), Au(111), Cu(111), and Pt(111). We deduced that the MPC-induced Raman enhancement is rationalized by the chemical effects. Among the three distinct chemical enhancement effects, the DFT calculations predicted that the electronic charge rearrangement at the ground state (i.e., change of the static Raman polarizability) cannot account for the observed enhancement factors. Therefore, we proposed that the characteristic enhancement at the MPC originates from additional charge-transfer and resonance Raman channels in the hybrid tip−C_{60}−surface system caused by renormalization and broadening of the local electronic states. This mechanism was further corroborated by examining the double-C_{60} junction where the charge transfer enhancement is significantly reduced due to the weak chemical interaction between the molecules. The exceptional sensitivity of MPC-TERS may extend the possibility of TERS to investigate catalytic and electrode reactions on transition metal surfaces. Our approach will also pave the way for studying light−matter coupling in nonequilibrium quantum transport systems[39] where Raman scattering can address fundamental physics in molecular optoelectronics[40] and optomechanics.[41]

■ ASSOCIATED CONTENT

ⓢ Supporting Information

The Supporting Information is available free of charge at https://pubs.acs.org/doi/10.1021/acs.nanolett.1c02626.

Materials and methods, incident laser power dependence of the TERS intensity in the tunneling regime, tip condition dependence of TERS for a C_{60} molecule on Ag(111), models used in the DFT calculations, projected electronic density of states, detailed analysis of the Raman active modes of C_{60} on Ag(111) and C_{60}-tip, Δz-dependent TERS of a C_{60}-tip on Ag(111) at small V_{bias}, enlarged Δz-dependent TERS of a C_{60}-tip on Ag(111) highlighting the shifting of the vibrational

modes, simulations of the static Raman polarizability of C_{60}, wavelength dependence of MPC-TERS (PDF)

■ AUTHOR INFORMATION

Corresponding Author

Takashi Kumagai − *Department of Physical Chemistry, Fritz-Haber Institute of the Max-Planck Society, 14195 Berlin, Germany; Center for Mesoscopic Sciences, Institute for Molecular Science, Okazaki 444-8585, Japan;* ● orcid.org/0000-0001-7029-062X; Email: kuma@ims.ac.jp

Authors

Borja Cirera − *Department of Physical Chemistry, Fritz-Haber Institute of the Max-Planck Society, 14195 Berlin, Germany*

Yair Litman − *MPI for Structure and Dynamics of Matter, 22761 Hamburg, Germany*

Chenfang Lin − *Department of Physical Chemistry, Fritz-Haber Institute of the Max-Planck Society, 14195 Berlin, Germany*

Alaa Akkoush − *MPI for Structure and Dynamics of Matter, 22761 Hamburg, Germany*

Adnan Hammud − *Department of Inorganic Chemistry, Fritz-Haber Institute of the Max-Planck Society, 14195 Berlin, Germany*

Martin Wolf − *Department of Physical Chemistry, Fritz-Haber Institute of the Max-Planck Society, 14195 Berlin, Germany*

Mariana Rossi − *MPI for Structure and Dynamics of Matter, 22761 Hamburg, Germany;* ● orcid.org/0000-0002-3552-0677

Complete contact information is available at:
https://pubs.acs.org/10.1021/acs.nanolett.1c02626

■ REFERENCES

(1) Zrimsek, A. B.; Chiang, N.; Mattei, M.; Zaleski, S.; McAnally, M. O.; Chapman, C. T.; Henry, A.-I.; Schatz, G. C.; Van Duyne, R. P. Single-Molecule Chemistry with Surface- and Tip-Enhanced Raman Spectroscopy. *Chem. Rev.* **2017**, *117* (11), 7583−7613.

(2) Lee, J.; Crampton, K. T.; Tallarida, N.; Apkarian, V. A. Visualizing vibrational normal modes of a single molecule with atomically confined light. *Nature* **2019**, *568*, 78−82.

(3) Zhang, Y.; Yang, B.; Ghafoor, A.; Zhang, Y.; Zhang, Y.-F.; Wang, R.-P.; Yang, J.-L.; Luo, Y.; Dong, Z.-C.; Hou, J. G. Visually Constructing the Chemical Structure of a Single Molecule by Scanning Raman Picoscopy. *Natl. Sci. Rev.* **2019**, *6* (6), 1169−1175.

(4) Benz, F.; Schmidt, M. K.; Dreismann, A.; Chikkaraddy, R.; Zhang, Y.; Demetriadou, A.; Carnegie, C.; Ohadi, H.; de Nijs, B.; Esteban, R.; Aizpurua, J.; Baumberg, J. J. Single-molecule optomechanics in "picocavities. *Science* **2016**, *354*, 726−729.

(5) Zhang, P.; Feist, J.; Rubio, A.; García-González, P.; García-Vidal, F. J. *Ab initio* nanoplasmonics: The impact of atomic structure. *Phys. Rev. B* **2014**, *90* (16), 161407.

(6) Urbieta, M.; Barbry, M.; Zhang, Y.; Koval, P.; Sánchez-Portal, D.; Zabala, N.; Aizpurua, J. Atomic-Scale Lightning Rod Effect in Plasmonic Picocavities: A Classical View to a Quantum Effect. *ACS Nano* **2018**, *12* (1), 585−595.

(7) Zhu, W.; Esteban, R.; Borisov, Ag. G.; Baumberg, J. J.; Nordlander, P.; Lezec, H. J.; Aizpurua, J.; Crozier, K. B. Quantum mechanical effects in plasmonic structures with subnanometre gaps. *Nat. Commun.* **2016**, *7*, 11495.

(8) Jensen, L.; Aikens, C. M.; Schatz, G. C. Electronic structure methods for studying surface-enhanced Raman scattering. *Chem. Soc. Rev.* **2008**, *37*, 1061−1073.

(9) Zhao, L. L.; Jensen, L.; Schatz, G. C. Surface-Enhanced Raman Scattering of Pyrazine at the Junction between Two Ag_{20} Nanoclusters. *Nano Lett.* **2006**, *6* (6), 1229−1234.

(10) Banik, M.; Apkarian, V. A.; Park, T.-H.; Galperin, M. Raman Staircase in Charge Transfer SERS at the Junction of Fusing Nanospheres. *J. Phys. Chem. Lett.* **2013**, *4* (1), 88−92.

(11) El-Khoury, P. Z.; Hu, D.; Apkarian, V. A.; Hess, W. P. Raman Scattering at Plasmonic Junctions Shorted by Conductive Molecular Bridges. *Nano Lett.* **2013**, *13* (4), 1858.

(12) Ward, D. R.; Halas, N. J.; Ciszek, J. W.; Tour, J. M.; Wu, Y.; Nordlander, P.; Natelson, D. Simultaneous Measurements of Electronic Conduction and Raman Response in Molecular Junctions. *Nano Lett.* **2008**, *8* (3), 919−924.

(13) Konishi, T.; Kiguchi, M.; Takase, M.; Nagasawa, F.; Nabika, H.; Ikeda, K.; Uosaki, K.; Ueno, K.; Misawa, H.; Murakoshi, K. Single Molecule Dynamics at a Mechanically Controllable Break Junction in Solution at Room Temperature. *J. Am. Chem. Soc.* **2013**, *135* (3), 1009−1014.

(14) Liu, Z.; Ding, S.-Y.; Chen, Z.-B.; Wang, X.; Tian, J.-H.; Anema, J. R.; Zhou, X.-S.; Wu, D.-Y.; Mao, B.-W.; Xu, X.; Ren, B.; Tian, Z.-Q. Revealing the molecular structure of single-molecule junctions in different conductance states by fishing-mode tip-enhanced Raman spectroscopy. *Nat. Commun.* **2011**, *2*, 305.

(15) Liu, S.; Cirera, B.; Sun, Y.; Hamada, I.; Müller, M.; Hammud, A.; Wolf, M.; Kumagai, T. Dramatic Enhancement of Tip-Enhanced Raman Scattering Mediated by Atomic Point Contact Formation. *Nano Lett.* **2020**, *20* (8), 5879−5884.

(16) Liu, S.; Hammud, A.; Wolf, M.; Kumagai, T. Atomic Point Contact Raman Spectroscopy of a Si(111)-7 × 7 Surface. *Nano Lett.* **2021**, *21* (9), 4057−4061.

(17) Trautmann, S.; Aizpurua, J.; Götz, I.; Undisz, A.; Dellith, J.; Schneidewind, H.; Rettenmayr, M.; Deckert, V. A classical description of subnanometer resolution by atomic features in metallic structures. *Nanoscale* **2017**, *9*, 391−401.

(18) Franke, K. J.; Pascual, J. I. Effects of electron−vibration coupling in transport through single molecules. *J. Phys.: Condens. Matter* **2012**, *24*, 394002.

(19) Li, H. I.; Pussi, K.; Hanna, K. J.; Wang, L.-L.; Johnson, D. D.; Cheng, H.-P.; Shin, H.; Curtarolo, S.; Moritz, W.; Smerdon, J. A.; McGrath, R.; Diehl, R. D. Surface Geometry of C_{60} on Ag(111). *Phys. Rev. Lett.* **2009**, *103* (5), 056101.

(20) Dong, Z.-H.; Zhou, P.; Holden, J. M.; Eklund, P. C.; Dresselhaus, M. S.; Dresselhaus, G. Observation of higher-order Raman modes in C_{60} films. *Phys. Rev. B* **1993**, *48* (4), 2862−2865.

(21) Jishi, R. A.; Mirie, R. M.; Dresselhaus, M. S. Force-constant model for the vibrational modes in C_{60}. *Phys. Rev. B* **1992**, *45* (23), 13685−13689.

(22) van Loosdrecht, P. H. M.; van Bentum, P. J. M.; Verheijen, M. A.; Meijer, G. Raman scattering in single crystal C_{60}. *Chem. Phys. Lett.* **1992**, *198* (6), 587−595.

(23) Rosenberg, A.; DiLella, D. P. Anomalously enhanced Raman scattering from C_{60} on Ag surfaces. *Chem. Phys. Lett.* **1994**, *223* (1−2), 76−81.

(24) Dey, S.; Banik, M.; Hulkko, E.; Rodriguez, K.; Apkarian, V. A.; Galperin, M.; Nitzan, A. Observation and analysis of Fano-like

lineshapes in the Raman spectra of molecules adsorbed at metal interfaces. *Phys. Rev. B* **2016**, *93* (3), 035411.

(25) Kröger, J.; Néel, N.; Limot, L. Contact to single atoms and molecules with the tip of a scanning tunnelling microscope. *J. Phys.: Condens. Matter* **2008**, *20*, 223001.

(26) Liu, H. W.; Nishitani, R.; Han, T. Z.; Ie, Y.; Aso, Y.; Iwasaki, H. STM fluorescence of porphyrin enhanced by a strong plasmonic field and its nanoscale confinement in an STM cavity. *Phys. Rev. B* **2009**, *79* (12), 125415.

(27) Schull, G.; Frederiksen, T.; Brandbyge, M.; Berndt, R. Passing Current through Touching Molecules. *Phys. Rev. Lett.* **2009**, *103* (20), 206803.

(28) Brand, J.; Néel, N.; Kröger, J. Probing relaxations of atomic-scale junctions in the Pauli repulsion range. *New J. Phys.* **2019**, *21*, 103041.

(29) Savage, K. J.; Hawkeye, M. M.; Esteban, R.; Borisov, A. G.; Aizpurua, J.; Baumberg, J. J. Revealing the quantum regime in tunnelling plasmonics. *Nature* **2012**, *491*, 574−577.

(30) Persson, B. N. J. On the theory of surface-enhanced Raman scattering. *Chem. Phys. Lett.* **1981**, *82* (3), 561.

(31) Oren, M.; Galperin, M.; Nitzan, A. Raman scattering from molecular conduction junctions: Charge transfer mechanism. *Phys. Rev. B* **2012**, *85* (11), 115435.

(32) Wang, L.-L.; Cheng, H.-P. Density functional study of the adsorption of a C_{60} monolayer on Ag(111) and Au(111) surfaces. *Phys. Rev. B* **2004**, *69* (16), 165417.

(33) Larsson, J. A.; Elliott, S. D.; Greer, J. C.; Repp, J.; Meyer, G.; Allenspach, A. Orientation of individual C_{60} molecules adsorbed on Cu(111): Low-temperature scanning tunneling microscopy and density functional calculations. *Phys. Rev. B* **2008**, *77* (11), 115434.

(34) Gieseking, R. L. M.; Lee, J.; Tallarida, N.; Apkarian, V. A.; Schatz, G. C. Bias-Dependent Chemical Enhancement and Non-classical Stark Effect in Tip-Enhanced Raman Spectromicroscopy of CO-Terminated Ag Tips. *J. Phys. Chem. Lett.* **2018**, *9* (11), 3074−3080.

(35) Braun, K.; Hauler, O.; Zhang, D.; Wang, X.; Chassé, T.; Meixner, A. J. Probing Bias-Induced Electron Density Shifts in Metal−Molecule Interfaces via Tip-Enhanced Raman Scattering. *J. Am. Chem. Soc.* **2021**, *143* (4), 1816−1821.

(36) Liu, P.; Chulhai, D. V.; Jensen, L. Single-Molecule Imaging Using Atomistic Near-Field Tip-Enhanced Raman Spectroscopy. *ACS Nano* **2017**, *11* (5), 5094−5102.

(37) Perry, S. S.; Hatch, S. R.; Campion, A. On the role of electromagnetic field gradients in surface Raman scattering by molecules adsorbed on single crystal metal surfaces. *J. Chem. Phys.* **1996**, *104*, 6856−6859.

(38) Yamada, S.; Noda, M.; Nobusada, K.; Yabana, K. Time-dependent density functional theory for interaction of ultrashort light pulse with thin materials. *Phys. Rev. B* **2018**, *98* (24), 245147.

(39) Galperin, M.; Ratner, M. A.; Nitzan, A. Raman scattering in current-carrying molecular junctions. *J. Chem. Phys.* **2009**, *130*, 144109.

(40) Galperin, M.; Nitzan, A. Molecular optoelectronics: the interaction of molecular conduction junctions with light. *Phys. Chem. Chem. Phys.* **2012**, *14*, 9421−9438.

(41) Roelli, P.; Galland, C.; Piro, N.; Kippenberg, T. J. Molecular cavity optomechanics as a theory of plasmon-enhanced Raman scattering. *Nat. Nanotechnol.* **2016**, *11*, 164−169.

■ NOTE ADDED AFTER ASAP PUBLICATION

This paper was published ASAP on February 21, 2022, with an error in Figure 4 due to a production error. The corrected version was reposted on February 21, 2022.

▢ Recommended by ACS

Revealing the Interaction of Charge Carrier–Phonon Coupling by Quantification of Electronic Properties at the SrTiO₃/TiO₂ Heterointerface

Ting-Xiao Qin, Zhong-Qun Tian, *et al.*

MARCH 22, 2022
NANO LETTERS   READ ▢

Femtosecond Thermal and Nonthermal Hot Electron Tunneling Inside a Photoexcited Tunnel Junction

Natalia Martín Sabanés, Melanie Müller, *et al.*

AUGUST 26, 2022
ACS NANO   READ ▢

Traversing Double-Well Potential Energy Surfaces: Photoinduced Concurrent Intralayer and Interlayer Structural Transitions in XTe₂ (X = Mo, W)

Yingpeng Qi, Ralph Ernstorfer, *et al.*

JULY 06, 2022
ACS NANO   READ ▢

Terahertz Nanoimaging of Perovskite Solar Cell Materials

Richard H. J. Kim, Jigang Wang, *et al.*

OCTOBER 17, 2022
ACS PHOTONICS   READ ▢

Get More Suggestions >

Supporting Information:

Charge Transfer Mediated Dramatic Enhancement of Raman Scattering upon Molecular Point Contact Formation

Borja Cirera[1], Yair Litman[2], Chenfang Lin[1], Alaa Akkoush[2], Adnan Hammud[3], Martin Wolf[1], Mariana Rossi[2], Takashi Kumagai[1,4]*

[1]*Department of Physical Chemistry, Fritz-Haber Institute of the Max-Planck Society, Faradayweg 4-6, 14195 Berlin, Germany.*

[2]*MPI for Structure and Dynamics of Matter, Luruper Chaussee 149 22761 Hamburg, Germany*

[3]*Department of Inorganic Chemistry, Fritz-Haber Institute of the Max-Planck Society, Faradayweg 4-6, 14195 Berlin, Germany.*

[4]*Center for Mesoscopic Sciences, Institute for Molecular Science, Okazaki 444-8585, Japan*

* Corresponding author: kuma@fhi-berlin.mpg.de; kuma@ims.ac.jp

Table of Contents

1. Materials and methods

Sample preparation: All experiments were performed in ultra-high vacuum chambers (base pressure $<5\times10^{-10}$ mbar). The Ag(111), Au(111) and Cu(111) surfaces were purchased from MaTeck GmbH and were cleaned by repeated cycles of Ar^+ sputtering and annealing up to 670 K, 600 K and 700 K, respectively. C_{60} was purchased from Sigma-Aldrich and used without further purification. The molecules were evaporated at ~610 K from a K-cell evaporator onto the substrates held at room temperature.

STM measurement: We used a low-temperature STM from UNISOKU Ltd. (modified USM-1400) that is operated with Nanonis SPM Controller from SPECS GmbH. The bias voltage (V_{bias}) was applied to the sample, and the tip was grounded. The tunneling current (j_{STM}) was collected from the tip. We have used Ag tips fabricated by focused ion beam milling.[1]

TERS measurement: The excitation laser was focused to the STM junction with an Ag-coated parabolic mirror (numerical aperture of ~0.6) mounted on the cold STM stage. The parabolic mirror was precisely aligned using piezo motors (Attocube GmbH) that allows three translational and two rotational motions. In the Raman measurements we used a solid-state lasers for 532 nm (Cobolt) and a HeNe laser for 633 nm, with a diameter of 2 mm. This results in a beam waist <2 μm using sources in the visible range. The incident beam is linearly polarized along the tip axis (p-polarization). The scattered photons are collected by the same parabolic mirror and detected outside of the UHV chamber with a grating spectrometer (AndorShamrock 303i). The spectra presented in this work have not been background corrected or any further data treatment.
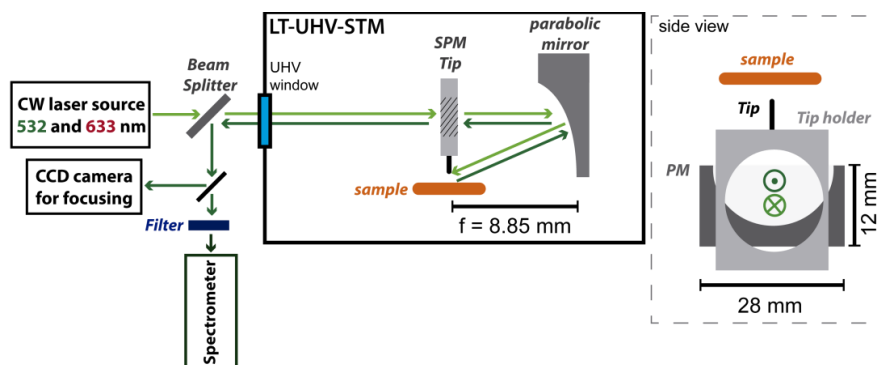
Scheme S1. Experimental set-up of the TERS measurement, with the dimensions and focal length of the parabolic mirror. The side view highlights the hollow tip holder, leaving a free path to/from the parabolic mirror (PM) for the the in- and out-coming beams.

DFT calculations: All the electronic structure calculations were carried out using FHI-aims; a numeric atom-centered orbitals, all-electron code,[2] the PBE exchange correlation functional augmented with pairwise van der Waals interactions was used.[3] When appropriate a specific modification of these corrections, aimed for surface adsorption calculations,[4] was used. "Light"

settings for numerical grids and basis sets were employed unless specified. The Ag(111) surface was represented by a (6 x 5) orthogonal surface unit cell containing three layers. A vacuum of 80 Å and a 3 x 3 x 1 k-point grid were used. Two pyramidal Ag tip structures were considered. The Tip A structure has five Ag layers with only one atom at the tip apex representing a total of 35 Ag atoms. Tip B was created by taking out one Ag atom from Tip A to produce a new tip with three atoms at the apex. The molecular point contact (MPC) structures were modeled using the Tip B structure, the C_{60} molecule and the Ag(111) surface. The MPC structure at equilibrium was constructed by placing the C_{60} molecule between the surface and the tip at the corresponding equilibrium adsorption distances. Compressed MPC structures were also considered by displacing the tip and the molecule towards the surface. All the geometries were relaxed keeping fixed the top two layers of the tip structures and the bottom layer of the surface. In **Fig. S3** we present all the structures models considered in this work. Harmonic frequencies of vibration were obtained through a symmetric finite-difference evaluation and subsequent diagonalization of the dynamical matrix. Atoms were displaced between 0.002 and 0.005 Å in all cartesian directions. The Raman active modes were identified from symmetry considerations and corroborated for the isolated molecule by computing the non-resonant vibrational Raman spectrum through density-functional perturbation theory calculations considering a homogeneous electric field perturbation, see **Table S1**, **S2**, and **S3**.[5] The response of electronic densities to homogeneous electric fields was calculated the isolated C_{60} molecule, the C_{60} molecule on a tip apex, the C_{60} molecule on the Ag(111) surface and for the C_{60} molecule in contact with both tip and surface, see **Fig. S4**. This quantity is directly related to the static polarizability of the molecule.[5]

Figure	λ_{ext} (nm)	Acquisition time (s)	Number of spectra	Grating (l/mm)	P_{inc} (mWμm^{-2})
1 (d)	532	15	1	1200	0.33
1 (e)	633	5	1	600	0.5
3	532	5	60	600	0.33
4 (a)	532	4	50	600	0.33
4 (b)	633	2	48	600	0.45
4 (c)	633	4	30	600	0.45
5 (b)	532	2	60	600	0.33
S1	532	4	1	600	-
S2	532	30	1	1200	0.33
S7 (a) (b) (c)	532	2	30	600	0.33

Table S1. Acquisition parameters of TERS.

2. Incident laser power dependence of TERS in the tunneling regime: C_{60} on Ag(111)

As shown in **Fig. S1**, TERS intensity of a C_{60} molecule on Ag(111) linearly depends on the incident laser power, indicating that the process is a spontaneous Raman scattering.
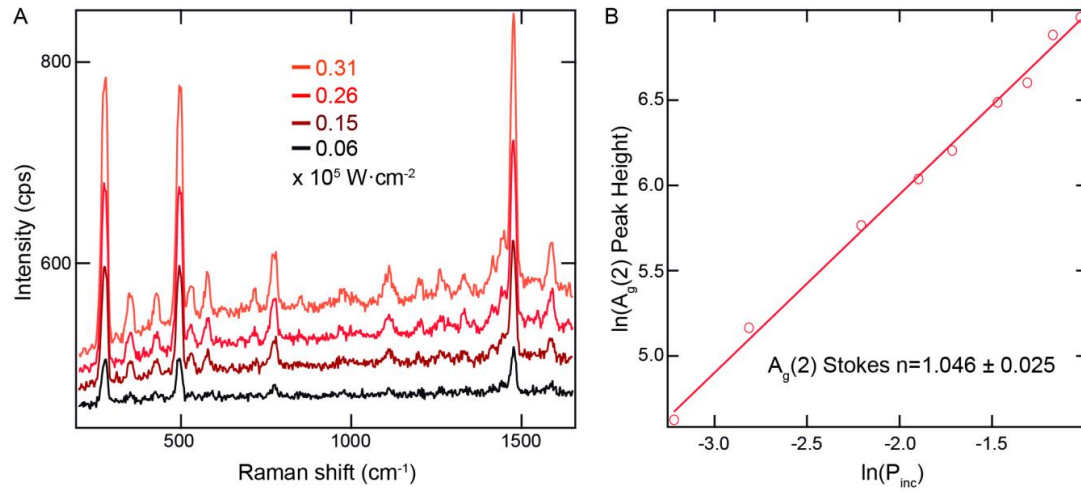
Figure S1. (a) Stokes Raman spectra at four different I_{inc}, under 532 nm illumination of a C_{60} film on Ag(111), measured with a clean Ag Tip (Initial set point: V_{bias}=50 mV, j_{STM} =2 nA, P_{inc} = 0.31×10^5 W cm^{-2}). **(b)** Log plot of Stokes intensity of $A_g(2)$ vs. P_{inc}, showing a power dependence with n=1.

3.   Tip condition dependence of TERS for a C_{60} molecule on Ag(111)

We found that the TERS intensity depends on the tip conditions. **Figure S2** shows the TER spectra recorded for a C_{60} molecule on Ag(111) under different tip conditions modified by poking the tip apex into the bare surface in a controlled manner. This procedure will change the atomic-scale structure of the tip apex. The change of the apex structure may be reflected in different spectral fingerprint at <200 cm^{-1} which can be assigned to the phonons of the Ag tip. It is likely that the different atomistic structures at the apex have a significant impact on the field enhancement and distribution in the STM junction.[6, 7]
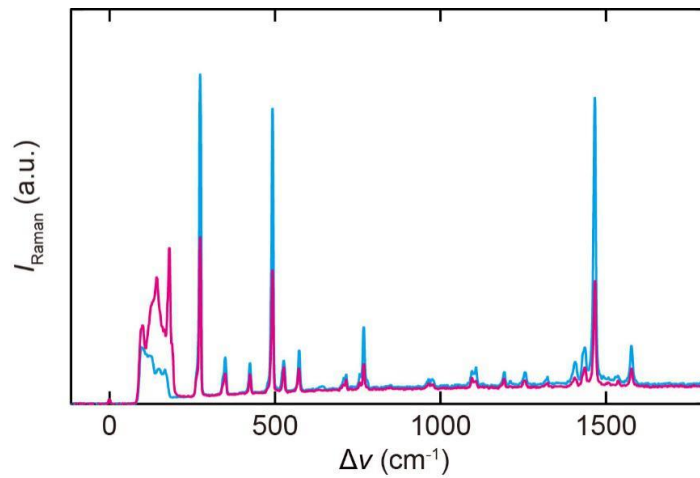
Figure S2. TER spectra recorded for a C_{60} molecule on the Ag(111) surface under different tip conditions (V_{bias}=0.1 V, j_{STM}=2.5 nA, λ_{ext}=532 nm, P_{inc}=0.33×10^5 W cm^{-2}, t_{exp}=30 s). The intensity is normalized by the Rayleigh line.

4.   Models of C_{60}-tip used in the DFT calculations

**Figure S3** shows the different structural models used for the DFT simulations.
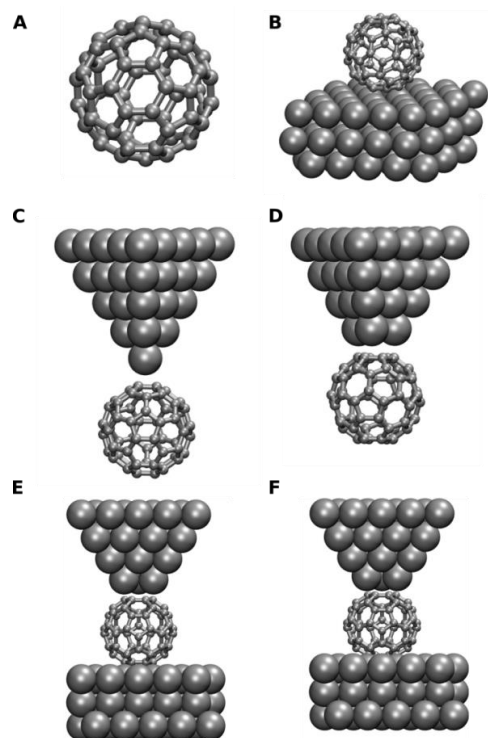
Figure S3. (a) Isolated C_{60} molecule. **(b)** C_{60} adsorbed on the Ag(111) surface. **(c)** Fused C_{60} tip with one atom at the tip apex (Tip A). **(d)** Fused C_{60} tip with three atoms at the tip apex (Tip B). **(e)** MPC structure at equilibrium. **(f)** MPC structure compressed by 1.5 Å.

5. Projected electronic density of states

Projected electronic density of states (PDOS) were simulated for the different structures in **Fig. S3** and are presented in **Fig. S4**. Additional calculations with the HSE06 exchange correlation functional[8] were performed and confirmed the results obtained with the PBE exchange correlation functional (see **Fig. S5**). Moreover, the LUMO of the C_{60} molecule is in resonance with the Fermi-level of the system, a phenomenon normally referred to as Fermi-level pinning. In these situations, the lack of band-gap renormalization upon adsorption 'cancels out' with the band-gap underestimation by the PBE functional and leads to a fortuitous cancellation of errors. As a result, it is obtained a better description of the orbitals than might be expected otherwise
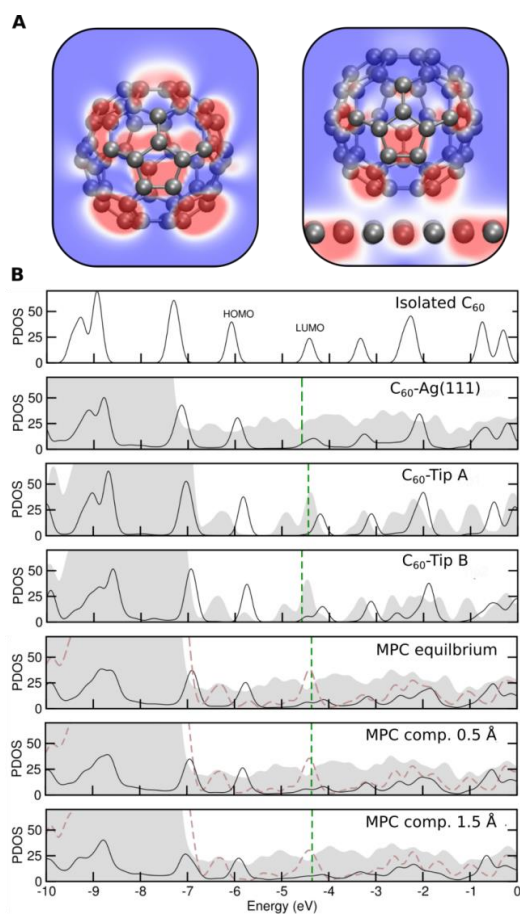
Figure S4. (**a**) Two-dimensional cuts of the spatial distribution of electronic density corresponding to the LUMO of isolated C_{60} molecule (left) and of the C_{60} molecule adsorbed on the Ag(111) surface (right). (**b**) Atom-projected electronic density of states (PDOS) for the different configurations (see **Fig. S3**). C atoms, Ag surface atoms and Ag tip atoms are depicted with solid black line, gray area, and dashed brown line, respectively. The Fermi energy is marked by a vertical green dashed line in each panel.
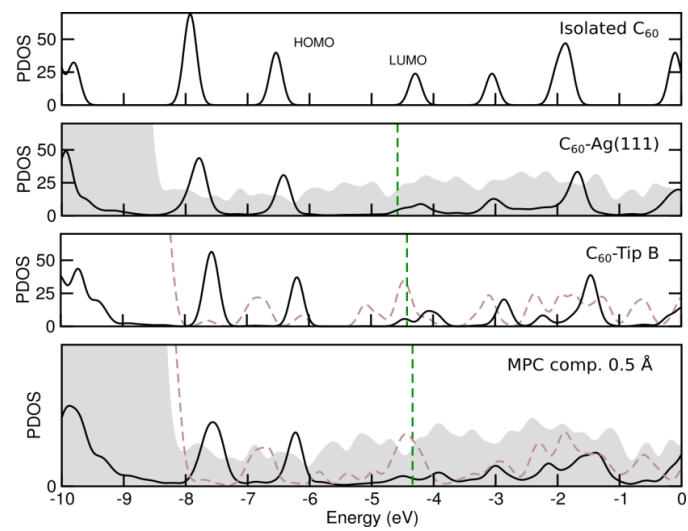
Figure S5. Same as **Fig. S4** using the HSE06 exchange correlation functional.

6. Detailed analysis of the Raman active modes of C_{60} on Ag(111) and C_{60}-tip

According to group theory, the normal modes belong to the following representations

$$\Gamma = 2A_g + 3F_{1g} + 4F_{2g} + 6G_g + 8H_g + A_u + 4F_{1u} + 5F_{2u} + 6G_u + 7H_u,$$

where subscripts g (gerade) and u (ungrade) represent the symmetry of the eigenvector under the action of the inversion operator and the symmetry labels refer to irreducible representations.[9] The icosahedral symmetry yields 10 distinct Raman-active modes ($2A_g+8H_g$) and 4 infrared active modes ($4F_{1u}$) up to first order. Calculated vibrational harmonic frequencies for the gas-phase C_{60} and C_{60} on Ag(111) are reported in **Table S1** (red background), in good agreement with the experimentally observed values (blue background). The comparison with the experimentally obtained frequencies in solid state (ref. 21 in the main text) offers information regarding the nature of the observed shifts. It can be seen that the coupling of the C_{60} molecule with Ag atoms breaks the 5-fold degeneracy of the H_g modes while the A_g modes do not present appreciable mixing (see also **Table S2**). The third column describes the calculated frequencies for the C_{60} monomer relaxed geometry upon adsorption on Ag(111), without taking into account the change in the electronic structure, by removing the substrate after relaxing the geometry. The forth column contains additionally the contribution of the surface, taking into account hybridization (electronic charge rearrangement). In all cases the vibrational frequencies are red-shifted in comparison to the isolated molecule showing an overall softening of the vibrational modes.

Mode	Solid state (Ref. 21)	Gas Phase (Sim.)	C_{60}-Ag(111) only Relaxed (Sim.)	C_{60}-Ag(111) relaxed+CT (Sim.)	C_{60} in an island (Exp.)
$H_g(8)$	1577.5	1565 (5)	1552-1559	1530-1550	1576.4 ± 0.2
$A_g(2)$	1470.0	1477 (1)	1464	1461	1466.1 ± 0.1
$H_g(7)$	1426.5	1426 (5)	1423	1377-1417	1435.4 ± 0.3
$H_g(6)$	1251.0	1248 (5)	1238-1249	1240-1244	1255.5 ± 0.5
$H_g(5)$	1101.0	1104 (5)	1099-1105	1082-1103	1103.0 ± 0.7
$H_g(4)$	775.0	775 (5)	769-773	763-769	768.1 ± 0.1
$H_g(3)$	711.0	702 (5)	703-704	621-699	711.6 ± 0.7
$A_g(1)$	497.5	491 (1)	487	488	492.4 ± 0.02
$H_g(2)$	432.5	424 (5)	425-428	405-416	423.3 ± 0.4
$H_g(1)$	273.0	258 (5)	258-259	255-266	273.8 ± 0.02

Table S2. Theoretical (red) and experimental (blue) vibrational harmonic frequencies. Only the modes that are Raman active in gas phase are presented. Numbers in parenthesis show the degeneracy of each mode in the gas phase and frequency intervals indicate the extent in which the degeneracy of the modes is broken. All mode frequencies in cm^{-1}.

In **Table S3**, the calculated vibrational frequencies of C_{60} adsorbed on the tips with slightly different geometries (Tip A and B in **Fig. S3**) are presented. The first column show results that only account for the effect of the relaxed geometry (deformation) of the C_{60} molecule adsorbed on Tip A, while column 2 also includes the effect of the electron transfer from Tip A. Similar data is presented in columns 3 and 4 for Tip B. The effect of mechanical deformation of an isolated C_{60} molecule is presented (C_{60} hexagon compressed) in the fifth column, in order to estimate the effect of such a deformation in the fused junctions. The molecule was deformed by bringing the six C atoms of opposing hexagonal rings of the molecule closer by 0.2 Å. These positions were fixed and all other degrees of freedom of the molecule were relaxed. In column 6, the frequencies calculated for the contact structure with Tip B are shown. The calculated frequencies of C_{60} upon adsorption on the tip show small differences for subtle variations of the tip apex structure, resulting from slightly different adsorption geometries of C_{60}, which eventually affect the electronic charge rearrangement between the molecule and the tip. This will account for the experimentally observed variations between different tips (**Table S3**).

Frequency (cm^{-1})	Mode decomposition
1550	$H_g(8)$ (36 %) + H_u (60 %)
1550	$H_g(8)$ (22 %) + H_u (56 %)
1547	$H_g(8)$
1546	$H_g(8)$ (46 %) + H_u (47 %)
1546	$H_g(8)$ (45 %) + H_u (47 %)
1530	$H_g(8)$ (52 %) + H_u (40 %)
1530	$H_g(8)$ (56 %) + H_u (37 %)
1461	$A_g(2)$
1417	$H_g(7)$ (15 %) + T_{1u} (50 %) + G_{1u} (17 %)
1396	$H_g(7)$
1396	$H_g(7)$ (55 %) + T_{1u} (26 %)
1395	$H_g(7)$
1378	$H_g(7)$
1377	$H_g(7)$
1244	$H_g(6)$
1244	$H_g(6)$
1243	$H_g(6)$
1240	$H_g(6)$
1240	$H_g(6)$
1103	$H_g(5)$
1100	$H_g(5)$
1094	$H_g(5)$ (40 %)+G_g (50 %)
1094	$H_g(5)$ (44 %)+G_g (52 %)
1094	$H_g(5)$ (22 %)+G_g (72 %)
1094	$H_g(5)$
1094	$H_g(5)$ (36 %)+G_g (63 %)
1083	$H_g(5)$
1082	$H_g(5)$
769	$H_g(4)$
769	$H_g(4)$
767	$H_g(4)$
766	$H_g(4)$
763	$H_g(4)$
488	$A_g(1)$
699	$H_g(3)$ (26 %) + $T_{3u}(2)$ (68 %)
699	$H_g(3)$ (35 %) + $T_{3u}(2)$ (64 %)
699	$H_g(3)$ (37 %) + $T_{3u}(2)$ (56 %)
689	$H_g(3)$ (69 %) + $T_{3u}(2)$ (26 %)
681	$H_g(3)$
681	$H_g(3)$

621	$H_g(3)$ (33 %) + $T_{3u}(2)$ (13 %)
416	$H_g(2)$
411	$H_g(2)$
411	$H_g(2)$
405	$H_g(2)$
405	$H_g(2)$ (75 %)
266	$H_g(1)$
258	$H_g(1)$
258	$H_g(1)$
255	$H_g(1)$
255	$H_g(1)$

Table S3. Normal modes decomposition for Raman active modes in the C_{60} on Ag(111). This decomposition was obtained by a projection of the normal modes calculated for the surface-adsorbed molecule on the modes calculated for the isolated molecule, which have the labeled symmetries. Only modes that contribute more than 10 % to a particular isolated-molecule mode are reported. Numbers in bold indicate the limit of the intervals reported in **Table S2**. Similar mixing is observed for the C_{60} on Tip B and C_{60} on Tip A (not shown).

Mode	C$_{60}$–Tip A (only relaxed)	C$_{60}$–Tip A (relaxed + charge trans.	C$_{60}$–Tip B (only relaxed)	C$_{60}$–Tip B (relaxed.+ charge trans.)	C$_{60}$ hex. compressed	C$_{60}$–Tip B on Ag(111) contact equilibrium	Ag tip #1 on Ag(111)		Ag tip #2 on Ag(111)		Ag tip #3 on Ag(111)	
							tunneling	MPC	tunneling	MPC	tunneling	MPC
$H_g(8)$	1560-1566	1535-1561	1555-1563	1536-1557	1566-1580	1507-1537	1572.7 ± 1.4	1537.9± 0.8	1594.2 ± 1.1	1586.6 ± 0.7	1590.0 ± 0.5	1587.4 ± 0.7
$A_g(2)$	1474	1471	1470	1465	1486	1447	1465.4 ± 0.1	1459.8 ± 0.1	1477.5 ± 0.2	1468.4 ± 0.2	1479.0 ± 0.2	1469.7 ± 0.3
$H_g(7)$	1403	1370-1410	1368	1370-1400	1427	1366-1384	1424.2 ± 1.0	1410.7 ± 0.5	1414.7 ± 1.1	1411.3 ± 0.4	1455.9 ± 1.8	1414.2 ± 0.2
$H_g(6)$	1241-1251	1244-1247	1239-1253	1236-1246	1242-1264	1231-1245	1260.0 ± 2.2	1262.0 ± 1.2	N.A.	1264.5 ± 1.6	1267.1 ± 0.9	1262.8 ± 1.2
$H_g(5)$	1100-1106	1096-1103	1098-1106	1081-1104	1109-1110	1070-1092	1105.7 ± 1.5	1110.0 ± 2.3	1110.6 ± 1.4	1104.0 ± 0.4	1105.3 ± 0.8	1102.2 ± 0.9
$H_g(4)$	773-776	770-774	768-775	763-772	770-783	753-767	773.6 ± 1.4	764.1 ± 0.6	773.8 ± 0.8	768.4 ± 0.3	775.7 ± 0.4	768.4 ± 0.3
$H_g(3)$	702-703	670-695	702-703	688-701	700-703	624-674	712.5 ± 3.0	704.8 ± 3.1	726.4 ± 3.0	723.6 ± 13.6	702.8 ± 3.8	704.0 ± 0.6
$A_g(1)$	490	490	489	488	494	489	488.4 ± 0.2	488.0 ± 0.1	491.6 ± 0.3	488.4 ± 0.1	492.4 ± 0.2	487.0 ± 0.2
$H_g(2)$	424-426	416-420	424-427	399-424	419-427	395-399	412.6 ± 0.9)	411.6 ± 1.2	428.4 ± 1.5	417.4 ± 0.3	420.4 ± 0.5	421.3 ± 0.2
$H_g(1)$	258-259	258-263	258-259	253-256	247-268	255-259	266.6 ± 0.6)	273.3 ± 0.1	270 ± 0.3	268.3 ± 0.1	266.2 ± 1.3	269.1 ± 0.1

Table S4. Calculated (red columns) and experimental (blue columns) frequencies of C$_{60}$ vibrations for different contact situations (calculation) and for different tips (experiment). Only the modes which are Raman active in the gas phase are presented. Units in cm^{-1}.

7. Δz- dependent TERS of a C_{60}-tip on Ag(111) at small V_{bias}

Various Δz-dependent TERS measured with increasing V_{bias} show that at this regime the TERS intensity at is not sensitive to changes in the direct current in the STM.
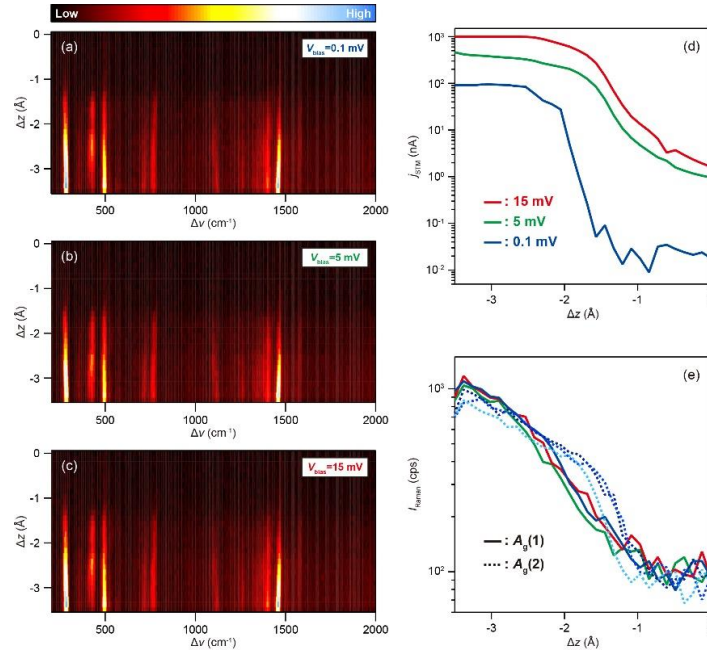
Figure S6. (a–c) Δz-dependent TER spectra of a C_{60}-tip approaching the Ag(111) surface at 0.1, 5 and 15 mV, respectively (λ_{ext}=532 nm, P_{inc}=0.33 mWµm^{-2}, 10 K). (d) Simultaneously obtained j_{STM}– Δz curves for the three different cases, with j_{STM} at contact differing by one order of magnitude. (e) Intensity of the $A_g(1)$ and $A_g(2)$ modes as a function of the Δz for the different V_{bias} (j_{STM}), showing almost no differences.

8. Enlarged Δz-dependent TERS of a C_{60}–tip on Ag(111) highlighting shifting of the vibrational modes

Figure S7 show the enlarged Δz-dependent TERS of a C_{60}–tip on Ag(111) in **Fig. 2c**.
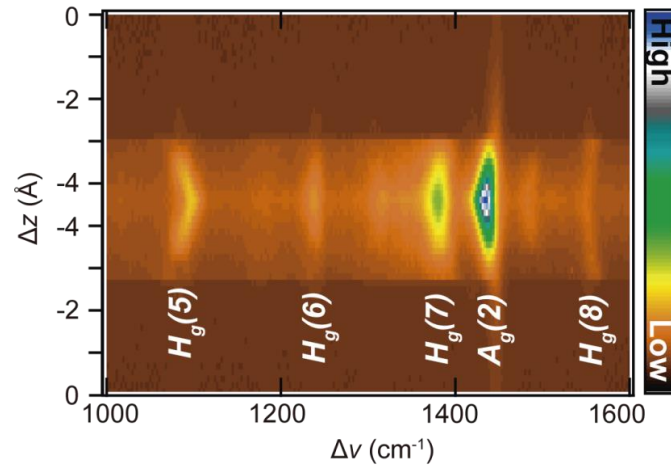
Figure S7. Enlarged Δz-dependent TERS of **Fig. 3** (λ_{ext}=532 nm, P_{inc}=0.33 mWμm^{-2}, 10 K).

9. Simulations of the non-resonant Raman intensity of in the various environments
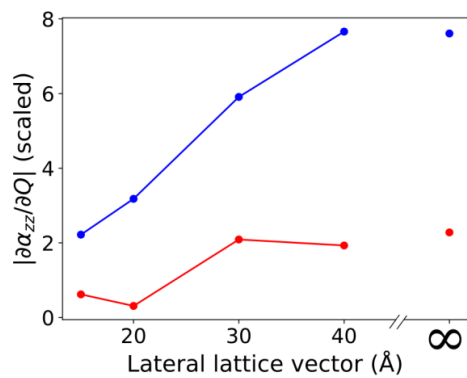
The zz component of the polarizability tensor of the systems was calculated through the explicit application of a homogeneous electric field in the z direction (perpendicular to the surface; see orientation of all systems in **Fig. S3**), with a subsequent finite-difference evaluation of the derivative of the dipole moment in the z direction. We applied fields of strengths 10^{-4} to 10^{-3} V/Å and converged densities down to 10^{-8} bohr^{-3}, in addition to employing *tight* settings of the FHI-aims code for these calculations. We then calculated the Raman intensities through finite differences of the zz component of the polarizability tensor with respect to the displacements along the normal modes. All simulations were performed with the PBE density functional and all finite difference derivatives were computed by central differences. We assessed that a possible numerical error of up to 20 % can be present in the numbers reported. We found that lateral interactions in the periodic simulations could strongly affect the calculated intensities. The overall effect of such interaction is a relative decrease of the derivative of the zz component of the polarizability tensor with respect to the isolated C_{60} value (see **Tables S5** and **S6**). By comparing to isolated calculations of the systems that do not contain the Ag(111) surface, we concluded that unit cells with at least 40 Å of length along the lateral distances were necessary to obtain the numbers reported in **Table S5** which are minimally affected by the spurious lateral interaction (see **Fig. S8**).

Mode	Isolated C_{60}	C_{60}-Ag(111)	C_{60}-Tip A	C_{60}-Tip B	MPC at equilibrium
$A_g(1)$	1.0	1.6	8.0	1.9	0.1
$A_g(2)$	1.0	4.7	33.1	7.7	0.2

Table S5. Derivative of the zz component of the polarizability tensor. The z axis is parallel to the surface normal and the derivatives were computed with respect to the displacements along $A_g(1)$ and $A_g(2)$ normal modes. Values are reported using the gas phase value as reference. A 46.981 Å x 40.687 Å x 104.795 Å simulation box was employed.

Mode	Isolated C_{60}	C_{60}-Ag(111)	C_{60}-Tip A	C_{60}-Tip B	MPC at equilibrium
$A_g(1)$	1.0	0.6	1.3	0.6	0.03
$A_g(2)$	1.0	2.1	6.3	2.2	0.06

Table S6. Same as **Table S5** for 14.681 Å x 15.251Å x 104.795 Å simulation box.

Figure S8. Derivative of the *zz* component of the polarizability tensor ($\frac{\partial \alpha}{\partial Q}$) with respect to $A_g(1)$ (red) and $A_g(2)$ (blue) normal modes as a function of the lateral lattice vectors magnitude obtained for the C_{60}-Tip B model. Infinite lateral lattice vectors refers to calculations performed without periodic boundary conditions.

10. Wavelength dependence of MPC-TERS

Figure S9 shows the waterfall plot of the TERS spectra recorded for Ag(111) and Au(111) at the excitation wavelength of 633 nm. For both surfaces, the strong Raman enhancement can be observed in the MPC regime. The enhancement factors are estimated to be $\rho_{MPC,\ Ag(111)} \sim 32.1$ and $\rho_{MPC,\ Au(111)} \sim 40.9$.
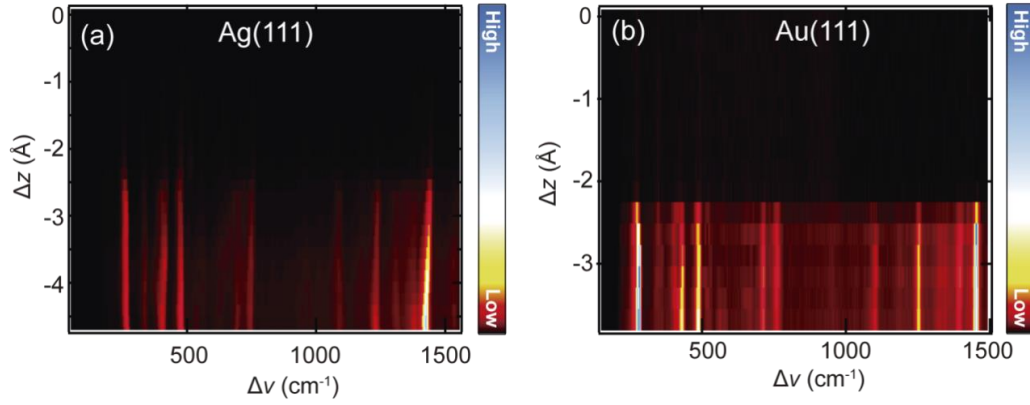
Figure S9. (a–b) Δz-dependent TERS spectra measured on the Ag(111) and Au(111) surface with λ_{ext}=633 nm (Ag(111): λ_{ext}=633 nm, P_{inc}=0.45 mWμm^{-2}, V_{bias} = 0 V, 10 K, Au(111): λ_{ext}=633 nm, P_{inc}=0.45 mWμm^{-2}, V_{bias} = 0 V, 10 K).

References

[1] Böckmann, H. *et al.* Near-Field Manipulation in a Scanning Tunneling Microscope Junction with Plasmonic Fabry-Pérot Tips. *Nano Lett.* **2019**, *19*, 3597.

[2] Blum, V. *et al*. *Ab initio* molecular simulations with numeric atom-centered orbitals. *Comp. Phys. Commun.* **2009**, *180*, 21752196.

[3] Tkatchenko, A.; Scheffler, M. Accurate Molecular Van Der Waals Interactions from Ground-State Electron Density and Free-Atom Reference Data. *Phys. Rev. Lett.* **2009**, *102*, 073005.

[4] Ruiz, V. G.; Liu, W.; Zojer, E.; Scheffler, M.; Tkatchenko, A. Density-Functional Theory with Screened van der Waals Interactions for the Modeling of Hybrid Inorganic-Organic Systems. *Phys. Rev. Lett.* **2012**, *108*, 146103.

[5] Shang, H.; Raimbault, N.; Rinke, P.; Scheffler, M.; Rossi, M.; Carbogno, C. All-electron, real-space perturbation theory for homogeneous electric fields: theory, implementation, and application within DFT. *New J. Phys.* **2018**, *20*, 073040.

[6] Zhang, P.; Feist, J.; Rubio, A.; García-González, P.; García-Vidal, F. J. *Ab initio* nanoplasmonics: The impact of atomic structure. *Phys. Rev.* B **2014**, *90*, 161407(R).

[7] Urbieta, M. *et al.* Atomic-Scale Lightning Rod Effect in Plasmonic Picocavities: A Classical View to a Quantum Effect. *ACS Nano* **2018**, *12*, 585.

[8] Krukau, A. V. *et al*. Influence of the exchange screening parameter on the performance of screened hybrid functionals, *J. Chem. Phys.* **2006**, *125*, 224106.

[9] Dresselhaus, M. S.; Dresselhaus, G.; Eklund, P. C. Raman Scattering in Fullerenes. *J. Raman Spectrosc.* **1996**, *27*, 351.

4 | Characterization of Point Defects in TMDC Monolayers

The significance of Raman and TERS techniques, particularly, the utilization of near-field techniques, has been emphasized in the previous chapter. One of the many capabilities of these techniques is to offer detailed information on the characteristic of defects within the crystal structure. In connection with these techniques, the electronic structure techniques discussed in chapter 2 need to be utilised in order to model and compute the basic properties of defected monolayers.

Previous studies have classified defects based on their dimensionality, with zero-dimensional defects including point defects like vacancies and adatoms, one-dimensional defects including line defects like dislocations, and two-dimensional defects including grain and phase boundaries [117]. This research primarily emphasizes the investigation and analysis of point defects.

Point defects can also be classified based on the electronic states associated with them like shallow, deep, donor and acceptor. A shallow defect state is when the energy levels are located very close to the valence or conduction band edges. The shallow dopant can be p−type (creates an energy level just below the conduction band) and n−type (creates an energy levels just above the valence band). On the other hand, defects states with energy levels located within the band gap are called deep states [118].

This chapter focuses on the theory for calculating the formation energies of neutral and charged point defects. It covers the techniques employed to mitigate artifacts arising from charged point defects images in the supercell. Additionally, the chapter explores the incorporation of temperature and pressure effects to investigate the stability of point defects, followed by a study of point defects in TMDC monolayers and explanatory characterization of their vibrational properties, through the TERS techniques presented at the end of this chapter.

4.1 Modeling Isolated Point Defects

This thesis focuses on a specific class of 2D materials called TMDCs (transition metal dichalcogenides) 1H monolayers. TMDCs consist of a transition metal atom (e.g., molybdenum, tungsten) sandwiched between two layers of chalcogen atoms (e.g., sulfur or selenium). These monolayers possess a hexagonal lattice structure, with the transition metal atom coordinated by chalcogen atoms in a trigonal prismatic arrangement. They exhibit remarkable electronic, optical, and mechanical properties, making them a subject of intense research interest and the focus of this part of the thesis.

To investigate the behavior of TMDC monolayers, we explore the impact of point defects on their lattice structure. In the presence of such defects, the translational symmetry of the monolayer is disrupted. Therefore, to model isolated point defects a larger supercell becomes necessary

as depicted in Figure 4.1, for WSe$_2$ monolayer with Se monovacancy. In this supercell, a low concentration (2%) of Se vacancy is present, so that defect-defect interaction is minimized. The size of the supercell has to ensure that the calculated defect formation energy reaches a sufficiently accurate and converged value. This indicates that the simulation has reached the dilute limit, where the interactions between defects are negligible.
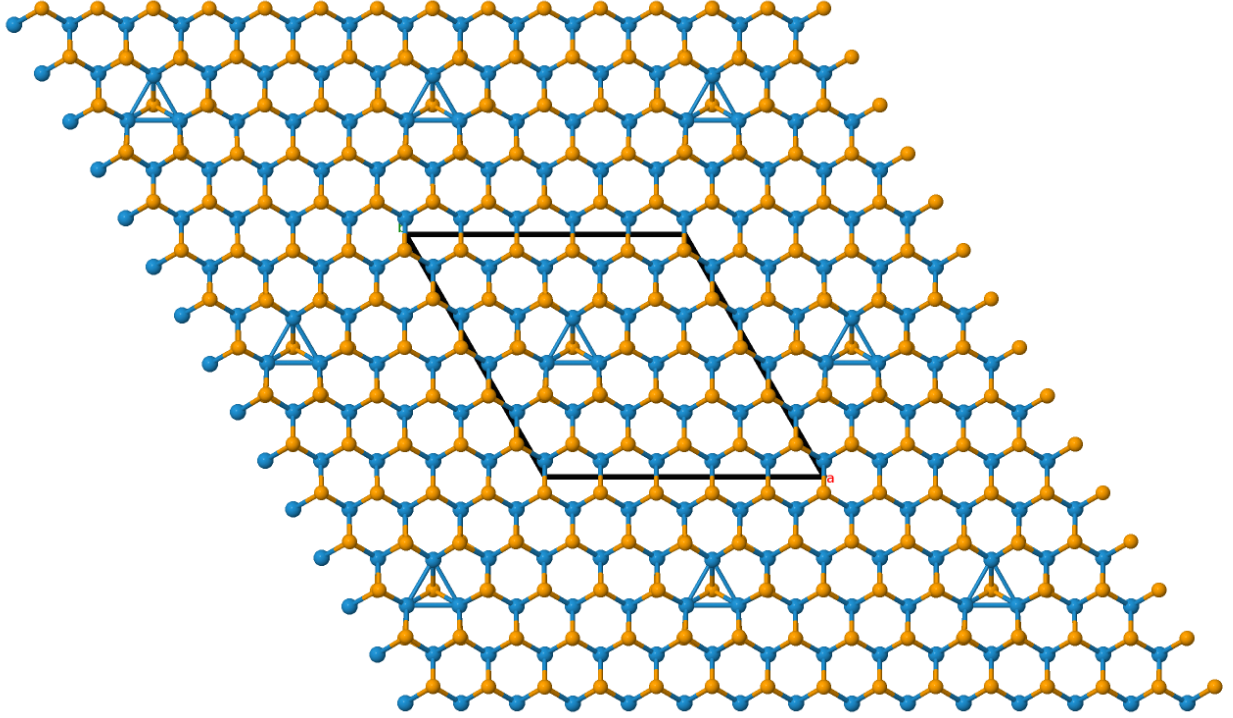
Figure 4.1: The model depicts a WSe$_2$ monolayer with a Se monovacancy embedded in a 5×5 supercell (marked in black). The periodicity and spacing of the defect sites are shown by repeating the supercell .

4.1.1 Calculating the formation energy of Isolated Point Defects

The formation energy of point defects is defined as the energy required to create or remove a defect, that can be either energetically favorable or costly to the system. The formation energy not only can provide interpretation on the stability of point defects, but also information about the equilibrium concentration of point defects.

To calculate the formation energy, the total energy of a defective supercell is compared to the total energy of a perfect supercell. In addition, the system is modelled to be in contact with a reservoir that can absorb or donate the atomic species involved in the defect formation. The chemical potential of the reservoir used in the calculation is usually taken from the elemental phases of the constituent atoms. That is translated into the following equation,

$$E_f = E_d(n_i + \Delta n_i) - E_p(n_i) + \sum_i \mu_i \Delta n_i, \qquad (4.1)$$

where E_d and E_p are the total energies of the defective and perfect crystal, respectively, μ_i is the

relevant chemical potential of the i_{th} element that is discussed in the section below for MX_2, and Δn_i is the number of atoms of the i_{th} element that are added/removed to/from the host crystal.

The above explanation applies to neutral defects but charged defects require an electron reservoir to maintain charge neutrality. The formation energy in this case is given by the equation,

$$E_f = E_d(n_i + \Delta n_i) - E_p(n_i) - \sum_i \Delta n_i \mu_i + qE_F + E_{corr}. \tag{4.2}$$

The term E_F accounts for the chemical potential of the electrons (Fermi energy) which were added or removed from the system in order to create the charged defect, and q is the charge of the defect. E_{corr} is added to eliminate the spurious interactions between charged defects in the supercell approach due to the long-range Coulomb interactions. This correction term is important when investigating charged point defects in the dilute limit, due to the fact that interaction between defects can be significant. There are several correction schemes available to calculate E_{corr}, for example, the ones proposed by Makov, Payne [119] and by Freysoldt et al. [120, 121], that are essential for accurately simulating charged defects in materials and minimizing the computational cost. These corrections are based on modelling the electrostatic interactions of charges with compensating backgrounds, and can be used in a post-processing manner. In our work, we took a different approach.

4.1.2 Virtual Crystal Approximation and Charged Defects

For simulating charges in the supercell approach the charge is periodically repeated and consequently the electrostatic potential sums up and diverges. In periodic calculations of charged systems, it is crucial to compensate for the charge to maintain the supercell's neutrality. This compensation ensures that the overall charge of the system is balanced, enabling accurate calculations within the periodic framework. For bulk systems, canceling the divergence through applying a uniform constant background charge density to the supercell is feasible, however, for surfaces the uniform charge density expands across the vacuum region between repeating slabs. This can be compensated by the corrections mentioned previously. Instead we utilized the virtual-crystal approximation (VCA) [122, 123].

VCA is a computational technique commonly used for surface or two-dimensional materials with charged defects and background charges to eliminate or mitigate the effects of the interactions between charged defects and the compensating background charge. VCA minimizes these effects and allows for more accurate calculations. In an all-electron code, the nuclear charges ($Z^{'}$) of specific atoms are modified so that the number of effective electrons in the system is adjusted, while the overall simulation is set to be electrically neutral. To ensure consistency in the calculations, the formation energy (equation 4.2) is calculated, so that the reference energies of both the pristine and defected systems are calculated under the same doping conditions. This means that the pristine system and the defected system are treated in a consistent manner regarding the doping levels or charge states.

Extrapolation to dilute limit

In order to eliminate or minimize the artifacts caused by lateral Coulomb interactions, the formation energies need to be extrapolated to an infinite-sized supercell. As such, the formation energies for a series of supercell sizes have to be calculated and fitted to a mathematical function that captures the size dependence.

For charged surface defects in the dilute limit, the VCA allows us to write a simple series expansion of the spurious Coulomb energy of interaction as [124],

$$E_f(L) = E_f(L \to \infty) + \frac{A_1}{L} + \frac{A_2}{L^2} + \frac{A_3}{L^3}. \tag{4.3}$$

In this formula, $E_f(L)$ is the defect formation energy in a supercell of lateral length L, which sets the distance between the charged defects. $E_f(L \to \infty)$ is the formation energy in an infinite sized supercell and A_1, A_2, and A_3 are coefficients determined from a fit. This means that the formation energy of defects with increasing supercell size needs to be calculated. Even though that represents an additional calculation cost, it tends to be quite feasible (see section 4.3) and yields a simple correction.

4.2 Thermodynamics of Defect Formation

In the thermodynamics of defects, the Gibbs free energy of formation (G) is a key quantity that describes the stability and formation of defects in a material expressed as,

$$\Delta G = G_{\mathrm{d}}(p,T) - G_{\mathrm{p}}(p,T) - \sum_i \Delta n_i \mu_i(p,T), \tag{4.4}$$

where $G_{\mathrm{d}}(p,T)$ and $G_{\mathrm{p}}(p,T)$ are the Gibbs energy of the system with defect and without defect, respectively, at pressure p and temperature T. The Gibbs energy of formation accounts for both the configurational and entropic contribution as Helmholtz free energy $F(V,T)$ and the mechanical contribution pV in the following manner $G(p,T) = F(V,T) + pV = E - TS + pV$, therefore,

$$G_f^d(p,T) = F_d(V,T) - F_p(V,T) + p\Delta V - \sum_i \Delta n_i \mu_i(p,T) \tag{4.5}$$

where $F_{\mathrm{d}}(V,T)$ and $F_{\mathrm{p}}(V,T)$ are the Helmholtz free energies of the system with the defect and the pristine system, respectively, and ΔV is the difference in volume between the two systems.

$F(V,T)$ can be decomposed into several contributions as follows:

$$F(V,T) = E_{\mathrm{DFT}}(V) + F^{\mathrm{el}}(V,T) + F^{\mathrm{h}}(V,T) + F^{\mathrm{ah}}(V,T) + F^{\mathrm{mag}}(V,T). \tag{4.6}$$

1. $E_{\mathrm{DFT}}(V)$: The ground state total energy of the system computed using DFT calculations.

Figure 4.2: Geometries of S_8 (left) of 2.04 Å bond length and Se_8 (right) of bond length 2.33 Å rings structures optimized with HSE06 functional.

It provides the electronic structure and the interaction between atoms in the system.

2. $F^{el}(V,T)$: The electronic Helmholtz free energy, is the temperature-dependent contribution from the electronic system, which can be estimated by considering the electronic density of states (DOS) at the Fermi level [125].

3. $F^{h}(V,T)$: The harmonic Helmholtz vibrational free energy contribution, it captures the effects of lattice vibrations on the system. It assumes that the system can be described as a collection of harmonic oscillators.

4. $F^{ah}(V,T)$: The anharmonic free energy contribution that captures effects beyond the harmonic approximation. It takes into account deviations from purely harmonic behavior.

5. $F^{mag}(V,T)$: The Helmholtz free energy specific to magnetic materials, it measures the effects of magnetic ordering, spin interactions, and other magnetic properties of the system.

In our work, we investigate point defects in semi-conductor TMDCs, such that, the anharmonic, electronic and magnetic contributions are less significant compared to the harmonic contribution to the free energy. Hence, we only consider the harmonic free energy. Moreover, we are neglecting cell-volume changes as the point defects we investigate do not introduce significant long-range lattice distortions or induce structural phase transitions.

4.2.1 Chemical potentials of sulfur and selenium

In this thesis, we focus on the semi-conductor of TMDCs : MoS_2, $MoSe_2$, WS_2 and WSe_2. To derive the chemical potential of the chalcogen constituents, we use the ideal gas law at constant temperature, we start by the differential form of the Gibbs free energy:

$$dG = V\,dp - S\,dT. \tag{4.7}$$

At constant temperature $dT = 0$, then,

$$dG = V\,dp. \tag{4.8}$$

Using the ideal gas law that states $pV = Nk_bT$, where N is the number of particles. We can replace V with Nk_bT/p, obtaining,

$$dG = \left(\frac{Nk_bT}{p}\right) dp, \tag{4.9}$$

integrating both sides of the equation between p_0 and p yields:

$$\int dG = \int_{p_0}^{p} \left(\frac{Nk_bT}{p}\right) dp \tag{4.10}$$

$$G - G_0 = Nk_bT \ln\left(\frac{p}{p_0}\right). \tag{4.11}$$

Knowing that $G = \mu N$ where μ is the chemical potential, we obtain,

$$\mu = \mu_0 + k_bT \ln\left(\frac{p}{p_0}\right). \tag{4.12}$$

For an ideal gas, the chemical potential can be expressed in terms of the molecular partition function Z as follows [126]:

$$\mu(T, p) = \frac{G}{N} = \frac{F + pV}{N} = \frac{-k_bT \ln Z + pV}{N}. \tag{4.13}$$

To find the canonical partition function Z, we assume an ideal gas like behaviour. As such, particles are indistinguishable and non-interacting.

$$Z = \frac{1}{N!} \left(z_{\text{trans}} \cdot z_{\text{vib}} \cdot z_{\text{rot}} \cdot z_{\text{e}} \cdot z_{\text{n}}\right)^N \tag{4.14}$$

Here, z_{trans}, z_{vib}, z_{rot}, z_{e}, and z_{n} are the partition functions corresponding to the translational, vibrational, rotational, electronic, and nuclear degrees of freedom, respectively. By incorporating the partition function Z into the chemical potential expression, we can evaluate the contributions of each degree of freedom to the overall chemical potential using statistical thermodynamics [126].

1. Translational part (z_{trans}): The partition function for a gas of N atoms or molecules, confined in a rectangular box, can be derived by considering their translational degrees of freedom. The energy of the system is given by:

$$E = \frac{h^2}{8mL^2}(n_x^2 + n_y^2 + n_z^2). \tag{4.15}$$

Therefore, it can be written as:

$$z_{\text{trans}} = \sum_{n_x,n_y,n_z=1}^{\infty} \exp\left(-\frac{\beta h^2}{8mL^2}n_x^2\right) \exp\left(-\frac{\beta h^2}{8mL^2}n_y^2\right) \exp\left(-\frac{\beta h^2}{8mL^2}n_z^2\right). \tag{4.16}$$

Assuming the dimensions of the box in each direction to be equivalent: $n_x = n_y = n_z = n$, then,

$$z_{\text{trans}} = \left[\sum_{n=1}^{\infty} \exp\left(-\frac{\beta h^2}{8mL^2} n^2 \right) \right]^3. \tag{4.17}$$

Since the translational energy levels are closely spaced, we can approximate the sum over n as an integral. This leads to:

$$z_{\text{trans}} = \left(\int_0^{\infty} \exp\left(-\frac{\beta h^2}{8mL^2} n^2 \right) \right)^3 dn \tag{4.18}$$

Using the fact that:

$$\int_0^{\infty} \exp(-\alpha x^2) dx = \sqrt{\frac{\pi}{4\alpha}} \tag{4.19}$$

This simplifies z_{trans} to

$$z_{\text{trans}} = \left(\frac{2\pi m k_b T L^2}{h^2} \right)^{\frac{3}{2}} = \left(\frac{2\pi m k_b T}{h^2} \right)^{\frac{3}{2}} V, \tag{4.20}$$

where m is the total mass of the system, h is Planck's constant , and $V = L^3$ is the volume of the box.

2. Rotational part (z_{rot}): The rotational energy levels of a polyatomic molecule can be described using the rigid rotor model.

   The formula for z_{rot} is given by [126],

$$z_{\text{rot}} = \frac{\sqrt{\pi}}{\sigma} \left(\frac{8\pi I_A k_b T}{h^2} \right)^{\frac{1}{2}} \left(\frac{8\pi I_B k_b T}{h^2} \right)^{\frac{1}{2}} \left(\frac{8\pi I_C k_b T}{h^2} \right)^{\frac{1}{2}}, \tag{4.21}$$

   where σ is the symmetry number that accounts for any symmetry degeneracies, the molecule possesses and I_A, I_B, and I_C are the moments of inertia of the molecule along its principal axes of rotation.

3. Vibrational part (z_{vib}): The vibrational energy of a nonlinear molecule with $3N-6$ degrees of freedom can be described as a harmonic oscillator. Mathematically, it is given by:

$$E_{\text{vib}}(n) = \left(n_i + \frac{1}{2} \right) \hbar \omega_i. \tag{4.22}$$

n_i represents the vibrational quantum number for each mode i, $\hbar$ is the reduced Planck's constant, and ω_i is the frequency of mode i.

The vibrational partition function, denoted as z_vib, is the product of vibrational contributions for each frequency. It can be expressed as:

$$z_\text{vib} = \prod_i^{3N-6} \sum_{n=0}^{\infty} \exp\left(-\beta E_\text{vib}\right). \tag{4.23}$$

Here $3N - 6$ refers to the total degrees of freedom of a nonlinear molecule with N being the number of atoms of a molecule.

Further simplification of the expression, yield,

$$z_\text{vib} = \prod_i^{3N-6} \exp\left(-\frac{\beta\hbar\omega_i}{2}\right) \left(\sum_{n=0}^{\infty} \exp\left(-\beta\hbar\omega_i\right)\right)^n. \tag{4.24}$$

Then, using the following geometric series sum formula,

$$\left(\sum_{n=0}^{\infty} \exp(-x)\right)^n = \frac{1}{1 - \exp(-x)}$$

The vibrational partition function can be rewritten as,

$$z_\text{vib} = \prod_i^{3N-6} \frac{\exp\left(-\frac{\beta\hbar\omega_i}{2}\right)}{1 - \exp(-\beta\hbar\omega_i)}. \tag{4.25}$$

4. Electronic Part (z_e): Molecules can have electrons excited to higher energy states, but at ordinary temperatures, most molecules are in their ground state, which we consider as having zero energy. Therefore, the electronic partition function z_e is given by:

$$z_e = g_1 \exp(-\beta E_{DFT}) \tag{4.26}$$

Here, g_1 represents the degeneracy of the ground state and it is 1, and E_{DFT} is its energy.

After summing up the contributions of the different degrees of freedom above to the logarithm part of the chemical potential as shown in equation 4.13 as,

$$\ln\left[\frac{1}{N!}\left(z_\text{trans} \cdot z_\text{vib} \cdot z_\text{rot} \cdot z_\text{e}\right)^N\right] \tag{4.27}$$

Breaking down the simplification of each term results in:

1.

$$\ln\left(\frac{z_{\text{trans}}^N}{N!}\right) = N\ln\left[\left(\frac{2\pi m k_b T}{h^2}\right)^{\frac{3}{2}} V\right] - N\ln(N) + N$$

$$= N\ln\left[\left(\frac{2\pi m k_b T}{h^2}\right)^{\frac{3}{2}} \frac{k_b T}{p}\right] + N$$

2.

$$\ln\left(z_{\text{rot}}^N\right) = N\ln\left[\frac{\sqrt{\pi}}{\sigma}\left(\frac{8\pi I_A k_b T}{h^2}\right)^{\frac{1}{2}}\left(\frac{8\pi I_B k_b T}{h^2}\right)^{\frac{1}{2}}\left(\frac{8\pi I_C k_b T}{h^2}\right)^{\frac{1}{2}}\right]$$

$$= N\ln\left(\frac{\sqrt{\pi}}{\sigma}\right) + N\ln\left[\left(\frac{8\pi k_b T}{h^2}\right)^{\frac{3}{2}}\left(I_A\right)^{\frac{1}{2}}\left(I_B\right)^{\frac{1}{2}}\left(I_C\right)^{\frac{1}{2}}\right]$$

3.

$$\ln\left(z_{\text{vib}}^N\right) = N\ln\left(\prod_i^{3N-6}\frac{\exp\left(-\frac{\beta\hbar\omega_i}{2}\right)}{1-\exp(-\beta\hbar\omega_i)}\right)$$

$$= N\sum_i^{3N-6}\ln\left(\frac{\exp\left(-\frac{\beta\hbar\omega_i}{2}\right)}{1-\exp(-\beta\hbar\omega_i)}\right)$$

$$= N\sum_i^{3N-6}\left(\ln\left(\exp\left(-\frac{\beta\hbar\omega_i}{2}\right)\right) - \ln\left(1-\exp(-\beta\hbar\omega_i)\right)\right)$$

$$= N\sum_i^{3N-6}\left(-\frac{\beta\hbar\omega_i}{2} - \ln\left(1-\exp(-\beta\hbar\omega_i)\right)\right)$$

4.

$$\ln(z_e^N) = N\ln(z_e)$$

$$= -N\beta E_{DFT}$$

By substituting the simplified values into equation 4.13, we obtain:

$$\mu = -k_b T\ln\left[\left(\frac{2\pi m k_b T}{h^2}\right)^{\frac{3}{2}} \frac{k_b T}{p}\right]$$

$$- k_b T\ln\left(\frac{\sqrt{\pi}}{\sigma}\right) - k_b T\ln\left[\left(\frac{8\pi k_b T}{h^2}\right)^{\frac{3}{2}}\left(I_A\right)^{\frac{1}{2}}\left(I_B\right)^{\frac{1}{2}}\left(I_C\right)^{\frac{1}{2}}\right]$$

$$+ \sum_i^{3N-6}\frac{\beta\hbar\omega_i}{2} + k_b T\sum_i^{3N-6}\left(\ln\left(1-\exp(-\beta\hbar\omega_i)\right)\right)$$

$$+ E_{DFT}.$$

We can add a zero term, $+k_b T \ln \frac{p_0}{p_0}$, to set a references for the chemical potential:

$$
\begin{aligned}
\mu(p, T) = {} & -k_b T \ln \left[\left(\frac{2\pi m k_b T}{h^2} \right)^{\frac{3}{2}} \frac{k_b T}{p_0} \right] \\
& - k_b T \ln \left(\frac{\sqrt{\pi}}{\sigma} \right) - k_b T \ln \left[\left(\frac{8\pi k_b T}{h^2} \right)^{\frac{3}{2}} (I_A)^{\frac{1}{2}} (I_B)^{\frac{1}{2}} (I_C)^{\frac{1}{2}} \right] \\
& + \sum_i^{3N-6} \frac{\hbar \omega_i}{2} + kT \sum_i^{3N-6} \ln \left(1 - \exp(-\beta \hbar \omega_i) \right) \\
& + E_{DFT} \\
& + k_b T \ln \frac{p}{p_0}.
\end{aligned}
\tag{4.28}
$$

Now, a comparison can be made between equations 4.12 and 4.28 leads to

$$
\begin{aligned}
\mu_0(T) = {} & -k_b T \ln \left[\left(\frac{2\pi m k_b T}{h^2} \right)^{\frac{3}{2}} \frac{k_b T}{p_0} \right] \\
& - k_b T \ln \left(\frac{\sqrt{\pi}}{\sigma} \right) + N \ln \left[\left(\frac{8\pi k_b T}{h^2} \right)^{\frac{3}{2}} (I_A)^{\frac{1}{2}} (I_B)^{\frac{1}{2}} (I_C)^{\frac{1}{2}} \right] \\
& + \sum_i^{3N-6} \frac{\hbar \omega_i}{2} - k_b T \sum_i^{3N-6} \ln \left(1 - \exp(-\beta \hbar \omega_i) \right) \\
& + E_{DFT}.
\end{aligned}
\tag{4.29}
$$

While $\mu_0(T)$ can be obtained from thermodynamic tables [127], in this study, it was theoretically calculated using the FHI-aims package.

4.3 Paper III: A Hybrid-DFT Study of Intrinsic Point Defects in MX_2 (M=Mo, W; X=S, Se) Monolayers

The electronic, optical, and mechanical properties of the material can be significantly influenced by the existence of point defects, especially for 2D materials. Therefore, investigating the characteristics and behavior of defects in 2D materials under different thermodynamic conditions is crucial for tailoring their properties and developing novel applications. In this section, we show a comprehensive study of the structural and electronic properties of point defects in monolayer transition metal dichalcogenides (MX_2) with M=Mo/W and X=S/Se.

First, we have studied the electronic structure of these monolayers through DFT calculations. In particular, we utilize the hybrid HSE06 exchange correlation functional along with many-body dispersion corrections between atoms that is very important for TMDCs. As such, the energetics and electronic properties of defects in TMDCs are accurately captured. We have investigated the stability of neutral defects within DFT, then we considered the simulation of charged defects, since charged states exert a substantial impact on the stability and characteristics of defects.

The simulation of charged S monovacancy in MoS_2 monolayer was done via charge compensation scheme based on the virtual crystal approximation (VCA). Furthermore, we have found a convincing evidence that this S monovacany has a negative charge when MoS_2 is supported on Au(111) substrate.

Furthermore, for a more realistic analysis of point defects in TMDCs we resort to ab initio atomistic thermodynamics in order to investigate the influence of finite-pressure and finite-temperature vibrational contributions on the stability and transition between defects. Neveretheless, we have proved that the vibrational contributions to the free energy is significant for the studied monolayer and cannot be disregarded as the alteration of the stability transition between adatoms and monovacancies can result in a temperature change of 300-400 K.

Finally, the vibrational fingerprint of defects using tip-enhanced Raman scattering (TERS) images have been investigated. This technique allowed us to probe the vibrational modes of S monovacany in MoS_2 clusters and provided valuable insights into the local environment in the vicinity of the defect and the structural changes in the system. This was not achievable using conventional homogeneous field Raman scattering.

In Figure 4 of the following paper, please note that the legend incorrectly labels the rich and poor conditions. To clarify, in the legend, the blue color corresponds to rich S-conditions, while the red color represents poor S-conditions.

A Hybrid-Density Functional Theory Study of Intrinsic Point Defects in MX$_2$ (M = Mo, W; X = S, Se) Monolayers

Alaa Akkoush, Yair Litman, and Mariana Rossi*

Defects can strongly influence the electronic, optical, and mechanical properties of 2D materials, making defect stability under different thermodynamic conditions crucial for material–property engineering. Herein, an account of the structural and electronic characteristics of point defects in monolayer transition metal dichalcogenides MX$_2$ with M = Mo/W and X = S/Se is investigated through density functional theory using the hybrid HSE06 exchange–correlation functional including many-body dispersion corrections. For the simulation of charged defects, a charge compensation scheme based on the virtual crystal approximation (VCA) is employed. The study relates the stability and the electronic structure of charged vacancy defects in monolayer MoS$_2$ to an explicit calculation of the S monovacancy in MoS$_2$ supported on Au(111), and finds convincing indication that the defect is negatively charged. Moreover, it is shown that the finite-temperature vibrational contributions to the free energy of defect formation can change the stability transition between adatoms and monovacancies by 300–400 K. Finally, defect vibrational properties are probed by calculating a tip-enhanced Raman scattering image of a vibrational mode of a MoS$_2$ cluster with and without an S monovacancy.

1. Introduction

Transition metal dichalcogenide (TMDC) materials are the subject of intense research, motivated by the possibility of realizing and exploiting novel material properties with ease. The chemical composition of these materials is MX$_2$, where M is a transition metal atom from groups IV–X and X are chalcogenide atoms, which are stacked in X–M–X layered structures in the bulk. The layers are bonded by van der Waals interactions and thus easy to exfoliate or grow as single layers. Semiconductor TMDCs with M = Mo, W and X = S, Se exhibit an indirect bandgap that becomes a direct gap at the Brillouin-zone K point in the monolayer limit, as a consequence of quantum confinement.[1,2] In addition, because of the moderate and quasi-2D electronic screening,[3] these materials also present a high exciton binding energy, resulting in stable excitons at elevated temperatures.[4] These characteristics make these materials highly desirable for optoelectronic and many other applications.[5–8]

Defects such as vacancies, intercalation, and substitutional atoms are inevitably present in TMDC monolayers generated by any experimental technique[9,10] and often also created on purpose. Because it is easy to reach a high concentration of defects in these materials and therefore induce significant changes in (opto)electronic properties,[11–13] the literature has given much attention to the characterization of defects in TMDCs.[14–20] The presence of defects can be detrimental or advantageous, depending on the targeted property. To cite a few examples, defect-bound neutral excitons have been shown to form characteristic features in the photoluminescence spectra of monolayer TMDCs[21] and chalcogen vacancies have been connected to the dynamics of grain boundaries that strongly impact electronic transport properties.[22] The presence of defects can also serve as an anchor to dock organic molecules and build robust organic–inorganic interfaces with 2D materials that allow, for example, the fabrication of field-effect transistor biosensors.[9,23]

Numerous theoretical studies, which we discuss throughout this article, were carried out on these systems. These studies have provided a comprehensive understanding of the stability of intrinsic point defects. Nevertheless, a few important aspects still deserve a closer examination, such as the vibrational contributions to the thermodynamic stability at elevated temperatures with accurate density functional theory (DFT) calculations, the impact of including many-body van der Waals corrections in calculations, the charge state of defects on metal-supported TMDCs, and the local vibrational properties related to the presence of defects.

A. Akkoush, M. Rossi
Fritz Haber Institute of the Max Planck Society
Faradayweg 4–6, 14195 Berlin, Germany
E-mail: akkoush@fhi-berlin.mpg.de; alaa.akkoush@gmail.com; mariana.rossi@mpsd.mpg.de

A. Akkoush, M. Rossi
Max Planck Institute for the Structure and Dynamics of Matter
Luruper Chaussee 149, 22761 Hamburg, Germany

Y. Litman
Yusuf Hamied Department of Chemistry
University of Cambridge
Lensfield Road, Cambridge CB2 1EW, UK

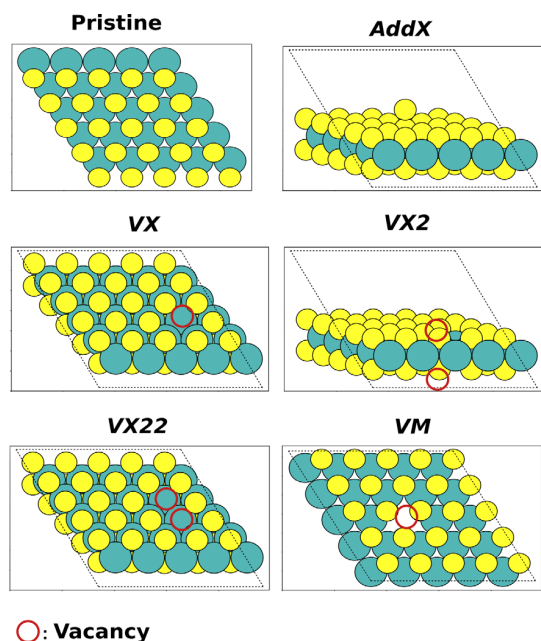The ORCID identification number(s) for the author(s) of this article can be found under https://doi.org/10.1002/pssa.202300180.

In this article, we report our results regarding the thermodynamic stability of neutral and charged point defects in monolayer MoS_2, $MoSe_2$, WS_2, and WSe_2 utilizing DFT with a hybrid exchange–correlation functional (HSE06)[24] and employing many-body van der Waals corrections (MBD).[25] We pay particular attention to the vibrational enthalpic and entropic contributions to the defect formation energies at elevated temperatures. For charged defects, we adopt the virtual crystal approximation (VCA)[26,27] scheme to obtain an effective charge compensation in periodic calculations. We present results with this technique, together with an analysis of the electronic structure of the charged systems and a discussion about the charge state of an S vacancy of monolayer MoS_2 adsorbed on Au(111). Finally, we report an analysis of the variations in space-resolved Raman scattering signals due to an S monovacancy in a MoS_2 cluster.

2. Results and Discussion

2.1. Formation Energies of Point Defects

We have considered monolayer 1H MX_2, where M stands for Mo, W and X for S, Se. We have investigated the following common intrinsic point defects: X monovacancy defects (VX); M monovacancy defects (VM); "up and down" divacancies (VX2), where we removed two X atoms from the top and bottom layers lying on coincident lattice sites; neighboring divacancies (VX22), in which two nearest-neighbor X atoms at the same layer are removed; and X adatoms (AddX), where one X atom is added on top of a host X atom. These defects are shown in **Figure 1**. For VX, we have also considered charged defects $(+1/-1)$, as discussed in Section 4.4.2.

We calculated the formation energies E_f^d as in Equation (1) for the various point defects shown in Figure 1, as a function of the possible chemical potentials of X = S, Se. The chemical potentials μ_X were varied between poor and rich X conditions, as defined in Section 4. We were interested in analyzing the differences between an evaluation of such energies with the PBE + MBD and the HSE06 + MBD functionals. These results are shown in **Figure 2**, where we referenced $\Delta\mu_X = 0$ to the X-rich conditions. Our results agree with results reported previously in the literature, such as the ones presented in refs. [16,17,28,29]. When improving the description of the electronic structure of these systems, by going from the PBE to the HSE06 functional, the energetic hierarchy among the various defects remains the same for all systems. However, the points at which stability transitions are observed change. In particular, for WSe_2 with HSE06 there is no stability transition between AddX and VX toward the poor X conditions. We observe the largest differences in formation energies between PBE and HSE06 for the transition metal vacancies VM in all cases. This observation could be correlated with differences between PBE and HSE06 predicted bandgaps. Among all defects studied here, the PBE bandgaps of VM lie in the range of 0.1–0.4 eV, being the smallest bandgaps of all defects, as shown in Table S3–S7, Supporting Information.
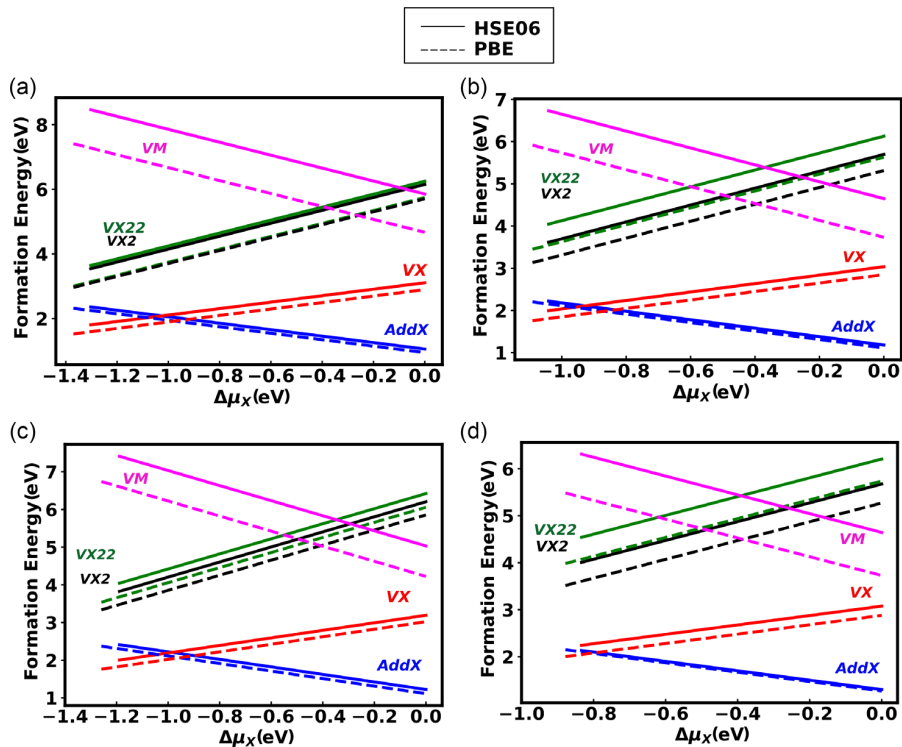
The formation energies of AddX and VX are always lower than those of the other vacancies in either X-rich or M-rich conditions. AddX appears as the most stable out of all neutral point defects at X-rich conditions and over the majority of the possible energy range of μ_X (as also reported in refs. [17,30,31]). As one could expect, the formation energy of divacancies amounts to around twice the formation energy of the monovacancy. However, the results show that for X = Se, the up and down divacancies VSe2 are more favorable than neighboring VSe22 in all investigated TMDCs (in agreement with ref. [29]).

The results presented in this section corroborate most previous work that have investigated defect formation energies in TMDCs.[16,17,29,32,31] The consideration of many-body van der Waals effects, absent in most publications in the literature, shows little impact on these ground-state formation energies.

2.2. Impact of Temperature and Pressure on Defect Stability

In order to obtain more insights on the defect stability at various thermodynamic conditions, we analyzed the connection of the transition points between the most stable defects with temperature and partial pressure. In the calculations, we considered the main contribution of pressure to stem from the chemical potential term, and disregarded lattice expansion effects on the TMDCs. We assume that volume-change contributions will largely cancel when evaluating formation energies. As shown in ref. [16], however, at temperatures above 1000 K, the volume changes can amount to differences of ≈0.2 eV in the formation energies.

We show in **Figure 3** the stability transition lines between VX and AddX for ML MoS_2, $MoSe_2$, and WS_2 as a function of temperature and partial S/Se pressure. We calculate these transitions with and without the temperature-dependent vibrational contributions from the term labeled $\Delta F(T)$ in Equation (11). We do not

Pristine   **AddX**

VX   **VX2**

VX22   **VM**

○: **Vacancy**

Figure 1. The geometries of the point defects under study for MX_2, M = W, Mo and X = Se, S. AddX stands for an X adatom, VX/M stands for X/M monovacancy, VX2 stands for X divacancies at the top and bottom coincident lattice sites, and VX22 stands for X divacancies at neighboring sites. We use these labels to refer to the defects throughout this article. M atoms are green and X atoms are yellow.

Figure 2. Variation of formation energy (eV) of point defects as a function of X chemical potential, referenced with respect to the X-rich conditions. Dashed lines represent formation energies computed with PBE + MBD and solid lines with HSE06 + MBD for a) MoS$_2$, b) MoSe$_2$, c) WS$_2$, and d) WSe$_2$.
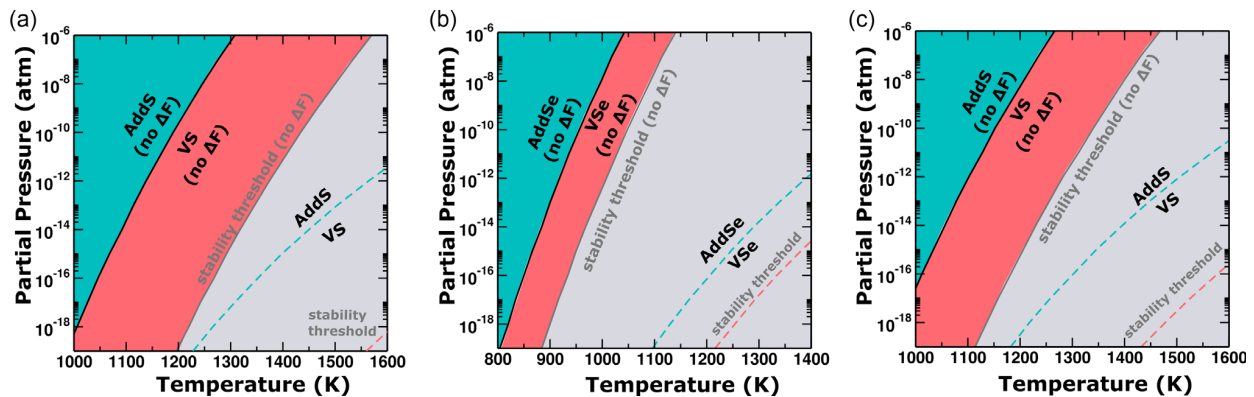
Figure 3. Stability transitions between AddX and VX at different temperatures and partial pressures of S or Se (Equation (12)) for a) MoS$_2$, b) MoSe$_2$, and c) WS$_2$. The full lines represent the boundaries without the vibrational contribution $\Delta F(T)$ and the dashed lines the full formation energy as in Equation (11).

show WSe$_2$ because no stability transition within the boundaries of the chemical potential are predicted for the HSE06 + MBD formation energies. We note that considering a different allotrope for the Se reference could slightly change this picture.

We first focus on the stability ranges obtained without considering the term labeled $\Delta F(T)$ in Equation (11). This term is the vibrational Helmholtz free energy difference between the pristine system and the system containing the defect. This term is commonly disregarded in these calculations because it tends

to be small in more traditional systems.[33] This means that the p, T dependence of the data represented in Figure 3 by the full lines stems only from the terms in Eq. 12. The data presented in Figure 2 are therefore equivalent to the one presented in Figure 3. However, Figure 3 makes it clear that while for MoSe$_2$ the vacancy is stable at much lower temperatures with respect to the S containing systems, its stability range is narrower because the monolayer material ceases to be stable also at lower temperatures when considering equilibrium with the these

reservoirs. The stability range of VS on MoS_2 and WS_2 is larger but starts at higher temperatures. VS in MoS_2 shows the largest temperature stability range.

We then quantify the impact of $\Delta F(T)$ in the defect formation energy of all materials shown in Figure 3. We observe that including ΔF (dashed lines in Figure 3) would increase the transition temperature between AddX and VX by 300–400 K, for a given partial pressure. We note that in this case the boundaries of the chemical potential at each temperature are also different because the temperature-dependent vibrational contributions to the bulk and the monolayer must be included in Equation (9). This naturally raises the question of why AddX defects are rarely observed in experiments. As AddX defects are the most stable over a wide range of temperatures and partial pressures, it may be easy to reach larger concentrations of these defects, making it likely that two or more such defects come into contact. For MoS_2 it was shown by Komsa and Krasheninnikov[16] that as two AddS defects meet, it becomes favorable to desorb a S_2 molecule, especially at elevated temperatures. The increased stability of VX at higher temperatures allied to the proposition that multiple AddX defects can easily desorb could explain why AddS and AddSe are rarely observed in chemical vapor deposition (CVD)-grown TMDCs, while monovacancies are very often observed.[34–36]

Therefore, we note that for monolayer TMDCs the vibrational contributions play an important role on the point defect stability. We note that probably this effect is more pronounced due to the high-temperature regimes relevant for these systems. At lower temperatures, for example, below 600 K, the effect of including or ignoring ΔF is much less pronounced, as exemplified in Figure S4, Supporting Information.

2.3. Charged Monovacancies

Next, we proceeded to analyze defects that carry an electric charge. Because we have established that the qualitative hierarchy of defect formation energies is similar for all systems, we focus on the case of MoS_2. In addition, we consider only charged S monovacancies (VS) because they are the most abundant charged defects appearing in experimentally relevant conditions.[37,38] In **Figure 4** we show the formation energies as calculated from Equation (2), with varying E_f and for $\mu_S = 0.0$ eV
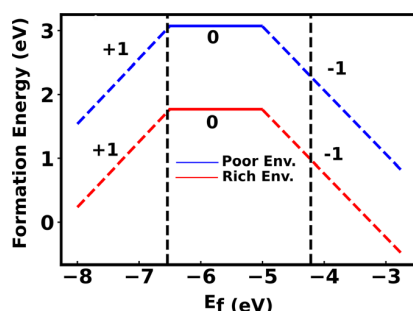
Figure 4. Formation energy of neutral and charged ($q = +1, 0, -1$) VS in MoS_2 computed with HSE06 + MBD as a function of Fermi level (E_f) in the S-rich (blue) and S-poor (red) conditions. E_f is referenced to the vacuum level. The dashed lines mark the position of the VBM and the CBM of the pristine MoS_2 ML.

(rich S) and $\mu_S = -1.3$ eV (poor S). We show the data obtained with the charge compensation scheme discussed in Section 4 including corrections to obtain the dilute limit. We note that we performed spin-polarized calculations for the charged defects.

In the pristine MoS_2 ML, the computed E_{VBM} is at -6.54 eV and the E_{CBM} is at -4.22 eV (HSE06) with respect to the vacuum level. These energies are marked in Figure 4. We observe that the positive charge state is predicted to be stable very close to the VBM (similar to what was reported in refs. [15,16]), while the $(0/-1)$ charge transition level is well within the gap and the negatively charged vacancy is stable for E_f values greater than 1.5 eV above the VBM.

In **Figure 5** we compare the electronic density of states (including spin–orbit coupling) of the pristine MoS_2 monolayer, the neutral S vacancy, and the charged S vacancies. In all cases, we obtain integer occupation of all energy levels and the ground state of the charged defects is a doublet. The results shown for the neutral VS confirm DFT results from other authors,[15,39,40] showing a shallow occupied defect state close to the VBM, and two spin-degenerate unoccupied states in the gap. All these states are of d character and arise from the dangling bonds of the Mo 4d orbitals and the reduced Mo 4d and S 3p orbital hybridization. The splitting between the two unoccupied states is due to spin–orbit coupling. A visualization of the state-resolved electronic density of these defect states is shown in Figure S5, Supporting Information.

We start by discussing the positively charged VS. An unoccupied state with the same character as the shallow occupied state in the neutral VS appears in the gap. This confirms that the orbital that lost one electron is the localized vacancy state, remembering that one spin-channel remains occupied. The vacancy states deep in the gap show a much larger splitting and are not anymore spin-degenerate. As shown in Figure S5, Supporting Information, the states are now grouped by their dominant spin character, and the splitting could be attributed to an exchange interaction with the singly occupied state that lost one electron. We do not observe a structural symmetry breaking around the vacancy. The three Mo atoms around the vacancy form an equilateral triangle with a side length of 3.13 Å. This is consistent with the fact that all vacancy states show the same character as they had in the neutral case, as shown in Figure S5, Supporting Information. It is worth noting that this geometry is, nevertheless, different from the neutral vacancy, where the equilateral triangle defined by the three neighboring Mo atoms surrounding the vacancy has a side of length 3.04 Å in our calculations.

The negatively charged S monovacancy causes a pronounced symmetry breaking on the electronic and atomic structure, characteristic of the Jahn–Teller effect, as discussed previously in ref. [15]. Whereas in ref. [15] the authors employed GGA and metaGGA functionals, we here corroborate the results with HSE06 and the inclusion of many-body vdW corrections. The structural distortion causes the Mo atoms close to the vacancy to form a isosceles triangle where two sides measure 3.04 Å and one side measures 3.16 Å. The occupied shallow defect state in the neutral case loses its spin degeneracy and one spin channel moves in the gap. The four unoccupied defect states from the neutral vacancy present mixed characters, as shown in Figure S5, Supporting Information, and one of them is fully occupied. The other three (unoccupied) states are found very close to the CBM of the bulk material.
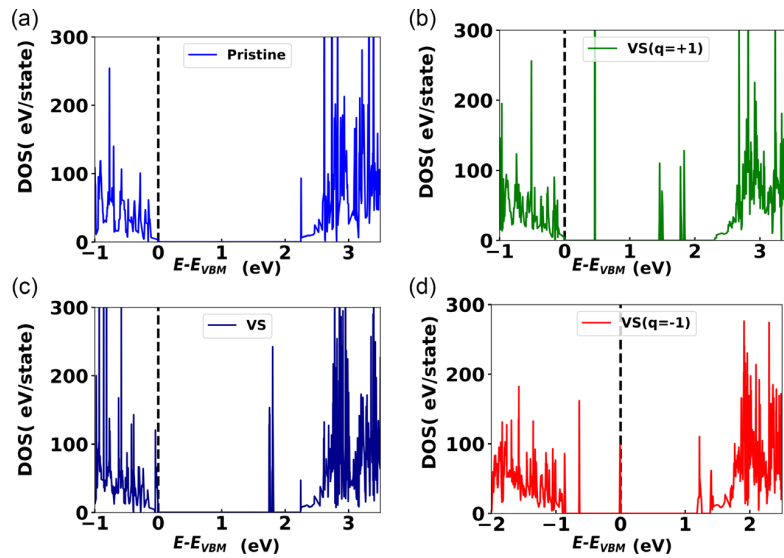
Figure 5. Electronic density of states calculated with the HSE06 functional for a) pristine MoS_2, b) MoS_2 with a positively charged VS ($q = +1$), c) MoS_2 with a neutral VS and d) MoS_2 with a negatively charged VS ($q = -1$).

The calculated stability of the defects and the electronic structure predicted in the calculations are consistent. For completeness, we report the density of states of all neutral point defects under study for MoS_2, $MoSe_2$, WS_2, and WSe_2 computed with HSE06 + MBD including SOC in Figure S6–S9, Supporting Information.

2.4. MoS₂ Monovacancy on Au(111)

In several situations of interest, MoS_2 is supported on an Au(111) substrate.[41,42] The bulk Au Fermi energy is calculated to be $-4.95\,eV$ with HSE06 and the basis sets used here, and therefore, it could act as a donating electron reservoir that stabilizes a negatively charged vacancy on MoS_2. Explicitly simulating the MoS_2 monolayer supported by a Au(111) slab requires the use of large supercells in order to minimize the strain induced by the lattice mismatch. We have considered a 8×8 supercell of MoS_2 on a 4-layer 9×9 Au(111) supercell, containing one S vacancy on the vacuum-facing side of MoS_2 (515 atoms), as shown in Figure 4. The MoS_2 ML is stretched by 4.8% in each direction considering HSE06 lattice constants, which induces a small but non-negligible strain on the sheet. However, reducing this number to 1% would require a 12×12 supercell of MoS_2 on a 4-layer 13×13 Au(111) surface, at which point the system becomes too large for obtaining results at this level of theory. We fully relaxed this structure with the HSE06 + MBD (same settings as previously in this article), including spin polarization. We fixed the two bottom Au layers during relaxation. Electronic density of states was calculated with a $4 \times 4 \times 1$ k-point grid for increased accuracy. Fully converging the self-consistent field (SCF) cycle for this structure with HSE06 functional and the FHI-aims code took around 20 h when parallelized over 2304 cores in the MPCDF Raven machine (Intel Xeon IceLake-SP 8360Y). We could not apply spin–orbit coupling corrections to this structure with this functional due to technical memory issues.

We observe a Moiré pattern formation and a nonuniform distance between the MoS_2 layer and Au(111), as also reported in ref. [42] where they studied similar systems with the PBE functional and dispersion corrections. In this article we are interested in understanding whether this vacancy can be considered negatively charged. We confirm that the structure is magnetic and the states with largest spin asymmetries are those of the d-orbitals of the Mo atoms around the vacancy. We also observe the tell-tale sign of the pronounced structural distortion around the vacancy,
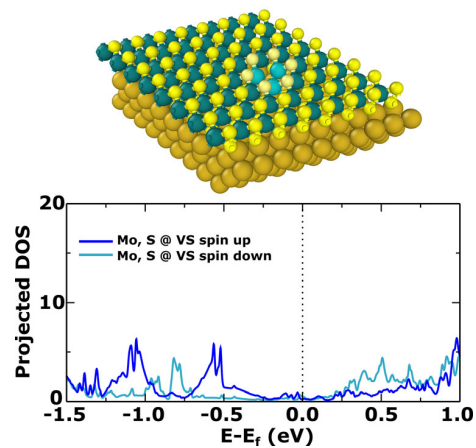
Figure 6. Top: Structure of the 8×8 supercell of MoS_2 on a 4-layer 9×9 Au(111), where we highlight the Mo and S atoms around the vacancy. Bottom: Projected electronic density of states on the highlighted atoms around the vacancy for spin up and spin down channels. Zero represents the Fermi level of the calculation (defined by the states from the Au surface, not shown), above that the states are unoccupied.

with the Mo atoms forming an isosceles triangle with two sides of 3.36 Å and one shorter side of 3.04 Å. Finally, when analyzing the electronic density projected solely on the atoms surrounding the vacancy, as marked and shown in **Figure 6**, we observe occupied states that can be assigned to the vacancy at about -0.5 eV, and we confirmed that they are of Mo d character. These states are also singly occupied, as evidenced by the pronounced spin asymmetry between the channels in this region. All of these observations, connected to the discussions in the previous section, point toward a negatively charged vacancy.

Without further analysis we cannot ascertain the amount of negative charge at the vacancy. Based on the current data we suppose it is at $a-1$ charge state. Previous studies that considered $a-2$ charge state did not find it stable for the monolayer.[16] We note that the structural symmetry breaking is more pronounced and different than the one observed for VS(-1) in free-standing MoS$_2$ in the previous section, which could be due to the structural strain in this case, or indeed a different charge state. We also note that the metallic substrate is known to induce a considerable gap renormalization on the TMDC monolayers due to screening.[43] A reduction of the bandgap would likely favor the VS(-1) state. Further studies addressing some of these shortcomings and reducing the cost of these large calculations will be the subject of a future work.

2.5. Local Vibrational Fingerprints

Raman spectroscopy is a widely used method to characterize the fundamental vibrational properties of 2D materials.[44] We were interested in exploring the feasibility of using tip-enhanced Raman scattering (TERS) signals to obtain a local description of vibrational properties of the vacancies. The cluster models we use for these calculations do not show the characteristic Raman active E_{2g}^1 (in-plane vibrations) and A_{1g} (out-of-plane vibrations) vibrational modes of monolayer MoS$_2$[44,45] due to local distortions, but many modes with similar characteristics are present. We show the nonresonant harmonic Raman spectra of the pristine cluster, and the one containing the vacancy in **Figure 7**. The Raman intensities shown in Figure 7 were calculated considering only the square of the variation of α_{zz}
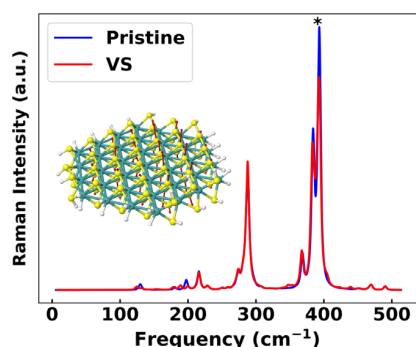
Figure 7. Raman spectra of the MoS$_2$ cluster with and without the sulfur vacancy. The mode shown in the inset is the one marked with an asterisk for the pristine cluster. The mode resembles the A_{1g} mode of the periodic structure.

component of the polarizability tensor with respect to the normal modes of the system. The cluster was oriented such that the z axis was perpendicular to the surface plane. Because of the presence of the edges, the clusters show many active Raman modes. The most intense peak for both systems, lying at 393 cm^{-1}, corresponds to a mode that resembles the A_{1g} mode in the periodic structure, and this is the mode that we chose to further characterize by means of a simulation of spatially resolved TERS.

We calculated the tip-enhanced Raman intensity according to the methodology proposed in ref. [46], over a region of 9×9 Å^2 covering the defect area. These results are presented in **Figure 8**. We observe that while the Raman spectra of the systems with and without the vacancy shown in Figure 7 are very similar, the TERS signals of the pristine system and the vacancy-containing system are substantially different around the vacancy, despite their very similar frequency and overall character. This result shows the possibility of identifying specific vibrational fingerprints of defects in 2D materials even at low defect concentrations.

We note that our calculations do not include excitonic states, but these could be included, at least approximately, by performing linear-response time-dependent (TD)-DFT calculations with an appropriate functional,[47] instead of density functional perturbation theory calculations within this method. Probably, such a combination would still be considerably more efficient than a full real-time TD-DFT calculation of the TERS signal.

3. Conclusions

We presented a hybrid DFT study of point defects on semiconductor TMDC monolayers MX$_2$. An analysis of the ground-state formation energy of neutral defects showed that adatom defects are the most stable defects at X-rich conditions and through a wide range of chemical potentials. TMDCs containing X = S show a small range of S monovacancy stability toward S poor conditions, while this range is reduced for TMDCs containing X = Se. A comparison of these formation energies obtained with the PBE + MBD and the HSE06 + MBD functionals shows that only quantitative changes in the energy hierarchy of defect formation energies take place. The largest difference was observed for the Mo and W monovacancies, which could be correlated with the extremely small bandgap predicted by PBE + MBD for these systems. Comparing the results obtained in this study and previous results in the literature that did not employ many-body van der Waals corrections, we also conclude that these have a minor quantitative impact on formation energies. This is not surprising because the main contribution to the defect formation energy in monolayer TMDCs stems from breaking or making covalent bonds. These corrections could have a larger impact in multilayered systems.

Analyzing the transitions between VX and AddX at temperature versus partial pressure diagrams, we concluded that VS is the most stable defect only at very elevated temperatures ($>$1000 K) for a wide range of partial pressures. VSe is stable at lower temperatures, but its temperature stability range is narrower due to the threshold imposed by the equilibrium with the reservoirs. We also explicitly quantified the effect of vibrational
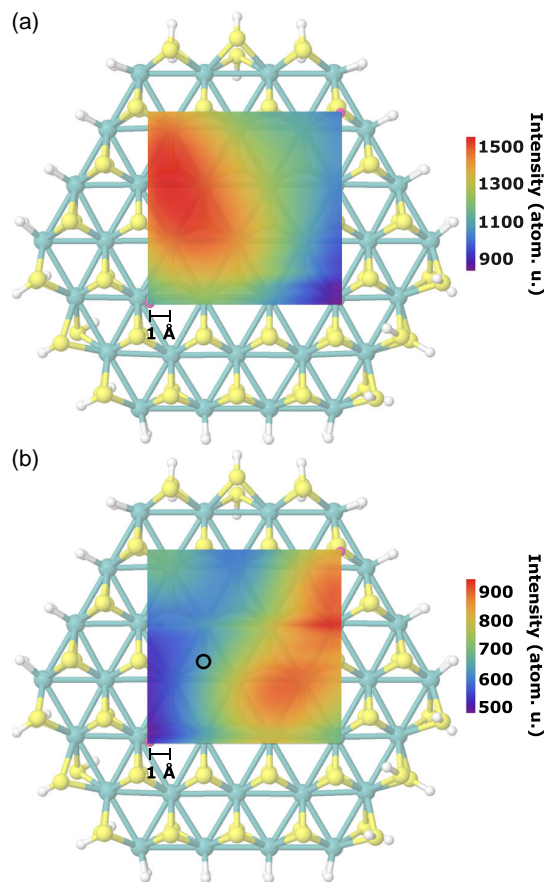
Figure 8. TERS image of the vibrational modes labeled with an asterisk in Figure 7 in the MoS$_2$ cluster corresponding. a) Pristine system. b) System including the S monovacancy. The position of the S vacancy is marked with a black circle and the pink dots are just visual markers to delimit the image area. Intensities are reported taking into account only the term corresponding to the polarizability variation.

contributions of the TMDC to the formation free energy. We find that these contributions stabilize AddX defects and destabilize VX defects. Disregarding such contributions would lead to a prediction of the stability crossover points between AddX and VX that would be underestimated by 300–400 K in all materials—an effect probably exacerbated by the high temperatures at which this transition occurs. These elevated temperatures are nevertheless relevant for some TMDC growth techniques such as chemical vapor deposition.

For charged defects, we find that the virtual crystal approximation (VCA) in an all-electron electronic structure infrastructure is a simple and powerful technique that allows the simulation of charged defects in these 2D systems within a periodic 3D setup. We combined it with a straightforward extrapolation correction for the remaining lateral interactions between charged defects to reach the dilute limit. With this technique, we could confirm the stability of the negatively charged S vacancy in MoS$_2$ with a (0/−1) charge transition level within the gap, and characterized the accompanying Jahn–Teller distortion at the electronic and the atomic structure levels. We then analyzed the electronic and atomic structure of the S monovacancy on a MoS$_2$ monolayer supported on Au(111)

with the HSE06 + MBD functional. This analysis and a comparison to the results of the S monovacancy in the free-standing monolayer led us to conclude that the vacancy is negatively charged in this structure. The VCA scheme can be extended to mimic the charge compensation at the Au substrate instead of within the layer and this is the subject of ongoing work. Many of the techniques discussed here could be used in a high-throughput workflow to augment or complement existing data in databases of defects in 2D materials.[19]

In the future, we plan to conduct a deeper analysis of the specific phonon modes that play a role on the stabilization and destabilization of different defects, and their real-space characteristics. In that respect, the exploratory tip-enhanced Raman scattering calculations presented in this work are very encouraging. We believe that a better characterization of the local Raman signal around defects in 2D materials and the possibility of a direct experiment-theory comparison in real space can give unique insights into the atomic motions that accompany charge localization, exciton trapping, and polaron formation. We consider such insights particularly interesting to guide the chemical design of organic–inorganic interfaces based on 2D materials for optoelectronic and sensor technologies.

4. Computational Section

Basic Parameters: Our calculations have been performed using the FHI-aims[48] program package and periodic boundary conditions. In order to approximate the dilute limit, we aimed at minimizing the interaction between defects in neighboring supercell images. As shown in Figure S1, Supporting Information, the variation of the defect formation energy between a 5×5 supercell and a 7×7 supercell did not exceed 0.03 eV in all studied monolayers. As discussed in the next section, for MoS_2 further corrections to the infinite-size limit brought a further 10 meV correction. We thus chose a 5×5 supercell to perform most calculations in this work and added a vacuum region of around 100 Å to decouple periodic images in the direction perpendicular to the monolayer surfaces. For charged defects we employ further corrections, as explained in section 4.2.

Electronic structure properties and geometry optimizations were obtained with the Perdew, Burke, and Ernzerhof (PBE)[49] and the HSE06 exchange–correlation functional as proposed by Heyd, Scuseria and Ernzerhof[50,51] with 25% exact exchange and the screening parameter $\omega = 0.11$ Bohr^{-1}. Van der Waals (VDW) interactions were accounted for using a many-body dispersion (MBD) model[52] (HSE06 + MBD and PBE + MBD). We performed spin polarized calculations and employed intermediate defaults for basis sets and numerical grid settings in the FHI-aims code.[53] A k-grid of $4 \times 4 \times 1$ was used for geometry optimizations, total energy evaluations and electronic-structure property calculations. We have included the effect of spin–orbit coupling, known to substantially affect the energy bands of TMDCs.[54] We employed a "post-processing" correction, applied only after the electronic ground state density is converged.[55] The HSE06 + MBD optimized (experimental) in-plane lattice constants of MoS_2, $MoSe_2$, WS_2, and WSe_2 primitive cells are 3.14 (3.16[56]), 3.26 (3.30[56]), 3.16 (3.15[57]), and 3.27 (3.28[57]) Å, respectively. To calculate phonons, the PBE + MBD functional in FHI-aims was employed with "tight" computational settings. The same van der Waals corrections as mentioned earlier (PBE + MBD) were applied. These settings allowed for the determination of vibrational contributions to the formation energy of defects.

TERS signals were computed using density functional perturbation theory (DFPT) with the local-density approximation (LDA) functional to compute the density response with respect to a localized electric near-field produced from the response of an Ag tetrahedral tip to an external electric field (**Figure 9**a). Details of the methodology are presented in ref. [46]. Technical problems prevent the near-field response calculation of periodic systems in FHI-aims, thus we employed a cluster approximation. To find a suitable cluster model, we investigated three possible structure forms: hexagonal, rhombic, and triangular (details in Supporting Information), with different types of hydrogen passivation at the edges. We fixed the positions of the Mo atoms at the edges of the clusters at their bulk positions. The choice of the clusters is motivated
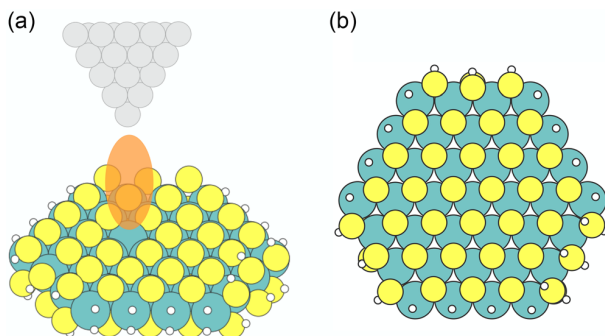
Figure 9. a) Schematic drawing of a TERS setup with an Ag tetrahedral tip over a vacancy defect on an MoS_2 cluster. The orange ellipse denotes the local electric field. b) Geometry of the MoS_2 cluster used in this study for the calculation of the TERS signals. White circles denote hydrogen atoms.

by studies in the literature such as refs. [58,59], where MoS_2 nanoclusters grown on Au(111) were characterized. We selected the cluster with the widest bandgap upon optimization at the PBE + MBD level. This was a hexagonal cluster of 109 atoms of Mo and S with ≈43% S coverage on the edges shown in Figure 7b. Moreover, we confirmed that passivating the cluster edges increased the energy gaps between the highest occupied and the lowest unoccupied molecular orbital due to the removal of the dangling bonds, as previously discussed in a DFT study that explored different sizes of MoS_2 nanoflakes.[60]

Defect Formation Energy: The formation energy of a defect can provide information about their stability under different thermodynamic conditions. We define this formation energy for neutral defects E_f^d as follows

$$E_f^d = E_d(n_i + \Delta n_i) - E_p(n_i) - \sum_i \Delta n_i \mu_i, \tag{1}$$

where E_d and E_p are the total energy of the defective system and the pristine system, respectively, μ_i is the chemical potential, and Δn_i is the number of atoms of type i that have been added/removed.

For charged defects, the formation energy gains an extra term that accounts for the equilibrium with an electron reservoir (Fermi energy)

$$E_f^d = E_d(n_i + \Delta n_i) - E_p(n_i) - \sum_i \Delta n_i \mu_i + q E_f \tag{2}$$

where q is the electron charge and E_f is effectively an adjustable parameter that depends on the specific conditions under consideration, and is computed relative to the valence band maximum (VBM) of the defect-free system. We only considered charged defects consisting of X vacancies.

In simulations of charged defects in (free standing) 2D materials using supercells with 3D periodic boundary conditions, we encounter the challenge of performing a charge compensation technique that does not generate spurious interactions. If such interactions do arise, they must be corrected.[61–64] The virtual-crystal approximation (VCA)[26,27,65] has been successful in simulating charged defects at bulk systems and surfaces in the past, and removes the spurious interaction of the charged defect with a homogeneous compensating background charge in surface or 2D-material simulations. In this approximation, when working in an all-electron code like FHI-aims, we modify the nuclear charges ($Z' = Z + \Delta Z$) of certain atoms to modify the number of effective electrons in the system, while the simulation as a whole remains neutral. The nuclear charges are modified as the following

$$\Delta Z = \begin{cases} + \frac{|q|}{N} & \text{for n} - \text{type doping} \\ - \frac{|q|}{N} & \text{for p} - \text{type doping} \end{cases} \tag{3}$$

where $|q|$ is the absolute value of the desired defect charge of the defect and N is the number of atoms for which the nuclear charge is modified. We note that when doping the system in this manner, the reference energies of the pristine and defected systems appearing in the expression of Equation (2) must be calculated with the same conditions of doping to give a consistent reference. Here, we compensate charges within the TMDC monolayer (ML) itself by modifying the nuclear charge of transition metal atoms through the VCA recipe. We correct the remaining lateral interactions of the charged defects by performing VCA calculations for increasing $L \times L$ supercells with $L = 4, 5, 6, 7, 10$ at the PBE + MBD level, fitting a $E_f^d(\infty) + b/L + c/L^2 + d/L^3$ function to the formation energies.[26] This correction is added to the HSE06 + MBD formation energies calculated with the 5×5 supercell and amounts to about -30 meV for neutral S vacancies and $+200$ meV for the charged S vacancies as shown in Figure S2, Supporting Information.

In all expressions above, the chosen values of the chemical potential μ_i are central to the formation energy analysis. We discuss how to model them in the section below.

Boundaries of Chemical Potentials μ: ML of TMDCs can exist in different conditions of excess of a particular constituent atom. In the calculations, we take these possible environments into account by varying the chemical potential μ_i between two extremes: rich X (poor M) and poor X (rich M) conditions.

For MX_2 MLs, one can consider the thermodynamic equilibrium conditions as

$$\mu_M + 2\mu_X = E_{MX_2}^{ML}$$
$$\mu_X = \frac{1}{2}\left(E_{MX_2}^{ML} - \mu_M\right) \tag{4}$$

where $E_{MX_2}^{ML}$ refers to the total energy of the primitive unit cell. The lower bound of μ_X takes place for M-rich conditions, here modeled by the chemical potential (atomization energy) of M in a bulk BCC structure $\mu_M = \mu_M^{Bulk}$. With that we obtain

$$\mu_X^{min} = \frac{1}{2}\left(E_{MX_2}^{ML} - \mu_M^{Bulk}\right) \tag{5}$$

The upper bound of μ_X (X-rich environment) is taken as the chemical potential of X in an 8-membered homoatomic ring molecule. This is a common reference in the literature.[66,67] The S_8 ring is a predominant S allotrope in the solid and gas phase,[68] while Se_8 is one of three predominately reported Se allotropes in the literature.[69,70]

Therefore

$$\mu_X^{max} = \frac{1}{8}E_{S_8/Se_8} \tag{6}$$

These considerations lead us to

$$\mu_M^{min} = \left(E_{MX_2}^{ML} - 2\mu_X\right) \tag{7}$$

We note that the expressions above automatically determine the boundaries of μ_M. The final boundaries of chemical potentials that we consider are

$$E_{MX_2}^{ML} - 2(E_{S_8/Se_8}/8) \leq \mu_M \leq \mu_M^{Bulk} \tag{8}$$

and

$$\frac{1}{2}\left(E_{MX_2}^{ML} - \mu_M^{Bulk}\right) \leq \mu_X \leq E_{S_8/Se_8}/8 \tag{9}$$

The ranges of chemical potentials $(\mu_X - \mu_X^{max})$ that we have considered for each system are shown in **Table 1**.

Temperature and Pressure Contributions to Formation Energy: In the following, we consider the temperature and partial pressure contributions on the defect formation energies. We consider the Gibbs energy of formation as $G(p,T) = F(V,T) + pV = E - TS + pV$, where F is the Helmholtz free energy, V is the total volume of the system, p stands for pressure, T is the temperature, and S is the entropy. The free energy of defect formation (here considering the case of neutral defects) is given by[61,71]

$$G_f^d(p,T) = G_d(p,T) - G_p(p,T) - \sum_i \Delta n_i \mu_i(p,T) \tag{10}$$

We consider harmonic vibrational contributions to the Helmholtz vibrational free energy $F(T)$, and a fixed volume. For the reference molecules (chemical potential) we take all vibrational frequencies ω_i and for the periodic systems we consider those at the Γ point of the Brillouin zone of the system supercell. Separating this term explicitly in Equation (10) we obtain

$$G_f^d(p,T) = \Delta E + \Delta F(T) - \sum_i \Delta n_i \mu_i(p,T) \tag{11}$$

where ΔE is the difference between defect and the pristine ground state total energy and $\Delta F(T)$ is the difference between the respective Helmholtz free energies. For the chemical potential $\mu_i(T,p)$, we can approximate the partition functions of the rotational, translational and vibrational degrees of freedom of the reference molecular reservoir.[72] This leads to the previously reported expressions[61,71]

$$\begin{aligned}
\mu(p,T) = \frac{1}{N_{at}}\Bigg\{ &-kT\ln\left[\left(\frac{2\pi M}{h^2}\right)^{\frac{3}{2}}\frac{(kT)^{\frac{5}{2}}}{p_0}\right] - kT\ln\left(\frac{\pi^{\frac{1}{2}}}{\sigma}\right) \\
&-kT\ln\left[\left(\frac{8\pi kT}{h^2}\right)^{\frac{3}{2}}I_A^{\frac{1}{2}}I_B^{\frac{1}{2}}I_C^{\frac{1}{2}}\right] + kT\sum_i \ln\left[1 - \exp\left(-\frac{\hbar\omega_i}{kT}\right)\right] \\
&+kT\ln\frac{p}{p_0} + E_{ref} + \sum_i \frac{\hbar\omega_i}{2}\Bigg\}
\end{aligned} \tag{12}$$

where N_{at} is the number of atoms in the molecule or unit cell, M is the total mass of the molecule, ω_i are the harmonic vibrational frequencies, p is the partial pressure of the species for which the chemical potential is being calculated, σ is a molecule-dependent symmetry factor, and I are the moments of inertia along the principle axis of rotation of the molecule. The rotational and translational terms are absent for solid-state references. We take $p_0 = 1$ atm and E_{ref} as the atomization energy of the chemical species under consideration, for the given standard reference. For S and Se our standard references were the S_8 and Se_8 molecules in the gas phase and for Mo and W, the BCC bulk structure. We note that other gas-phase allotropes of S and Se are more stable at elevated temperatures.[68]

Supporting Information

Supporting Information is available from the Wiley Online Library or from the author.

Acknowledgements

Conflict of Interest

The authors declare no conflict of interest.

Data Availability Statement

The data showcased in this paper can be accessed in the NOMAD Lab database under the DOI address https://doi.org/10.17172/NOMAD/2023.04.29-1.

Keywords

Table 1. Lower boundaries of $\frac{1}{2}\Delta\mu_M^{min} = \Delta\mu_X^{min} = \frac{1}{2}(E_{MX_2}^{ML} - \mu_M^{Bulk}) - E_{X_8}/8$ for the TMDCs under study using HSE06 + MBD (PBE + MBD). Values are in eV.

	MoS_2	$MoSe_2$	WS_2	WSe_2
$\Delta\mu_X^{min}$	−1.30 (−1.37)	−1.04 (−1.09)	−1.19 (−1.26)	−0.83 (−0.88)

[1] K. F. Mak, C. Lee, J. Hone, J. Shan, T. F. Heinz, *Phys. Rev. Lett.* **2010**, *105*, 136805.

[2] A. Splendiani, L. Sun, Y. Zhang, T. Li, J. Kim, C.-Y. Chim, G. Galli, F. Wang, *Nano Lett.* **2010**, *10*, 1271.

[3] K. S. Thygesen, *2D Mater.* **2017**, *4*, 022004.

[4] M. M. Ugeda, A. J. Bradley, S.-F. Shi, F. H. Da Jornada, Y. Zhang, D. Y. Qiu, W. Ruan, S.-K. Mo, Z. Hussain, Z.-X. Shen, F. Wang, S. G. Louie, M. F. Crommie, *Nat. Mater.* **2014**, *13*, 1091.

[5] J. S. Ross, P. Klement, A. M. Jones, N. J. Ghimire, J. Yan, D. Mandrus, T. Taniguchi, K. Watanabe, K. Kitamura, W. Yao, D. H. Cobden, X. Xu, *Nat. Nanotechnol.* **2014**, *9*, 268.

[6] H. Zeng, J. Dai, W. Yao, D. Xiao, X. Cui, *Nat. Nanotechnol.* **2012**, *7*, 490.

[7] Y. Yoon, K. Ganapathi, S. Salahuddin, *Nano Lett.* **2011**, *11*, 3768.

[8] S. Park, H. Wang, T. Schultz, D. Shin, R. Ovsyannikov, M. Zacharias, D. Maksimov, M. Meissner, Y. Hasegawa, T. Yamaguchi, S. Kera, A. Aljarb, M. Hakami, L. Li, V. Tung, P. Amsalem, M. Rossi, N. Koch, *Adv. Mater.* **2021**, *33*, 2008677.

[9] Z. Lin, B. R. Carvalho, E. Kahn, R. Lv, R. Rao, H. Terrones, M. A. Pimenta, M. Terrones, *2D Mater.* **2016**, *3*, 022002.

[10] S. Ding, F. Lin, C. Jin, *Nanotechnology* **2021**, *32*, 255701.

[11] S. Tongay, J. Suh, C. Ataca, W. Fan, A. Luce, J. S. Kang, J. Liu, C. Ko, R. Raghunathanan, J. Zhou, F. Ogletree, J. Li, J. C. Grossman, J. Wu, *Sci. Rep.* **2013**, *3*, 2657.

[12] W. Zhou, X. Zou, S. Najmaei, Z. Liu, Y. Shi, J. Kong, J. Lou, P. M. Ajayan, B. I. Yakobson, J.-C. Idrobo, *Nano Lett.* **2013**, *13*, 2615.

[13] A. McCreary, A. Berkdemir, J. Wang, M. A. Nguyen, A. L. Elías, N. Perea-López, K. Fujisawa, B. Kabius, V. Carozo, D. A. Cullen, T. E. Mallouk, J. Zhu, M. Terrones, *J. Mater. Res.* **2016**, *31*, 931.

[14] Q. Liang, Q. Zhang, X. Zhao, M. Liu, A. T. S. Wee, *ACS Nano* **2021**, *15*, 2165.

[15] A. M. Z. Tan, C. Freysoldt, R. G. Hennig, *Phys. Rev. Mater.* **2020**, *4*, 064004.

[16] H.-P. Komsa, A. V. Krasheninnikov, *Phys. Rev. B* **2015**, *91*, 125304.

[17] K. C. Santosh, R. C. Longo, R. Addou, R. M. Wallace, K. Cho, *Nanotechnology* **2014**, *25*, 375703.

[18] Y.-C. Lin, S. Li, H.-P. Komsa, L.-J. Chang, A. V. Krasheninnikov, G. Eda, K. Suenaga, *Adv. Funct. Mater.* **2018**, *28*, 1704210.

[19] F. Bertoldo, S. Ali, S. Manti, K. S. Thygesen, *npj Comput. Mater.* **2022**, *8*, 56.

[20] C. Murray, C. van Efferen, W. Jolie, J. A. Fischer, J. Hall, A. Rosch, A. V. Krasheninnikov, H.-P. Komsa, T. Michely, *ACS Nano* **2020**, *14*, 9176.

[21] P. K. Chow, R. B. Jacobs-Gedrim, J. Gao, T.-M. Lu, B. Yu, H. Terrones, N. Koratkar, *ACS Nano* **2015**, *9*, 1520.

[22] J. Lin, S. T. Pantelides, W. Zhou, *ACS Nano* **2015**, *9*, 5189.

[23] P. Fathi-Hafshejani, N. Azam, L. Wang, M. A. Kuroda, M. C. Hamilton, S. Hasim, M. Mahjouri-Samani, *ACS Nano* **2021**, *15*, 11461.

[24] A. V. Krukau, O. A. Vydrov, A. F. Izmaylov, G. E. Scuseria, *J. Chem. Phys.* **2006a**, *125*, 224106.

[25] J. Hermann, A. Tkatchenko, *Phys. Rev. Lett.* **2020a**, *124*, 146401.

[26] N. A. Richter, S. Sicolo, S. V. Levchenko, J. Sauer, M. Scheffler, *Phys. Rev. Lett.* **2013**, *111*, 045502.

[27] N. A. Richter, Ph.D. Thesis, Technische Universität Berlin **2014**.

[28] N. Guo, X. Fan, Z. Chen, Z. Luo, Y. Hu, Y. An, D. Yang, S. Ma, *Comput. Mater. Sci.* **2020**, *176*, 109540.

[29] D. Yang, X. Fan, F. Zhang, Y. Hu, Z. Luo, *Nanoscale Res. Lett.* **2019**, *14*, 1.

[30] S. Haldar, H. Vovusha, M. K. Yadav, O. Eriksson, B. Sanyal, *Phys. Rev. B* **2015**, *92*, 235408.

[31] W.-F. Li, C. Fang, M. A. van Huis, *Phys. Rev. B* **2016**, *94*, 195425.

[32] H. Shu, D. Zhou, F. Li, D. Cao, X. Chen, *ACS Appl. Mater. Interfaces* **2017**, *9*, 42688.

[33] J. Rogal, K. Reuter, Experiment, Modeling and Simulation of Gas Surface Interactions for Reactive Flows in Hypersonic Flights, 2–1 – 2–18, **2007**.

[34] X. Ling, Y.-H. Lee, Y. Lin, W. Fang, L. Yu, M. S. Dresselhaus, J. Kong, *Nano Lett.* **2014**, *14*, 464.

[35] X. Wang, Y. Gong, G. Shi, W. L. Chow, K. Keyshar, G. Ye, R. Vajtai, J. Lou, Z. Liu, E. Ringe, B. K. Tay, P. M. Ajayan, *ACS Nano* **2014**, *8*, 5125.

[36] J. Hong, Z. Hu, M. Probert, K. Li, D. Lv, X. Yang, L. Gu, N. Mao, Q. Feng, L. Xie, J. Zhang, D. Wu, Z. Zhang, C. Jin, W. Ji, X. Zhang, J. Yuan, Z. Zhang, *Nat. Commun.* **2015**, *6*, 6293.

[37] P. D. Cunningham, K. M. McCreary, A. T. Hanbicki, M. Currie, B. T. Jonker, L. M. Hayden, *J. Phys. Chem. C* **2016**, *120*, 5819.

[38] H. Nan, Z. Wang, W. Wang, Z. Liang, Y. Lu, Q. Chen, D. He, P. Tan, F. Miao, X. Wang, J. Wang, Z. Ni, *ACS Nano* **2014**, *8*, 5738.

[39] B. Zhao, C. Shang, N. Qi, Z. Chen, Z. Chen, *Appl. Surf. Sci.* **2017**, *412*, 385.

[40] K. Santosh, R. C. Longo, R. Addou, R. M. Wallace, K. Cho, *Nanotechnology* **2014**, *25*, 375703.

[41] N. Krane, C. Lotze, K. J. Franke, *Surf. Sci.* **2018**, *678*, 136.

[42] F. Tumino, C. S. Casari, A. L. Bassi, S. Tosoni, *J. Phys. Chem. C* **2020**, *124*, 12424.

[43] M. H. Naik, M. Jain, *Phys. Rev. Mater.* **2018**, *2*, 084002.

[44] W. M. Parkin, A. Balan, L. Liang, P. M. Das, M. Lamparski, C. H. Naylor, J. A. Rodríguez-Manzo, A. C. Johnson, V. Meunier, M. Drndic, *ACS Nano* **2016**, *10*, 4134.

[45] S. Gupta, A. Johnston, S. Khondaker, *J. Appl. Phys.* **2022**, *131*, 164303.

[46] Y. Litman, F. P. Bonafé, A. Akkoush, H. Appel, M. Rossi, **2022**.

[47] Y.-M. Byun, J. Sun, C. A. Ullrich, *Electron. Struct.* **2020**, *2*, 023002.

[48] V. Blum, R. Gehrke, F. Hanke, P. Havu, V. Havu, X. Ren, K. Reuter, M. Scheffler, *Comput. Phys. Commun.* **2009**, *180*, 2175.

[49] J. P. Perdew, K. Burke, M. Ernzerhof, *Phys. Rev. Lett.* **1996**, *77*, 3865.

[50] J. P. Perdew, M. Ernzerhof, K. Burke, *J. Chem. Phys.* **1996**, *105*, 9982.

[51] A. V. Krukau, O. A. Vydrov, A. F. Izmaylov, G. E. Scuseria, *J. Chem. Phys.* **2006b**, *125*, 224106.

[52] J. Hermann, A. Tkatchenko, *Phys. Rev. Lett.* **2020b**, *124*, 146401.

[53] S. V. Levchenko, X. Ren, J. Wieferink, R. Johanni, P. Rinke, V. Blum, M. Scheffler, *Comput. Phys. Commun.* **2015**, *192*, 60.

[54] Z. Y. Zhu, Y. C. Cheng, U. Schwingenschloegl, *Phys. Rev. B* **2011**, *84*, 153402.

[55] W. P. Huhn, V. Blum, *Phys. Rev. Mater.* **2017**, *1*, 033803.

[56] T. Böker, R. Severin, A. Müller, C. Janowitz, R. Manzke, D. Voß, P. Krüger, A. Mazur, J. Pollmann, *Phys. Rev. B* **2001**, *64*, 235305.

[57] W. J. Schutte, J. L. De Boer, F. Jellinek, *J. Solid State Chem. France* **1987**, *70*, 207.

[58] J. V. Lauritsen, J. Kibsgaard, S. Helveg, H. Topsøe, B. S. Clausen, E. Lægsgaard, F. Besenbacher, *Nat. Nanotechnol.* **2007**, *2*, 53.

[59] S. S. Grønborg, N. Salazar, A. Bruix, J. Rodríguez-Fernández, S. D. Thomsen, B. Hammer, J. V. Lauritsen, *Nat. Commun.* **2018**, *9*, 2211.

[60] M. Javaid, D. W. Drumm, S. P. Russo, A. D. Greentree, *Sci. Rep.* **2017**, *7*, 1.

[61] C. Freysoldt, B. Grabowski, T. Hickel, J. Neugebauer, G. Kresse, A. Janotti, C. G. Van de Walle, *Rev. Mod. Phys.* **2014**, *86*, 253.

[62] C. Freysoldt, J. Neugebauer, C. G. Van de Walle, *Phys. Rev. Lett.* **2009**, *102*, 016402.

[63] H.-P. Komsa, N. Berseneva, A. V. Krasheninnikov, R. M. Nieminen, *Phys. Rev. X* **2014**, *4*, 031044.

[64] O. T. Hofmann, E. Zojer, L. Hörmann, A. Jeindl, R. J. Maurer, *Phys. Chem. Chem. Phys.* **2021**, *23*, 8132.

[65] L. Bellaiche, D. Vanderbilt, *Phys. Rev. B* **2000**, *61*, 7877.

[66] O. Lehtinen, H.-P. Komsa, A. Pulkin, M. B. Whitwick, M.-W. Chen, T. Lehnert, M. J. Mohn, O. V. Yazyev, A. Kis, U. Kaiser, A. V. Krasheninnikov, *ACS Nano* **2015**, *9*, 3274.

[67] C. Jia, B. Zhou, Q. Song, X. Zhang, Z. Jiang, *RSC Adv.* **2018**, *8*, 18837.

[68] R. Steudel, B. Eckert, *Elemental Sulfur and Sulfur-rich Compounds I* Springer, Berlin, Heidelberg **2003**, pp. 1–80.

[69] I. Haiduc, D. B. Sowerby, *The Chemistry of Inorganic Homo-and Heterocycles*, Vol. 2, Academic Press, New York **1987**.

[70] F. A. Devillanova, W.-W. Du Mont, *Handbook of Chalcogen Chemistry: New Perspectives in Sulfur, Selenium and Tellurium*, Vol. 1, Royal Society of Chemistry, Cambridge **2013**.

[71] K. Reuter, C. Stampf, M. Scheffler, *Handbook of Materials Modeling*, Springer, Netherlands **2005**, pp. 149–194.

[72] D. McQuarrie, *Statistical Mechanics*, Sterling Publishing Company **2000**.

Supporting Information: A Hybrid-DFT Study of Intrinsic Point Defects in MX_2 (M=Mo, W; X=S, Se) Monolayers

A. Akkoush,[1,2] Yair Litman,[3] and M. Rossi[1,2]

[1]*Fritz Haber Institute of the Max Planck Society, Faradayweg 4–6, 14195 Berlin, Germany*
[2]*MPI for the Structure and Dynamics of Matter,*
Luruper Chaussee 149, 22761 Hamburg, Germany
[3]*Yusuf Hamied Department of Chemistry, University of Cambridge, Lensfield Road, Cambridge, CB2 1EW,UK*
(Dated: April 28, 2023)

S1. SIMULATION DETAILS

A. Supercell Convergence

In order to identify the appropriate size of the supercell that prevents any potential interaction between defects, we have computed the formation energy difference of VX for the studied TMDC's with respect to various supercell sizes (fig.S1). The calculation is carried out using the PBE+MBD functional.
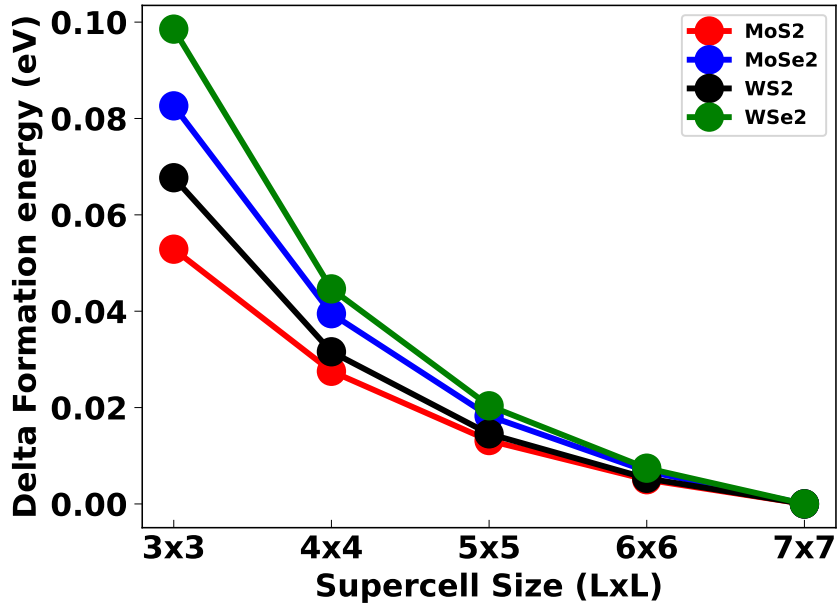

FIG. S1: Formation energy convergence of VX in MX_2 mono layers with supercell size.
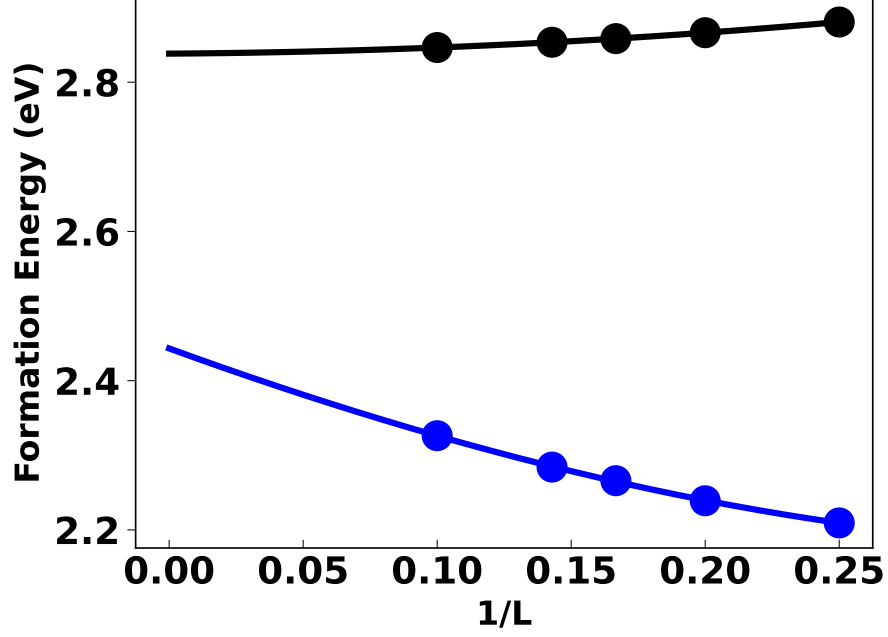
B. Charge Correction

FIG. S2: Formation energy of VS (-1) in blue and neutral VS in black created in MoS_2 monolayer using PBE, calculated via the VCA. Solid lines show the defect formation energies extrapolated to the dilute limit of a single defect in an extended material ($1/L \rightarrow 0$) where L is the multiple of the lattice constant.

C. Structure Optimization

TABLE S1: Geometry Relaxation with HSE06+MBD, a. shows the bond length between X and its corresponding additional X atom on top, b. shows the change between $M - M$ bond lengths of the equilateral triangle upon the introduction of X vacancy.

<table>
<tr><td colspan="4">(a)Add$X$</td></tr>
<tr><td>MoS_2</td><td>$MoSe_2$</td><td>WS_2</td><td>WSe_2</td></tr>
<tr><td>1.93</td><td>2.23</td><td>1.94</td><td>2.24</td></tr>
</table>

<table>
<tr><td colspan="4">(b)VX</td></tr>
<tr><td>MoS_2</td><td>$MoSe_2$</td><td>WS_2</td><td>WSe_2</td></tr>
<tr><td>0.10</td><td>0.17</td><td>0.15</td><td>0.22</td></tr>
</table>

D. Cluster Search

Different cluster shapes and sizes have been investigated in our search to find an optimal structure. Mainly, we show three types of clusters with different edge atoms (fig.S3). We show in the table S3 the bandgap using HSE06 and PBE for these clusters. In this work we have considered the hexagonal structure with 43% S edges based on band gap calculations as in table S2. The cluster was passivated by hydrogens to ensure a higher band gap and no edge electron states dominance as shown for the chosen cluster S3.
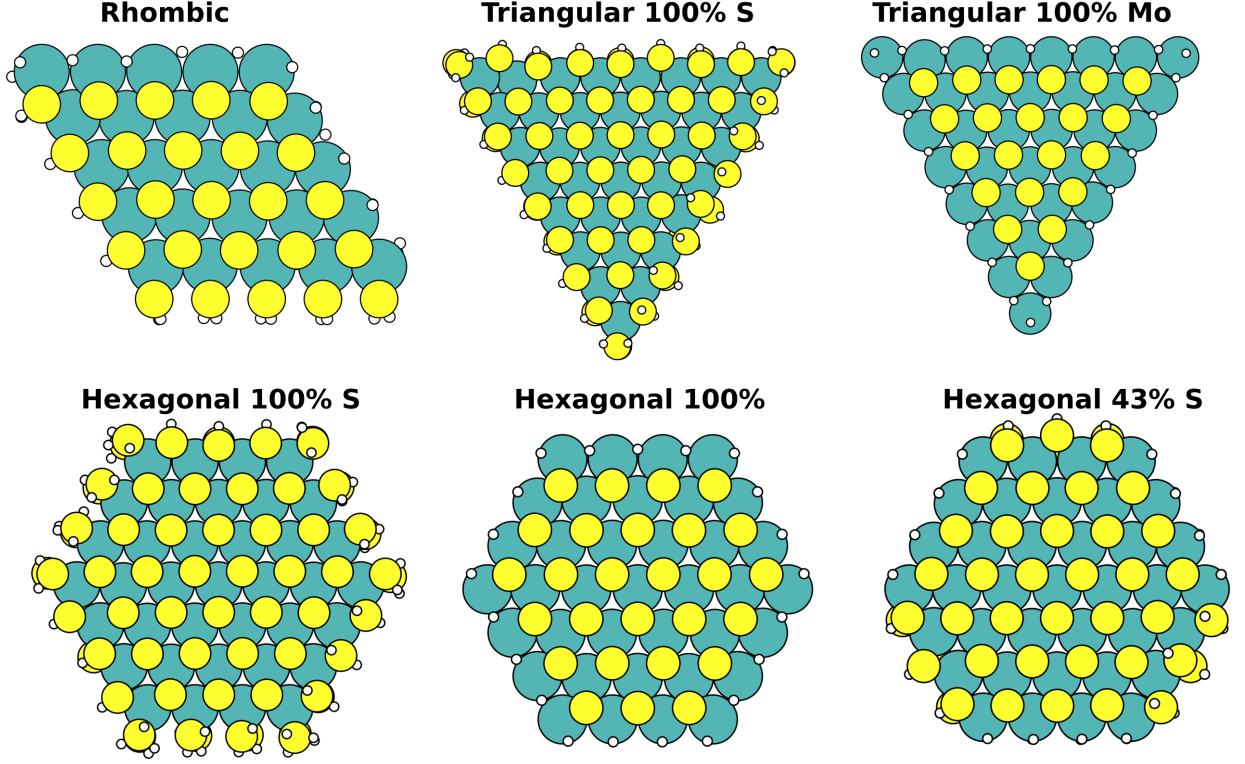
Rhombic **Triangular 100% S** **Triangular 100% Mo**

Hexagonal 100% S **Hexagonal 100%** **Hexagonal 43% S**

FIG. S3: MoS_2 cluster structures that has been investigated in this work

Systems	Rhombic 50% S	Triangular 100% S	Triangular 100% Mo	Hexagonal 100% S	Hexagonal 43% S (VS)	Hexagonal 100% Mo
E_{gap}[eV] (PBE)	0.139	0.045	0.024	0.014	0.226 (0.218)	0.0266
E_{gap}[eV] (HSE06)	0.093	0.141	0.177	0.030	0.676 (0.662)	0.274

TABLE S2: HOMO-LUMO bandgap of MoS_2 clusters using HSE06 and PBE functionals.

E. Band Gaps of Point Defects in MX_2

Systems	MoS_2	$MoSe_2$	WS_2	WSe_2
E_{gap}[eV] (PBE)	0.358	0.329	0.408	0.121
E_{gap}[eV] (HSE06)	0.694	0.621	0.871	0.730

TABLE S3: The bandgap variation between HSE06 and PBE of VM point defect in MX_2.

Systems	MoS_2	$MoSe_2$	WS_2	WSe_2
E_{gap}[eV] (PBE)	1.760	1.381	1.619	1.435
E_{gap}[eV] (HSE06)	2.194	1.935	2.242	1.813

TABLE S4: The bandgap variation between HSE06 and PBE of $AddX$ point defect in MX_2.

Systems	MoS$_2$	MoSe$_2$	WS$_2$	WSe$_2$
E_{gap}[eV] (PBE)	1.201	1.048	1.125	1.219
E_{gap}[eV] (HSE06)	1.768	1.546	1.736	1.475

TABLE S5: The bandgap variation between HSE06 and PBE of VX point defect in MX_2.

Systems	MoS$_2$	MoSe$_2$	WS$_2$	WSe$_2$
E_{gap}[eV] (PBE)	1.151	1.069	1.017	0.836
E_{gap}[eV] (HSE06)	1.688	1.512	1.603	1.374

TABLE S6: The bandgap variation between HSE06 and PBE of $VX2$ point defect in MX_2.

Systems	MoS$_2$	MoSe$_2$	WS$_2$	WSe$_2$
E_{gap}[eV] (PBE)	0.963	0.908	1.200	1.068
E_{gap}[eV] (HSE06)	1.525	1.458	1.675	1.440

TABLE S7: The bandgap variation between HSE06 and PBE of $VX22$ point defect in MX_2.

F. Impact of Temperature on the Formation Energy of Defects
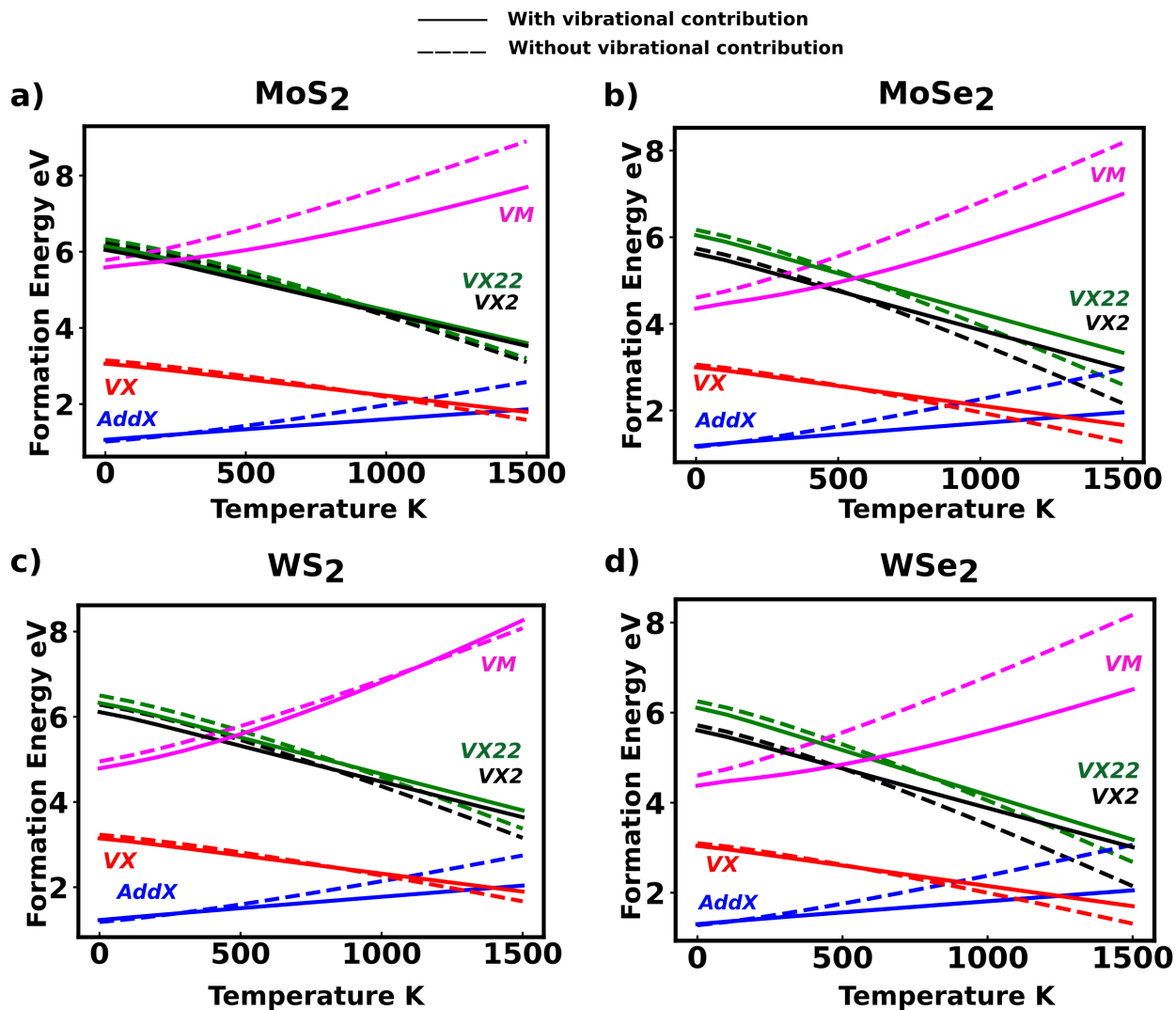
FIG. S4: Variation of formation energy (eV) of point defects for MX_2 monolayers as a function of temperature calculated with the HSE06+MBD functional at a S and Se partial pressure $p = 10^{-14}$ atm. The dashed lines represent the formation energy without the vibrational contribution $\Delta F(T)$ of the TMDCs and the solid lines the full formation energy.

G. Density of States of S Monovacancy in MoS$_2$ at Different Charge States
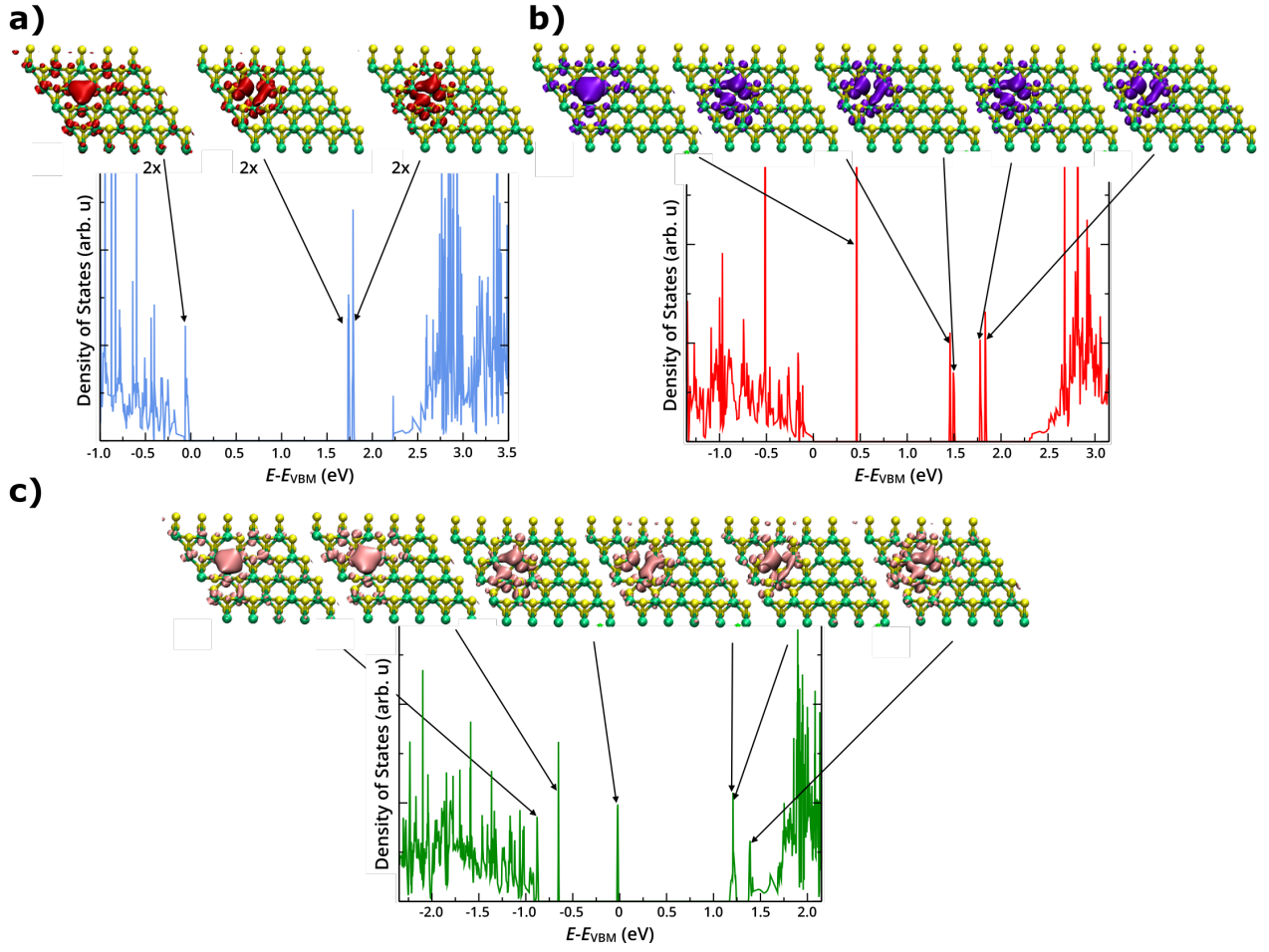
FIG. S5: Density of states and state-resolved electronic density of an MoS$_2$ monolayer containing (a) a neutral S monovacancy, (b) a positively charged S monovacancy and (c) a negatively charged S monovacancy, employing the HSE06 functional and including SOC.

H.   Density of States of Point Defects in MX$_2$ (HSE06)
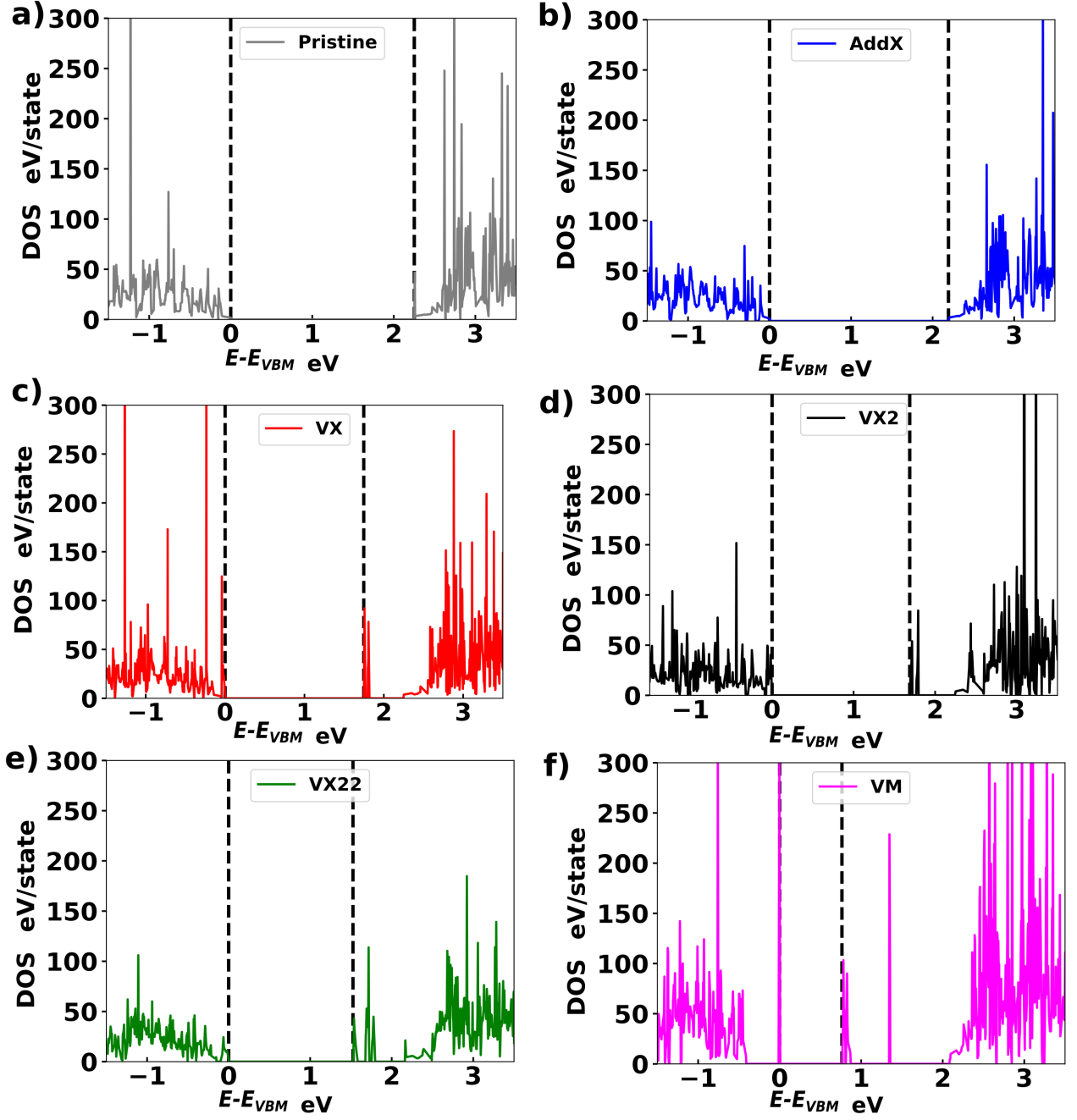
FIG. S6: Density of states of MoS$_2$ monolayer for the pristine and point defects under study using HSE06 exchange correlation and SOC.
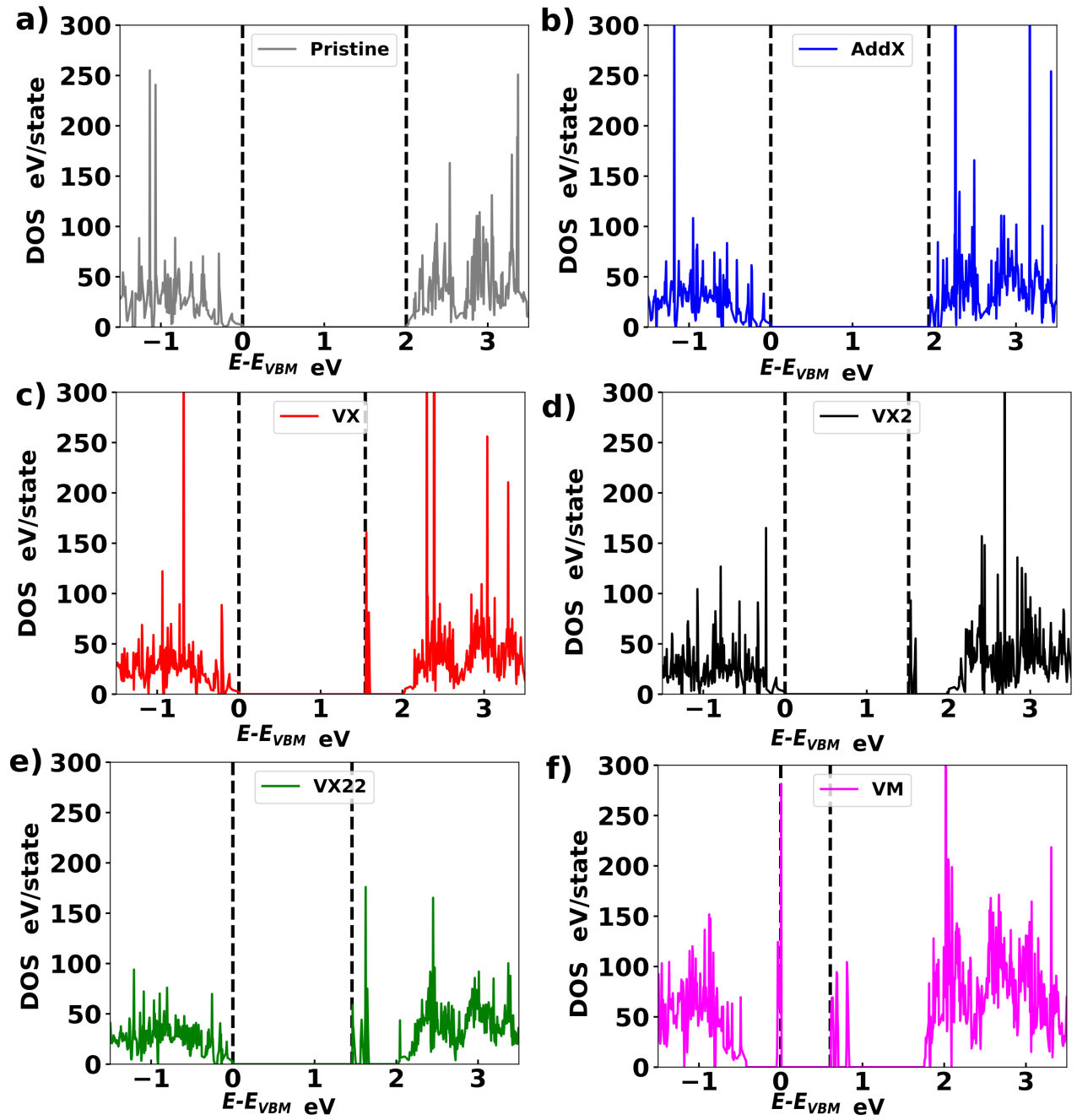
FIG. S7: Density of states of MoSe$_2$ monolayer for the pristine and point defects under study using HSE06 exchange correlation and SOC.
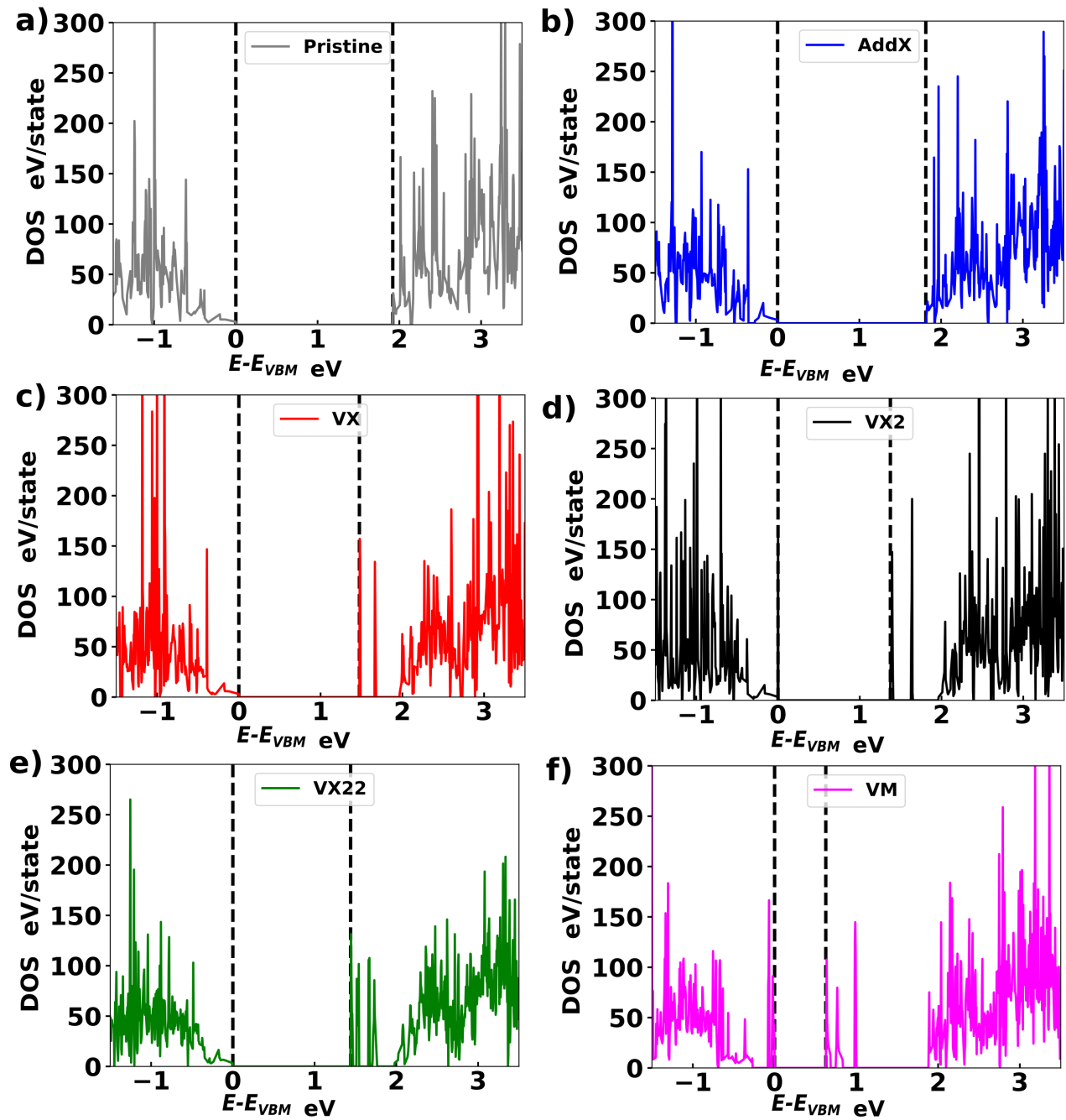
FIG. S8: Density of states of WS$_2$ monolayer for the pristine and point defects under study using HSE06 exchange correlation and SOC.
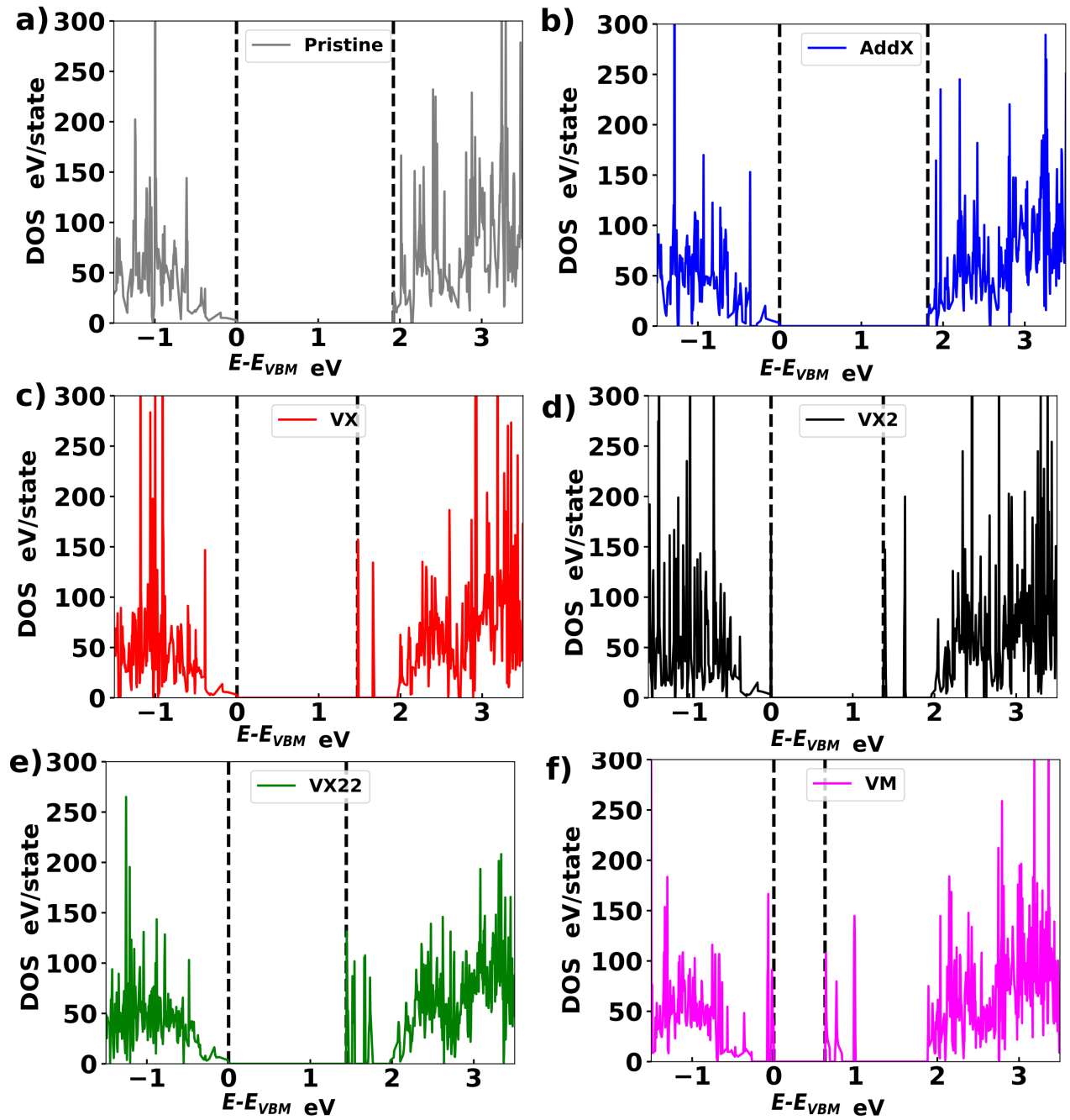
FIG. S9: Density of states of WSe$_2$ monolayer for the pristine and point defects under study using HSE06 exchange correlation and SOC.

5 | Conclusion

The motivation behind this thesis stems from the revolutionizing impact of 2D TMDC materials within the realm of materials science. In a quest to understand local vibrational fingerprints within these systems, I have discussed the significance of Raman spectroscopy as a widespread technique in fundamental research and materials characterization. Moreover, I have described how to calculate non-resonant Raman intensities using first principles methods like DFPT through the calculation of the electronic response to external electric field. This is the method used in this work. I have provided a case study that focused on pristine MoS_2 bulk and monolayer.

I have discussed the fact that Raman spectroscopy is subject to limitations such as the diffraction limit, which restricts the lateral resolution to approximately half the wavelength of the excitation laser. The small cross sections of Raman signals also poses challenges in observing molecules in nanoscale samples due to reduced interactions. To address these limitations, TERS is a novel method that offers access to physical, chemical, and dynamical properties at the nanoscale.

The enhancement mechanisms induced by TERS are primarily categorized into two components: chemical enhancements and electromagnetic enhancements. Chemical enhancement arises from the interaction between the molecule and the substrate or tip in the electronic ground state (chem-GS), the resonance between the applied electric field and molecular electronic state (chem-R), as well as charge transfer phenomena between the molecule and the substrate or tip (chem-CT).

Within the framework of the work towards this thesis, I have contributed to a paper (section 3.4) where a novel method based on first principles was introduced for calculating TERS. This method overcomes limitations of previous theoretical approaches that mainly rely on crude approximations of the local field. The presented method combines TD-DFT and DFPT in order to provide a realistic description of the electrical near field, with low computational costs. The method primarily focuses on describing the (EM) enhancements and chem-GS. This research highlights the significant role of chem-GS effects in shaping and intensifying TERS images, in particular for chemisorbed molecules, which is often overlooked in existing literature. For future developments, the evaluation of frequency-dependent polarizability tensors using TD-DFT would account for chem-R. Additionally, the development of a model enabling molecular point contact holds promise for significant enhancements through charge transfer. In fact, the importance of the enhancement of Raman scattering through charge transfer, was the subject of another paper, presented in section 3.5, to which I have contributed. A remarkable enhancement of Raman scattering upon the formation of a molecular point contact (MPC) of single C60 molecule junction using Ag tip adsorbed on Ag surface was observed. The findings provide valuable insights into the role of charge transfer in Raman scattering enhancement and shed light on the involvement of resonance Raman channels.

With these tools in hand, I could investigate the applications of TERS in two-dimensional TMDCs monolayers. In particular, I utilized TERS to study and understand the properties of defects in these materials. This was part of a comprehensive study, presented in section 4.3, where I have discussed the theoretical methods to characterize neutral and charge point defects in TMDC monolayers. I have explored the thermodynamics of defect formation theoretically and applied it to semi-conductor monolayer TMDCs like MoS_2, $MoSe_2$, WS_2, and WSe_2. This gave insights into the stability and relevance of different point defects, especially on vibrational contributions to defect stability. My focus was directed towards the examination of the sulfur monovacancy in MoS_2 through TERS. The TERS images revealed distinct variations in the vicinity of the defect that were not observable through traditional Raman techniques. The TERS calculations presented in this study offer encouraging results for future investigations. These findings lay the groundwork for a more extensive and detailed characterization of the local Raman signal surrounding defects in 2D material.

For future research, exploring molecules on defective surfaces could be promising, for example to investigate the behavior of molecules in the vicinity of such defects. This can provide insights into the adsorption, reactivity, and structural modifications of such a system. By combining experimental techniques, such as TERS, with advanced theoretical modeling discussed above, a potential for a comprehensive understanding of these molecular-surface interactions can be provided. As an example, MoS_2 produced via chemical vapor deposition with varied defect densities was subjected to 4-aminothiophenol (ATP), biphenyl-4-thiol (BPT) and 4-nitrothiophenol (NTP) molecules. The study employed x-ray photoelectron, Raman and photoluminescence spectroscopy to show that these molecules effectively repaired defects in single-layer MoS_2 and BPT functionalization led to increased photoluminescence intensity [128].

Bibliography

1. Borja Cirera, Yair Litman, Chenfang Lin, Alaa Akkoush, Adnan Hammud, Martin Wolf, Mariana Rossi, and Takashi Kumagai. Charge transfer-mediated dramatic enhancement of raman scattering upon molecular point contact formation. *Nano Letters*, 22(6):2170–2176, 2022.

2. Yair Litman, Franco P Bonafé, Alaa Akkoush, Heiko Appel, and Mariana Rossi. First-principles simulations of tip enhanced raman scattering reveal active role of substrate on high-resolution images. *The Journal of Physical Chemistry Letters*, 14:6850–6859, 2023.

3. Alaa Akkoush, Yair Litman, and Mariana Rossi. A hybrid-dft study of intrinsic point defects in mx2 (m= mo, w; x= s, se) monolayers. *physica status solidi (a)*, 2023.

4. C. V. Raman. A change of wave-length in light scattering. *Nature*, 121(3051):619, 4 1928.

5. A. C. Ferrari, J. C. Meyer, V. Scardaci, C. Casiraghi, M. Lazzeri, F. Mauri, S. Piscanec, D. Jiang, K. S. Novoselov, S. Roth, and A. K. Geim. Raman spectrum of graphene and graphene layers. *Phys. Rev. Lett.*, 97:187401, Oct 2006.

6. Gitti L. Frey, Reshef Tenne, Manyalibo J. Matthews, M. S. Dresselhaus, and G. Dresselhaus. Raman and resonance raman investigation of mos$_2$ nanoparticles. *Phys. Rev. B*, 60:2883–2892, Jul 1999.

7. H. Harima, T. Inoue, S. Nakashima, K. Furukawa, and M. Taneya. Electronic properties in p-type GaN studied by Raman scattering. *Applied Physics Letters*, 73(14):2000–2002, 10 1998.

8. Yanlin Sun, Xiaoshuang Chen, Lizhong Sun, Xuguang Guo, and Wei Lu. Nanoring structure and optical properties of ga8as8. *Chemical Physics Letters*, 381(3):397–403, 2003.

9. L.M. Malard, M.A. Pimenta, G. Dresselhaus, and M.S. Dresselhaus. Raman spectroscopy in graphene. *Physics Reports*, 473(5):51–87, 2009.

10. Rusen Yan, Jeffrey R. Simpson, Simone Bertolazzi, Jacopo Brivio, Michael Watson, Xufei Wu, Andras Kis, Tengfei Luo, Angela R. Hight Walker, and Huili Grace Xing. Thermal conductivity of monolayer molybdenum disulfide obtained from temperature-dependent raman spectroscopy. *ACS Nano*, 8(1):986–993, 2014. PMID: 24377295.

11. Namphung Peimyoo, Jingzhi Shang, Weihuang Yang, Yanlong Wang, Chunxiao Cong, and Ting Yu. Thermal conductivity determination of suspended mono- and bilayer ws2 by raman spectroscopy. *Nano Research*, 8(4):1210–1221, 04 2015.

12. G. Plechinger, S. Heydrich, J. Eroms, D. Weiss, C. Schüller, and T. Korn. Raman spectroscopy of the interlayer shear mode in few-layer MoS2 flakes. *Applied Physics Letters*, 101(10):101906, 09 2012.

13. Alexander A. Puretzky, Liangbo Liang, Xufan Li, Kai Xiao, Kai Wang, Masoud Mahjouri-Samani, Leonardo Basile, Juan Carlos Idrobo, Bobby G. Sumpter, Vincent Meunier, and David B. Geohegan. Low-frequency raman fingerprints of two-dimensional metal dichalcogenide layer stacking configurations. *ACS Nano*, 9(6):6333–6342, 2015. PMID: 25965878.

14. Ayse Berkdemir, Humberto R. Gutiérrez, Andrés R. Botello-Méndez, Néstor Perea-López, Ana Laura Elías, Chen-Ing Chia, Bei Wang, Vincent H. Crespi, Florentino López-Urías, Jean-Christophe Charlier, Humberto Terrones, and Mauricio Terrones. Identification of individual and few layers of ws2 using raman spectroscopy. *Scientific Reports*, 3(1):1755, 04 2013.

15. Sajedeh Manzeli, Dmitry Ovchinnikov, Diego Pasquier, Oleg V. Yazyev, and Andras Kis. 2d transition metal dichalcogenides. *Nature Reviews Materials*, 2(8):17033, 06 2017.

16. Marco Bernardi, Can Ataca, Maurizia Palummo, and Jeffrey C. Grossman. Optical and electronic properties of two-dimensional layered materials. *Nanophotonics*, 6(2):479–493, 2017.

17. B. Radisavljevic, A. Radenovic, J. Brivio, V. Giacometti, and A. Kis. Single-layer mos2 transistors. *Nature Nanotechnology*, 6(3):147–150, 03 2011.

18. William M. Parkin, Adrian Balan, Liangbo Liang, Paul Masih Das, Michael Lamparski, Carl H. Naylor, Julio A. Rodríguez-Manzo, A. T. Charlie Johnson, Vincent Meunier, and Marija Drndić. Raman shifts in electron-irradiated monolayer mos2. *ACS Nano*, 10(4):4134–4142, 2016. PMID: 26998814.

19. E. Abbe. Beiträge zur theorie des mikroskops und der mikroskopischen wahrnehmung. *Archiv für Mikroskopische Anatomie*, 9(1):413–468, 12 1873.

20. Andreas Otto. *Surface-enhanced Raman scattering: "Classical" and "Chemical" origins*, pages 289–418. Springer Berlin Heidelberg, Berlin, Heidelberg, 1984. ISBN 978-3-540-39522-5.

21. Raoul M. Stöckle, Yung Doug Suh, Volker Deckert, and Renato Zenobi. Nanoscale chemical analysis by tip-enhanced raman spectroscopy. *Chemical Physics Letters*, 318(1):131–136, 2000.

22. Achim Hartschuh, Erik J Sánchez, X Sunney Xie, and Lukas Novotny. High-resolution near-field raman microscopy of single-walled carbon nanotubes. *Physical Review Letters*, 90(9):095503, 2003.

23. Bruno Pettinger, Bin Ren, Gennaro Picardi, Rolf Schuster, and Gerhard Ertl. Nanoscale probing of adsorbed species by tip-enhanced raman spectroscopy. *Phys. Rev. Lett.*, 92:096101, Mar 2004.

24. Ryo Kato, Takayuki Umakoshi, Rhea Thankam Sam, and Prabhat Verma. Probing nanoscale defects and wrinkles in MoS2 by tip-enhanced Raman spectroscopic imaging. *Applied Physics Letters*, 114(7):073105, 02 2019.

25. Kyoung-Duck Park, Omar Khatib, Vasily Kravtsov, Genevieve Clark, Xiaodong Xu, and

Markus B. Raschke. Hybrid tip-enhanced nanospectroscopy and nanoimaging of monolayer wse2 with local strain control. *Nano Letters*, 16(4):2621–2627, 2016. PMID: 26937992.

26. Yung-Chang Lin, Dumitru O. Dumcenco, Ying-Sheng Huang, and Kazu Suenaga. Atomic mechanism of the semiconducting-to-metallic phase transition in single-layered mos2. *Nature Nanotechnology*, 9(5):391–396, 05 2014.

27. Qing Hua Wang, Kourosh Kalantar-Zadeh, Andras Kis, Jonathan N. Coleman, and Michael S. Strano. Electronics and optoelectronics of two-dimensional transition metal dichalcogenides. *Nature Nanotechnology*, 7(11):699–712, 11 2012.

28. Kin Fai Mak, Changgu Lee, James Hone, Jie Shan, and Tony F. Heinz. Atomically thin mos$_2$: A new direct-gap semiconductor. *Phys. Rev. Lett.*, 105:136805, Sep 2010.

29. A. Kuc, N. Zibouche, and T. Heine. Influence of quantum confinement on the electronic structure of the transition metal sulfide ts_2. *Phys. Rev. B*, 83:245213, Jun 2011.

30. Goki Eda, Hisato Yamaguchi, Damien Voiry, Takeshi Fujita, Mingwei Chen, and Manish Chhowalla. Photoluminescence from chemically exfoliated mos2. *Nano letters*, 11(12): 5111–5116, 2011.

31. Deoukchen Ghim, Qisheng Jiang, SiSi Cao, Srikanth Singamaneni, and Young-Shin Jun. Mechanically interlocked 1t/2h phases of mos2 nanosheets for solar thermal water purification. *Nano Energy*, 53:949–957, 2018.

32. Masaki Nakano, Yue Wang, Yuta Kashiwabara, Hideki Matsuoka, and Yoshihiro Iwasa. Layer-by-layer epitaxial growth of scalable wse2 on sapphire by molecular beam epitaxy. *Nano letters*, 17(9):5595–5599, 2017.

33. J. Wang, T. Li, Q. Wang, W. Wang, R. Shi, N. Wang, A. Amini, and C. Cheng. Controlled growth of atomically thin transition metal dichalcogenides via chemical vapor deposition method. *Materials Today Advances*, 8:100098, 2020.

34. Sajedeh Manzeli, Dmitry Ovchinnikov, Diego Pasquier, Oleg V Yazyev, and Andras Kis. 2d transition metal dichalcogenides. *Nature Reviews Materials*, 2(8):1–15, 2017.

35. Sujuan Ding, Fang Lin, and Chuanhong Jin. Quantify point defects in monolayer tungsten diselenide. *Nanotechnology*, 32(25):255701, 2021.

36. Lesheng Li and Emily A Carter. Defect-mediated charge-carrier trapping and nonradiative recombination in wse2 monolayers. *Journal of the American Chemical Society*, 141(26): 10451–10461, 2019.

37. Saboura Salehi and Alireza Saffarzadeh. Atomic defect states in monolayers of mos2 and ws2. *surface science*, 651:215–221, 2016.

38. Shang-Chun Lu and Jean-Pierre Leburton. Electronic structures of defects and magnetic impurities in mos 2 monolayers. *Nanoscale research letters*, 9:1–9, 2014.

39. Karsten Reuter, Catherine Stampf, and Matthias Scheffler. *AB Initio Atomistic Thermodynamics and Statistical Mechanics of Surface Properties and Functions*, pages 149–194.

Springer Netherlands, Dordrecht, 2005. ISBN 978-1-4020-3286-8.

40. Pierre Hohenberg and Walter Kohn. Inhomogeneous electron gas. *Physical review*, 136 (3B):B864, 1964.

41. Walter Kohn and Lu Jeu Sham. Self-consistent equations including exchange and correlation effects. *Physical review*, 140(4A):A1133, 1965.

42. John P Perdew and Karla Schmidt. Jacob's ladder of density functional approximations for the exchange-correlation energy. In *AIP Conference Proceedings*, volume 577, pages 1–20. American Institute of Physics, 2001.

43. Michael Rohlfing, Ruslan Temirov, and Frank Stefan Tautz. Adsorption structure and scanning tunneling data of a prototype organic-inorganic interface: Ptcda on ag (111). *Physical Review B*, 76(11):115421, 2007.

44. Lorenz Romaner, Dimitri Nabok, Peter Puschnig, Egbert Zojer, and Claudia Ambrosch-Draxl. Theoretical study of ptcda adsorbed on the coinage metal surfaces, ag (111), au (111) and cu (111). *New Journal of Physics*, 11(5):053010, 2009.

45. José I Martínez, Enrique Abad, Fernando Flores, and Jose Ortega. Simulating the organic-molecule/metal interface tcnq/au (111). *physica status solidi (b)*, 248(9):2044–2049, 2011.

46. John P Perdew, John A Chevary, Sy H Vosko, Koblar A Jackson, Mark R Pederson, Dig J Singh, and Carlos Fiolhais. Atoms, molecules, solids, and surfaces: Applications of the generalized gradient approximation for exchange and correlation. *Physical review B*, 46 (11):6671, 1992.

47. John P Perdew, Kieron Burke, and Matthias Ernzerhof. Generalized gradient approximation made simple. *Physical review letters*, 77(18):3865, 1996.

48. Philipp Haas, Fabien Tran, and Peter Blaha. Calculation of the lattice constant of solids with semilocal functionals. *Physical Review B*, 79(8):085104, 2009.

49. Philipp Haas, Fabien Tran, and Peter Blaha. Calculation of the lattice constant of solids with semilocal functionals. *Physical Review B*, 79(8):085104, 2009.

50. Fabien Tran, Robert Laskowski, Peter Blaha, and Karlheinz Schwarz. Performance on molecules, surfaces, and solids of the wu-cohen gga exchange-correlation energy functional. *Physical review B*, 75(11):115131, 2007.

51. Yingkai Zhang and Weitao Yang. Comment on "generalized gradient approximation made simple". *Physical Review Letters*, 80(4):890, 1998.

52. John P Perdew, Adrienn Ruzsinszky, Gábor I Csonka, Oleg A Vydrov, Gustavo E Scuseria, Lucian A Constantin, Xiaolan Zhou, and Kieron Burke. Restoring the density-gradient expansion for exchange in solids and surfaces. *Physical review letters*, 100(13):136406, 2008.

53. BHLB Hammer, Lars Bruno Hansen, and Jens Kehlet Nørskov. Improved adsorption energetics within density-functional theory using revised perdew-burke-ernzerhof functionals.

Physical review B, 59(11):7413, 1999.

54. Alessandro Stroppa and Georg Kresse. The shortcomings of semi-local and hybrid functionals: what we can learn from surface science studies. *New Journal of Physics*, 10(6): 063020, 2008.

55. Chen Li, Xiao Zheng, Neil Qiang Su, and Weitao Yang. Localized orbital scaling correction for systematic elimination of delocalization error in density functional approximations. *National Science Review*, 5(2):203–215, 09 2017.

56. Yingkai Zhang and Weitao Yang. A challenge for density functionals: Self-interaction error increases for systems with a noninteger number of electrons. *The Journal of chemical physics*, 109(7):2604–2608, 1998.

57. M Van Faassen, PL De Boeij, R Van Leeuwen, JA Berger, and JG Snijders. Ultranonlocality in time-dependent current-density-functional theory: Application to conjugated polymers. *Physical review letters*, 88(18):186401, 2002.

58. Paula Mori-Sánchez, Qin Wu, and Weitao Yang. Accurate polymer polarizabilities with exact exchange density-functional theory. *The Journal of chemical physics*, 119(21):11001–11004, 2003.

59. Aron J Cohen, Paula Mori-Sánchez, and Weitao Yang. Fractional charge perspective on the band gap in density-functional theory. *Physical Review B*, 77(11):115123, 2008.

60. F Flores, J Ortega, and H Vázquez. Modelling energy level alignment at organic interfaces and density functional theory. *Physical Chemistry Chemical Physics*, 11(39):8658–8675, 2009.

61. Xiao Zheng, Chen Li, Dadi Zhang, and Weitao Yang. Scaling correction approaches for reducing delocalization error in density functional approximations. *Science China Chemistry*, 58:1825–1844, 2015.

62. Aron J Cohen, Paula Mori-Sánchez, and Weitao Yang. Insights into current limitations of density functional theory. *Science*, 321(5890):792–794, 2008.

63. John P Perdew, Matthias Ernzerhof, and Kieron Burke. Rationale for mixing exact exchange with density functional approximations. *The Journal of chemical physics*, 105(22): 9982–9985, 1996.

64. Joachim Paier, Martijn Marsman, and Georg Kresse. Why does the b3lyp hybrid functional fail for metals? *The Journal of chemical physics*, 127(2):024103, 2007.

65. Xinming Qin, Honghui Shang, Lei Xu, Wei Hu, Jinlong Yang, Shigang Li, and Yunquan Zhang. The static parallel distribution algorithms for hybrid density-functional calculations in honpas package. *The International Journal of High Performance Computing Applications*, 34(2):159–168, 2020.

66. Jochen Heyd, Gustavo E Scuseria, and Matthias Ernzerhof. Hybrid functionals based on a screened coulomb potential. *The Journal of chemical physics*, 118(18):8207–8215, 2003.

67. Jochen Heyd and Gustavo E Scuseria. Efficient hybrid density functional calculations in solids: Assessment of the heyd–scuseria–ernzerhof screened coulomb hybrid functional. *The Journal of chemical physics*, 121(3):1187–1192, 2004.

68. Jochen Heyd, Juan E Peralta, Gustavo E Scuseria, and Richard L Martin. Energy band gaps and lattice parameters evaluated with the heyd-scuseria-ernzerhof screened hybrid functional. *The Journal of chemical physics*, 123(17):174101, 2005.

69. Peter Deák, Bálint Aradi, Thomas Frauenheim, Erik Janzén, and Adam Gali. Accurate defect levels obtained from the hse06 range-separated hybrid functional. *Phys. Rev. B*, 81: 153203, Apr 2010.

70. Th Böker, R Severin, A Müller, C Janowitz, R Manzke, D Voß, P Krüger, A Mazur, and JJPRB Pollmann. Band structure of mos 2, mose 2, and α- mote 2: Angle-resolved photoelectron spectroscopy and ab initio calculations. *Physical Review B*, 64(23):235305, 2001.

71. WJ Schutte, JL De Boer, and F Jellinek. Crystal structures of tungsten disulfide and diselenide. *Journal of Solid State Chemistry*, 70(2):207–209, 1987.

72. Jochen Heyd, Gustavo E Scuseria, and Matthias Ernzerhof. Hybrid functionals based on a screened coulomb potential. *The Journal of chemical physics*, 118(18):8207–8215, 2003.

73. Guo-Xu Zhang, Alexandre Tkatchenko, Joachim Paier, Heiko Appel, and Matthias Scheffler. Van der waals interactions in ionic and semiconductor solids. *Physical review letters*, 107(24):245501, 2011.

74. F. London. Zur Theorie und Systematik der Molekularkräfte. *Zeitschrift fur Physik*, 63 (3-4):245–279, March 1930.

75. Henrik Rydberg, DC Langreth, M Dion, and BI Lundqvist. Long-and medium-ranged nonlocal correlations in density functional theory. *preparation for PRB*, 2001.

76. P Lazić, M Alaei, N Atodiresei, V Caciuc, R Brako, and S Blügel. Density functional theory with nonlocal correlation: A key to the solution of the co adsorption puzzle. *Physical Review B*, 81(4):045401, 2010.

77. Julien Toulouse, Elisa Rebolini, Tim Gould, John F Dobson, Prasenjit Seal, and János G Angyán. Assessment of range-separated time-dependent density-functional theory for calculating c 6 dispersion coefficients. *The Journal of chemical physics*, 138(19):194106, 2013.

78. Axel D Becke and Erin R Johnson. A unified density-functional treatment of dynamical, nondynamical, and dispersion correlations. *The Journal of chemical physics*, 127(12): 124108, 2007.

79. Axel D Becke and Erin R Johnson. Exchange-hole dipole moment and the dispersion interaction revisited. *The Journal of chemical physics*, 127(15):154108, 2007.

80. Xiang Chu and Alexander Dalgarno. Linear response time-dependent density functional theory for van der waals coefficients. *The Journal of chemical physics*, 121(9):4083–4088,

2004.

81. Alexandre Tkatchenko and Matthias Scheffler. Accurate molecular van der waals interactions from ground-state electron density and free-atom reference data. *Phys. Rev. Lett.*, 102:073005, Feb 2009.

82. Evgenni Mikhailovich Lifshitz, M Hamermesh, et al. The theory of molecular attractive forces between solids. In *Perspectives in theoretical physics*, pages 329–349. Elsevier, 1992.

83. E. Zaremba and W. Kohn. Van der waals interaction between an atom and a solid surface. *Phys. Rev. B*, 13:2270–2285, Mar 1976.

84. Victor G. Ruiz, Wei Liu, Egbert Zojer, Matthias Scheffler, and Alexandre Tkatchenko. Density-functional theory with screened van der waals interactions for the modeling of hybrid inorganic-organic systems. *Phys. Rev. Lett.*, 108:146103, Apr 2012.

85. Alexandre Tkatchenko, Robert A DiStasio Jr, Roberto Car, and Matthias Scheffler. Accurate and efficient method for many-body van der waals interactions. *Physical review letters*, 108(23):236402, 2012.

86. Jan Hermann and Alexandre Tkatchenko. Density functional model for van der waals interactions: Unifying many-body atomic approaches with nonlocal functionals. *Phys. Rev. Lett.*, 124:146401, Apr 2020.

87. Wei Liu, Friedrich Maaß, Martin Willenbockel, Christopher Bronner, Michael Schulze, Serguei Soubatch, F Stefan Tautz, Petra Tegeder, and Alexandre Tkatchenko. Quantitative prediction of molecular adsorption: structure and binding of benzene on coinage metals. *Physical review letters*, 115(3):036104, 2015.

88. Jie Jiang, Ruth Pachter, and Shin Mou. Tunability in the optical response of defective monolayer wse 2 by computational analysis. *Nanoscale*, 10(28):13751–13760, 2018.

89. John B Goodenough. Spin-orbit-coupling effects in transition-metal compounds. *Physical Review*, 171(2):466, 1968.

90. William P. Huhn and Volker Blum. One-hundred-three compound band-structure benchmark of post-self-consistent spin-orbit coupling treatments in density functional theory. *Phys. Rev. Mater.*, 1:033803, Aug 2017.

91. Honghui Shang, Nathaniel Raimbault, Patrick Rinke, Matthias Scheffler, Mariana Rossi, and Christian Carbogno. All-electron, real-space perturbation theory for homogeneous electric fields: theory, implementation, and application within dft. *New Journal of Physics*, 20(7):073040, 2018.

92. Volker Blum, Ralf Gehrke, Felix Hanke, Paula Havu, Ville Havu, Xinguo Ren, Karsten Reuter, and Matthias Scheffler. Ab initio molecular simulations with numeric atom-centered orbitals. *Computer Physics Communications*, 180(11):2175–2196, 2009.

93. D.A. Long. *The Raman Effect: A Unified Treatment of the Theory of Raman Scattering by Molecules*. Wiley, 2002. ISBN 9780471490289.

94. B. Baumslag and B. Chandler. *Schaum's Outline of Group Theory*. Schaum's outline series in mathematics. McGraw-Hill Education, 1968. ISBN 9780070041240.

95. Georg Placzek. Rayleigh-streuung und raman-effekt. *(No Title)*, 1934.

96. William Hayes and Rodney Loudon. Scattering of light by crystals. *(No Title)*, 1978.

97. YU Peter and Manuel Cardona. *Fundamentals of semiconductors: physics and materials properties*. Springer Science & Business Media, 2010.

98. Xin Zhang, Qing-Hai Tan, Jiang-Bin Wu, Wei Shi, and Ping-Heng Tan. Review on the raman spectroscopy of different types of layered materials. *Nanoscale*, 8(12):6435–6450, 2016.

99. E.H. Synge. A suggested method for extending microscopic resolution into the ultra-microscopic region. *The London, Edinburgh, and Dublin Philosophical Magazine and Journal of Science*, 6(35):356–362, 1928.

100. Dieter W Pohl, Winfried Denk, and Mark Lanz. Optical stethoscopy: Image recording with resolution $\lambda/20$. *Applied physics letters*, 44(7):651–653, 1984.

101. Gerd Binnig, Calvin F Quate, and Ch Gerber. Atomic force microscope. *Physical review letters*, 56(9):930, 1986.

102. John Wessel. Surface-enhanced optical microscopy. *J. Opt. Soc. Am. B*, 2(9):1538–1541, Sep 1985.

103. Daniel Courjon and C Bainier. Near field microscopy and near field optics. *Reports on progress in Physics*, 57(10):989, 1994.

104. RC Reddick, RJ Warmack, and TL Ferrell. New form of scanning optical microscopy. *Physical Review B*, 39(1):767, 1989.

105. Eric Betzig, A Lewis, A Harootunian, M Isaacson, and E Kratschmer. Near field scanning optical microscopy (nsom): development and biophysical applications. *Biophysical journal*, 49(1):269–279, 1986.

106. AMAA Lewis, Michael Isaacson, Alec Harootunian, and A Muray. Development of a 500 å spatial resolution light microscope: I. light is efficiently transmitted through $\lambda/16$ diameter apertures. *Ultramicroscopy*, 13(3):227–231, 1984.

107. Xiaolei Shi and Lambertus Hesselink. Mechanisms for enhancing power throughput from planar nano-apertures for near-field optical data storage. *Japanese journal of applied physics*, 41(3S):1632, 2002.

108. Achim Hartschuh, Erik J. Sánchez, X. Sunney Xie, and Lukas Novotny. High-resolution near-field raman microscopy of single-walled carbon nanotubes. *Phys. Rev. Lett.*, 90:095503, Mar 2003.

109. Yasushi Inouye and Satoshi Kawata. Near-field scanning optical microscope with a metallic probe tip. *Optics letters*, 19(3):159–161, 1994.

110. FYHK Zenhausern, Y Martin, and HK Wickramasinghe. Scanning interferometric apertureless microscopy: optical imaging at 10 angstrom resolution. *Science*, 269(5227):1083–1085, 1995.

111. Lukas Novotny and Bert Hecht. *Principles of nano-optics.* Cambridge university press, 2012.

112. D Roy, CM Williams, and K Mingard. Single-crystal gold tip for tip-enhanced raman spectroscopy. *Journal of Vacuum Science & Technology B, Nanotechnology and Microelectronics: Materials, Processing, Measurement, and Phenomena*, 28(3):631–634, 2010.

113. Weihua Zhang, Boon Siang Yeo, Thomas Schmid, and Renato Zenobi. Single molecule tip-enhanced raman spectroscopy with silver tips. *The Journal of Physical Chemistry C*, 111(4):1733–1738, 2007.

114. Lasse Jensen, Christine M Aikens, and George C Schatz. Electronic structure methods for studying surface-enhanced raman scattering. *Chemical Society Reviews*, 37(5):1061–1073, 2008.

115. Chao Zhang, Bao-Qin Chen, and Zhi-Yuan Li. Optical origin of subnanometer resolution in tip-enhanced raman mapping. *The Journal of Physical Chemistry C*, 119(21):11858–11871, 2015.

116. Federico Latorre, Stephan Kupfer, Thomas Bocklitz, Daniel Kinzel, Steffen Trautmann, Stefanie Gräfe, and Volker Deckert. Spatial resolution of tip-enhanced raman spectroscopy–dft assessment of the chemical effect. *Nanoscale*, 8(19):10229–10239, 2016.

117. Wei Cai and William D Nix. *Imperfections in crystalline solids.* Cambridge University Press, 2016.

118. Christoph Freysoldt, Blazej Grabowski, Tilmann Hickel, Jörg Neugebauer, Georg Kresse, Anderson Janotti, and Chris G Van de Walle. First-principles calculations for point defects in solids. *Reviews of modern physics*, 86(1):253, 2014.

119. G Makov and MC Payne. Periodic boundary conditions in ab initio calculations. *Physical Review B*, 51(7):4014, 1995.

120. Christoph Freysoldt, Jörg Neugebauer, and Chris G Van de Walle. Fully ab initio finite-size corrections for charged-defect supercell calculations. *Physical review letters*, 102(1):016402, 2009.

121. Christoph Freysoldt, Jörg Neugebauer, and Chris G Van de Walle. Electrostatic interactions between charged defects in supercells. *physica status solidi (b)*, 248(5):1067–1076, 2011.

122. N.J Ramer and A.M Rappe. Application of a new virtual crystal approach for the study of disordered perovskites. *Journal of Physics and Chemistry of Solids*, 61(2):315–320, 2000.

123. L. Bellaiche and David Vanderbilt. Virtual crystal approximation revisited: Application to dielectric and piezoelectric properties of perovskites. *Phys. Rev. B*, 61:7877–7882, Mar

2000.

124. Norina A. Richter, Sabrina Sicolo, Sergey V. Levchenko, Joachim Sauer, and Matthias Scheffler. Concentration of Vacancies at Metal-Oxide Surfaces: Case Study of MgO(100). *Physical Review Letters*, 111(4):045502, 2013.

125. Xi Zhang, Blazej Grabowski, Tilmann Hickel, and Jörg Neugebauer. Calculating free energies of point defects from ab initio. *Computational Materials Science*, 148:249–259, 2018.

126. D.A. McQuarrie. *Statistical Mechanics*. G - Reference,Information and Interdisciplinary Subjects Series. University Science Books, 2000. ISBN 9781891389153.

127. MW Chase, CA Davies, JR Downey, DJ Frurip, RA McDonald, and AN Syverud. Nist-janaf thermodynamic tables. *J. Phys. Chem. Ref. Data Monograph*, 9, 1998.

128. Giovanna Feraco, Oreste De Luca, Ali Syari'ati, Sardar Hameed, Abdurrahman Ali El Yumin, Jianting Ye, Raffaele G Agostino, and Petra Rudolf. Different healing characteristics of thiol-bearing molecules on cvd-grown mos2. *Journal of Physics: Materials*, 6(3):034006, jul 2023.

129. John P. Perdew, Robert G. Parr, Mel Levy, and Jose L. Balduz. Density-functional theory for fractional particle number: Derivative discontinuities of the energy. *Phys. Rev. Lett.*, 49:1691–1694, Dec 1982.

130. Yingkai Zhang and Weitao Yang. A challenge for density functionals: Self-interaction error increases for systems with a noninteger number of electrons. *The Journal of chemical physics*, 109(7):2604–2608, 1998.

131. Paula Mori-Sánchez, Aron J. Cohen, and Weitao Yang. Localization and delocalization errors in density functional theory and implications for band-gap prediction. *Phys. Rev. Lett.*, 100:146401, Apr 2008.

A | Appendix

Electron Delocalization:

The energy of the system in DFT has to follow Perdew-Parr-Levy-Balduz (PPLB)[129,130] condition, that states that the total energy $E(N)$, should follow a linear relationship as a function of the number of electrons, N, interpolating between integer values. PPLB holds true for the exact functional, however, when it is violated delocalization/localization error arises[129,130]. PPLB can be mathematically expressed as:

$$E_{\text{gap}}^{integer} = [E(N+1) - E(N)] - [E(N) - E(N-1)] = I - A \qquad (A.1)$$

where $E_{gap}^{integer}$ represents the energy of the gap, I and A are the ionization energy and the electron affinity, respectively.

Alternatively, the energy of the gap can also be expressed as the difference between the left and right energy derivatives with respect to the electron number at the integer point N[131]:

$$E_{\text{gap}}^{deriv} = \left.\frac{\partial E}{\partial N}\right|_{N+\delta} - \left.\frac{\partial E}{\partial N}\right|_{N-\delta} \qquad (A.2)$$

It has been demonstrated that when the exchange-correlation energy can be expressed as a specific function of electron density or the Kohn-Sham reduced density matrix, it is possible to differentiate this functional explicitly as,

$$\epsilon_{\text{LUMO}} = \lim_{\delta \to 0} \left.\frac{\partial E}{\partial N}\right|_{N+\delta}$$

$$\epsilon_{\text{HOMO}} = \lim_{\delta \to 0} \left.\frac{\partial E}{\partial N}\right|_{N-\delta}$$

ϵ_{HOMO} and ϵ_{LUMO} represent the Kohn-Sham eigenvalues associated with highest occupied molecular orbital and lowest unoccupied molecular orbital, respectively. Therefore, $E_{\text{gap}}^{deriv} = \epsilon_{gap}^{KS} = \epsilon_{LUMO} - \epsilon_{HOMO}$. However, the exact PPLB condition can be expressed as:

$$\lim_{\delta \to 0} \left.\frac{\partial E}{\partial N}\right|_{N+\delta} = \epsilon_{HOMO} = -I$$

and

$$\lim_{\delta \to 0} \frac{\partial E}{\partial N}\bigg|_{N-\delta} = \epsilon_{LUMO} = -A$$

The above leads to the fact that $E_{gap}^{integer} = E_{gap}^{deriv}$. However, inherent delocalization or localization errors are present, for example, LDA and GGA tend to produce convex energy $E(N)$ (delocalization). As a result, these methods typically predict ϵ_{HOMO} that are too high and ϵ_{LUMO} that are too low, leading to an underestimation of the E_{gap}^{deriv}. While, HF method often yields concave energy and leads to localization of electrons[61].